ABSTRACT

Title of Dissertation:	WATER, ION, AND GRAPHENE: AN ODYSSEY THROUGH THE MOLECULAR SIMULATIONS
	Yanbin Wang Doctor of Philosophy, 2019
Dissertation directed by:	Professor Siddhartha Das, Mechanical Engineering

Water is known as the most common and complicated liquid on earth. Meanwhile, graphene, defined as single/few layer graphite, is the first member in the 2-dimensional materials family and has emerged as a magic material. Interactions between water and graphene generate many interesting phenomena and applications. This thesis focuses on applying molecular dynamics (MD), a powerful computational tool, for investigating the graphene-water interactions associated with various energetic and environmental applications, ranging from the wettability modification, species adsorption, and nanofluidic transport to seawater desalination. A key

component of one domain of applications involves a third component, namely salt ions. This thesis attempts that and discovers a fundamentally new way in which the behavior of ions with the air-water interfaces should be probed.

In Chapter 1, we introduce the motivation and methods and the overall structure of this thesis. Chapter 2 focuses on how MD simulations connect the statistical mechanics theory with the experimental observations. Chapter 3 discusses the simulation results revealing that the spreading of a droplet on a nanopillared graphene surface is driven by a pinned contact line and bending liquid-surface dynamics. Chapter 4 probes the interactions between a water drop and a holey graphene membrane, which is prepared by removing carbon atoms in a circular shape and which can serve as catalyst carriers. Accordingly, chapter 5 studies the effects of various terminations on water-holey graphene interactions, showing that water flows faster and more thoroughly through the membrane with hydrophobic terminations, compared to that with hydrophilic terminations. In chapter 6, simulations describe the generation of enhanced water-graphene surface area during the water-holey-graphene interactions in presence of an applied time-varying force on the water drop. In chapter 7, we focus on the ion-water interaction at the water-air interface to fully understand the fluidic dynamics during any seawater desalination. Our research revisits the energetic change while ion approaches water-air interface and shows that the presence of ion at the interface enhances capillary-wave fluctuation. Finally, in chapter 8 we summarize the main findings of the thesis and provide the scope of future research.

WATER, ION, AND GRAPHENE: AN ODYSSEY THROUGH THE MOLECULAR SIMULATIONS

By

Yanbin Wang

Dissertation submitted to the Faculty of the Graduate School of the

University of Maryland, College Park, in partial fulfillment

of the requirements for the degree of

Doctor of Philosophy

2019

Advisory Committee:

Professor Siddhartha Das, Chair

Professor Amir Riaz

Professor Peter Chung

Professor Yifei Mo

Professor Liangbing Hu

Acknowledgements

Throughout the days of my Ph.D. journey, I have been improving myself in the scientific understandings and problem-solving skills. Of course, this cannot be done without helps and guidance. Here, I would like to use this chance to express my appreciations to the people open their minds to interact with me in a beautiful way.

First, I would like to express my appreciation to my advisor Prof. Siddhartha Das who gave me enormous and unconditional support since the very first day I began my Ph.D. journey. I am extremely grateful to have the opportunity to join the group and work with my groupmates. As I focused on experimental research during my Master program at Materials Science and Engineering department, I lacked skills to conduct numerical analysis and computational simulations. But Prof. Das was very patient with me and offered tremendous amount of support without pressurizing me to produce quick results. Under Dr. Das' kind and care supervision, I developed a firm understanding on statistical mechanics and molecular dynamics simulations. Furthermore, I appreciate Dr. Das' initiative to ensure that I could attend multiple conferences to present my research and meet with other researchers from various institutes.

Second, I would like to express my deep gratitude to Prof. Liangbing Hu, who was my Master supervisor. During my Masters program, Prof. Hu guided me into the field of research in the first two-year of my study at the University of Maryland. Furthermore, I received systematic training from Dr.Wei Luo, Dr. Kun Fu, Dr. Chaoji Chen, Dr. Zhen Liu, the post-docs at that time on multiple projects. The experimental experience assists me to combine the experimental observations with my theoretical research in my Ph.D. program. What really touched my emotions was the moment that Prof. Hu allowed me to continue to use the laboratory in my first

year of Ph.D. when Prof. Das had a funded experimental project, but the lab was still under preparation. Both Prof. Hu and Prof. Das have immensely contributed to my personal and professional development in my 5 years journey at UMD.

Then, I must thank my committee members, Prof. Das, Prof. Hu, Prof. Ryan Sochol, Prof. Amir Riaz, Prof. Peter Chung, and Prof. Yifei Mo for offering me critical comments on thesis and constructive suggestions on my work. I also thank Prof. Ryan Sochol for offering me teaching assistant position in the first semester of my Ph.D., which I really learned a lot of knowledge about 3D printing. Such knowledge is critical to me and to our group as we received multiple sources of funding on 3D printing. Also, I thank Dr. Chandra Thamire and Prof. Jungho Kim for offering me TA positions.

Since my Ph.D. research focuses on carrying out computational simulations to investigate the chemical physical problems, I must thank the Deepthought2 High-Performance Computing (HPC) cluster at UMD for providing computational source. Besides, I must thank Prof. Davinder Anand and Mr. Dylan Hazelwood from Center for Engineering Concepts Development (CECD), who generously provided funding supports in the first two years of my Ph.D. journey.

Here, I would like to thank my friends at UMD. The great company is crucial to me to study, work and research at a place 10,000 miles away from my hometown. Dr. Chen Guang, Dr. Shayandev Sinha, Haoyuan Jing, Parth Desai, Harnoor Sachar, Bhargav Chava from Prof. Das group, who work with me for years and offer priceless discussions on many problems. I truly appreciate their help. Besides, Dr. Yanan Chen, Dr. Yonggang Yao, Dr. Mingwei Zhu, Dr. Jiayu Wan, Dr. Yubing Zhou, Xie Hua from Prof. Hu group are always by my side whenever I encounter any difficulties. I really enjoy my Ph.D. because of so many great companies.

Lastly, but the most importantly, I thank my wife Xuewen Zhou to be there in my life from the beginning of my Ph.D. and encouraging me to explore the exciting world of science and engineering. Whenever I get stuck with difficult problems, her support is just like the first light flying through the darkest dawn. Only with her, I could have made this far.

Yanbin Wang

October 23, 2019

Articles Resulting from this Thesis

Chapter 3 ***Y.Wang.***, *J.Andrews., L.Hu.,S.Das.* Drop spreading on a superhydrophobic surface: pinned contact line and bending liquid surface. *Phys. Chem. Chem. Phys*., 2017,19, 14442-14452

Chapter 4 ***Y.Wang.***, *S.Shiha., L.Hu.,S.Das.* Interaction between a water drop and holey graphene: retarded imbibition and generation of novel water–graphene wetting states. *Phys. Chem. Chem. Phys***.**, 2017,**19**, 27421-27434

Chapter 5 ***Y.Wang.***, *S.Shiha., L.Hu.,S.Das.* Dynamics of a Water Nanodrop through a Holey Graphene Matrix: Role of Surface Functionalization, Capillarity, and Applied Forcing. *J. Phys. Chem. C* 2018, 122, 23, 12243-12250

Chapter 6 ***Y.Wang.***, *K.Ahuja.,S.Shiha., P.Desai.,,S.Das.* Water–Holey-Graphene Interactions: Route to Highly Enhanced Water-Accessible Graphene Surface Area. *ACS Appl. Nano Mater.* 2018, 1, 10, 5907-5919

Chapter 7 ***Y.Wang.***, *S.Shiha., P.Desai.,,H.Jing., S.Das.* Ion at Air–Water Interface Enhances Capillary Wave Fluctuations: Energetics of Ion Adsorption. *J. Am. Chem. Soc.* 2018, 140, 40, 12853-12861

Table of Contents

Acknowledgements ii
Articles Resulting from this Thesis v
Table of Contents vi
List of Figures x
Chapter 1: Background and motivation 1
1.1 Introduction to water/graphene interactions 1
1.2 Introduction to molecular dynamics simulations 4
1.3 Thesis Structure 9
Chapter 2: Basics of Molecular Dynamics Simulations Relevant for the Present Thesis 10
2.1 Fundamentals of molecular dynamics simulations 10
2.2. Thermodynamics 13
2.3 Dynamics 17
2.3 Post-analysis 24
Chapter 3: Drop spreading on a superhydrophobic surface: pinned contact line and bending liquid surface Introduction 26
3.1 Introduction 26
3.2 Molecular dynamics simulations 30
3.3 Results 39
3.4. Discussions 49
3.5 Comparison with the experimental findings 53
3.6 Choice of the simulation system 54
3.7 Conclusions 54
Chapter 4: Interaction between a water drop and holey graphene: retarded imbibition and generation of novel water–graphene wetting states 56
4.1 Introduction 56
4.2 Molecular dynamics simulations 59
4.2.1 Summary of simulation procedure 59
4.2.2 Motivation for the choice of system geometry 62
4.3 Results 82

4.3.1 Case 1: combined spreading–imbibition dynamics for large vertical inter-stack separation (ISS). 83
4.3.2 Case 2: combined spreading–imbibition dynamics for intermediate vertical inter-stack separation (ISS). 86
4.3.3 Case 3: combined spreading–imbibition dynamics for small vertical inter-stack separation (ISS). 89
4.4 Discussions 94
4.4.1 Phase space for imbibition and wetting states 94
4.4.2 Comparison of results of the present study with those of pressure-driven transport across single- or few-layer nanoporous graphene 97
4.2.3 History and drop-size dependence of nanodrop imbibition– spreading dynamics of holey graphene 98
4.5 Conclusions 99
Chapter 5: Dynamics of a Water Nanodrop through a Holey Graphene Matrix: Role of Surface Functionalization, Capillarity, and Applied Forcing 101
5.1 Introduction 101
5.2 Materials and Methods 105
5.2.1 System description 105
5.3 Results and Discussion 115
5.3.1 Flux and Volume of the Transported Water 115
Transport for F = 0.03 kcal/(mol Å) 117
Transport for F = 0.0125 kcal/(mol Å) 118
5.3.3 Effect of the System Parameters. 125
Effect of Variation of the Vertical Spacing d between the Graphene Stacks on the Drop Dynamics 125
Effect of Variation of the Vertical Spacing d between the Hole Dimension δ on the Drop Dynamics 126
Effect of Variation of the Number of Graphene Layers in Each Stack on the Drop Dynamics 127
5.3.4 Graphene Stacking Stability in an Aqueous Environment 127
5.4 Conclusions 130
Chapter 6: Water−Holey-Graphene Interactions: Route to Highly Enhanced Water-Accessible Graphene Surface Area 133
6.1 Introduction 133
6.2 Molecular Dynamics Simulations 137

6.2.1 System Description 138
6.2.2 Simulation Model 139
6.3 Results 149
6.4 Discussions 164
6.4.1 Applications of Generating Enhanced Water-Accessible Graphene Surface Area Using HG 164
6.4.2 Results for Other Combinations of the System Parameters 166
6.4.3 Simulation Results for the HG Architecture with Experimentally Motivated . 170
6.5 Conclusions 173
Chapter 7 175
Ion at Air−Water Interface Enhances Capillary Wave Fluctuations: Energetics of Ion Adsorption 175
7.1 Introduction 175
7.2 Materials and Methods 177
7.2.1 Justifications of simulations 178
Liquid Phase Volume 179
Liquid-Phase Pressure 180
7.2.2. Measurement of fluctuations 181
7.3 Results 184
7.3.1 Evidence of the Increase in CW Fluctuations with Ion at the Air−Water Interface ... 184
7.3.2 Energy Map of the Water Molecules, Ion Enforced Redistribution of Water Molecules, and the Resulting ΔH 188
7.3.3 Wave Characteristics of the Capillary Waves in the Presence of the Ion and the Resulting PV Work and the Change in Enthalpy 191
7.3.4 Variation of the Enthalpy, Entropy, and Gibbs Free Energy 196
7.4 Discussions 197
7.4.1 Importance of the Present Study in the Context of the Experiments Studying Ion Adsorption/Desorption at the Air−Water Interfaces 197
Winter et al.[251] 204
Tetrabutyl ammonium ion and Iodide ion 204
Ghosal et al.[247] 204
Bromide and Iodide ions from KBr and KI salts 204
Cheng et al.[248] 204
Cl^- ion obtained from the NaCl and RbCl salts 204

7.4.2 Significance of the Present Study: Technical and Broader Perspective 205
Hydrated Excess Protons and Hydroxide Anions 209
7.4.3 Results for the simulation in a smaller simulation box 211
7.5 Conclusions 215
8. Conclusions and outlook 217
8.1 Thesis summary 217
8.2 Key scientific findings and future directions 218
8.2.1 Wetting dynamics of nano-structured graphene (Chapter 3) 218
8.2.2 Water interactions with holey-graphene membrane (Chapter 4-6) 218
8.2.3 Ion adsorption at the air-water interface (Chapter 7) 219
8.3 Outlook 220
Reference 221

List of Figures

Figure. 1.1 Simple structure, great potential. (Left) In graphene, carbon atoms (green dots) are bonded together through sp2 hybridization (orange lines). (Right) Shiny and flexible graphene paper is formed by controlled restacking of graphene sheets (Adapted from Ref 4. Copyright © 2008 American Association for the Advancement of Science). 1

Figure 1.2. Hydrogenated (a) and hydroxylated (b) graphene pores, and (c) side view of the computational system investigated in this work (adapted from Ref 15. Copyright © 2012 American Chemical Society). 3

Figure 1.3 Structure of the thesis. 9

Figure 2.1 | Porous graphene membranes. a, Schematic and SEM image of a single-layer graphene suspended on a 5-μm-diameter hole. For nanoporous graphene fabrication, several approaches have been utilized: bombardment by ions, by electrons and via O2 plasma treatment. b, Raman spectra (514 nm excitation) of suspended graphene after different exposure times to oxygen plasma. (Adapted from Ref 14. Copyright © 2015 Nature Publication Group) 13

Figure 2.2 Schematic of applying Langevin equation as a stochastic thermostat in MD simulations. (a) Langevin equation applied to describe the motion of a Brownian particle (Green circle) moving along an arbitrary direction (Black arrow) in a medium consisting of smaller particles (Orange and blue circles). The collisions between Brownian particle and the particles (constituting the medium) having velocities in a direction opposite to that of the Brownian particle (Blue circles) result in slowing down of the Brownian particle. In the Langevin equation, the resulting friction force is defined to be varying linearly with the magnitude of the local velocity. At the same time, the collisions between Brownian particle and the particles (constituting the medium) having velocities in a direction similar to that of the Brownian particle (Orange circles) result in slowing down of the Brownian particle. Since the orange and blue particles are essentially interchangeable, the connection leads to the fluctuation-dissipation theorem. (b) In simulations, the system is immersed in a heat bath with infinitely large heat capacity in order to keep its temperature constant. The medium particles described in (a) acts as the particles in such heat bath, and the simulation does not explicitly describe the position and the conjugate momentum of the heat bath particles, i.e., it does not directly show up in the system Hamiltonian. Instead, the effects of the collision force acting on the Brownian particle (atoms in simulation) keeps mimicking the interactions of atoms and its surrounding heat bath particles. 21

Fig. 3.1 Schematic illustrating the spreading process on a standard non-SH surface – the spreading occurs by the motion of the TPCL with a progressive decrease in the local three-phase contact angle. This progressive lowering of the local contact angle is illustrated in the inset – the dynamic contact angle progressively decreases from θ_i to θ_{ii}..... 27

Fig. 3.2 Schematic illustrating the proposed spreading mechanism on an SH surface (constituting an array of nanopillars). We propose this mechanism based on the MD simulations that we report in this study. Unlike the case of the non-SH surface, the spreading occurs with the TPCL remaining pinned at the edge of the nanopillar. More importantly, the corresponding liquid vapor interface ‘‘bends’’ down, evidenced by the fact that the corresponding local three-phase contact angle increases from θ_i to θ_{ii} (please see the inset). This enhanced contact angle θ_{ii} can be larger than 180°, indicating a bending of the liquid surface even below the horizontal plane of the nanopillars. This bending eventually ensures the wetting of the adjacent nanopillar and this wetting is characterized by the attainment of a new three-phase contact angle θ_{iii}, where $\theta_{iii} < \theta_{ii}$ (please see the inset). Therefore, the spreading occurs not by the motion of the TPCL, but by the bending of the liquid–vapor interface of the TPCL that remains pinned..... 28

Fig. 3.3 Spreading of a water nanodrop in a superhydrophobic CB state on graphene nanopillars supported on bare gold. (a–c) represent the case where $N = N_1$, while (d–f) represent the case where $N = N_2$. (a) MD simulation snapshots (the corresponding time is indicated for each snapshot) illustrating the spreading of a water nanodrop containing $N = N_1 =$ 4500 molecules. (b) Temporal evolution of the right local contact angle of this drop with $N = N_1$ = 4500 molecules. In insets (i–iii), we provide the magnified views of the right three-phase contact line at three different time instants (namely, t = 45, 80, 145 ps). The snapshots of the entire drop corresponding to these time instants are shown in (a). (c) Temporal evolution of the left local contact angle of this drop with $N = N_1 = 4500$ molecules. In insets (i–iii), we provide the magnified views of the left three-phase contact line at three different time instants (namely, t = 45, 80, 145 ps). (d) MD simulation snapshots (the corresponding time is indicated for each snapshot) illustrating the spreading of a water nanodrop containing $N = N_2 = 4000$ molecules. (e) Temporal evolution of the right local contact angle of this drop with $N = N_2 = 4000$ molecules. In insets (i–iii), we provide the magnified views of the right three-phase contact line at three different time instants (namely, t = 40, 110, 125 ps). The snapshots of the entire drop corresponding to these time instants are shown in (d). (f) Temporal evolution of the left local contact angle of this drop with $N = N_2 = 4000$ molecules. In insets (i–iii), we provide the magnified views of the left three-phase contact line at three different time instants (namely, t = 40, 110, 125 ps)..... 35

Fig. 3.4 Temporal evolution of the right local contact angle (for $N = N_1 = 4500$) for three different starting trajectories (T_1, T_2, and T_3) of a water nanodrop. Here, T_1 refers to the trajectory where the water nanodrop contacts the nanostructured graphene surface with the drop center vertically aligned with the middle of the groove surface (or the part of the surface without nanopillars). Fig. 3.3 is obtained with trajectory T_1. T_2 and T_3 refer to the trajectories where, at the time when the nanodrop contacts the nanostructured surface, the center of the nanodrop is horizontally shifted to the left by 0.1 nm and 0.2 nm (with respect to the drop center corresponding to trajectory T_1), respectively. All the contact angles are provided for the case where the nanodrop spreads in a superhydrophobic CB state on graphene nanopillars supported on bare gold (the structure is depicted in Fig. 3.3)..... 36

Fig. 3.5 Temporal evolution of the left local contact angle (for $N = N_1 = 4500$) for three different starting trajectories (T_1, T_2, and T_3) of a water nanodrop. Here, T_1 refers to the trajectory where the water nanodrop contacts the nanostructured graphene surface with the drop center vertically aligned with the middle of the groove surface (or the part of the surface without nanopillars). Fig. 3.3 is obtained with trajectory T_1. T_2 and T_3 refer to the trajectories where, at the time when the nanodrop contacts the nanostructured surface, the center of the nanodrop is horizontally shifted to the left by 0.1 nm and 0.2 nm (with respect to the drop center corresponding to trajectory T_1), respectively. All the contact angles are provided for the case where the nanodrop spreads in a superhydrophobic CB state on graphene nanopillars supported on bare gold (the structure is depicted in Fig. 3.3)..... 37

Fig. 3.6 Temporal evolution of the right local contact angle (for $N = N_2 = 4000$) for three different starting trajectories (T_1, T_2, and T_3) of a water nanodrop. Here, T_1 refers to the trajectory where the water nanodrop contacts the nanostructured graphene surface with the drop center vertically aligned with the middle of the groove surface (or the part of the surface without nanopillars). Fig. 3.3 is obtained with trajectory T_1. T_2 and T_3 refer to the trajectories where, at the time when the nanodrop contacts the nanostructured surface, the center of the nanodrop is horizontally shifted to the left by 0.1 nm and 0.2 nm (with respect to the drop center corresponding to trajectory T_1), respectively. All the contact angles are provided for the case where the nanodrop spreads in a superhydrophobic CB state on graphene nanopillars supported on bare gold (the structure is depicted in Fig. 3.3)..... 38

Fig. 3.7 Temporal evolution of the right local contact angle (for $N = N_2 = 4000$) for three different starting trajectories (T_1, T_2, and T_3) of a water nanodrop. Here, T_1 refers to the trajectory where the water nanodrop contacts the nanostructured graphene surface with the drop center vertically aligned with the middle of the groove surface (or the part of the surface without nanopillars). Fig. 3.3 is obtained with trajectory T_1. T_2 and T_3 refer to the trajectories where, at the time when the nanodrop contacts the nanostructured surface, the center of the nanodrop is horizontally shifted to the left by 0.1 nm and 0.2 nm (with respect to the drop center corresponding to trajectory T_1), respectively. All the contact angles are provided for the case where the nanodrop spreads in a superhydrophobic CB state on graphene nanopillars supported on bare gold (the structure is depicted in Fig. 3.3)..... 39

Fig. 3.8 Spreading of a water nanodrop in a superhydrophobic CB state on graphene nanopillars supported on a gold-supported graphene monolayer. (a–c) represent the case where $N = N_1$, while (d–f) represent the case where $N = N_2$. (a) MD simulation snapshots (the corresponding time is indicated for each snapshot) illustrating the spreading of a water nanodrop containing $N = N_1 = 4500$ molecules. (b) Temporal evolution of the right local contact angle of this drop with $N = N_1 = 4500$ molecules. In insets (i–iii), we provide the magnified views of the right three-phase contact line at three spreading on SH surfaces. Here, we try to understand the origin of such a bending. Different instants (namely, t = 40, 90, 140 ps). The snapshots of the entire drop corresponding to these time instants are shown in (a). (c) Temporal evolution of the left local contact angle of this drop with $N = N_1 = 4500$ molecules. In insets (i–iii), we provide the magnified views of the left three-phase contact line at three different instants (namely, t = 40, 90, 140 ps). (d) MD simulations snapshots (the corresponding time is indicated for each snapshot)

illustrating the spreading of a water nanodrop containing $N = N_2 = 4000$ molecules. (e) Temporal evolution of the right local contact angle of this drop with $N = N_2 = 4000$ molecules. In insets (i–iii), we provide the magnified views of the right three-phase contact line at three different time instants (namely, t = 40, 75, 125 ps). The snapshots of the entire drop corresponding to these time instants are shown in (d). (f) Temporal evolution of the left local contact angle of this drop with $N = N_2 = 4000$ molecules. In insets (i–iii), we provide the magnified views of the left three-phase contact line at three different time instants (namely, t = 40, 75, 125 ps)..... 43

Fig. 3.9 Temporal evolution of the (a) right local contact angle (for $N = N_1 = 4500$) for three different starting trajectories (T_1, T_2, and T_3) of a water nanodrop. Here, T_1 refers to the trajectory where the water nanodrop contacts the nanostructured graphene surface with the drop center vertically aligned with the middle of the groove surface (or the part of the surface without the nanopillars). Fig. 3.3 is obtained with trajectory T_1. T_2 and T_3 refer to the trajectories where, at the time when the nanodrop contacts the nanostructured surface, the center of the nanodrop is horizontally shifted to the left (with respect to the drop center corresponding to trajectory T_1) by 0.1 nm and 0.12 nm for $N = N_1$ (0.1 nm and 0.15 nm for $N = N_2$), respectively. All the contact angles are provided for the case of where the nanodrop spreads in a superhydrophobic CB state on graphene nanopillars supported on a gold-supported graphene monolayer (the structure is depicted in Fig. 3.8). 44

Fig. 3.10 Temporal evolution of the local contact angle (for $N = N_1 = 4500$) for three different starting trajectories (T_1, T_2, and T_3) of a water nanodrop. Here, T_1 refers to the trajectory where the water nanodrop contacts the nanostructured graphene surface with the drop center vertically aligned with the middle of the groove surface (or the part of the surface without the nanopillars). Fig. 3.3 is obtained with trajectory T_1. T_2 and T_3 refer to the trajectories where, at the time when the nanodrop contacts the nanostructured surface, the center of the nanodrop is horizontally shifted to the left (with respect to the drop center corresponding to trajectory T_1) by 0.1 nm and 0.12 nm for $N = N_1$ (0.1 nm and 0.15 nm for $N = N_2$), respectively. All the contact angles are provided for the case of where the nanodrop spreads in a superhydrophobic CB state on graphene nanopillars supported on a gold-supported graphene monolayer (the structure is depicted in Fig. 3.8). 45

Fig. 3.11 Temporal evolution of the right local contact angle (for $N = N_2 = 4000$) for three different starting trajectories (T_1, T_2, and T_3) of a water nanodrop. Here, T_1 refers to the trajectory where the water nanodrop contacts the nanostructured graphene surface with the drop center vertically aligned with the middle of the groove surface (or the part of the surface without the nanopillars). Fig. 3.3 is obtained with trajectory T_1. T_2 and T_3 refer to the trajectories where, at the time when the nanodrop contacts the nanostructured surface, the center of the nanodrop is horizontally shifted to the left (with respect to the drop center corresponding to trajectory T_1) by 0.1 nm and 0.12 nm for $N = N_1$ (0.1 nm and 0.15 nm for $N = N_2$), respectively. All the contact angles are provided for the case of where the nanodrop spreads in a superhydrophobic CB state on graphene nanopillars supported on a gold-supported graphene monolayer (the structure is depicted in Fig. 3.8). 46

Fig. 3.12 Temporal evolution of the right local contact angle (for $N = N_2 = 4000$) for three different starting trajectories (T_1, T_2, and T_3) of a water nanodrop. Here, T_1 refers to the

trajectory where the water nanodrop contacts the nanostructured graphene surface with the drop center vertically aligned with the middle of the groove surface (or the part of the surface without the nanopillars). Fig. 3.3 is obtained with trajectory T_1. T_2 and T_3 refer to the trajectories where, at the time when the nanodrop contacts the nanostructured surface, the center of the nanodrop is horizontally shifted to the left (with respect to the drop center corresponding to trajectory T_1) by 0.1 nm and 0.12 nm for $N = N_1$ (0.1 nm and 0.15 nm for $N = N_2$), respectively. All the contact angles are provided for the case of where the nanodrop spreads in a superhydrophobic CB state on graphene nanopillars supported on a gold-supported graphene monolayer (the structure is depicted in Fig. 3.8). 47

..... 50

Fig. 3.13 Illustration of the forces on liquid mass (shown in green) in the vicinity of the three-phase contact line. We consider this fluid mass corresponding to a liquid drop spreading on a non-SH surface. One can clearly witness the symmetry of the underlying solid with respect to this mass, ensuring that the horizontal component of attraction forces from the underlying solid cancel each other. 50

Fig. 3.14 Illustration of the forces on liquid mass (shown in green) in the vicinity of the three-phase contact line. We consider the fluid mass corresponding to a liquid drop pinned at the edge of the pillars (nanopillars or micropillars). The underlying solid is no longer symmetric to this fluid mass, enabling the generation of a pinning force (equal to the difference of the horizontal components of these forces resulting from the asymmetry in the solid on two sides of the liquid mass) that balances the driving force for spreading..... 51

Fig. 4.1 Drop imbibition in a holey graphene structure for lateral ISS (δ) of 4 nm and vertical ISS (d) of 4 nm. MD simulation snapshots showing drop dynamics at different time instants. 63

Fig. 4.2 Drop imbibition in a holey graphene structure for lateral ISS (δ) of 4 nm and vertical ISS (d) of 4 nm. Time variation of contact angles θ_1, θ_2, θ_3, and θ_4 identified in Fig.4.1. 64

Fig. 4.3 Drop imbibition in a holey graphene structure for lateral ISS (δ) of 4 nm and vertical ISS (d) of 4 nm. Time variation of contact radii r_1 and r_2 identified in Fig.4.1. 65

Fig. 4.4 Drop imbibition in a holey graphene structure for lateral ISS (δ) of 6 nm and vertical ISS (d) of 4 nm. MD simulation snapshots showing drop dynamics at different time instants. 66

Fig. 4.5 Drop imbibition in a holey graphene structure for lateral ISS (δ) of 6 nm and vertical ISS (d) of 4 nm. Time variation of contact angles θ_1, θ_2 and θ_3 identified in Fig.4.4..... 67

Fig. 4.6 Drop imbibition in a holey graphene structure for lateral ISS (δ) of 8 nm and vertical ISS (d) of 4 nm (see Fig. 4.1 and 4.4 for the definitions of δ and d). MD simulation snapshots showing drop dynamics at different time instants. 68

Fig. 4.7 Drop imbibition in a holey graphene structure for lateral ISS (δ) of 8 nm and vertical ISS (d) of 4 nm (see Fig. 4.1 and 4.4 for the definitions of δ and d). Time variation of contact angles θ_1, θ_2 and θ_3 identified in Fig.4.6. 69

Fig. 4.8 Drop imbibition in a holey graphene structure for lateral ISS (δ) of 4 nm and vertical ISS (d) of 2.5 nm (see Fig. 4.1 and 4.4 for the definitions of δ and d). MD simulation snapshots showing drop dynamics at different time instants. 70

Fig. 4.9 Drop imbibition in a holey graphene structure for lateral ISS (δ) of 4 nm and vertical ISS (d) of 2.5 nm (see Fig. 4.1 and 4.4 for the definitions of δ and d). Time variation of contact angles θ_1, θ_2, θ_3, and θ_4 identified in Fig. 4.8. 71

Fig. 4.10 Drop imbibition in a holey graphene structure for lateral ISS (δ) of 4 nm and vertical ISS (d) of 2.5 nm (see Fig. 4.1 and 4.4 for the definitions of δ and d). Time variation of contact radii r_1 and r_2 identified in Fig. 4.8. 71

Fig. 4.11 Drop imbibition in a holey graphene structure for lateral ISS (δ) of 6 nm and vertical ISS (d) of 2.5 nm (see Fig. 4.1 and 4.4. for the definitions of δ and d). MD simulation snapshots showing drop dynamics at different time instants. 72

Fig. 4.12 Drop imbibition in a holey graphene structure for lateral ISS (δ) of 6 nm and vertical ISS (d) of 2.5 nm (see Fig. 4.1 and 4.4 for the definitions of δ and d). Time variation of contact angles θ_1, θ_2, θ_3, θ_4, and θ_5 identified in Fig. 4.11. 73

Fig. 4.13 Drop imbibition in a holey graphene structure for lateral ISS (δ) of 6 nm and vertical ISS (d) of 2.5 nm (see Fig. 4.1 and 4.4 for the definitions of δ and d). Time variation of contact radii r_1, r_2 and r_3 identified in Fig. 4.11. 74

Fig. 4.14 Drop imbibition in a holey graphene structure for lateral ISS (δ) of 8 nm and vertical ISS (d) of 2.5 nm (see Fig. 4.1 and 4.4 for the definitions of δ and d). MD simulation snapshots showing drop dynamics at different time instants. 75

Fig. 4.15 Drop imbibition in a holey graphene structure for lateral ISS (δ) of 8 nm and vertical ISS (d) of 2.5 nm (see Fig. 4.1 and 4.4 for the definitions of δ and d). Time variation of contact angles θ_1, θ_2, and θ_3 identified in Fig. 4.14. 76

Fig. 4.16 Drop imbibition in a holey graphene structure for lateral ISS (δ) of 4 nm and vertical ISS (d) of 1 nm (see Fig. 4.1 and 4.4 for the definitions of δ and d). MD simulation snapshots showing drop dynamics at different time instants. 77

Fig. 4.17 Drop imbibition in a holey graphene structure for lateral ISS (δ) of 4 nm and vertical ISS (d) of 1 nm (see Fig. 4.1 and 4.4 for the definitions of δ and d). Time variation of contact angles θ_1, θ_2, θ_3, and θ_4 identified in Fig. 4.16 78

Fig. 4.18 Drop imbibition in a holey graphene structure for lateral ISS (δ) of 4 nm and vertical ISS (d) of 1 nm (see Fig. 4.1 and 4.4 for the definitions of δ and d). Time variation of contact radii r_1 and r_2 identified in Fig. 4.16. 78

Fig. 4.19 Drop imbibition in a holey graphene structure for lateral ISS (δ) of 6 nm and vertical ISS (d) of 1 nm (see Fig. 4.1 and 4.4 for the definitions of δ and d). MD simulation snapshots showing drop dynamics at different time instants. 79

Fig. 4.20 Drop imbibition in a holey graphene structure for lateral ISS (δ) of 6 nm and vertical ISS (d) of 1 nm (see Fig. 4.1 and 4.4 for the definitions of δ and d). Time variation of contact angles θ_2, θ_3, and θ_4 identified in Fig.4.19. 79

Fig. 4.21 Drop imbibition in a holey graphene structure for lateral ISS (δ) of 6 nm and vertical ISS (d) of 1 nm (see Fig. 4.1 and 4.4 for the definitions of δ and d). Time variation of the contact radius r_2 identified in Fig.4.19. 80

Fig. 4.22 Drop imbibition in a holey graphene structure for lateral ISS (δ) of 8 nm and vertical ISS (d) of 1 nm (see Fig. 4.1 and 4.4 for the definitions of δ and d). MD simulation snapshots showing drop dynamics at different time instants. 80

Fig. 4.23 Drop imbibition in a holey graphene structure for lateral ISS (δ) of 8 nm and vertical ISS (d) of 1 nm (see Fig. 4.1 and 4.4 for the definitions of δ and d). Time variation of contact angles θ_2, θ_3, and θ_4 identified in Fig. 4.22. 81

Fig. 4.24 Drop imbibition in a holey graphene structure for lateral ISS (δ) of 8 nm and vertical ISS (d) of 1 nm (see Fig. 4.1 and 4.4 for the definitions of δ and d). Time variation of contact radius r_2 identified in Fig. 4.22. 81

Fig. 4.25 d–δ phase space summarizing imbibition behavior of water nanodrop interacting with a multilevel holey graphene structure. 91

Fig. 4.26 d–δ phase space summarizing equilibrium wetting behavior of water nanodrop interacting with a multilevel holey graphene structure. 91

Fig. 4.27 Variation in $r_{w,NG}/r_w$ as a function of lateral ISS δ for different values of vertical ISS d during water–holey graphene interactions. 92

Fig. 4.28 Drop imbibition in a holey graphene structure for lateral ISS (d) of 8 nm and vertical ISS (d) of 4 nm (see Fig. 4.1 and 4.4 for the definitions of d and d). The same geometry has been used as in Fig. 4.6-4.7. However, here the drop starts from a location between the graphene stacks at levels L_1 and L_2, while in Fig. 4.6-4.7, the drop starts from above the graphene stacks at level L_1 (see Fig. 4.1 and 4.4 for the definitions of levels L_1 and L_2). As can be seen from the figure, very little change in drop configuration occurs between t = 30 ps and t = 300 ps, indicating that the drop attains its final configuration rather quickly. 93

Fig. 4.29 Drop imbibition in a holey graphene structure for lateral ISS (d) of 8 nm and vertical ISS (d) of 2.5 nm (see Fig. 3.1 and 3.2 for the definitions of d and d). The same geometry has been used as in Fig. 4.14-4.15. However, here the drop starts from a location between the graphene stacks at levels L_1 and L_2, while in Fig. 4.14-4.15, the drop starts from above the graphene stacks at level L_1 (see Fig. 4.1 and 4.4 for the definitions of levels L_1 and L_2). As can be seen from the figure, not a significant amount of change in drop configuration is noted between t = 20 ps and t = 300 ps, indicating that the drop attains its final configuration rather quickly..... 93

Fig. 4.30 Drop imbibition in a holey graphene structure for lateral ISS (δ) of 6 nm and vertical ISS (d) of 2.5 nm (see Fig. 4.1 and 4.4 for the definitions of δ and d). The same geometry has been used as in Fig. 4.14-4.15. However, here we consider a much larger drop containing N = 5000 molecules, while for all other simulations, we use N = 3000 molecules. 93

Figure 5.1. Schematic of the nanodrop dynamics in HGA with different functionalizations of the hole. The stack levels L_1–L_3 are the upper, middle, and lower stacks, with each stack consisting of three layers of graphene. Figure 5.5 identifies these stacks as well as the lateral interstack

separation or ISS (δ) and vertical ISS (d) in a two-dimensional (2-D) representation. (a, b) Nanodrop dynamics for small forces (F < 0.1 kcal/(mol Å)) in HG with (a) hydrophilic functionalization (HIF) and (b) hydrophobic functionalization (HOF). The process is dominated by (i) the retention of water due to arrested dewetting for HG with HIF (see the larger water mass on graphene stacks in level L_1 for HG with HIF) and (ii) reduced flow rate and hence reduced flux due to HIF-water attraction (see the thinner velocity arrows near the graphene edges for graphene stacks in level L_3 for the HG with HIF). 104

Figure 5.5. Flux-vs-force variation for the HGA with HIF and HOF. In the figure, we demonstrate $dN/dt \sim F^{\alpha}$ (where α_{HIF} = 1.3 and α_{HOF} = 1.7) from small force values. 111

Figure 5.6. N_{max}/N_{total}-vs-force variation for the HGA with HIF and HOF. Here, N_{max} is the maximum amount of water molecules that leaves the HG, whereas N_{total} is the number of water molecules present in the water nanodrop. 112

Figure 5.7 Time variation of the cumulative number of water molecules N leaving the HGA for (a) HG with HIF and (b) HG with HOF. In the inset of each of (a) and (b), we zoom the region of linear slope of the N-vs-t curve [this region is highlighted in (a) and (b)], clearly depicting how the flux (dN/dt) is larger for the HG with HOF. 113

Figure 5.8 Time snapshots showing the dynamics of water drop through the HG system for (top) HOF and (bottom) HIF. The time corresponding to these snapshots are identified in the figure. We consider an applied force of F = 0.03 kcal/(mol Å) for this case. 113

Figure 5.9. Time snapshots showing the dynamics of water drop through the HG system for (top) HOF and (bottom) HIF. The time corresponding to these snapshots are identified in the figure. We consider an applied force of F = 0.0125 kcal/(mol Å) for this case. 114

Figure 5.10. Variation of the flux for different values of the vertical spacing d (see Figure 5.8 for the definition) for two force levels (F = 0.03, 0.0125 kcal/(mol Å)) and for HG with both HOF and HIF. All other parameters are same as that in Figures 5.5−5.9. 120

Figure 5.11 (a) Variation of the flux and (b) variation of N_{max}/N_{total} for different values of the vertical spacing d (see Figure 5.8 for the definition) for two force levels (F = 0.03, 0.0125 kcal/(mol Å)) and for HG with both HOF and HIF. All other parameters are same as that in Figures 5.5−5.9. 121

Figure 5.12 (a) Variation of the flux and (b) variation of N_{max}/N_{total} for different values of the hole dimension (which is also the horizontal gap δ between the graphene stacks, see Figure 5.8 for the definition of δ) for two force levels (F = 0.03, 0.0125 kcal/(mol Å)) and for HG with both HOF and HIF. All other parameters are same as that in Figures 5.5−5.9. 122

Figure 5.13 (a) Variation of the flux and (b) variation of N_{max}/N_{total} for different values of the hole dimension (which is also the horizontal gap δ between the graphene stacks, see Figure 5.8 for the definition of δ) for two force levels (F = 0.03, 0.0125 kcal/(mol Å)) and for HG with both HOF and HIF. All other parameters are same as that in Figures 5.5−5.9. 123

Figure 5.14 Variation of the flux for different number of graphene layers constituting each graphene stack for two force levels (F = 0.03, 0.0125 kcal/(mol Å)) and for HG with both HOF and HIF. All other parameters are same as that in Figures 5.5−5.9. 124

Figure 5.15 Variation of N_{max}/N_{total} for different number of graphene layers constituting each graphene stack for two force levels (F = 0.03, 0.0125 kcal/(mol Å)) and for HG with both HOF and HIF. All other parameters are same as that in Figures 5.5−5.9. 125

Figure 5.16 (a) the interlayer distance d is arbitrarily chosen in previous research. (b) the graphene stacking is most stable without accommodating any water molecules. (c-d) graphene stackings reach metastable states when there are one-layer or two-layers water in between graphene sheets. 129

Figure 5.17. Normalized PMF(Φ) curve of graphene stacking using the interlayer distance d as a reaction coordinate, in four different environments: pure water without pressure gradient, ionic solution without pressure gradient, pure water with pressure gradient, and ionic solution with pressure gradients..... 130

Figure 6.1. (a-i) Schematic of the actual experimentally fabricated holey-graphene architecture (Reprinted with permission from ref 98. Copyright © 2014 Nature Publishing Group.). The yellow arrows in the picture represent the direction of ion transport through the HG (see ref 66). (a-ii) Magnified section of this HG system that we attempt to simulate. (a-iii) Schematic representation of our simulation geometry trying to represent the magnified section in a-ii in a two-dimensional setting. (Reprinted with permission from ref 181. Copyright © 2017 PCCP Owner Societies). The HG is characterized by the dimensions δ (lateral separation between graphene stacks), δl (horizontal span of the graphene stack), and d (vertical separation between graphene stacks) [kindly compare a-ii and a-iii]. (b-i) Schematic of the generation of wetting states that ensure enhanced water-accessible graphene surface area by the interaction between water and HG. This enhanced water−graphene surface area is represented by the contact area ($r_{w,HG}$) over which water and HG surfaces interact and is compared (see b-ii) with respect to the contact area ($r_{w,G}$) of water on nonporous graphene. $r_{w,G}$ is the contact area achieved when a water nanodrop spreads on nonporous graphene. Given that the nonporous graphene is impenetrable, $r_{w,G}$ remains unchanged regardless of whether the drop interacts with the nonporous surface in the presence or absence of a force as long as the drop does not break down into smaller parts. For the HG, the edges of the graphene holes are colored in order to represent the presence of the functional groups (either−OH or −H) that saturate the unsaturation at the holes. For the nonporous graphene, we choose eight layers of graphene as the substrate, which ensures that it behaves as graphite and there is no chance of any change in the contact area due to the wetting translucency effect of graphene.[5,69,176–179] 135

Figure 6.4 Snapshots elucidating the dynamics of the water nanodrop interacting with the HGA for −OH functionalization. In both a and b, i−v provides the snapshots corresponding to different times. Below each of these snapshots, the corresponding time is also noted. For both cases a and b, d = 1 nm, δ = 6 nm, and δ_l = 4 nm, and we consider that a force of F = 0.005 kcal/mol·A is applied for t =600 ps. 144

Figure 6.5 Snapshots elucidating the dynamics of the water nanodrop interacting with the HGA for −H functionalization. In both a and b, i−v provides the snapshots corresponding to different times. Below each of these snapshots, the corresponding time is also noted. For both a and b, d =

2.5 nm, δ = 6 nm, and δ_l = 4 nm, and we consider that a force of F = 0.005 kcal/mol·A is applied for t =200 ps for the case with HIF and for t = 300 ps for the case with HOF. 145

Figure 6.6 Variation of the $r_{w,HG}/r_{w,G}$ with time for different values of d and F for −H functionalization of the graphene holes. For a given d−F combination, the force is applied for a time t which ensures maximum value of $(r_{w,HG}/r_{w,G})_{transient}$ (for a given t) as well as maximum $(r_{w,HG}/r_{w,G})_{equilibrium}$. This value of t is summarized below (with F in kcal/mol·A): $(t)_{d=1nm,F=0.003,OH}$ = 700 ps, $(t)_{d=1nm,F=0.003,H}$ =700 ps, $(t)_{d=2.5nm,F=0.003,OH}$ = 450 ps, $(t)_{d=2.5nm,F=0.003,H}$ = 800 ps, $(t)_{d=1nm,F=0.005,OH}$ = 600 ps, $(t)_{d=1nm,F=0.005,H}$ = 600 ps, $(t)_{d=2.5nm,F=0.005,OH}$ = 200 ps, $(t)_{d=2.5nm,F=0.005,H}$ = 300 ps, $(t)_{d=1nm,F=0.006,OH}$ = 350 ps, $(t)_{d=1nm,F=0.006,H}$ = 350 ps, $(t)_{d=2.5nm,F=0.006,OH}$ = 200 ps, $(t)_{d=2.5nm,F=0.006,H}$ = 200 ps. Other dimensions are same as those in Figures 6.4 and 6.5. The transient wetting is characterized by the transient variation of $r_{w,HG}/r_{w,G}$; in other words, the duration of the transient wetting process is the period of time for which $r_{w,HG}/r_{w,G}$ varies with time before attaining equilibrium..... 146

Figure 6.7 Variation of the $r_{w,HG}/r_{w,G}$ with time for different values of d and F for −OH functionalization of the graphene holes. For a given d−F combination, the force is applied for a time t which ensures maximum value of $(r_{w,HG}/r_{w,G})_{transient}$ (for a given t) as well as maximum $(r_{w,HG}/r_{w,G})_{equilibrium}$. This value of t is summarized below (with F in kcal/mol·A): $(t)_{d=1nm,F=0.003,OH}$ = 700 ps, $(t)_{d=1nm,F=0.003,H}$ =700 ps, $(t)_{d=2.5nm,F=0.003,OH}$ = 450 ps, $(t)_{d=2.5nm,F=0.003,H}$ = 800 ps, $(t)_{d=1nm,F=0.005,OH}$ = 600 ps, $(t)_{d=1nm,F=0.005,H}$ = 600 ps, $(t)_{d=2.5nm,F=0.005,OH}$ = 200 ps, $(t)_{d=2.5nm,F=0.005,H}$ = 300 ps, $(t)_{d=1nm,F=0.006,OH}$ = 350 ps, $(t)_{d=1nm,F=0.006,H}$ = 350 ps, $(t)_{d=2.5nm,F=0.006,OH}$ = 200 ps, $(t)_{d=2.5nm,F=0.006,H}$ = 200 ps. Other dimensions are same as those in Figures 6.4 and 6.5. The transient wetting is characterized by the transient variation of $r_{w,HG}/r_{w,G}$; in other words, the duration of the transient wetting process is the period of time for which $r_{w,HG}/r_{w,G}$ varies with time before attaining equilibrium..... 147

Figure 6.8 Summary of the $(r_{w,HG}/r_{w,G})_{transient,peak}$ [i.e., the maximum value of $(r_{w,HG}/r_{w,G})_{transient}$] and $(r_{w,HG}/r_{w,G})_{equilibrium}$ values for different combinations of d, F (expressed in kcal/mol·A), and hole functionalization. For a given d−F combination, the force is applied for a time t which ensures maximum value of $(r_{w,HG}/r_{w,G})_{transient,peak}$ (for a given t) as well as maximum $(r_{w,HG}/r_{w,G})$equilibrium. We provide $(r_{w,HG}/r_{w,G})_{transient,peak}$ only for d = 1 nm since we do not witness any significant peak in the $(r_{w,HG}/r_{w,G})_{transient,peak}$ variation for d = 2.5 nm (see Figure 6.6-6.7). Other dimensions are same as those in Figures 6.4 and 6.5. 148

Figure 6.9 Snapshots elucidating the dynamics of the water nanodrop interacting with the HGA for −OH functionalization. In both a and b, i−v provides the snapshots corresponding to different times. Below each of these snapshots, the corresponding time is also noted. For both a and b, d = 1 nm, δ = 5.9 nm, and δ_l = 6.2 nm, and we consider that a force of F = 0.005 kcal/mol·A is applied for t = 1000 and 1100 ps for the HG with HIF and HOF, respectively. 155

Figure 6.10 Snapshots elucidating the dynamics of the water nanodrop interacting with the HGA for −H functionalization. In both a and b, i−v provides the snapshots corresponding to different times. Below each of these snapshots, the corresponding time is also noted. For both a and b, d = 2.5 nm, δ = 5.9 nm, and δ_l = 6.2 nm, and we consider that a force of F = 0.005 kcal/(mol·A) is applied for t =330 and 420 ps for the HG with HIF and HOF, respectively. 156

Figure 6.11 Variation of the $r_{w,HG}/r_{w,G}$ with time for different values of d and F (expressed in kcal/mol·A) (other dimensions are same as those in Figures 6.9 and 6.10) for −H functionalization of the graphene holes. For a given *d*−*F* combination, the force is applied for a time t which ensures maximum value of $(r_{w,HG}/r_{w,G})_{transient}$ (for a given t) as well as maximum $(r_{w,HG}/r_{w,G})_{equilibrium}$. This value of t is summarized below (with *F* in kcal/mol·A): $(t)_{d=1nm,F=0.005,OH}$ = 1000 ps, $(t)_{d=1nm,F=0.005,H}$ = 1100 ps, $(t)_{d=2.5nm,F=0.005,OH}$ = 330 ps, $(t)_{d=2.5nm,F=0.005,H}$ =420 ps, $(t)_{d=1nm,F=0.006,OH}$ = 900 ps, $(t)_{d=1nm,F=0.006,H}$ = 980 ps, $(t)_{d=2.5nm,F=0.006,OH}$ = 220 ps, $(t)_{d=2.5nm,F=0.006,OH}$ = 380 ps. The transient wetting is characterized by the transient variation of the $r_{w,HG}/r_{w,G}$; in other words, the duration of the transient wetting process is the period of time for which $r_{w,HG}/r_{w,G}$ varies with time before attaining equilibrium. 157

Figure 6.12 Variation of the $r_{w,HG}/r_{w,G}$ with time for different values of d and F (expressed in kcal/mol·A) (other dimensions are same as those in Figures 6.9 and 6.10) for −OH functionalization of the graphene holes. For a given *d*−*F* combination, the force is applied for a time t which ensures maximum value of $(r_{w,HG}/r_{w,G})$transient (for a given t) as well as maximum $(r_{w,HG}/r_{w,G})$equilibrium. This value of t is summarized below (with *F* in kcal/mol·A): $(t)_{d=1nm,F=0.005,OH}$ = 1000 ps, $(t)_{d=1nm,F=0.005,H}$ = 1100 ps, $(t)_{d=2.5nm,F=0.005,OH}$ = 330 ps, $(t)_{d=2.5nm,F=0.005,H}$ =420 ps, $(t)_{d=1nm,F=0.006,OH}$ = 900 ps, $(t)_{d=1nm,F=0.006,H}$ = 980 ps, $(t)_{d=2.5nm,F=0.006,OH}$ = 220 ps, $(t)_{d=2.5nm,F=0.006,OH}$ = 380 ps. The transient wetting is characterized by the transient variation of the $r_{w,HG}/r_{w,G}$; in other words, the duration of the transient wetting process is the period of time for which $r_{w,HG}/r_{w,G}$ varies with time before attaining equilibrium. 158

Figure 6.13 Snapshots elucidating the dynamics of a large water nanodrop (*N* = 30 000, while for all other simulations we use *N* = 3000) interacting with the HGA for H functionalization (or HOF). Parts i−iv provide the snapshots corresponding to different times. Below each of these snapshots, the corresponding time is also noted. Other parameters are *d* = 2.5 nm, δ = 6 nm, and δ_l = 4 nm, and we consider that a force of *F* = 0.005 kcal/mol·A. The force is maintained throughout the time the simulation is run. 159

Figure 6.14 Variation of the $r_{w,HG}/r_{w,G}$ with time for different values of *F* (expressed in kcal/mol·A) for a large water drop passing through the HG matrix (see Figure 6.13 for the parameters of the HG matrix). 160

Figure 6.15 (a top) Scanning electron microscopy images depicting the cross-section of the layered graphene gel (LGG) membranes with interlayer separation of 3.2 nm (left) and 0.5 nm (right), respectively. (upper left corner) Actual LGG membrane. (bottom) Corresponding SANS patterns. (b) Schematic showing the manner in which the LGG membrane may be represented as parallel stacking of graphene nanosheets with dimensions L (equivalent to δ_l for our considered HG architecture), d, and δ (the dimensions d and δ have the same implications in our considered architecture as well). (c) Reduced 1D SANS data showing the existence of different possible values of the interlayer separation (namely 0.5, 2.2, 3.9, and 7 nm) (Parts a−c are reprinted with permission from ref [108]. Copyright © 2016 American Association for the Advancement of Science). (d) Microscopic image showing the top view of a nanoporous graphene. (Reprinted with permission from ref [189]. Copyright © 2011 American Association for the Advancement of Science). (e) Histogram analysis of the pore size distribution in part d. (f) Side view of the HG structure that we consider. The HG matrix is dictated by the dimensions $d_1 = d_3$ = 1 nm, d_2 = 2.5

nm, δ = 4 nm, δ_{l1} = 3 nm, δ_{l2} = 7.5 nm, δ_{l3} = 4 nm, and δ_{l4} = 5 nm. In the text, we discuss in detail how these dimensions are directly obtained from the experiments. 161

Figure 6.16 Snapshots elucidating the dynamics of the drop in the holey graphene matrix (shown in Figure 6.15f) with both −H termination (a−d) and −OH termination (e−h). For both of the cases, the water drop consists of 4000 water molecules and is subjected to a constant force of F = 0.006 kcal/(mol·Å), which is removed after t = 400 ps. 162

Figure 6.18 Variation of $r_{w,HG}/r_{w,G}$ with time for the HG architecture described in Figure 6.15f. Results are shown for both the −OH termination. For both of the cases, the water drop consists of 4000 water molecules and is subjected to a constant force of F =0.006 kcal/mol·Å, which is removed after t = 400 ps. 163

Figure 7.1: Variation of the volume of the simulation slab as the ion moves from the bulk..... 180

(quantified by the ion z position with z⩽62 Å) to the a/w interface (quantified by the ion z position..... 180

with z⩾66 Å). We find very little variation in the volume as the ion moves from the bulk to the 180

interface. Therefore, we ascribe an average value (shown by red dotted line) to this volume,.. 180

which is used while calculating the PV work. 180

Figure 7.2: Variation of the pressure change within the simulation slab as the ion moves from the 181

bulk (quantified by the ion z position with z⩽62 Å) to the a/w interface (quantified by the ion z 181

position with z⩾66 Å)..... 181

Figure 7.4: A series of 2D views of liquid-vapor interface with ion locations shown by the red 183

stars. 183

Figure 7.5 (a) Root mean square (RMS) of the CW fluctuations with the cation at three different locations [green circles: cation at the a/w interface, i.e., at z = 67 Å; red squares: cation at the NIR (please see the text for the definition of NIR or near-interface region), i.e., z = 65 Å; blue triangles: cation in the bulk, i.e., z = 57 Å]. The lines parallel to the horizontal axis denote the average of the fluctuations. (b−d) Distribution of the water molecules distinguished in terms of their interaction energies with the cation for (b) cation at the a/w interface, (c) cation at the NIR, and (d) cation in the bulk. (e−g) Distribution of the water molecules distinguished in terms of their interaction energies with the other water molecules for (e) cation in the bulk, (f) cation at the NIR, and (g) cation at the a/w interface. 184

Figure 7.6 Variation of the average number of surface and coordinated water molecules for different distances of the cation (measured in Å) from the bottom of the simulation box. A distance of 66−68 Å represents the cation at the a/w interface and a distance of <63 Å represents the cation in the bulk. For this plot, we first identify what differentiates between the different

types of water molecules (surface, coordinate, and bulk). The bulk and the surface water molecules are identified by studying the corresponding local number densities ρ_{local} around these water molecules. A water molecule is considered a bulk water molecule if $\rho_{local} = 0.032/Å^3$ and a surface water molecule if $\rho_{surface\ water} = 0.016/Å^3$. In contrast, a coordinated water molecule is the water molecule at a radial distance of 5 Å from the ion center. 188

Figure 7.7 Variation of the parameter A_ξ/A_0 associated with a given mode for the different modes constituting the CWs for different ion positions. This parameter A_ξ/A_0 dictates the contribution of a given mode in the CW. The physical interpretation of A_ξ and A_0 are provided in the main text..... 190

Figure 7.8 Variation of ΔU (change in internal energy), P−V work [or Δ(PV)], and ΔH with respect to the cation distance from the bottom of the simulation box. 191

Figure 7.9 Variation of ΔH, −TΔS, and ΔG with respect to the cation distance from the bottom of the simulation box..... 196

Figure 7.10: (a) The simulation set up with small simulation box size. (b) Variation of Δ(PV), ΔH, ... 213

and ΔU for different ion positions obtained from the simulations for this small simulation box. 213

(c) Variation of ΔH, −TΔS, and ΔG for different ion positions obtained from the simulations for 213

this small simulation box. In (b) and (c), we consider the movement of the ion from the bulk. 213

(quantified by the ion z position with z<16 Å) to the a/w interface (quantified by the ion z..... 213

position with z⩾20 Å)..... 213

Figure 7.11: (a) A 3D view of a liquid-vapor interface showing the effect of the periodic boundary 214

conditions on the corrugations at the boundaries. A schematic of unphysical surface corrugation 214

due to the application of the periodic boundary condition to a system with (b) a large simulation 214

volume and (c) a small simulation volume. 214

Figure 7.12: The RMS (Root Mean Square) of the CW fluctuations with the cation at two 215

different Z locations (in Å) for simulations using a small simulation box: Z=15 Å represents the 215

ion in the bulk, while Z= 21 Å represents the ion at the interface. 215

Figure 7.13: (a) Variation of the ratio Aξ / A0 characterizing the amplitude of the CWs, with the 215

number of modes for two different Z values (in Å) of the ion (Z=15 Å represents the ion in the 215

bulk, while Z= 21 Å represents the ion at the interface). (b) Ratio of A/A0 (where A represents 215
the sum of A_ξ corresponding to all the modes) as a function of the ion position. 215

Chapter 1: Background and motivation

1.1 Introduction to water/graphene interactions

Graphene, defined as an atomic thin layer of carbon (Fig.1.1), has been attracting attention from the research community ever since it was discovered, isolated, and characterized in 2004 due to its unique physical and chemical properties[1–4].

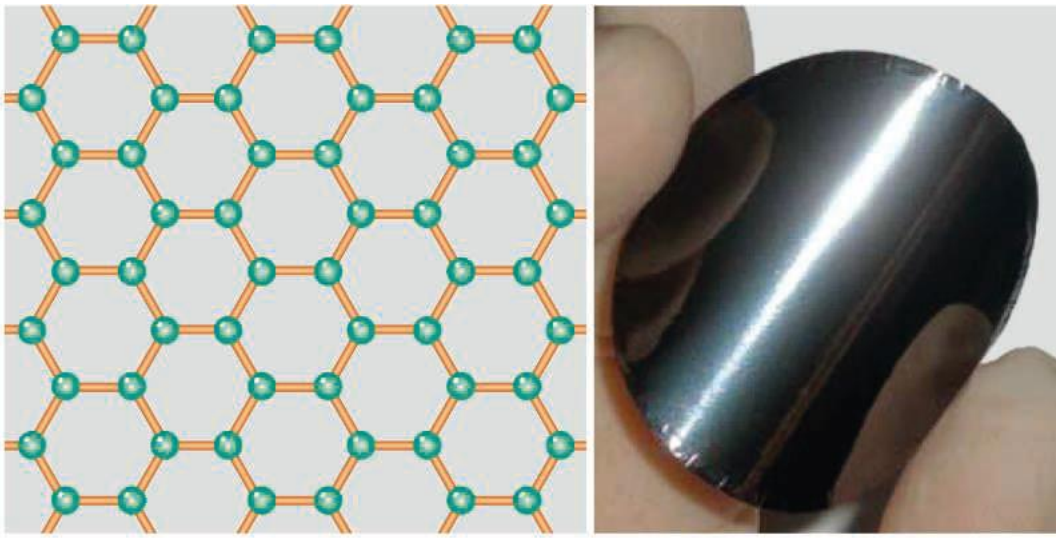

Figure. 1.1 Simple structure, great potential. (Left) In graphene, carbon atoms (green dots) are bonded together through sp2 hybridization (orange lines). (Right) Shiny and flexible graphene paper is formed by controlled restacking of graphene sheets (Adapted from Ref 4. Copyright © 2008 American Association for the Advancement of Science).

Because of its ultra-thin nature, graphene shows many fascinating phenomena, among which wetting transparency effect has roused massive interests and surprises in the wetting community. Raifee *et al.* first reported that the wetting behavior of a monolayer graphene supported on a hydrophilic solid is different from that of bulk graphite[5]. Raifee *et al.* pointed out that such a behavior is due to the fact that the wetting property of the monolayer graphene is controlled by the van der Waals (vdW) interactions and for conditions where the vdW interactions between the water and the underlying hydrophilic substrate massively dominates the vdW interactions

between the water and the monolayer graphene, it is possible that the graphene coating becomes entirely *transparent to the drop* and the drop contact angle is entirely dictated by this underlying solid[5]. This observation was extremely important and raised researchers explored all possible situations making claims of complete, partial, and negligible wetting transparency of graphene (depending on the nature of the underlying substrate). Accordingly, it is crucial whether the contact angle is quantified on supported (and the nature of the supporting solid) or unsupported graphene. It is experimentally confirmed that the presence of air-borne contaminants on graphene surface makes the surface appear to be more hydrophobic (contact angle~80°) as compared to contaminant-free (contact angle~60°) graphene. Wetting transparency effect demands a larger contact angle (weaker vdW interaction) of water on graphene, which makes the effect of the underlying hydrophilic solid much stronger. The presence of the contaminant and the resulting hydrophobization (increase in the contact angle), therefore, promotes this *wetting transparency effect*[6]. So, the wetting of graphene itself needs to be investigated with more care, including the wetting of nanostructured graphene and its dynamics.

Besides pristine graphene, nano-porous graphene is an important member of the graphene family[7–10]. One of the important applications of the nano-porous graphene is to serve as a desalination member to remove ions in aqueous ionic solution or seawater[11–17]. The nano-sized pores on graphene allow water molecules to penetrate while repelling hydrated ions and other species. Many factors control the permeation, including the pore-ion size ratio, functional groups at the edges of the pores, and the stacking structure of nano-porous graphene stacking. However, the details of the permeation dynamics are still not well-established. Therefore, my dissertation focuses on investigating the wetting and permeation dynamics of water and nano-porous/nanostructured graphene.

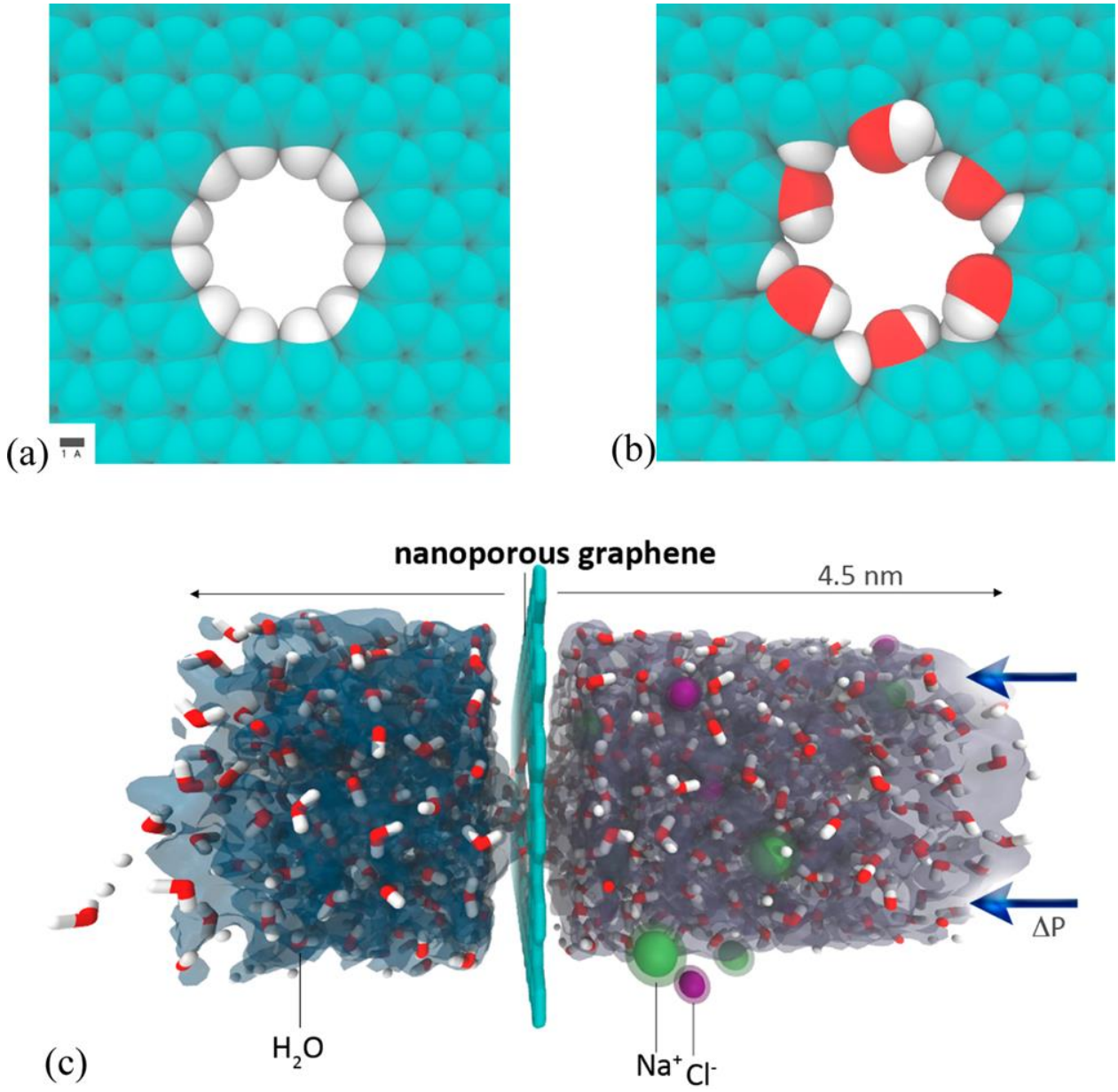

Figure 1.2. Hydrogenated (a) and hydroxylated (b) graphene pores, and (c) side view of the computational system investigated in this work (adapted from Ref 15. Copyright © 2012 American Chemical Society).

1.2 Introduction to molecular dynamics simulations

Experimental observations are critical to discover the fascinating physical and chemical properties of graphene. However, it is not easy to specify the fundamental mechanisms dictating these observations by merely employing the experimental methods. Under these circumstances, computational simulations, especially with the assistance of fast developing of computational power and capacity, can help unraveling these mechanisms. In general, two kinds of MD simulation approaches are relevant here: first is the *ab initio* molecular dynamics (MD) simulations that consider electron-electron interaction explicitly using a density functional theory model and second is the classical MD simulations considering electron-electron interaction implicitly using various force-field models. The ab initio simulation methods are so computationally expensive that it can only capture a finite-size system (~hundreds of atoms) for only a small time scale (~ps). On the other hand, the classical MD simulations are capable of simulating much larger system (~10 thousands of atoms) for a relatively large time scale (~10 ns). For the wetting problems, the size of simulations should be large enough to eliminate the line tension effect so that the result using a nano-system can match the physical observations in a micro-system (experimentally accessible scale). Furthermore, the wetting process usually takes several nano-seconds to complete, which also requires the simulations to have a capacity to capture that time scale. Therefore, the classical force field MD simulation method is the most suitable approach to investigate the problems discussed in this dissertation.

In MD simulations, the motion of the molecules is governed by the Newton's second law, in which the intermolecular force is the negative gradient of the inter-molecular potential (force field). At the beginning of a timestep, the system first calculates the acceleration of each atom from the net force acting on it, and then Verlet integration is applied to evaluate the trajectory of

the atoms at the end of that time step. Using classical statistical mechanics principles, the system can be expressed by a function of the kinetic energy and potential energy carried by every atom. Therefore, there are 3 degrees of freedom for kinetic energy and 3 degrees of freedom for potential energy for each atom, making it a total of 6N dimensions (where N is the number of atoms). Accordingly, a microstate of the system can be represented by a single point in this 6N dimensional space, also called the *phase space*. Under this setting, the system is brought into a thermodynamic equilibrium using various ensembles, which contains all possible microstates (locations of the points in the phase space) under a specific ensemble. For example, if a microcanonical (NVE) ensemble to the system, only those locations of the points in the phase space that yield the total energy of $E+\Delta E$ (where E is the initial system energy) of the system can be accepted. In other words, the microcanonical ensemble ensures that the simulation follows the adiabatic boundary condition. In most of the simulations, the system temperature is usually kept constant similar to what happens in an experiment. Therefore, for most of the cases canonical (NVT) or grand canonical (μVT) ensembles are normally applied. Please note that the application of ensembles is only important for a small system far away from the thermodynamic limit ($N \approx 10^{23}$). After an ensemble with constant temperature is decided, statistical methods, popularly known as *thermostats* are employed to maintain the system temperature. Therefore, for any classical MD simulation, there are three key factors to specify and decide: force fields, ensemble, and thermostats.

Force fields

As mentioned above, the intermolecular interaction is fundamentally controlled by the input force field parameters. In this dissertation, water/graphene interaction is described using a pairwise potential that captures the intermolecular interactions. These interactionscan be decomposed into electrostatics, exchange, and induction contributions. The pairwise potential we use consists of Lenard-Jones (LJ) potential and electrostatic force. LJ potential is well-known as a good approximation to capture pairwise additive interactions, including the exchange (repulsion) and induction (attraction) interactions. The electrostatic interaction is included separately by fixing a partial charge to each oxygen and hydrogen atom. However, the force field used here does not correctly capture the induction contribution, which is not strictly pairwise additive due its vector-like nature. Such a many-body interaction cannot be described by a LJ potential. To solve the problem, we employed a LJ potential that is optimized by fitting the parameters to match the experimental water-drop contact angle on graphite. There are other emerging potentials that consider the induction contribution self-consistently by using a Drude oscillator model. Here, however, we shall continue with the classical MD simulation description since we are only concerned if the applied force field applied can provide the correct contact angle and its dynamics. Using a more specific model to revisit the problems would give more accurate result, but it is beyond the context of this thesis. It is worthy to mention that the LJ interaction excludes the interaction between hydrogen and any other type of atoms, because the electron density around hydrogen is so low that it barely alters the overall exchange and dispersion interactions. While some research suggests that including hydrogen interaction in LJ potential improves the accuracy, it is not well accepted by the research community.

Ensembles

This thesis employs canonical ensemble, which maintains the total number of atoms (N) and temperature (T) of the system constant for most of the problems. In other words, only the microstates with the constant temperature (kinetic energy) can be accepted. The system can be viewed as a small system connected to a sufficiently large thermal reservoir so that the thermal fluctuations in the small system can be suppressed at a significantly fast rate. This will eventually ensure the Boltzmann distribution, where the probability of observing one energy level (P(U)) is proportional to exp(-U/kT). Using such an ensemble, the system is brought to a thermal equilibrium by minimizing the Boltzman free energy.

Thermostats

Following the choice of the ensemble applied to the system, the simulations should be conducted in such a manner that temperature of the system remains constant. However, it is not realistic to generate a large physical thermal reservoir coupled with the simulation system due to the limitation of the computational resources. Therefore, in our simulations we employed the Nosé–Hoover thermostat, which is a deterministic algorithm that directly adds new degrees of freedom to the system Hamiltonian, for all the equilibrium simulations. The algorithm is designed to directly remove/add kinetic energy (part of the system Hamiltonian) from the system when the current temperature is above/below the target temperature. It provides more thermal stability to the system and generates negligibly small thermal fluctuations since the system always knows whether energy shall be added or removed. However, the Nosé–Hoover thermostat does not work well in a non-equilibrium MD simulation since it controls the temperature through rewriting the Hamiltonian, implying that any microstate that carries the acceptable kinetic energy gets accounted for without any loss or gain of energy from the image thermal reservoir. Although

not reported by any other work, we experienced the flying ice cube effect while using the Nosé–Hoover thermostat for simulating the motion of water between two graphene sheets, in which the high-frequency motion of water was suppressed to transfer the corresponding kinetic energy to low-frequency motion (in particular the translational motion). The observation is unrealistic as it violates the equipartition law that each degree of freedom of a motion has the same energy (1/2 kT per degree). However, the Nosé–Hoover thermostat will still accept such kinetic energy distribution as long as the sum total of the kinetic energy components matches the target total system kinetic energy. To bypass this issue, we employed a stochastic thermostat, namely the *Langevin thermostat*, which is a random force added directly to each atom in the system as if the atom is in a Brownian motion inside a thermal reservoir. By applying the Langevin thermostat, the possible long-range correlated motion is suppressed to ensure that the equipartition law is satisfied. However, water is a complex liquid where the intermolecular interactions get dictated by the formation of a strong hydrogen bond network (HBN). The HBN creates local ordering of water, which gets suppressed when the Langevin thermostat is employed. Therefore, the thermostat needs to be carefully chosen in a non-equilibrium MD simulation. Details will be further discussed in later chapters.

After the system reaches its equilibrium or quasi-equilibrium, further post analyses are required to reveal the corresponding mechanisms. The analyses methods will be described separately in each chapter separately.

1.3 Thesis Structure

This thesis work investigates the water interaction with the aqueous environment. Various problems have been studied to probe various issues pertaining to the water/graphene interactions. Figure 1.3 shows the structure of this dissertation.

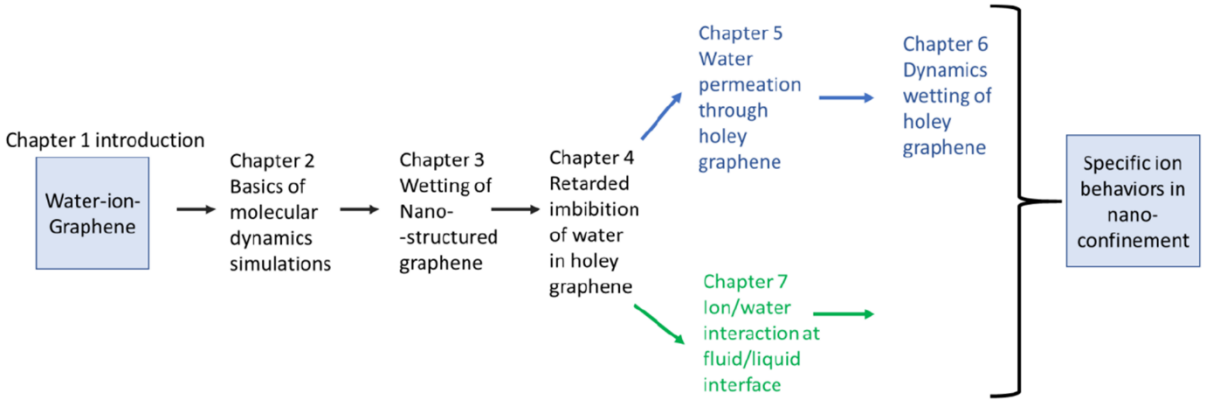

Figure 1.3 Structure of the thesis.

Chapter 2: Basics of Molecular Dynamics Simulations Relevant for the Present Thesis

In this chapter, we introduce some basic concepts related to Molecular Dynamics (MD) simulations that are directly connected to the simulations conducted for obtaining the results provided throughout this dissertation.

2.1 Fundamentals of molecular dynamics simulations

Molecular dynamics (MD) simulation is a useful tool to investigate the thermodynamic properties of physical and chemical systems and for shedding light into the controlling mechanisms behind experiments involving these different systems. Ever since the MD simulation algorithms became well established and the computational resources became more powerful, it has been extensively employed for providing information and predictions about many exciting phenomena.

For example, MD simulations are applied to study the fast water transport in carbon nanotubes (CNTs). In 2001, Hummer *et.al*. employed MD simulations to investigate the highly counter-intuitive water occupancy and transport in a carbon nanotube (CNT)[18]. The findings of this study were soon confirmed by experiments. In 2006, Holt *et.al.* fabricated a CNT membrane, and they observed an ultra-high mass transport rate through the CNT membrane[19]. They also experimentally reported for the first time the large slip lengths associated with the water transport in CNTs. Subsequently, MD simulations were carried out systematically by Kannam *et.al.* and Kerstin *et.al.* for studying the effects of CNT diameters on these large slip lengths[20,21]. Their studies attributed these large slip lengths to the radial curvature of the CNTs. Furthermore, compared to flat graphene sheet, a curved CNT surface has a smoother potential energy surface,

which facilitates the fast water transport through the CNT. These simulations have allowed the research community to develop the consensus that the large flow rate inside the CNT is due to a large slip length, which is curvature dependent. In 2016, the radial curvature dependence slip length was confirmed experimentally by Eleonora *et.al.*[22]. In other words, the predictions made by MD simulations have been confirmed experimentally, and the experimental result supports the hypothesis made on the basis of the simulations. From this perspective, MD simulations not only acted as a good back up to experimental observations but also a strong tool to propose novel theoretical hypothesis.

The study of nanoflow in the one-dimensional confinement of CNT has been intensively conducted, and such confinement leads to a myriad of extraordinary phenomena.

When the radius of a CNT is set to be infinitely large, the one-dimensional CNT becomes a two-dimensional graphene sheet. Importantly, two graphene sheets that are parallel to each other can act as a confinement as well. *This dissertation will focus on investigating the nanofluidic behavior in the confined space created by the graphene and its derivatives.*

An example that is more closely related to this dissertation and has been inspired by by MD simulations is the problem of using nano-porous graphene as a water desalination membrane. In 2012, Grossman et.al. employed MD simulations to predict that a nano-porous graphene membrane can serve as a filter to remove salt from seawater[15] (Fig.1.2). The nano-porous graphene is able to sustain a high pressure gradient across its surface, thereby making it a great candidate material for a reverse osmosis membrane[23–26]. Also, the nano-pores on the graphene sheet provide an entry passage to the water molecules to allow fast water transport and at the same time serves as a barrier to the hydrated salt ions. This eventually allows the production of clean water by removing salt from seawater. Therefore, the functioning of the nano-porous

graphene membrane is due to the size effect: a water molecule is about five times smaller than a fully hydrated sodium or chloride ion, and therefore passes through the graphene nanopores, which in turn blocks the passage of the hydrated ions. Since the hydration free energy of an ion is typically ~100 times larger than the thermal energy of a particle at room temperature[27–31], it is unlikely for an ion to reduce its size during the interactions with the nano-pores in a liquid phase. Therefore, the idea of using nano-porous graphene as a desalination membrane can be realistic only if the experimentalists come up with a method to precisely control the pore size distribution. In this work[15], the authors also investigated the effect of terminations around the nano-pores. In 2015, Surwade et.al. used an oxygen plasma etching process to obtain nano-porous graphene with uniform size distribution and proved that a nano-porous graphene indeed can serve as a membrane for water desalination[14]. This time, MD simulations not only predicted the potential applications of existing materials but also pointed out the necessary directions to the experimentalists for inventing new fabrication approaches.

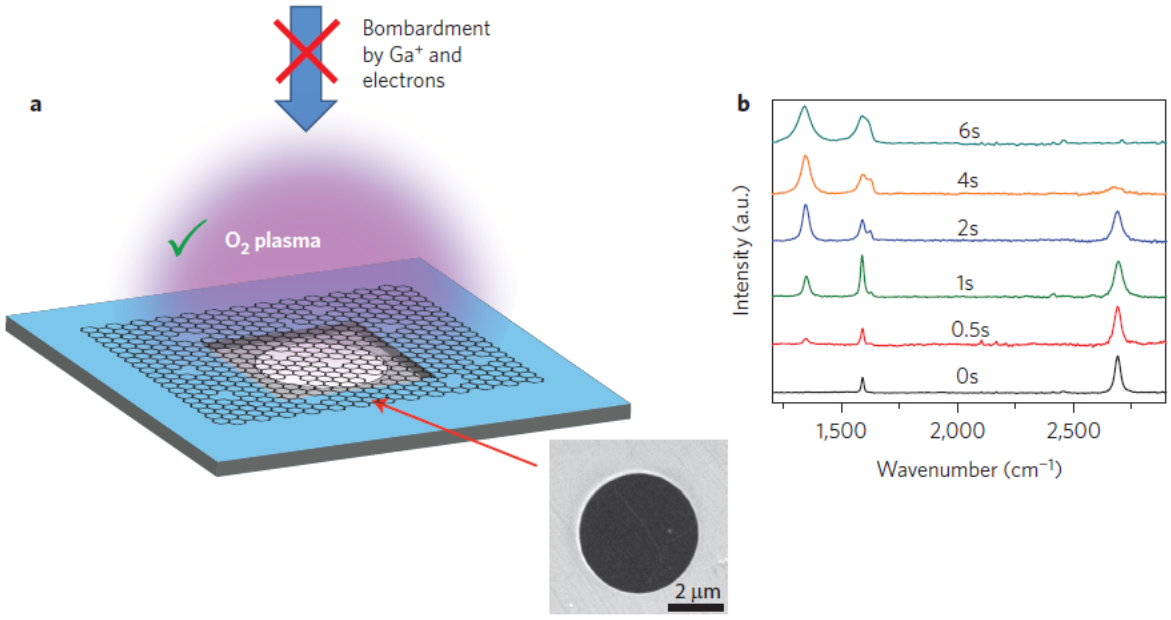

Figure 2.1 | Porous graphene membranes. a, Schematic and SEM image of a single-layer graphene suspended on a 5-µm-diameter hole. For nanoporous graphene fabrication, several approaches have been utilized: bombardment by ions, by electrons and via O2 plasma treatment. b, Raman spectra (514 nm excitation) of suspended graphene after different exposure times to oxygen plasma. (Adapted from Ref 14. Copyright © 2015 Nature Publication Group)

2.2. Thermodynamics

Currently, due to the limit of the accessible computational resources, a typical classical MD simulation consists of up to 10^8 atoms and with a time scale of nanoseconds to microseconds, which is obviously far away from the thermodynamic limit (10^{23} atoms) and experimentally realistic timescales. So, a system must be examined with care to avoid large disparities between simulations and experiments[32].

It is crucial to determine the parameters needed to describe a system. Just like conducting an experiment, we need to set up a description of the system using thermodynamic measurements. In general, both extensive and intensive variables can be used, but they are not completely independent of each other. So, we need to know the least set of parameters required to uniquely

define a system. To understand this concept, we start with the most fundamental thermodynamics equation with the quasi-static assumptions (assumes that the mechanical and chemical forces are constant and only the displacement or atomic number vary in the process of applying work to the system):

$$dE = TdS + \boldsymbol{J} \cdot d\boldsymbol{x} + \mu \cdot dN, \tag{2.1}$$

where E is the system energy, T is the system temperature in Klevin, S is the system entropy, J is the mechanical force, x is the displacement, μ is the chemical potential of a certain species, and N is the number of the species.

Since the entropy, displacement, and number of atoms are all extensive quantities, the energy of the system is proportional to such extensive quantities. Therefore, we can write:

$$E(\lambda S, \lambda x, \lambda N) = \lambda E(S, x, N), \tag{2.2}$$

where λ is a constant. So, it is safe to specify $\lambda = 1$. After integration, the system energy becomes

$$E = TS + \boldsymbol{J} \cdot \boldsymbol{x} + \mu \cdot N. \tag{2.3}$$

We can once again differentiate the system energy, which leads to the Gibbs-Duhem relation:

$$SdT + \boldsymbol{x} \cdot d\boldsymbol{J} + N \cdot d\mu = 0, \tag{2.4}$$

which indicates that the intensive quantities $T, \boldsymbol{J}, \mu$ are not independent of each other. In other words, we do not need to constrain all these three intensive quantities to define a system. Constraining one or two of them will be sufficient.

As it is mentioned above, three parts contribute to the overall energy of the system: heat, mechanical work, and chemical work. Obviously, one constraining condition must be assigned to each of these three energetic contributions, but at least one extensive quantity should be included as the intensive quantities are not independent. Typically, temperature T is a default controlling

parameter as it does not vary in experiment when the system is at equilibrium. If we further assume that the system does not undergo a chemical reaction and the mass is conserved through the equilibration, the atom number N is constrained to a constant value. Last, for mechanical work part, we can choose to set the volume V as a constant (isothermal process) or the pressure P as a constant (isothermal-isobaric process).

We now consider using purely extensive quantities, say in a non-reactive system with constraints of E, N and V (three extensive quantities). It is a common starting ensemble (a set of microstates gives the same macroscopic observation) to understand related statistical mechanics concepts. Classically, the essential quantity associated with the ensemble is a partition function, which carries all the information needed to describe a system at thermodynamic equilibrium. For NVE ensemble, the probability to find one microstate (one point in phase space) is same for any other state carrying the same energy, i.e., the states at same energy level. In this way, the system entropy is maximized:

$$S(\varepsilon) = k_B In\, \Omega(\varepsilon), \tag{2.5}$$

where S is the definition of entropy in NVE ensemble and $\Omega(\varepsilon)$ is the NVE partition function (density of states at energy level E).

Another commonly used ensemble is canonical ensemble (NVT), with an intensive constrain (temperature) added to the system. The probability to find a state is weighted by the Boltzmann distribution factor:

$$p(\varepsilon) = \frac{\Omega(\varepsilon)e^{-\beta\varepsilon}}{Z}, \tag{2.6}$$

where ε is the energy level, $\Omega(\varepsilon)$ is the energy degeneracy, i.e., the NVE partition function, $Z = \sum_{\mu} e^{-\beta\mu}$ is the canonical partition function.

After some rearrangement, the probability [expressed in eq.(2.6)] becomes

$$p(\varepsilon) = \frac{\Omega(\varepsilon)e^{-\beta\varepsilon}}{Z} = \frac{1}{Z}exp\left[\frac{S(\varepsilon)}{k_B} - \frac{\varepsilon}{k_B T}\right] = \frac{1}{Z}exp\left[-\frac{F(\varepsilon)}{k_B T}\right], \quad (2.7)$$

where $F(\varepsilon) = \varepsilon - TS(\varepsilon)$ is the Helmholtz free energy. Obviously, the system is at equilibrium when the Helmholtz free energy reaches its minimum possible value, which is in line with the conclusion obtained from other derivation.

Let us take a closer look at the NVT partition function, $Z = \sum_\mu e^{-\beta\mu} = \sum_\varepsilon e^{-\beta F(\varepsilon)}$. When the system is at thermodynamic limit (i.e., system atom number $N \sim 10^{23}$), the summation over exponentials for a large number limit of states would be highly peaked at its maximum value (saddle point integration). Under such conditions, $Z = \sum_\mu e^{-\beta\mu} = \sum_\varepsilon e^{-\beta F(\varepsilon)} \approx e^{-\beta F(\varepsilon^*)}$, which is the energy level that minimizes the Helmholtz free energy. In this way, the system at large number limit with NVT ensemble stays at an energy level that minimizes the Helmholtz free energy, which becomes indistinct from a system described by NVE ensemble. Similarly, in experiments, there is no constraint on the total system energy, but the system energy remains constant at equilibrium.

However, the situation is different in MD simulations. Taking the LAMMPS simulator as an example, when NVE ensemble is applied to the system, the motion of the atoms is merely controlled by Newtonian equation. However, the initial configuration is usually not at equilibrium and the energy would increase or decrease arbitrarily. In the simulation timescale, the system is not likely to find its equilibrium. Therefore, putting intensive constraints to the system can facilitate the equilibration process since it confines the path of the phase point motion. Furthermore, if the intensive condition is introduced into the system in a way that reproduces the properties in a thermodynamic limit, the simulation will be able to provide insights into the details of the atomic arrangements only by a small subset of atoms (10^3-10^5).

2.3 Dynamics

Before investigating the method to control the system temperature, it is important to understand how simulator propagates the motions of atoms.

In classical mechanics, the motion of the atoms is governed by the Newton's second law:

$$m_i \frac{d^2}{dt^2} r_i = -\frac{\partial}{\partial r_i} V(r_1, \cdots, r_N), \tag{2.8}$$

where $r_1, \cdots, r_N$ describe the positions of each atom in the system and m_i is the mass of the atom *i.* Clearly, this Newtonian picture to describe the atomic motions is fundamentally true for a non-interactive classical system. At the thermodynamic limit (with the atom number N~10^{23}), the simulation result would automatically align with the experimental results. However, the computational cost to explicitly describe a system in thermodynamic limit is significantly higher than afforded by any accessible recourse. Even in some microscopic system (with the atom number N~10^3 -10^5), the simulations could be extremely time-consuming.

However, there are usually only a few degrees of freedom among the total N degrees of freedom that attract attentions in the study of the dynamics of problems. For example, to observe the ion transport through membranes, it is reasonable to focus only on the motion of the center of mass of ions, while ignoring other degrees of freedom, such as the stretching of water bonds, rotation of water molecule, and ion solvation dynamics.

Under the assumptions that only a few degrees of freedom is of our interests, one can describe a system with a small subset of degrees of freedom and consider the remainder degrees of freedom as the effective potential fields. Thus, it enables the application of Langevin's equation to describe to motion of atoms in a macroscopic system.

To introduce the Langevin's equation, we start with the classical Newtonian equation. Simply consider a one-dimensional case for a particle moving in a fluid medium (with viscosity η). The motion of the particle is governed by

$$m\frac{dv}{dt} = F_{total}(t), \tag{2.9}$$

where $F_{total}(t)$ is the total force that the particle experiences at time *t*. This force can be understood as the force that is acted upon the particle by its surrounding liquid medium. Since the force is a function of time, the force itself cannot be totally 'random'. According to the experiments in a large scale, the force can be treated as the 'friction' whose magnitude is proportional to the velocity of the moving particle. If only the friction is considered, the equation of motion becomes

$$m\frac{dv}{dt} = -\xi v, \tag{2.10}$$

where ξ is a positive quantity has the same unit of viscosity. As we can see, it is a first-order differential equation, and its solution is:

$$v(t) = e^{-\xi t/m}\, v(0). \tag{2.11}$$

This solution indicates that the velocity of the particle decays to zero in the long-time limit, which is not in line with the experimental observations on Brownian motion of particles. Also, the solution violates the equipartition law at thermal equilibrium, which suggests that $< v^2 >= k_B T/m$. Therefore, the particle shall have finite velocity even at the long-time limit. Obviously, more terms should be added to the equation to account for the effects of the medium on the motion of particles. The appropriate additional terms needed to modify the equation of motion is a 'random' force δF(t) to the calculation of total force. Then the equation of motion becomes:

$$\frac{dp}{dt} = m\frac{dv}{dt} = -\xi v + \delta F(t). \tag{2.12}$$

It is the famous Langevin equation for the Brownian particle. In the Langevin language, the total force on the particle can be divided into a systematic part (friction) and a fluctuating part (noise). The friction and noise are not totally disconnected, rather they are strongly correlated through the fluctuation-dissipation theorem. One can think that this correlation is due to the fact that both the friction and noise are caused by the interaction between the particle and the surrounding liquid molecules. In other words, the surrounding molecules work together to act as a 'heat bath', providing kinetic energy to the particle through the noise term and stopping the particle from moving too fast so as to ensure that the equipartition law remains valid. In this way, a small set of molecules described using Langevin equation could be thought as if they are immersed in a heat bath maintained at a constant temperature, so that a microscopic simulation can provide a macroscopic picture of atomic motions. Now, the correlation of the friction and noise needs to be further determined.

Several assumptions are required to establish the noise term, or the force induced by thermal fluctuations. In general, the noise force comes from the frequent collisions between the particle and its surrounding medium. Then the force can be understood as the consequence of the effective collisions. If the surrounding medium considered to be homogenous and spherically symmetric, in a long-time limit, the average value of the noise force should go to zero. The other important assumption is that the noise force at time t has no correlation with the noise force at any other time, since the time duration of a collision is much shorter than the time scale of particle motion. The two assumptions can be written as

$$\langle \delta F(t) \rangle = 0, \langle \delta F(t) \delta F(t') \rangle = 2B\delta F(t - t'), \tag{2.13}$$

where B is the strength of the fluctuation force, which remains to be determined. Note that the Langevin equation is a first-order linear differential equation, and it can be solved analytically yielding:

$$\langle v(t) \rangle = e^{-\zeta t/m}\, v(0) + \frac{\int_0^t dt' e^{-\zeta(t-t')/m} \delta F(t')}{m}. \tag{2.14}$$

In order to satisfy the equipartition law, we check $\langle v(t)^2 \rangle$. After expansion, it is obvious that any term that involves $e^{-\zeta t/m}\, v(0)$ decays to zero in long-time limit, and the surviving term is

$$\int_0^t dt'\, e^{-\zeta(t-t')/m} \frac{\delta F(t') \int_0^t dt'' e^{-\zeta(t-t'')/m} \delta F(t'')}{m^2}. \tag{2.15}$$

Inserting the noise term, we can write:

$$\langle v(t)^2 \rangle = e^{-2\zeta t/m}\, v(0)^2 + \frac{B}{\zeta m}\left(1 - e^{-2\zeta t/m}\right). \tag{2.16}$$

We can clearly see that, in the long-time limit

$$\langle v(t)^2 \rangle = \frac{B}{\zeta m}\,. \tag{2.17}$$

To meet the equipartition law, we need

$$\langle v(t)^2 \rangle = \frac{k_B T}{m}. \tag{2.18}$$

Therefore,

$$B = \zeta k_B T\,. \tag{2.19}$$

Till now, we can see that the friction coefficient ζ and the noise strength B are closely related to mimic the effective interaction between a small set of molecules and their surrounding medium with constant temperature. In a simple explanation, the noise term keeps the system 'hot', and

the friction term prevents the system to be 'overheated'. The result is known as fluctuation-dissipation theorem.

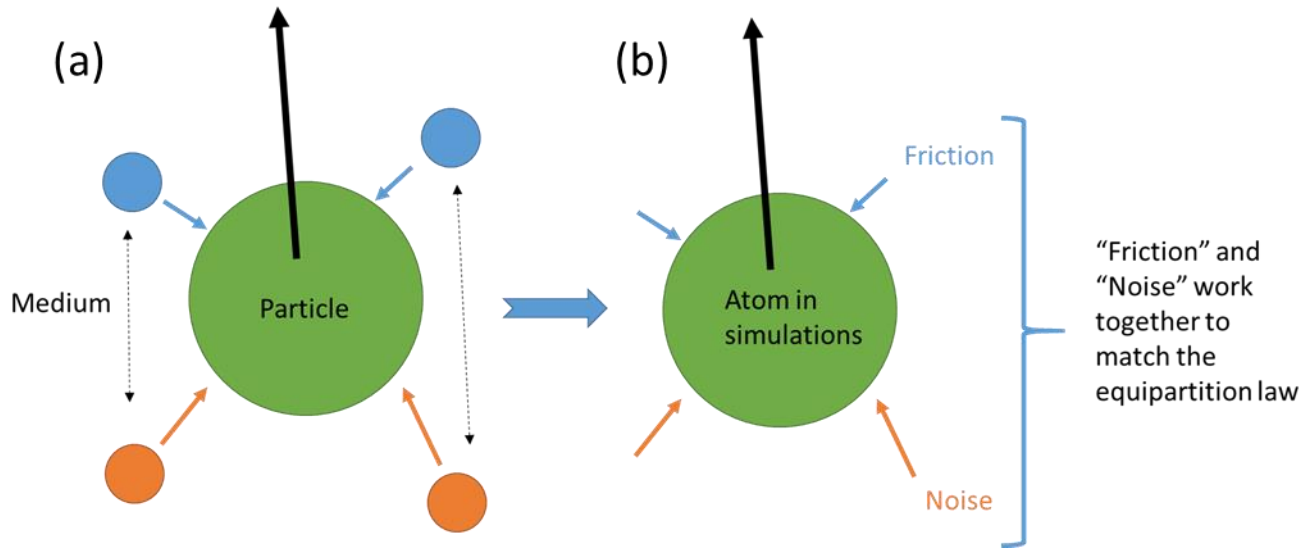

Figure 2.2 Schematic of applying Langevin equation as a stochastic thermostat in MD simulations. (a) Langevin equation applied to describe the motion of a Brownian particle (Green circle) moving along an arbitrary direction (Black arrow) in a medium consisting of smaller particles (Orange and blue circles). The collisions between Brownian particle and the particles (constituting the medium) having velocities in a direction opposite to that of the Brownian particle (Blue circles) result in slowing down of the Brownian particle. In the Langevin equation, the resulting friction force is defined to be varying linearly with the magnitude of the local velocity. At the same time, the collisions between Brownian particle and the particles (constituting the medium) having velocities in a direction similar to that of the Brownian particle (Orange circles) result in slowing down of the Brownian particle. Since the orange and blue particles are essentially interchangeable, the connection leads to the fluctuation-dissipation theorem. (b) In simulations, the system is immersed in a heat bath with infinitely large heat capacity in order to keep its temperature constant. The medium particles described in (a) acts as the particles in such heat bath, and the simulation does not explicitly describe the position and the conjugate momentum of the heat bath particles, i.e., it does not directly show up in the system Hamiltonian. Instead, the effects of the collision force acting on the Brownian particle (atoms in simulation) keeps mimicking the interactions of atoms and its surrounding heat bath particles.

MD simulation is a useful tool to investigate the dynamic problems; however, the results related to system dynamics is not as accurate as the thermodynamic result. The disparity can be regarded due to the assumption made to approximate the Newtonian equation of motion by the Langevin equation of motion. Some simulators, like LAMMPS, have options to modify the general Langevin equation by introducing rotational degrees of freedom to the system. Equivalently, the random force is replaced by random torque and the atomic mass is replaced by the inertia; as a

consequence, the rotational energy also follows the equipartition law. This is important for problems where rotation is important, e.g., the relaxation of ion solvation shell structures. Other details related to the differences in the sizes and masses of the particles can also be modified. However, these modifications are not deterministic, and there is no way to verify that any modification of the general Langevin equation would make the dynamics more accurate at such a small scale.

In a long-time limit, a simulation where the atomic motion is described by the Langvein equation matches the equipartition law, which indicates that it can serve as a thermostat algorith to control the system temperature. Similar to the Langevin thermostat, other methods also try to involve a small subset of atom motion to reproduce the atomic time evolution in a much larger scale.

For example, Berendsen thermostat creates a physical model that immerses the atoms in a heat bath with a constant temperature T_0

$$\frac{dp}{dt} = -U'(q) - \frac{p}{\tau_T}\left[\frac{T_0}{T} - 1\right], \tag{2.20}$$

where p is the momentum of a particle, q is the position of the particle, $-U'(q)$ is the effective force under external potential field, τ_T is the relaxation constant that controls the acceleration of an atom moving from its current temperature state (T) to its target temperature T_0, which is also the temperature of the heat bath surrounding the system. One can picture this model as if the system exchanges its thermal energy with a heat bath at a finite rate. In other words, the system is weakly coupled with the heat bath to maintain its temperature. Obviously, in a long-time limit, the system temperature approaches the target temperature closely enough so that only some little amount of fluctuation exists.

Another commonly used thermostat is the Nosé-Hoover thermostat. It extends the Hamiltonian of the system by a new degree of freedom. i.e., it writes the heat bath directly into the equation of motion

$$\frac{dp}{dt} = -U'(q) - \frac{p_\eta}{Q}p, (2.21)$$

$$\frac{dp_\eta}{dt} = \sum_i^N \frac{|p_i|^2}{2m_i} - \frac{3}{2}nk_BT, (2.22)$$

where Q with a unit of energy.time^2 is also called 'imaginary mass', $k_B$is the Boltzmann constant, T is the target system temperature. Here, the equation of motion for an atom is controlled by the overall temperature of the system. Simply, it means that the energy added to or subtracted from a single atom is same for other atoms in the system in a microstate.

Theoretically, any successful thermostat can bring the system to equilibrium under NVT ensemble. One way to check the equilibrium is to remove thermostats and run the simulation without adding any constrains (NVE). If the system energy does not change any more, it means the system has already at a state that minimizes the Boltzman free energy, and there is no difference between ensembles.

However, the dynamics of the system varies with the thermostats used. Consider water flow as an example. If the flow temperature is controlled by the Langevin equation, the motion of each water molecule in the stream has a very weak correlation with its surrounding water molecules due to the applied random force. However, it is well known that water forms a strong hydrogen bond network and the correlations between the motions of different water molecules are very strong. In this way, a pressure driven flow controlled by Langevin thermostat has a different flow rate compared to that controlled by the Nosé-hoover thermostat. Therefore, the choice of

thermostats can affect the dynamics of the system dramatically, and it has to be carefully chosen for specific problems.

2.3 Post-analysis

Free energy calculation is the most important post-analysis of MD simulations. Considering that the simulation has been performed under NVT ensemble, as an example, the Helmholtz free energy $F(\varepsilon) = \varepsilon - TS(\varepsilon)$ contains the information of both internal energy and entropy. Internal energy can be output directly from the LAMMPS simulator, and the entropy can be obtained by subtracting the internal energy contribution from the free energy. Since the entropic contribution is very hard to obtain, even in simulations, the decomposition of free energy is especially important to evaluate the individual contributions, such as determining if a process is enthalpy driven or entropy driven.

First, let us introduce a concept of potential of mean force (PMF) with respect to a reaction coordinate (a reaction path along the free energy surface). A PMF curve along one reaction coordinate provides the information of how the system arranges its atoms according to the changes in the reaction coordinate. For example, the calculation of hydration free energy of an ion can be obtained through scratching the free energy curve connecting the state where the ion is in bulk (fully hydrated) and the state where the ion is in vacuum (fully dehydrated); accordingly, the reaction coordinate can be chosen as the distance between the ion locations for these two cases (fully hydrated and fully dehydrated). In this dissertation, the Weighted Histogram Analysis Method (WHAM) is applied to generate the PMF curves.

As it is shown in equation 2.7, the essential information desired from numerical simulations is the probability distribution at each energy level, or at each of the energetic density of states.

Since the rare events barely occur in the simulation timescale, a biased potential is added to each point along the reaction coordinate to encourage the system to visit the rare event states within a reasonable timescale. As the additional biased potential, the result is not the exact density of states but the best estimation of the real distribution. The weighted function is considered in a way so as to minimize the overall statistical errors. In order to ensure the best evaluation of the real curve, the histogram distribution in each simulation with the biased potential needs to have sufficient overlap with its neighboring simulations.

Chapter 3: Drop spreading on a superhydrophobic surface: pinned contact line and bending liquid surface Introduction

3.1 Introduction

Superhydrophobicity is fundamental to the functioning and survival of several plants and animals[33–35] and for developing water-repelling surfaces for applications such as self-cleaning,[36] enhanced fluid flow,[37] environmental remediation,[38] thermal management,[39] energy harnessing,[40] *etc.* Natural and nature- inspired engineered superhydrophobic (SH) surfaces have invariably been characterized by static equilibrium contact angles with very little attention on the dynamics of spreading on such SH surfaces. Most of the spreading literature, summarized excellently in several review articles,[41–44] primarily focuses on partially wetting or fully wetting surfaces revealing a strong dependence of the dynamic contact angle (θ_D) on the velocity (U) of the three-phase contact line (TPCL) or the corresponding dimensionless capillary number ($Ca = \eta U/\gamma$, where η is the dynamic viscosity of the liquid and γ is the liquid–vapor surface tension). Primarily, two separate theories have known to dictate the interrelationship between θ_D and Ca. The first theory, well- known as the Cox–Voinov model,[45–52] describes the spreading dynamics in terms of viscous dissipation within the liquid drop and the slip length at the TPCL and proposes $\theta_D \sim Ca^{35}$. The second theory, on the other hand, relates the spreading dynamics to the molecular adsorption and desorption processes at the TPCL – this theory relates the dynamic contact angle to parameters such as the distance between the adsorption sites on the solid surface and the frequency of random molecular displacements at the TPCL.[53–57] There have also been a large number of studies that have (a) probed different

facets of these two theoretical models,[48–50,58] and (b) probed cases where these models may no longer be appropriate.[59,60] Despite such extensive research on the spreading dynamics of liquid drops, very little research has been conducted for elucidating the drop spreading and the relevant θ_D versus Ca behavior on SH surfaces. Only very recently, in a couple of papers, experiments were conducted to elucidate how the advancing and receding contact angles evolve temporally as functions of the capillary number (Ca).[61,62] While both these papers reported the advancing contact angles to remain constant and independent of Ca, they demonstrated the opposite dependence of the receding contact angles on Ca. There are also a few recent studies that elucidate issues such as energy change during drop spreading on SH surfaces,[63] the role of temperature decreases in enabling spreading on SH surfaces,[64] etc.

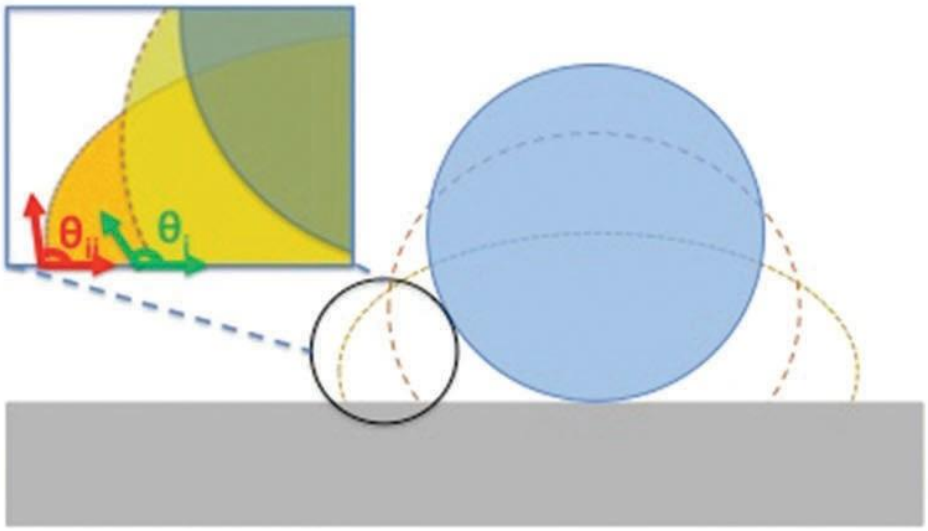

Fig. 3.1 Schematic illustrating the spreading process on a standard non-SH surface – the spreading occurs by the motion of the TPCL with a progressive decrease in the local three-phase contact angle. This progressive lowering of the local contact angle is illustrated in the inset – the dynamic contact angle progressively decreases from θ_i to θ_{ii}

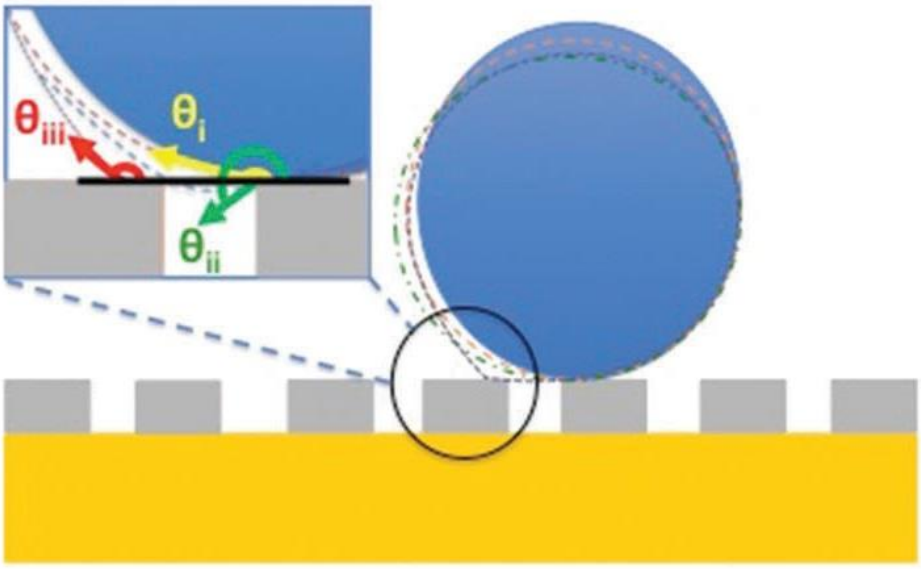

Fig. 3.2 Schematic illustrating the proposed spreading mechanism on an SH surface (constituting an array of nanopillars). We propose this mechanism based on the MD simulations that we report in this study. Unlike the case of the non-SH surface, the spreading occurs with the TPCL remaining pinned at the edge of the nanopillar. More importantly, the corresponding liquid vapor interface ‘‘bends’’ down, evidenced by the fact that the corresponding local three-phase contact angle increases from θ_i to θ_{ii} (please see the inset). This enhanced contact angle θ_{ii} can be larger than 180°, indicating a bending of the liquid surface even below the horizontal plane of the nanopillars. This bending eventually ensures the wetting of the adjacent nanopillar and this wetting is characterized by the attainment of a new three-phase contact angle θ_{iii}, where $\theta_{iii} < \theta_{ii}$ (please see the inset). Therefore, the spreading occurs not by the motion of the TPCL, but by the bending of the liquid–vapor interface of the TPCL that remains pinned.

In this chapter, we investigate at the atomistic scale drop spreading on a SH surface – we develop a molecular dynamics (MD) simulation framework to study the spreading of a water nanodrop on a SH surface consisting of graphene nanopillars supported on an extremely hydrophilic (bare gold) and a much less hydrophilic (gold-supported graphene monolayer) solid. There has been considerable prior research on the use of MD simulations for studying drop dynamics; [65–78] however, very little effort has been devoted to quantifying the drop behavior on SH surfaces over atomistic length scales. The central result of our simulations is as follows: on a SH surface, the liquid drop does not spread by the motion of the TPCL;

rather the TPCL remains pinned and the drop spreads by the bending of the liquid–air interface of this pinned TPCL (see Fig. 3.2). This bending, which ensures that the drop wets the adjacent solid surface (here nanopillars), is quantified both from the simulation snapshot as well as from noting a progressive increase (and not decrease) of the advancing local contact angle (identified in Fig. 3.2) up to a value close to or even greater than 180º. This is a most outstanding finding in light of the fact that this is for the first time one witnesses drop spreading without the actual physical motion of the TPCL (see Fig. 3.1 and Fig. 3.2 for a pictorial comparison). Consequently, the drop spreading (or equivalently the dynamic contact angles) no longer depends on the capillary number. There have been previous studies elucidating the role of pinning forces in the interaction of water with a nanorough/ nanostructured surface;[70,79] however, in this paper we elucidate for the first time the significance of these pinning forces in triggering the bending-induced spreading on SH surfaces. More importantly, we find experimental confirmation of such air–liquid-interface-bending induced drop motion on SH surfaces. In a very recent study, Butt and co-workers experimentally demonstrated the rolling motion of millimetric water drops on SH surfaces – they noted that the drops moved by such bending of the air–liquid interface.[80] Our simulations and this recent experimental study allow us to infer that drops on SH surfaces, regardless of the system dimensions, demonstrate a universal tendency to move (spread or roll) by the bending of the liquid–vapor interface and not by the motion of the TPCL. We anticipate that this finding will be of immense fundamental interest for a better understanding of drop dynamics on SH surfaces, thereby enabling a more successful and efficient design of SH surfaces for a plethora of applications ranging from self-cleaning and energy harvesting to rapid cooling and enhanced drag reduction.

3.2 Molecular dynamics simulations

Our MD simulation framework closely follows our previous works on drop dynamics on continuous supported and unsupported graphene layers[68] and graphene nanopillars.[69] In this study, we carry out MD simulations of a two-dimensional water nanodrop on (i) graphene nanopillars (consisting of 4 graphene layers) supported on bare gold (the corresponding drop equilibrium contact angle is 140 ± 2º) and (ii) graphene nanopillars (consisting of 3 graphene layers) on a gold-supported graphene monolayer (the corresponding drop equilibrium contact angle is 138 ± 3°). Such a system ensures that the substrates supporting the nanopillars exhibit distinctly different wettabilities – for example bare gold is more hydrophilic (the water drop contact angle on bare gold is 29º) than the gold-supported graphene monolayer (the water drop contact angle on the gold-supported graphene monolayer is 75º).[68] Here, we summarize the important details of the different simulation steps. The Large-scale Atomic/Molecular Massively Parallel Simulator (LAMMPS) [81] software package has been used to carry out the MD simulations.

Furthermore, the Open Visualization Tool (OVITO)[82] is used to render the simulations, while the post-processing for quantifying the time evolution of the local contact angle is carried out using MATLAB.

In these simulations, similar to our previous studies,[68,69] a quasi-2D simulation geometry is employed to ensure that the curvature-induced line tension at the TPCL gets eliminated. For 3D nanoscale drops, the line tension effect leads to a substantial deviation of the observed contact angle (θ) from Young's angle (θ_Y):[83]

$$cos\theta = cos\theta_Y - \frac{\tau}{\gamma r}, \quad (3.1)$$

where τ is the line tension and r is the wetted radius of the contact line. In contrast, by implementing this quasi-2D, cylindrical drop configuration, we ensure that the contact line becomes straight, which in turn eliminates the system-size- dependence of the contact angle.[5,83] In our simulations, we employ the SPC/E model (extended simple point charge) to model the water drop.[84] This model is characterized by the water molecules interacting with each other via a 12-6 Lennard- Jones (LJ) potential as well as Columbic electrostatic inter-actions. For the LJ interactions, the LJ site has been localized on the oxygen atom (with LJ parameters ε_{OO} = 0.650 kJ mol^{-1}, σ_{OO} = 0.3166 nm). On the other hand, Columbic electrostatic interactions are accounted for by considering that the oxygen hydrogen atoms carry charges (q_O = -0.8476e and q_H = 0.4238e, where *e* is the electronic charge). In our model, water–graphene interactions are modeled using the C–O LJ potential, with the LJ parameters being obtained from the work by Werder et al. (ε_{CO} = 0.392 kJ mol^{-1} and σ_{CO} = 0.319 nm).[85] The gold substrate is modeled such that the Au(111) surface is aligned with the graphene lattice, which is stretched by ~1.5%. Here, the Au–O LJ potential of Merabia et al. (ε_{AuO} = 2.469 kJ mol^{-1} and σ_{AuO} = 0.36 nm) has been used to model the gold–water interactions.[86] We employ a cutoff radius of 10 Å for all the LJ interactions. Finally, we ensure that the substrate atoms are held fixed at their lattice positions throughout the simulations – this approach has been borrowed from similar MD studies of drop wetting ensuring substantial reduction of the computational expense without significantly affecting the observed contact angles. A more detailed description of the entire simulation procedure can be obtained from our previous papers.[68,69]

A key issue here is the choice of the number of water molecules. For the present study, we consider two geometries – four-layered graphene nanopillars supported on bare gold and three-layered graphene nanopillars supported on a gold- supported graphene monolayer. For both these geometries, simulations are carried out by varying the number of water molecules. This is done in order to ensure that our simulations yield both the advancing and receding contact angles, corresponding to the wetting of a given number of pillars. Following Koishi et al.,[87] we define the receding and advancing contact angles as the angles made by the drop containing $N = N_{min}$ and $N = N_{max}$ number of water molecules, respectively. Here, we define N_{min} as follows: for any N (number of water molecules) such that $N < N_{min}$, the water nanodrop at equilibrium fails to wet the chosen number of pillars. On the other hand, N_{max} is defined as follows: for any N (number of water molecules) such that $N > N_{max}$, the water nanodrop at equilibrium wets a greater number of pillars than the chosen number or transits from the CB to the Wenzel state. For the present study, the chosen number of pillars is 3 for both the nanopillared geometries.

In this study, drop dynamics on nanopillared surfaces are analyzed. In order to form the nanopillars, we first create bulk graphene having the desired number of layers and then remove the carbon atoms from the specified locations ensuring that the nanopillars (having both width and spacing of 13 Å) are left behind. This spacing (and width) is chosen such that it is larger than the molecular size of water but smaller than the water drop size (drop radius is ~40 Å). Further, this value of the spacing and the width ascertains that all nanopillar edges will have a ‘‘zig-zag’’ configuration that is a stable edge configuration of a graphene sheet.[88]

There are two key phases for the simulations – the first is the drop equilibration (and in the process carefully study the dynamics of the drop and the temporal evolution of the contact line and the contact angle) and the second is the data collection. Both the steps are performed in the NVT ensemble where a time step of 1 fs is used. Furthermore, the temperature control is ensured using a Nosé–Hoover thermostat.[89] For the drop equilibration phase, we start by initializing the water molecules in an ordered, box-like configuration far from the substrate. We subsequently increase the system temperature from 1 K to 300 K in 50 K increments. We held the intermediate temperatures for 50 ps intervals and the final 300 K is held for 200 ps. This procedure ensures a well-formed, equilibrated drop and in the process provides vital information about the drop dynamics. In the subsequent data collection phase, we bring this equilibrated drop to within ~3 Å of the substrate. Finally, we allow the system to evolve forward in time again for 500 ps or 1000 ps, allowing the drop to spread on the surface.

In order to calculate equilibrium, contact angles, we import the atomic position coordinate data into MATLAB. These data are subsequently sorted into 2 Å by 2 Å square bins in the x–z plane, which eventually allows markers to be placed along the edge of the drop thereby confirming the drop profile. In the next step, we fit a circle to these markers using a least squares regression. We then calculate the tangent to the circle where it intersects with the horizontal upper surface of the substrate, and the equilibrium contact angle is easily quantified from this tangent line. For the present study, the quantification of the temporal variation of the contact angles is equally important. They are quantified (at several time instants during the spreading) by manual measurement (as shown in Fig. 3.3 and 3.4-3.7), since the circle fitting procedure does not yield reliable results in this case. This manual

measurement is carried out as follows: Firstly, we draw a horizontal line coinciding with the top surface of the nanopillar at the edge of which the TPCL of the nanodrop gets pinned. Subsequently, we draw a tangent to the instantaneous location of the air–water interface of this pinned TPCL. The instantaneous local angle is defined as the angle made between these two lines with the angle obtained by traversing from the top of the nanopillar to the air–liquid interface of the drop. The figures in the insets of Fig. 3.3 (b, c, e, f) and 3.8 (b, c, e, f) illustrate this measurement of the instantaneous local contact angle. Of course, the experiments described in ref. 80 prescribe an exactly similar method for quantifying the time-dependent contact angle of the drop.

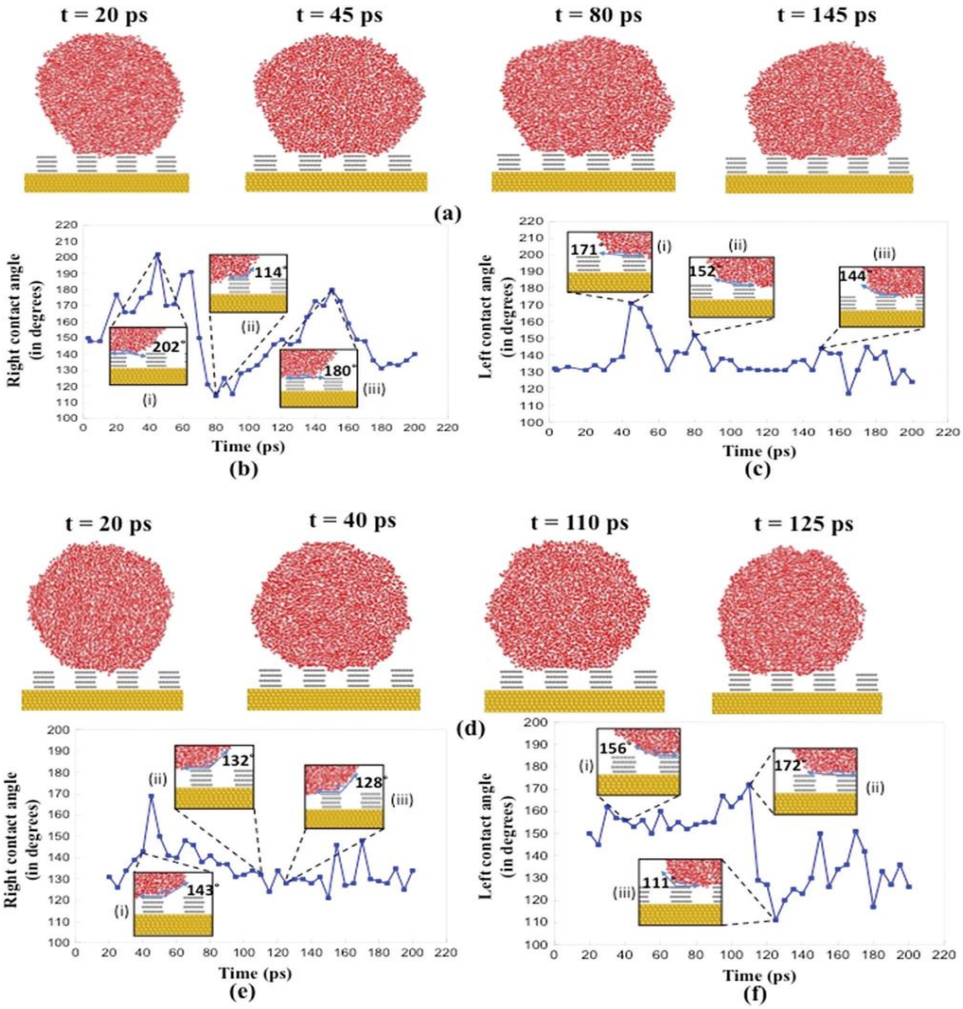

Fig. 3.3 Spreading of a water nanodrop in a superhydrophobic CB state on graphene nanopillars supported on bare gold. (a–c) represent the case where $N = N_1$, while (d–f) represent the case where $N = N_2$. (a) MD simulation snapshots (the corresponding time is indicated for each snapshot) illustrating the spreading of a water nanodrop containing $N = N_1 = 4500$ molecules. (b) Temporal evolution of the right local contact angle of this drop with $N = N_1 = 4500$ molecules. In insets (i–iii), we provide the magnified views of the right three-phase contact line at three different time instants (namely, t = 45, 80, 145 ps). The snapshots of the entire drop corresponding to these time instants are shown in (a). (c) Temporal evolution of the left local contact angle of this drop with $N = N_1 = 4500$ molecules. In insets (i–iii), we provide the magnified views of the left three-phase contact line at three different time instants (namely, t = 45, 80, 145 ps). (d) MD simulation snapshots (the corresponding time is indicated for each snapshot) illustrating the spreading of a water nanodrop containing $N = N_2 = 4000$ molecules. (e) Temporal evolution of the right local contact angle of this drop with $N = N_2 = 4000$ molecules. In insets (i–iii), we provide the magnified views of the right three-phase contact line at three different time instants (namely, t = 40, 110, 125 ps). The snapshots of the entire drop corresponding to these time instants are shown in (d). (f) Temporal evolution of the left local contact angle of this drop with $N = N_2 = 4000$ molecules. In insets (i–iii), we provide the magnified views of the left three-phase contact line at three different time instants (namely, t = 40, 110, 125 ps).

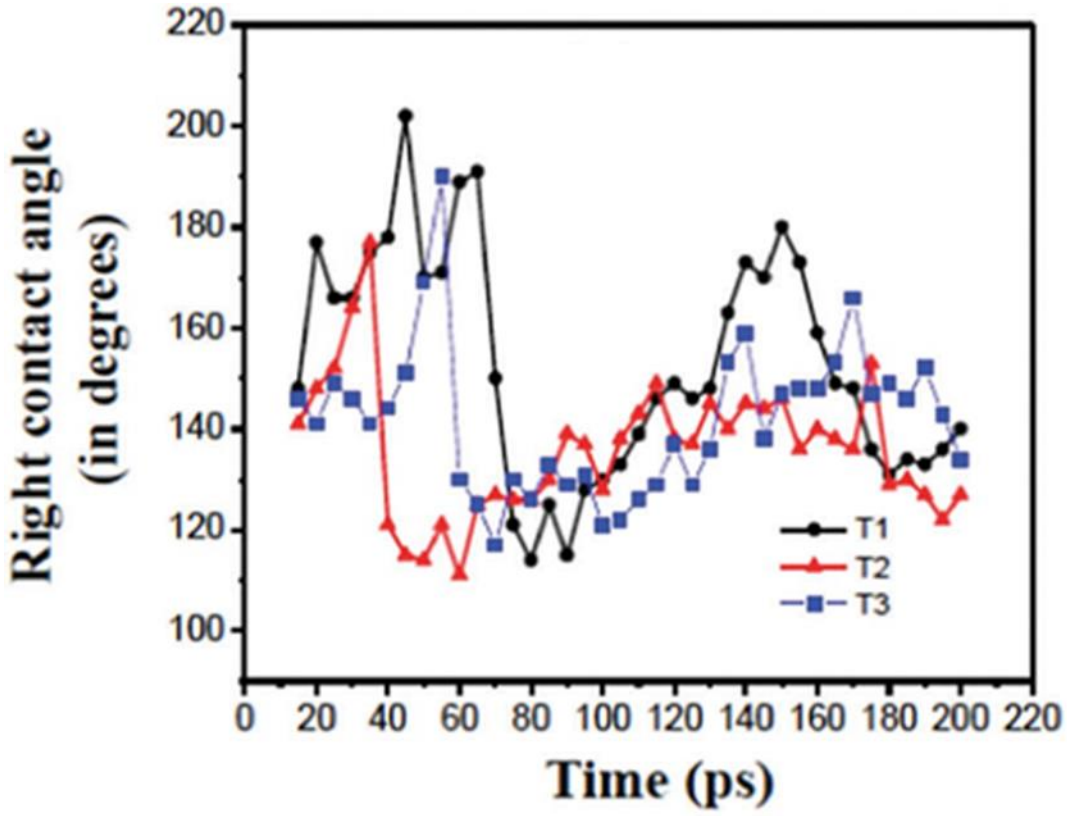

Fig. 3.4 Temporal evolution of the right local contact angle (for $N = N_1 = 4500$) for three different starting trajectories (T_1, T_2, and T_3) of a water nanodrop. Here, T_1 refers to the trajectory where the water nanodrop contacts the nanostructured graphene surface with the drop center vertically aligned with the middle of the groove surface (or the part of the surface without nanopillars). Fig. 3.3 is obtained with trajectory T_1. T_2 and T_3 refer to the trajectories where, at the time when the nanodrop contacts the nanostructured surface, the center of the nanodrop is horizontally shifted to the left by 0.1 nm and 0.2 nm (with respect to the drop center corresponding to trajectory T_1), respectively. All the contact angles are provided for the case where the nanodrop spreads in a superhydrophobic CB state on graphene nanopillars supported on bare gold (the structure is depicted in Fig. 3.3).

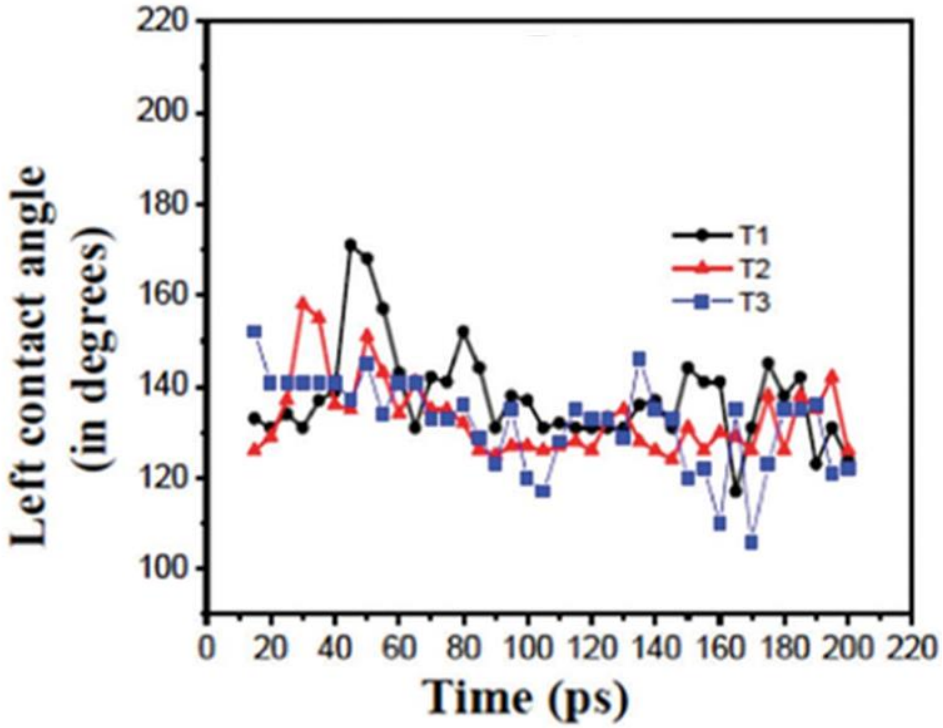

Fig. 3.5 Temporal evolution of the left local contact angle (for $N = N_1 = 4500$) for three different starting trajectories (T_1, T_2, and T_3) of a water nanodrop. Here, T_1 refers to the trajectory where the water nanodrop contacts the nanostructured graphene surface with the drop center vertically aligned with the middle of the groove surface (or the part of the surface without nanopillars). Fig. 3.3 is obtained with trajectory T_1. T_2 and T_3 refer to the trajectories where, at the time when the nanodrop contacts the nanostructured surface, the center of the nanodrop is horizontally shifted to the left by 0.1 nm and 0.2 nm (with respect to the drop center corresponding to trajectory T_1), respectively. All the contact angles are provided for the case where the nanodrop spreads in a superhydrophobic CB state on graphene nanopillars supported on bare gold (the structure is depicted in Fig. 3.3).

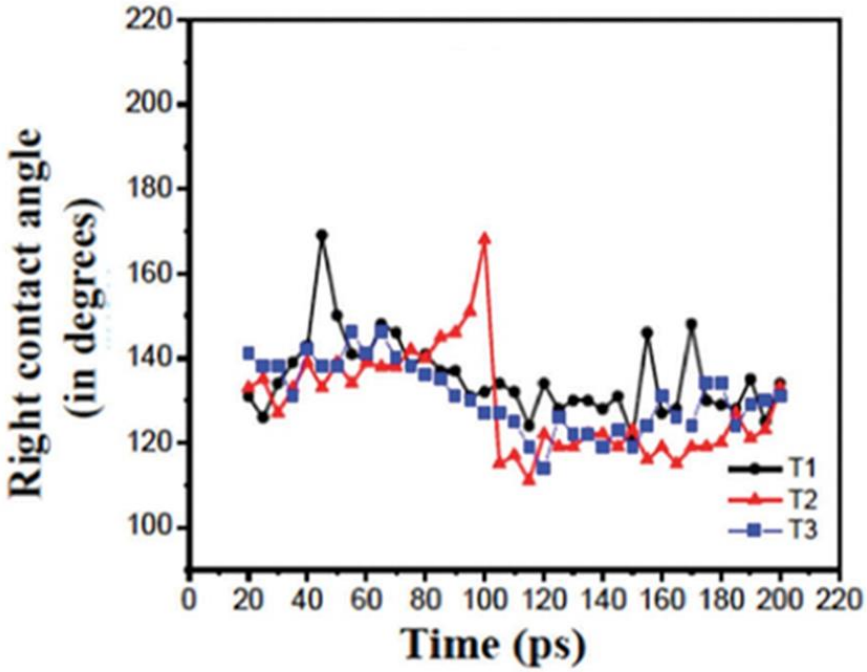

Fig. 3.6 Temporal evolution of the right local contact angle (for $N = N_2 = 4000$) for three different starting trajectories (T_1, T_2, and T_3) of a water nanodrop. Here, T_1 refers to the trajectory where the water nanodrop contacts the nanostructured graphene surface with the drop center vertically aligned with the middle of the groove surface (or the part of the surface without nanopillars). Fig. 3.3 is obtained with trajectory T_1. T_2 and T_3 refer to the trajectories where, at the time when the nanodrop contacts the nanostructured surface, the center of the nanodrop is horizontally shifted to the left by 0.1 nm and 0.2 nm (with respect to the drop center corresponding to trajectory T_1), respectively. All the contact angles are provided for the case where the nanodrop spreads in a superhydrophobic CB state on graphene nanopillars supported on bare gold (the structure is depicted in Fig. 3.3).

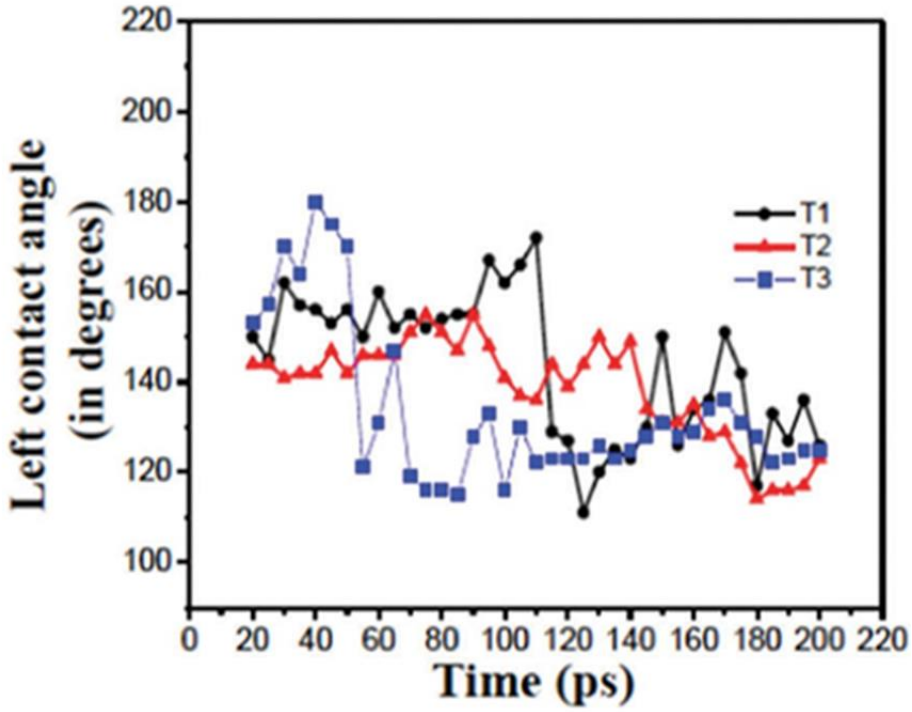

Fig. 3.7 Temporal evolution of the right local contact angle (for $N = N_2 = 4000$) for three different starting trajectories (T_1, T_2, and T_3) of a water nanodrop. Here, T_1 refers to the trajectory where the water nanodrop contacts the nanostructured graphene surface with the drop center vertically aligned with the middle of the groove surface (or the part of the surface without nanopillars). Fig. 3.3 is obtained with trajectory T_1. T_2 and T_3 refer to the trajectories where, at the time when the nanodrop contacts the nanostructured surface, the center of the nanodrop is horizontally shifted to the left by 0.1 nm and 0.2 nm (with respect to the drop center corresponding to trajectory T_1), respectively. All the contact angles are provided for the case where the nanodrop spreads in a superhydrophobic CB state on graphene nanopillars supported on bare gold (the structure is depicted in Fig. 3.3).

3.3 Results

Drop spreading with pinned TPCL and bending of the liquid–vapor interface of the TPCL

Fig. 3.3 and 3.8 describe the dynamics of spreading of a water nanodrop on an SH surface with the drop being in the CB state. In Fig. 3.3, the nanopillars (made of graphene) enforcing the drop into an SH CB state are on bare gold, which is a hydrophilic substrate. In Fig. 3.8, on the other hand, the nanopillars are on a gold-supported graphene monolayer, which is a substantially less hydrophilic substrate. For either of the cases, we study drop spreading for two different numbers

of water molecules, N_1 and N_2, which enforce advancing and receding contact angles, respectively (see Section 3.2 for the definitions of N_1 and N_2). In the present study, for both the cases (studied in Fig.3.3 and 3.8), N_1 = 4500 and N_2 = 4000.

In Fig.3.3 (a), we provide the snapshots illustrating drop spreading on graphene nanopillars supported on bare gold for $N = N_1$. The snapshots reveal that the drop spreads to the right and wets a nanopillar on the right (please see the snapshot corresponding to t = 45 and 80 ps), while there is no spreading to the left. In Fig. 3.3(b) and (c), we quantify the corresponding temporal dynamics of the right and the left three-phase local contact angles, as explicated in the magnified snapshots of the locations of the three-phase contact line [see insets (i)–(iii) in both Fig. 3.3(b) and (c)]. These magnified snapshots, shown for t = 45, 80, and 145 ps [the corresponding snapshots for the entire drop are given in Fig. 3.3(a)], illustrate the method of obtaining the instantaneous local contact angles (described at the end of section 3.2). More importantly, these snapshots point to a most remarkable spreading behavior. The spreading occurs with the contact line remaining pinned, but the liquid surface (or the liquid–vapor interface of this pinned TPCL) bending and contacting the adjacent pillars. The time evolution of these resulting local contact angles confirms the bending. We witness that the right local contact angle first increases and attains a value greater than 180º [please see the temporal variation of the right local contact angle in the period 0 to 50 ps in Fig. 3.3(b) and also inset (i) in Fig. 3.3(b)]. In fact, this enhanced local contact angle can be even more than 200º. This signals a definite ‘‘bending’’ of the liquid surface even below the horizontal nanopillar surface, which eventually ensures that the adjacent pillar on the right gets wetted.

This approach of describing the liquid surface (air–liquid inter- face) to be ‘‘bent’’, commensurate with the fact that the local instantaneous contact angle becomes greater than or

comparable to 180º, has been borrowed from the experimental study of ref. 80 where such bending-induced drop motion of SH surfaces was first experimentally reported. Immediately after the occurrence of this wetting, there is a drastic lowering of the right three-phase local contact angle, as evident from inset (ii) in Fig. 3.3(b) [also see the temporal variation of the right local contact angle in the period 50 to 100 ps in Fig. 3.3(b)]. After this wetting of the adjacent nanopillar, the newly formed TPCL (please note that this new contact line is formed on account of the liquid-surface-bending-induced wetting of the adjacent right nanopillar) gets pinned once again. Subsequently, the right local contact angle increases once again, indicating the bending of the liquid–vapor interface [please see the temporal variation of the right local contact angle in the period 100 to 150 ps in Fig. 3.3(b) and inset (iii) in Fig. 3.3(b)]; however, this extent of bending or equivalently the increase in the right local contact angle (which may increase to as large a value as 180º) is not large enough to cause the wetting of the next pillar. Accordingly, this right contact angle fluctuates between large and small values, without actually ensuring the bending-induced wetting of the adjacent right nanopillar [please see the temporal variation of the right local contact angle in the period 150 to 200 ps in Fig. 3.3(b)].

Fig. 3.3(c) depicts the behavior of the left contact line and the left contact angle. The left contact line remains pinned as well and there is indeed a bending of the corresponding liquid–vapor interface, as evident from the progressive increase in the left local three-phase contact angle [please see the time variation of the left local contact angle in the period 20 to 50 ps in Fig. 3.3(c) and inset (i) in Fig. 3.3(c)]. However, this bending is not large enough (or equivalently the increase in the left local contact angle is not large enough) to trigger the wetting of the adjacent pillars. Therefore, during the entire time the contact line remains pinned and the left local contact angle fluctuates; but there is no physical spreading to the adjacent pillar.

In Fig. 3.3(d–f), we consider the spreading of a water nanodrop with N_2 number of water molecules with the drop being in the CB state on bare-gold-supported graphene nanopillars. The simulation snapshots illustrating the entire spreading process are shown in Fig. 3.3(d) – unlike the case with $N = N_1$ [see Fig. 3.3(a)] here the drop spreads to the left and wets a nanopillar on the left (please see the snapshot corresponding to t = 110 and 125 ps), while there is no spreading to the right. Therefore, we can infer that the qualitative behaviors of the left and the right contact angles are reversed as compared to the case of $N = N_1$ [please see Fig. 3.3(a–c)]. The left TPCL remains pinned and the left local contact angle [see Fig. 3.3(f)] progressively increases (or equivalently the liquid–vapor interface of the left TPCL bends) eventually wetting the adjacent left nanopillar. On the other hand, the right contact line remains pinned and the right local contact angle fluctuates with the liquid surface failing to bend sufficiently to cause the wetting [see Fig. 3.3(e)]. The key difference in this case of $N = N_2$ is that this bending-induced spreading is achieved at a much lesser value of this enhanced local left contact angle (~172^o).

In Fig. 3.3(a–f) we study the drop dynamics for a given starting trajectory of the drop. By this starting trajectory, we imply the relative location of the drop center with respect to the location of a nanopillar at the time when the drop contacts the nano- pillared surface. In Fig. 3.4-3.7, we study and compare the time evolution of the right and left local contact angles of the drop for both $N = N_1$ (case of advancing contact angle) and $N = N_2$ (case of receding contact angle) for two more initial trajectories of the drop (see the caption for details). We witness a pretty similar temporal evolution of the contact angles.

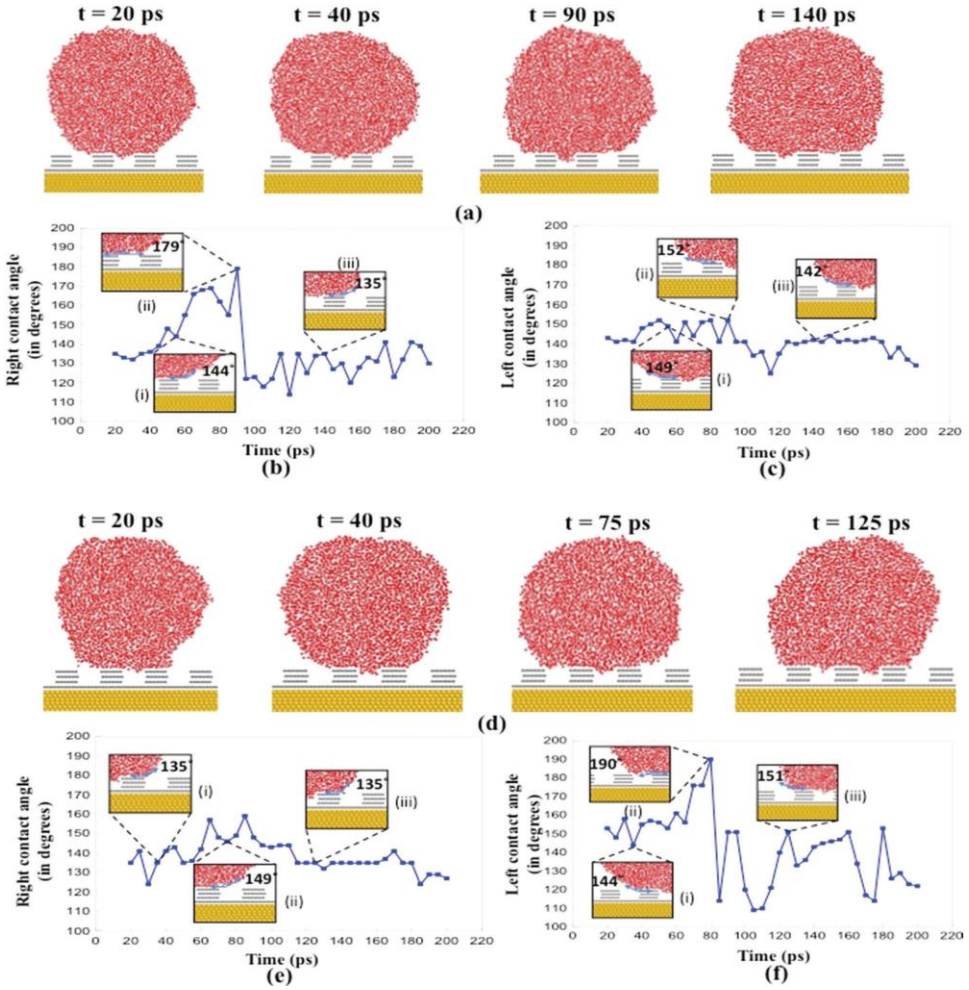

Fig. 3.8 Spreading of a water nanodrop in a superhydrophobic CB state on graphene nanopillars supported on a gold-supported graphene monolayer. (a–c) represent the case where $N = N_1$, while (d–f) represent the case where $N = N_2$. (a) MD simulation snapshots (the corresponding time is indicated for each snapshot) illustrating the spreading of a water nanodrop containing $N = N_1$= 4500 molecules. (b) Temporal evolution of the right local contact angle of this drop with $N = N_1$= 4500 molecules. In insets (i–iii), we provide the magnified views of the right three-phase contact line at three spreading on SH surfaces. Here, we try to understand the origin of such a bending. Different instants (namely, t = 40, 90, 140 ps). The snapshots of the entire drop corresponding to these time instants are shown in (a). (c) Temporal evolution of the left local contact angle of this drop with $N = N_1$= 4500 molecules. In insets (i–iii), we provide the magnified views of the left three-phase contact line at three different instants (namely, t = 40, 90, 140 ps). (d) MD simulations snapshots (the corresponding time is indicated for each snapshot) illustrating the spreading of a water nanodrop containing $N = N_2$ = 4000 molecules. (e) Temporal evolution of the right local contact angle of this drop with $N = N_2$ = 4000 molecules. In insets (i–iii), we provide the magnified views of the right three-phase contact line at three different time instants (namely, t = 40, 75, 125 ps). The snapshots of the entire drop corresponding to these time instants are shown in (d). (f) Temporal evolution of the left local contact angle of this drop with $N = N_2$ = 4000 molecules. In insets (i–iii), we provide the magnified views of the left three-phase contact line at three different time instants (namely, t = 40, 75, 125 ps).

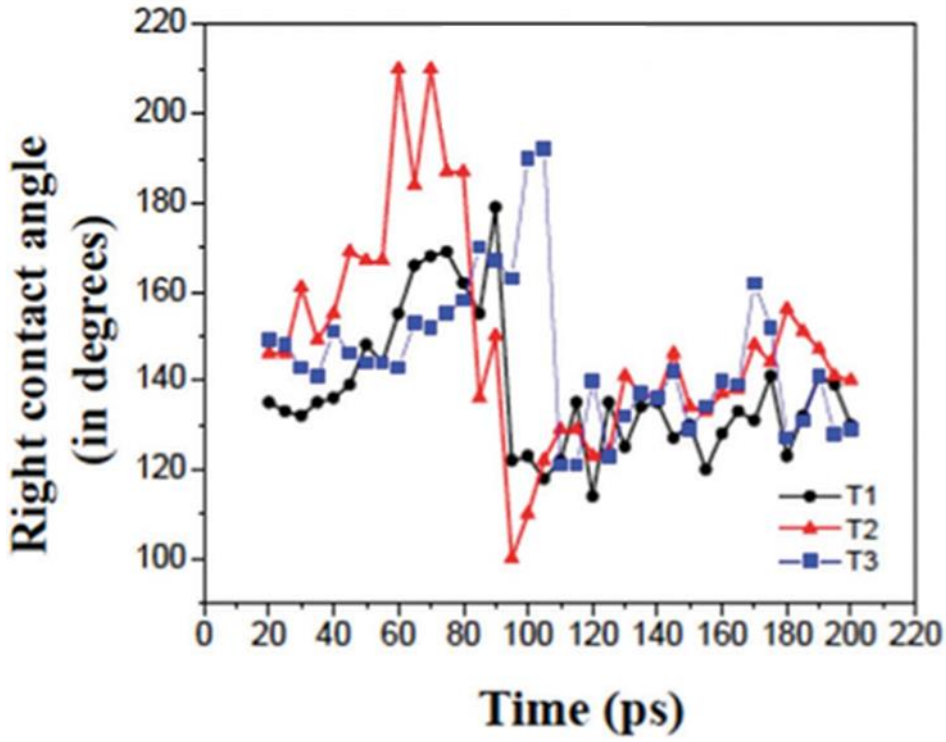

Fig. 3.9 Temporal evolution of the (a) right local contact angle (for $N = N_1 = 4500$) for three different starting trajectories (T_1, T_2, and T_3) of a water nanodrop. Here, T_1 refers to the trajectory where the water nanodrop contacts the nanostructured graphene surface with the drop center vertically aligned with the middle of the groove surface (or the part of the surface without the nanopillars). Fig. 3.3 is obtained with trajectory T_1. T_2 and T_3 refer to the trajectories where, at the time when the nanodrop contacts the nanostructured surface, the center of the nanodrop is horizontally shifted to the left (with respect to the drop center corresponding to trajectory T_1) by 0.1 nm and 0.12 nm for $N = N_1$ (0.1 nm and 0.15 nm for $N = N_2$), respectively. All the contact angles are provided for the case of where the nanodrop spreads in a superhydrophobic CB state on graphene nanopillars supported on a gold-supported graphene monolayer (the structure is depicted in Fig. 3.8).

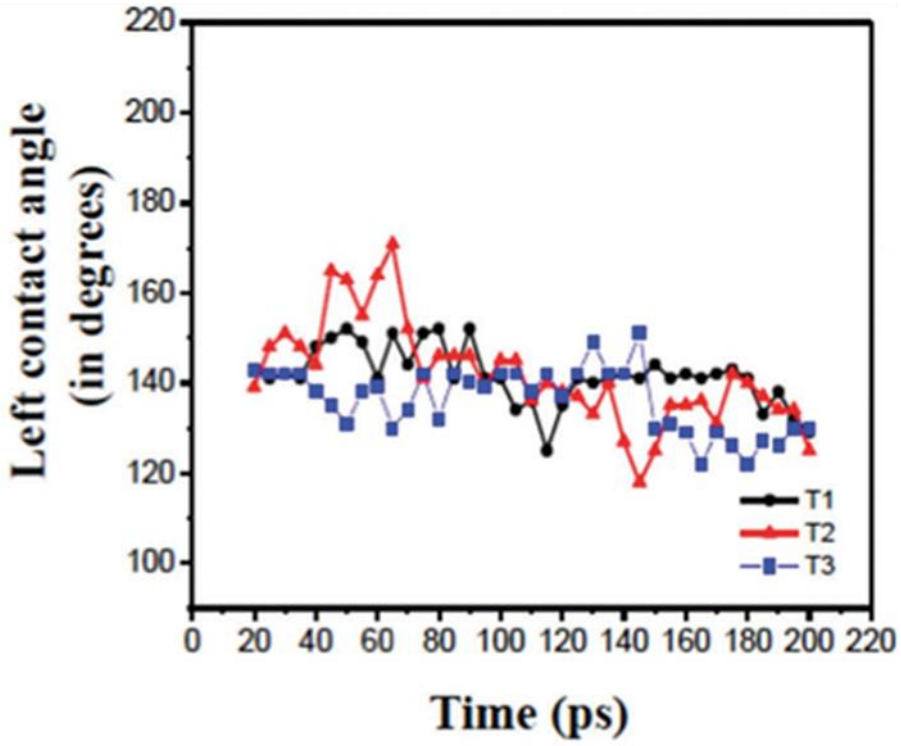

Fig. 3.10 Temporal evolution of the local contact angle (for $N = N_1 = 4500$) for three different starting trajectories (T_1, T_2, and T_3) of a water nanodrop. Here, T_1 refers to the trajectory where the water nanodrop contacts the nanostructured graphene surface with the drop center vertically aligned with the middle of the groove surface (or the part of the surface without the nanopillars). Fig. 3.3 is obtained with trajectory T_1. T_2 and T_3 refer to the trajectories where, at the time when the nanodrop contacts the nanostructured surface, the center of the nanodrop is horizontally shifted to the left (with respect to the drop center corresponding to trajectory T_1) by 0.1 nm and 0.12 nm for $N = N_1$ (0.1 nm and 0.15 nm for $N = N_2$), respectively. All the contact angles are provided for the case of where the nanodrop spreads in a superhydrophobic CB state on graphene nanopillars supported on a gold-supported graphene monolayer (the structure is depicted in Fig. 3.8).

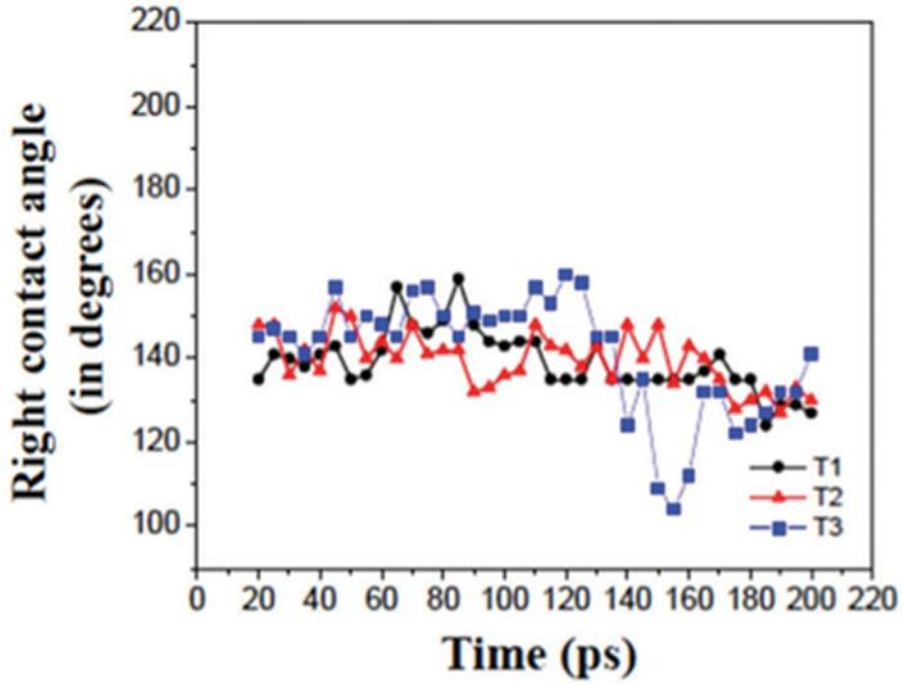

Fig. 3.11 Temporal evolution of the right local contact angle (for $N = N_2 = 4000$) for three different starting trajectories (T_1, T_2, and T_3) of a water nanodrop. Here, T_1 refers to the trajectory where the water nanodrop contacts the nanostructured graphene surface with the drop center vertically aligned with the middle of the groove surface (or the part of the surface without the nanopillars). Fig. 3.3 is obtained with trajectory T_1. T_2 and T_3 refer to the trajectories where, at the time when the nanodrop contacts the nanostructured surface, the center of the nanodrop is horizontally shifted to the left (with respect to the drop center corresponding to trajectory T_1) by 0.1 nm and 0.12 nm for $N = N_1$ (0.1 nm and 0.15 nm for $N = N_2$), respectively. All the contact angles are provided for the case of where the nanodrop spreads in a superhydrophobic CB state on graphene nanopillars supported on a gold-supported graphene monolayer (the structure is depicted in Fig. 3.8).

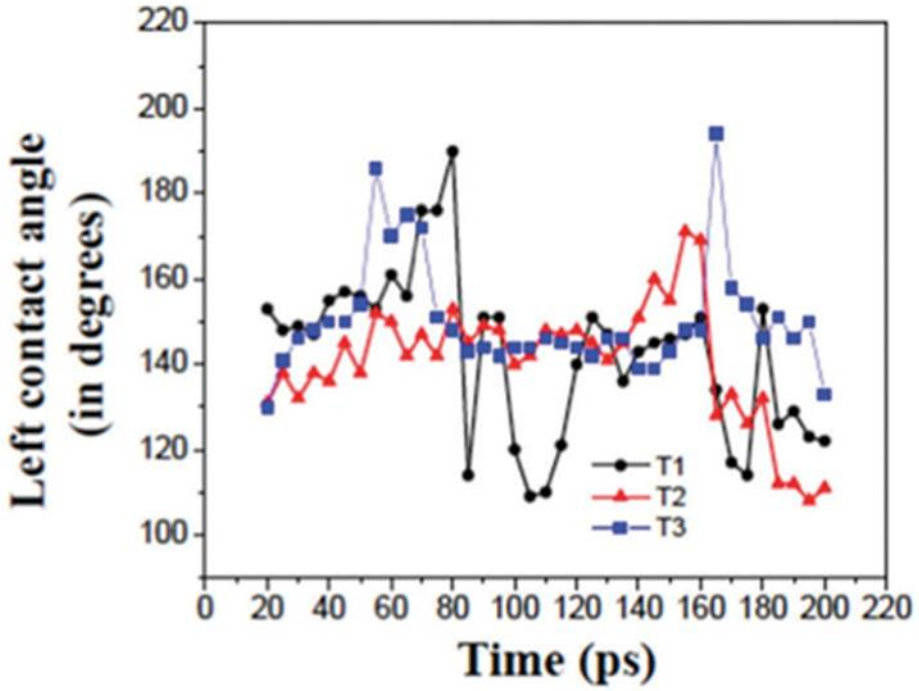

Fig. 3.12 Temporal evolution of the right local contact angle (for $N = N_2 = 4000$) for three different starting trajectories (T_1, T_2, and T_3) of a water nanodrop. Here, T_1 refers to the trajectory where the water nanodrop contacts the nanostructured graphene surface with the drop center vertically aligned with the middle of the groove surface (or the part of the surface without the nanopillars). Fig. 3.3 is obtained with trajectory T_1. T_2 and T_3 refer to the trajectories where, at the time when the nanodrop contacts the nanostructured surface, the center of the nanodrop is horizontally shifted to the left (with respect to the drop center corresponding to trajectory T_1) by 0.1 nm and 0.12 nm for $N = N_1$ (0.1 nm and 0.15 nm for $N = N_2$), respectively. All the contact angles are provided for the case of where the nanodrop spreads in a superhydrophobic CB state on graphene nanopillars supported on a gold-supported graphene monolayer (the structure is depicted in Fig. 3.8).

In Fig. 3.8, we repeat these results for a water nanodrop on graphene nanopillars on a much less hydrophilic surface, namely the gold-supported graphene monolayer. In a recent paper, ref.77, we have studied drop dynamics on an exactly similar system; however, we did not probe the spreading dynamics in detail. Furthermore, the time instants corresponding to which we probe the drop dynamics are different from those probed in ref. 77. In Fig. 3.8, qualitatively very similar results to that of Fig. 3.3 are obtained. Firstly, for $N = N_1$ [see Fig. 3.8(a) for the corresponding snapshots], we observe an increase in the right local contact angle to a value

~180º [see insets (i) and (ii) in Fig. 3.8(b) and the time variation of the right local contact angle in the period 40 to 80 ps in Fig. 3.8(b)]. This leads to an equivalent liquid-surface-bending-driven spreading of the drop to the adjacent right pillar. Here too, the right contact line remains pinned and the entire spreading event takes place by a ‘‘large-enough’’ bending of the liquid–vapor interface of this pinned contact line. In Fig. 3.8(c), we study the temporal behavior of the corresponding left local contact angle. The left contact line remains pinned and the left local contact angle increases (or equivalently, the corresponding liquid– vapor interface bends). However, this bending (or the increase in the left local contact angle) is not large enough to ensure the wetting of the adjacent left nanopillar. As a result, the left local contact angle fluctuates and there is no spreading to the adjacent left nanopillar. Fig. 3.8(d–f) illustrate the case for $N = N_2$. For this case, the behaviors of the left and the right local contact angles are reversed. Here, the left contact line remains pinned with the left local contact angle increasing to a value as large as 190º and causing a large enough bending of the corresponding liquid–vapor interface ensuring a spreading to the adjacent left nanopillar [see Fig. 3.8(f)]. However, the right local contact angle shows a much weaker increase (to ~150º), so the bending of the liquid surface is too small to cause any wetting of the adjacent right nanopillar [see Fig. 3.8(e)]. Similar to Fig. 3.4-3.7, in Fig. 3.9-3.12 we provide the variation of the left and right contact angles for $N = N_1$, N_2 for two more different initial trajectories of the drop (for details, kindly refer to the caption of Fig. 3.9-3.12).

From Fig. 3.3 and 3.8, we can infer that the spreading on SH surfaces, regardless of the wettability of the base surface, invariably occurs by the bending of the liquid surface (or the air–liquid interface) forming a part of the TPCL that remains pinned. This bending is characterized by an increase in the local three-phase contact angle to values close to 180º or even more than

180º. This phenomenon where the liquid surface bends and the contact line remains pinned ensures that the spreading occurs by the transfer of water molecules, which are originally far away from the pinned three-phase contact line, to the adjacent non-wetted nanopillar. This is in sharp contrast to the spreading behavior on non-SH surfaces, where the spreading invariably implies transfer of molecules at the TPCL to the adjacent non-wetted regions [also see Fig. 3.1 and 3.2 for a pictorial representation of this comparison]. Furthermore, it is worthwhile to note that in Fig. 3.3 and 3.8, the drop spreads to the right for $N = N_1$, while the drop spreads to the left for N_2. We believe that this is an entirely random process since for both $N = N_1$and $N = N_2$ in Fig. 3.3 and 3.8, we ensure that at the start when the drop first contacts the nanostructured surface, the drop center is vertically aligned with the middle of the groove surface (or the part of the surface without the nanopillars). In other words, for neither of these cases, the drop is under any bias to move either to the left or to the right.

3.4. Discussions

What causes the bending?

Our results clearly indicate the central role of bending of the liquid–vapor interface of the pinned TPCL in causing the spreading on SH surfaces. Here, we try to understand the origin of such a bending.

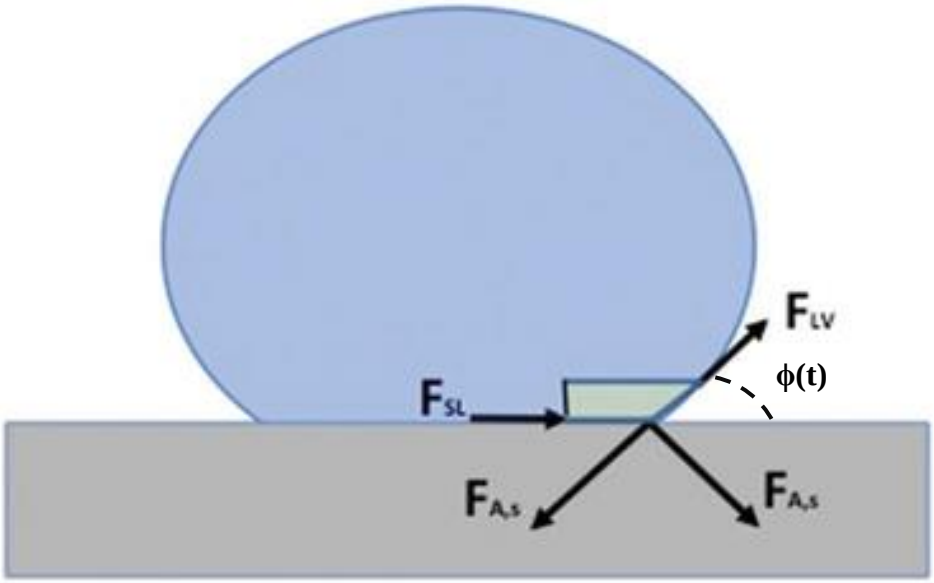

Fig. 3.13 Illustration of the forces on liquid mass (shown in green) in the vicinity of the three-phase contact line. We consider this fluid mass corresponding to a liquid drop spreading on a non-SH surface. One can clearly witness the symmetry of the underlying solid with respect to this mass, ensuring that the horizontal component of attraction forces from the underlying solid cancel each other.

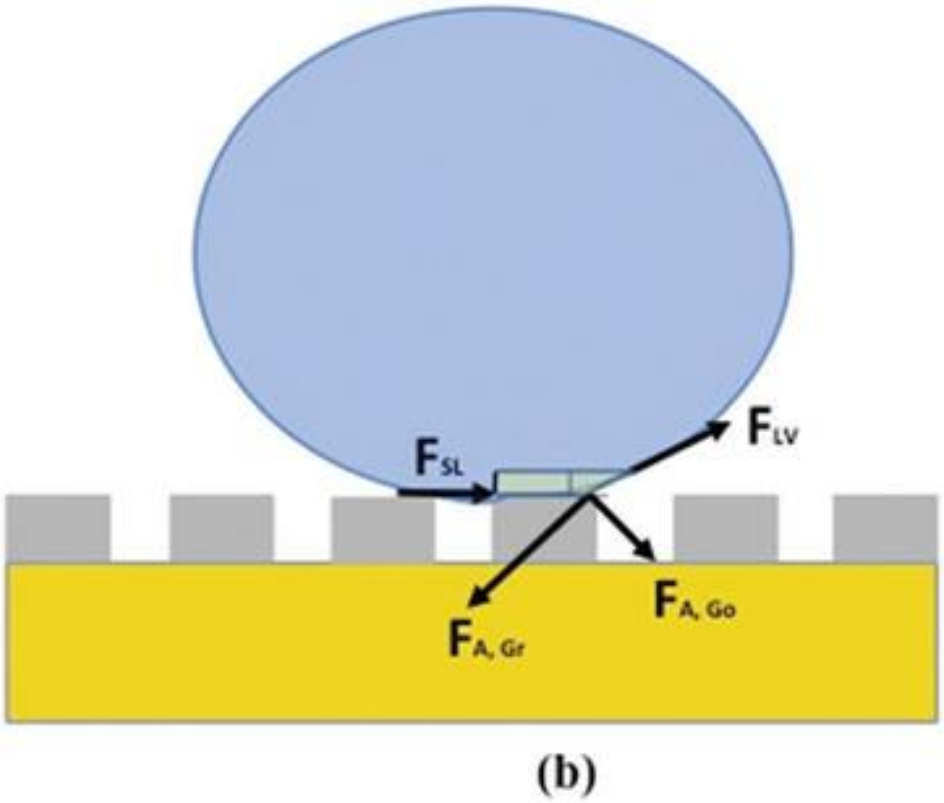

Fig. 3.14 Illustration of the forces on liquid mass (shown in green) in the vicinity of the three-phase contact line. We consider the fluid mass corresponding to a liquid drop pinned at the edge of the pillars (nanopillars or micropillars). The underlying solid is no longer symmetric to this fluid mass, enabling the generation of a pinning force (equal to the difference of the horizontal components of these forces resulting from the asymmetry in the solid on two sides of the liquid mass) that balances the driving force for spreading.

On any surface, during the spreading the mass at the TPCL is under the action of several forces. In Fig. 3.13, we show these forces for a drop spreading on a standard non-SH and non- pillared surface. The symmetry of the underlying solid with respect to the mass at the TPCL [see Fig. 3.13] will imply that the horizontal force (per unit length of the contact line) responsible for the spreading (namely $F_{Sp,H}$) can be expressed as (please note that $\phi + \theta = \pi$, where θ is the instantaneous drop contact angle and we use the method of Marchand et al.[90] for expressing different forces in terms of the surface energies):

$$\frac{F_{sp,H}}{l} = \frac{F_{SL} + F_{LV}\cos[\phi(t)]}{l} = (\gamma_{SV} - \gamma_{SL}) + \gamma_{SL}\cos[\phi(t)] = \gamma_{LV}\{\cos\theta_Y - \cos[\pi - \phi(t)]\} =$$

$$=\gamma_{LV}\{cos\theta_Y - cos\theta(t)\} \quad (3.2)$$

i.e., we get back the classical ''Δ cos'' form of the spreading force, which confirms the classical result that as the spreading occurs (*i.e.*, θ(t) goes down) there is a lowering of the spreading force.

We next study the force balance during the drop spreading on an SH surface, with the TPCL being pinned on the nanopillar (see Fig. 3.14). In this case, the solid is no longer symmetric with respect to the mass in the vicinity of the TPCL and the force balance in the horizontal direction reads (under the pinning conditions):

$$\frac{F_{Sp,H} + F_{pin}}{l} = 0 \Rightarrow \gamma_{LV}\{cos\theta_Y - cos\theta(t)\} = \frac{F_{A,Gr,H}}{l} - \frac{F_{A,Go,H}}{l}, \quad (3.3)$$

where $F_{A,Gr,H}$ and $F_{A,Go,H}$ are the horizontal components of the vastly unequal (with $F_{A,Gr}$ >> $F_{A,Go}$) attractive forces from the graphene layers and gold. As the pinning prevents the contact line from moving, the drop tries to increase the spreading force by increasing θ(t) [eqn (3.2) clearly shows that increasing θ(t) will increase the spreading force], which is equivalent to the bending of the liquid surface. While the spreading force on the contact line, despite such bending, is still not large enough to overcome the large pinning force, this bending (if large enough) eventually ensures that the liquid molecules away from the TPCL can wet the adjacent nanopillar, thereby ensuring spreading. Therefore, the bending phenomenon is effectively caused by the large pinning effect and the consequent tendency of the contact line to spread by overcoming this pinning effect.

3.5 Comparison with the experimental findings

Recent experiments on the rolling of liquid drops on a SH surface (i.e., a surface where the liquid drop is in a Cassie–Baxter state supported on pillars) have shown the exact same mechanism where the drop advances by the liquid-surface-bending-induced wetting of the adjacent pillars.[80] The apparent contact angle can actually exceed 180º, just like what we witness in our simulations. Most remarkably, these experiments are carried out with drops of radius ~1 mm on surfaces having pillars of dimensions ~10 mm. On the other hand, our simulations are for drops of radius of few nanometers on nanopillars of dimensions ~1 nm. Secondly, for our case we study the problem of drop spreading, while in ref. 80 the researchers study the problem of drop rolling. Despite the differences in these two issues (i.e., the system dimensions and the nature of the contact line motion), we find a very similar qualitative behavior that causes the drop motion, namely the liquid-surface-bending and the consequent augmentation of the local contact angle. Therefore, we believe that the present simulation and the experiments of ref. 80 confirm that regardless of the nature of the drop motion (spreading or rolling) and the dimensions of the system (millimetric or nanometric), drop motion on SH surfaces will inevitably occur by the liquid-surface-bending-driven migration. Also, these two studies (ref. 80 and the present simulation) clearly establish that it is not advisable to describe the spreading on SH surfaces in terms of the corresponding capillary number (Ca).[61,62] This stems from the fact that Ca depends on the contact line velocity, which is not relevant in this case. Furthermore, this may be a possible reason for which one witnesses Ca-independent advancing contact angles in ref. 61 and 62 and an apparent contradiction between the results of ref. 61 and 62 regarding the Ca-dependence of the receding contact angle.

3.6 Choice of the simulation system

Simulations are carried out here for layered solids like graphene. However, the qualitative facets of the findings (e.g., liquid-surface-bending-induced spreading) will be true regardless of the nature of the solid, as long as the solid structure enforces the drops into a stable SH CB state. A key motivation behind choosing such a layered solid is to ensure that it is much easier to control the heights of the nanopillars by simply changing the number of graphene layers.

The nanopillar and the liquid drop dimensions that we use here are motivated by recent simulation studies on layered materials.[87,91] To the best of our knowledge, there has been no experimental study with configurations similar to what we propose here in context of the graphene nanopillared surfaces. The purpose of choosing these configurations (particularly the pillar spacing and the pillar width) is to ensure that we can employ MD simulations in a computationally manageable setting for unraveling the unique drop spreading dynamics on SH surfaces over atomistic length and time scales. Obviously, actual experiments will involve much larger length scales of the nanostructured graphene surface (~100 nm),[92] which stem from the fact that the current technology (e.g., FIB etching) can produce nanoscale features in 2D materials only up to such a (~100 nm) resolution.[93] Consequently, much larger water drops ($R >$ 100 nm) will be needed to exhibit the corresponding wetting dynamics. The required number of water molecules for such a drop ($>10^7$) will make the MD simulation extremely expensive and hence unfeasible.

3.7 Conclusions

We have carried out MD simulations to unravel how a water nanodrop spreads on a SH surface – we witness that the spreading occurs with the TPCL remaining pinned, but the liquid–vapor

interface of the TPCL bending and wetting the adjacent nanopillar. This bending process, which we justify from a force balance argument, ensures a most remarkable situation where the corresponding local contact angle of the drop (i.e., the local angle made by the liquid–vapor interface with respect to the horizontal nanopillar at which the TPCL is pinned) may exceed 180º. The fact that very recently such bending induced drop motion was experimentally reported for the rolling of millimetric drops on SH surfaces (see Ref. 80) is even more remarkable. Therefore, we believe that the combination of our simulations and the experiments of ref. 80 establishes a universal picture of drop motion on SH surfaces that is valid over multitude of length and time scales – the motion will invariably occur by the bending of the liquid surface and a progressive increase of the local contact angle.

Chapter 4: Interaction between a water drop and holey graphene: retarded imbibition and generation of novel water–graphene wetting states

4.1 Introduction

Holey graphene and discontinuous graphene sheets containing discontinuities in the form of nanoscopic holes have emerged as extremely important forms of nanostructured graphene with applications in a plethora of disciplines.[94,95] Holey graphene possesses the same stable chemical and physical properties as graphene.[96] In addition, its high porosity enforces enlarged effective available surface area. These factors interplay to broaden the scope of employability of holey graphene as an activated material in supercapacitors and batteries,[97–100] as a substrate for enhancing oxygen reduction reactions,[101] as a catalyst for reactions in an aqueous medium (*e.g.*, to facilitate water-splitting reactions),[102] as an agent to ensure selective carbon capture from post-combustion gases,[103] *etc*. In addition to these widespread applications, rather recently, such holey or nanoporous graphene has been extensively applied as membranes for water desalination,[14–16,101,104,105] water–ethanol separation,[106,107] improved ion migration,[11,108] *etc*.

Understanding how water interacts with such nanoporous or holey graphene is fundamentally important. The purpose of this chapter is to employ molecular dynamics (MD) simulations to probe this fundamental issue by unraveling water nanodrop imbibition mechanism through a multilevel holey graphene structure in the absence of any external driving pressure gradient. To the best of our knowledge, all previous studies have considered water transport through

nanoporous holey graphene in the presence of a finite pressure drive.[11,14–16,104–108] This pressure drive helps water overcome the wetting barrier imposed by graphene layers stemming from the fact that graphene is not hydrophilic. Therefore, our study will probe for the first time this completely new issue of no-force water– holey graphene interactions (henceforth, known as ‘‘no-force’’ interaction; we would be implying capillarity-driven spontaneous imbibition) and will shed light on how such interactions regulate water-imbibition behavior in a holey graphene structure, which may eventually help control graphene-induced water localization. It is worthwhile to note here that while there have been many studies employing MD simulations for investigating water wicking/imbibition in nanochannels and nanopores,[109–112] to the best of our knowledge, this is the first study on water wicking in a holey graphene structure. In order to ascertain that the influence of line tension effect in a nanoscale aqueous system is eliminated, we carry out our MD simulations in two-dimensional architecture[5,57,68] representing a ‘‘slice’’ of the cross section of a three-dimensional multilayer holey graphene structure. Accordingly, our geometry (see Fig. 4.1–4.24 and 4.26-4.27) manifests as a system consisting of a periodically arranged, finite-length graphene stacks interspersed with vertical and lateral gaps. Henceforth, the fluid dynamics of the water nanodrop will be described as a parametric variation of these lateral and vertical inter-stack separations (ISSs). The composition of each stack can vary in terms of the number of graphene layers it consists: for the present case, we consider each stack to consist of three layers of graphene. Finally, in our simulations, the dimensions of the holes (which appear as lateral separation between graphene stacks in our 2-D geometry) as well as inter-stack distances in vertical directions are assigned values observed in actual experiments,[96,108,113] in an effort to ensure that our MD results provide realistic and experimentally realizable predictions about water–holey graphene interactions.

The central result of the study is that a water nanodrop wicks through a multilayer holey graphene structure by selecting a plethora of combined imbibition and wetting states dictated by the interplay of lateral and vertical separation of the stacks of the graphene layers. We witness a complete absence of imbibition for cases of large vertical ISS. The reason is that the imbibing water nanodrop does not encounter a large enough attractive pull from the lower stack of the graphene layers and as a result remains localized on top of the uppermost stack. On the contrary, a lowering of the vertical ISS ensures partial imbibition of the drop from the upper to the lower stack, although the drop invariably fails to go beyond this lower stack. A myriad of wetting states accompanies this imbibition process. These wetting states can be highly non-trivial, such as simultaneous wetting of top and bottom surface of a given graphene stack (which is equivalent to fiber-like wetting or wetting-mediated ‘‘encapsulation’’ of the graphene stack), simultaneous wetting of multiple surfaces of vertically and laterally separated graphene stacks, and wetting in presence of simultaneously pinned and unpinned contact lines in vertically separated graphene stacks. Furthermore, this combined imbibition and wetting states effectively ensure, for certain lateral and vertical ISSs, a significant enhancement in effective water– graphene contact area. It is for the first time that such a situation, which may significantly improve applications requiring the presence of larger water–graphene contact areas (*e.g.*, fabrication of graphene–EDL-based supercapacitors,[114] graphite-based compact heat exchangers,[115] and graphene-nanoflake-based nanofluid for freezing water[116]), has been unraveled in the context of water– holey graphene interactions. Overall, therefore, the present study has two key objectives. First, it studies a new wetting problem, namely the problem of no-force water-drop imbibition in holey graphene. Second and more important, it leverages imbibition- induced new graphene–water wetting states for conceiving improvements in realistic applications involving graphene–water interactions.

4.2 Molecular dynamics simulations

4.2.1 Summary of simulation procedure

The basic molecular dynamics simulations framework used in this study closely resembles that of our previous studies on graphene wetting dynamics.[68,69] In this section, we summarize the essential simulation details. We use Large-scale Atomic/Molecular Massively Parallel Simulator (LAMMPS)[81] software package to carry out the simulations. On the other hand, OVITO or The Open Visualization Tool [117] is employed for rendering the simulated drop motions. Finally, post-processing of data is carried out using MATLAB.

Similar to that in our previous studies,[68,69] here we employ a quasi-2D simulation geometry in order to ensure that curvature- induced line tension at the three-phase contact line of the water nanodrop is eliminated. Such an approach has been adopted by other studies exploring water nanodrop behavior using MD simulations.[5,67,83,118] It is also worthwhile to note that such a 2-D model of a water nanodrop (or a cylindrical water nanodrop) has been routinely used in a large number of MD studies, elucidating the phenomena driven by wetting interactions.[5,67–69,83,118–122]

We use the extended simple point charge (SPC/E) model to model the water nanodrop.[122] The relevant details of the interactions quantifying the SPC/E model used in this study can be found in our previous reports.[68,69] In this study, simulations are carried out with a fixed size of the water drop (N = 3000 and diameter = 6.5 nm). Simulations elucidate how this constant- size water drop interacts with a multilayer holey graphene structure with varying lateral and vertical inter-stack separations (ISSs). It is again worthwhile to point out here that there has been a plethora of studies that have used this SPC/E model to simulate the dynamics of a cylindrical water nanodrop.[5,68,69,118,123–129]

Water–graphene (or water–carbon) interactions are captured via a C–O LJ potential with ε_{CO} = 0.392 kJ mol^{-1} and σ_{CO} = 3.19 Å.[85] In our two-dimensional simulation system, the multilevel holey graphene structure consists of periodically placed graphene stacks with fixed lateral and vertical ISSs. This study provides results on the no-force drop imbibition in such a holey graphene structure by varying these lateral and vertical ISSs. Each of the stacks, except the bottom stack, is self-supporting and consists of 3 layers of graphene. The bottom-most stacks are supported by gold (Au) with Au(111) surface being aligned with the graphene lattice, which is stretched by ~1.5%. Furthermore, Au–O LJ potentials ($\varepsilon_{Au–O}$ = 2.469 kJ mol^{-1} and $\sigma_{Au–O}$ = 3.6 Å)[86] are used to model gold– water interactions. For the entire simulation, all LJ interactions are imposed with a cutoff radius of 10 Å. It is worthwhile to note that throughout our simulations, which are analogous to those of MD studies on drop dynamics,[5,85] we hold the substrate atoms fixed at their lattice positions; such a step significantly reduces computational expense without compromising the accuracy of prediction of drop dynamics.

The periodically spaced graphene stacks are created by first creating bulk graphene having the desired number of layers (herein, 3, since each stack consists of unsupported graphene trilayer) at different vertical locations. Selection of these different vertical locations confirms our desired vertical ISSs. Subsequently, C atoms from a given layer of bulk graphene (at a particular depth) are removed so as to ensure that we get stacks that are discontinuous laterally. This results in the ‘‘hole’’ creation in a continuous graphene sheet to make it holey graphene. The locations from where we remove the C atoms determine the lateral ISSs. We consider three different values of lateral ISSs (d = 4 nm, 6 nm, and 8 nm) and three different values of vertical ISSs (δ = 1 nm, 2.5 nm, and 4 nm). Later (please see the next subsection), we explain how the selection of d and d is motivated by recent experiments on holey graphene.[96,108,113] It is also worthwhile to note that

there will be an inherent unsaturation of carbon valence at the location of the edges of the graphene holes.[89,104] Such an unsaturation needs to be saturated by binding to –H. Such an issue at the edges of holey graphene has not been considered in the presented charge-free model of graphene.

Simulations are carried out in two distinct phases: in the first phase, the drop is equilibrated far from the holey graphene structure, and in the second phase, the combined imbibition– spreading dynamics of the drop in contact with the holey graphene structure (and the subsequent data collection) is investigated. Simulations in both these phases are performed on the *NVT* ensemble, where the temperature is controlled *via* a Nosé–Hoover thermostat[89] in presence of a simulation timestep of 1 fs. In the first phase, we equilibrate the drop (see ref. 90 and 105 for the detailed procedure). In the second phase, in which drop dynamics is studied along with data collection, the equilibrated drop is brought to within ~3 Å from the top surface of the holey graphene structure. The system is then evolved forward in time again for several hundreds of picoseconds, and in the process, the dynamics of the drop and relevant data characterizing drop dynamics are collected.

The drop dynamics, in addition to corresponding MD simulation snapshots (see figures later), is quantified by corresponding time evolution of the angles and spreading radii made by the drop on different surfaces of the holey graphene structure. These values are calculated by tracking the atomic position coordinate data imported to MATLAB. For more details, please refer to our previous studies.[68,69]

4.2.2 Motivation for the choice of system geometry

The dimensions for the multilayer holey graphene structure used in our simulations have been inspired from similar experiments. Lateral ISS is equivalent to the dimensions of the holes. We used three lateral separation values of 4 nm, 6 nm and 8 nm. These are perfectly commensurate with the hole dimensions of 2–10 nm often witnessed in experiments of holey graphene.[96] On the other hand, we used vertical separations of 1–4 nm. Such vertical ISS distances are commensurate with experimental findings that are found to achieve inter-stack separation ranging from 0.5 nm to 7 nm by employing techniques such as vacuum filtration and dry pressing.[11,96,113]

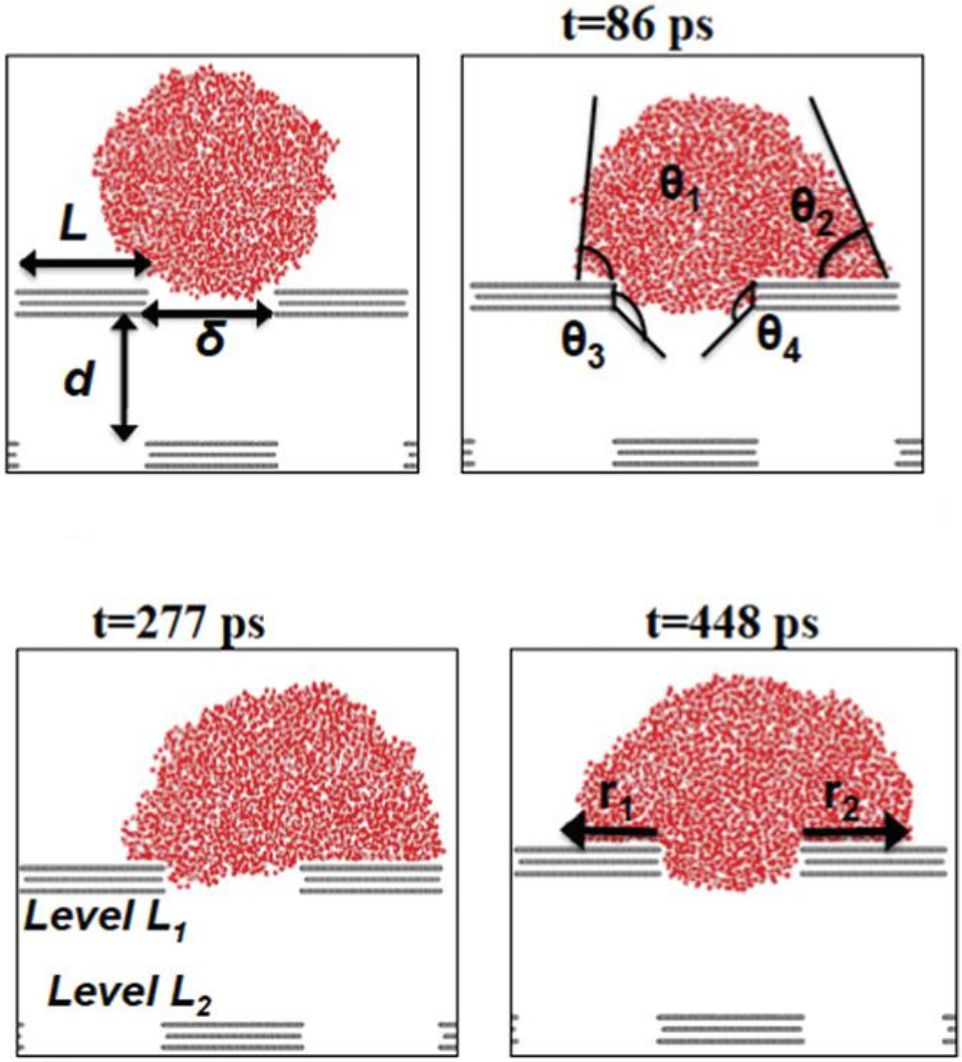

Fig. 4.1 Drop imbibition in a holey graphene structure for lateral ISS (δ) of 4 nm and vertical ISS (d) of 4 nm. MD simulation snapshots showing drop dynamics at different time instants.

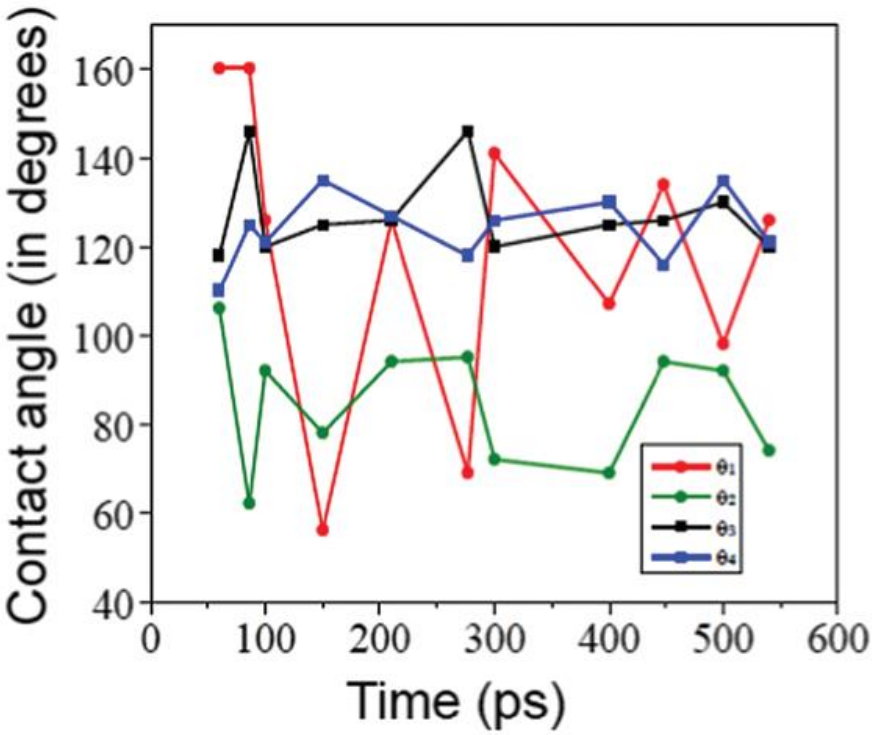

Fig. 4.2 Drop imbibition in a holey graphene structure for lateral ISS (δ) of 4 nm and vertical ISS (d) of 4 nm. Time variation of contact angles θ_1, θ_2, θ_3, and θ_4 identified in Fig.4.1.

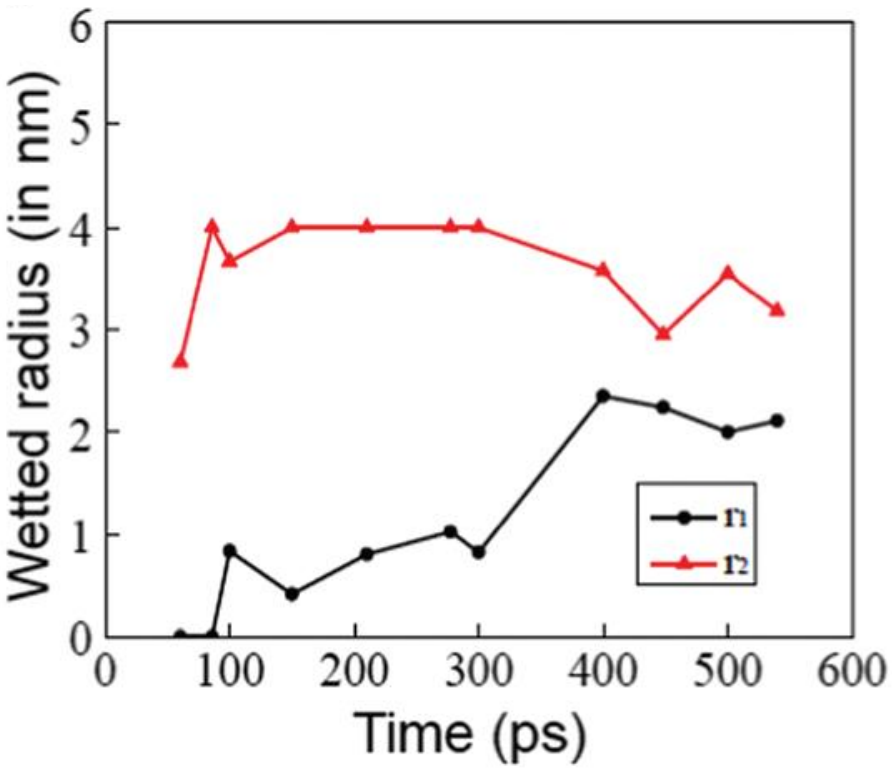

Fig. 4.3 Drop imbibition in a holey graphene structure for lateral ISS (δ) of 4 nm and vertical ISS (d) of 4 nm. Time variation of contact radii r_1 and r_2 identified in Fig.4.1.

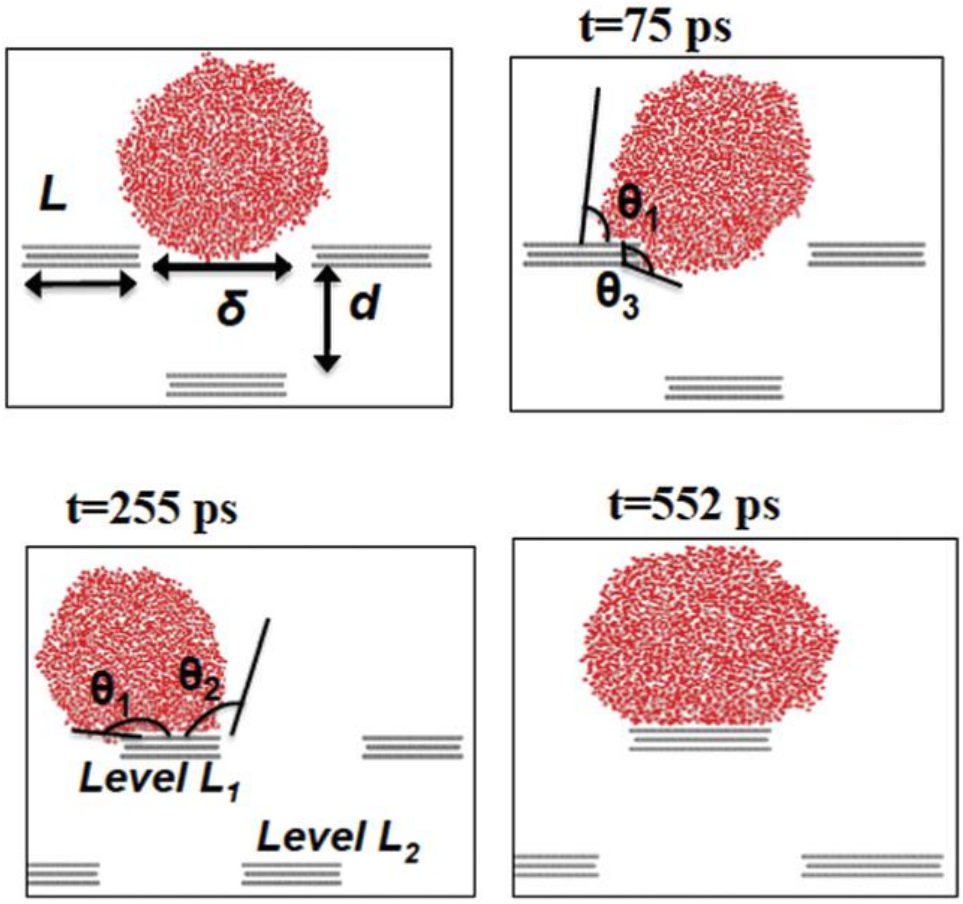

Fig. 4.4 Drop imbibition in a holey graphene structure for lateral ISS (δ) of 6 nm and vertical ISS (d) of 4 nm. MD simulation snapshots showing drop dynamics at different time instants.

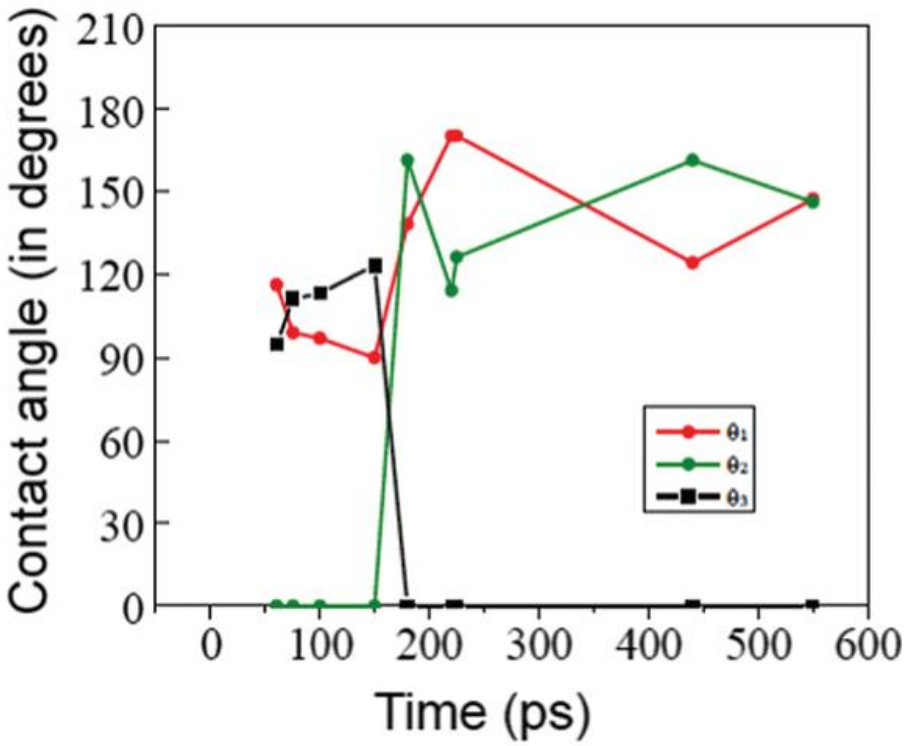

Fig. 4.5 Drop imbibition in a holey graphene structure for lateral ISS (δ) of 6 nm and vertical ISS (d) of 4 nm. Time variation of contact angles θ_1, θ_2 and θ_3 identified in Fig.4.4.

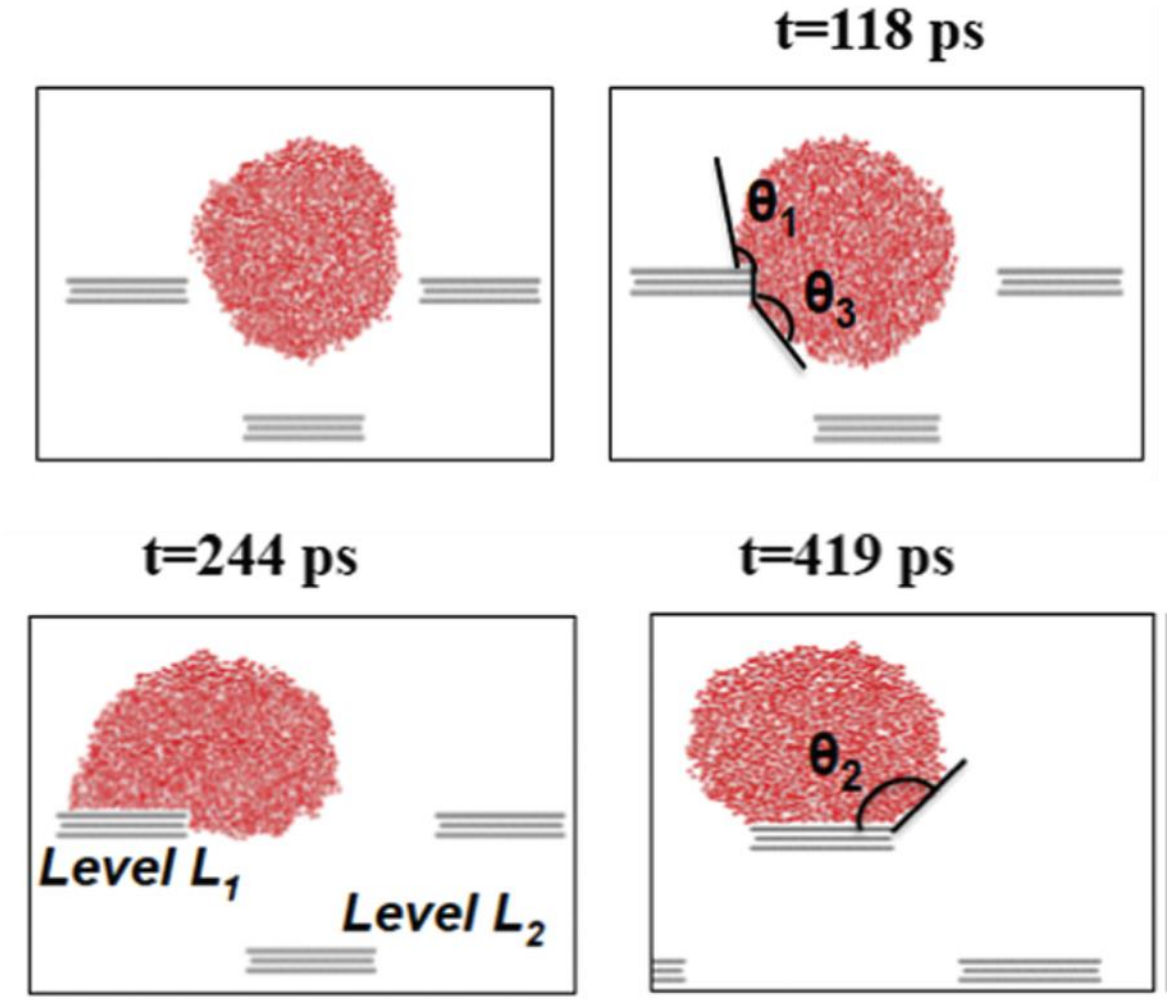

Fig. 4.6 Drop imbibition in a holey graphene structure for lateral ISS (δ) of 8 nm and vertical ISS (d) of 4 nm (see Fig. 4.1 and 4.4 for the definitions of δ and d). MD simulation snapshots showing drop dynamics at different time instants.

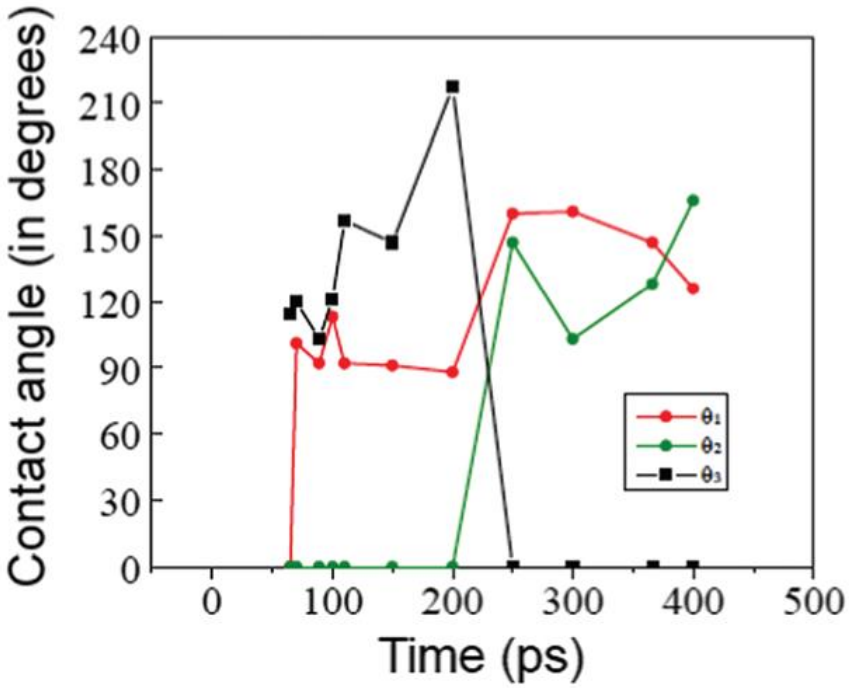

Fig. 4.7 Drop imbibition in a holey graphene structure for lateral ISS (δ) of 8 nm and vertical ISS (d) of 4 nm (see Fig. 4.1 and 4.4 for the definitions of δ and d). Time variation of contact angles θ_1, θ_2 and θ_3 identified in Fig.4.6.

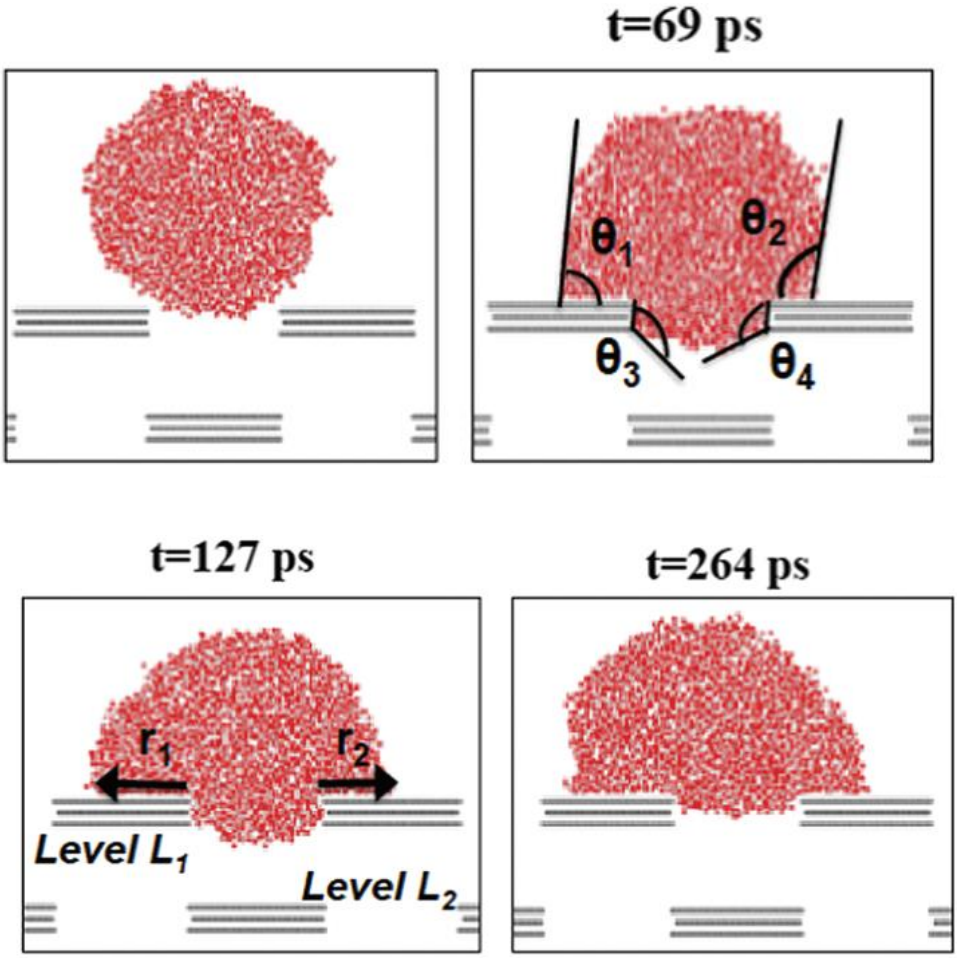

Fig. 4.8 Drop imbibition in a holey graphene structure for lateral ISS (δ) of 4 nm and vertical ISS (d) of 2.5 nm (see Fig. 4.1 and 4.4 for the definitions of δ and d). MD simulation snapshots showing drop dynamics at different time instants.

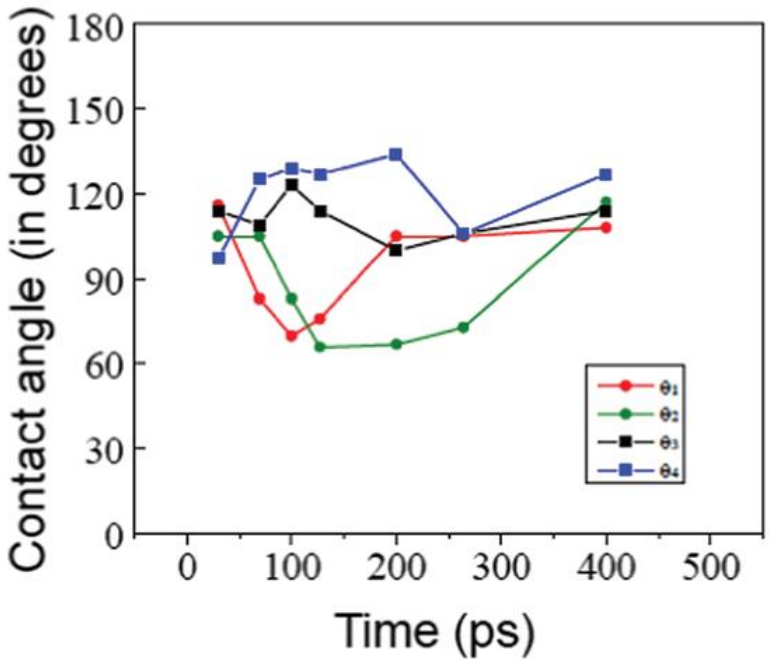

Fig. 4.9 Drop imbibition in a holey graphene structure for lateral ISS (δ) of 4 nm and vertical ISS (d) of 2.5 nm (see Fig. 4.1 and 4.4 for the definitions of δ and d). Time variation of contact angles θ_1, θ_2, θ_3, and θ_4 identified in Fig. 4.8.

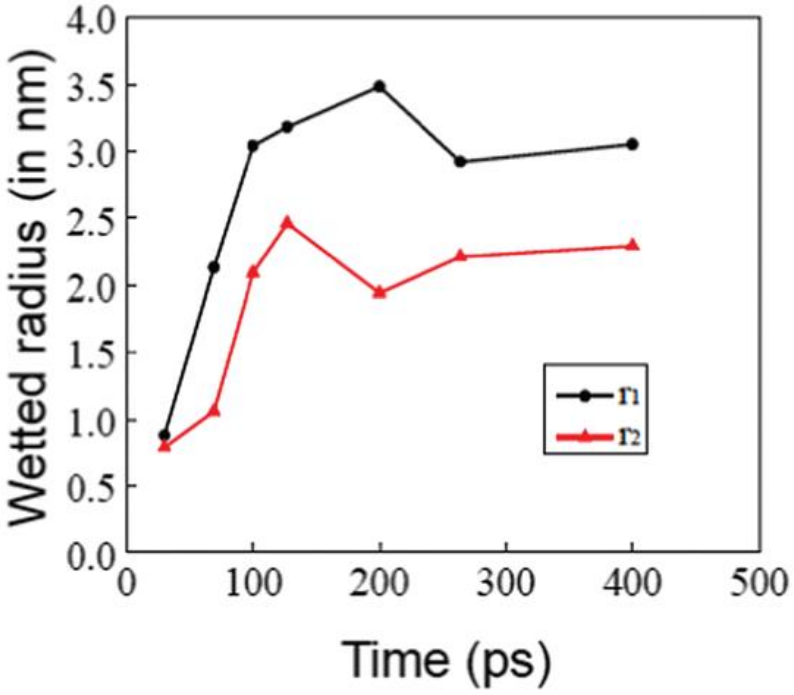

Fig. 4.10 Drop imbibition in a holey graphene structure for lateral ISS (δ) of 4 nm and vertical ISS (d) of 2.5 nm (see Fig. 4.1 and 4.4 for the definitions of δ and d). Time variation of contact radii r_1 and r_2 identified in Fig. 4.8.

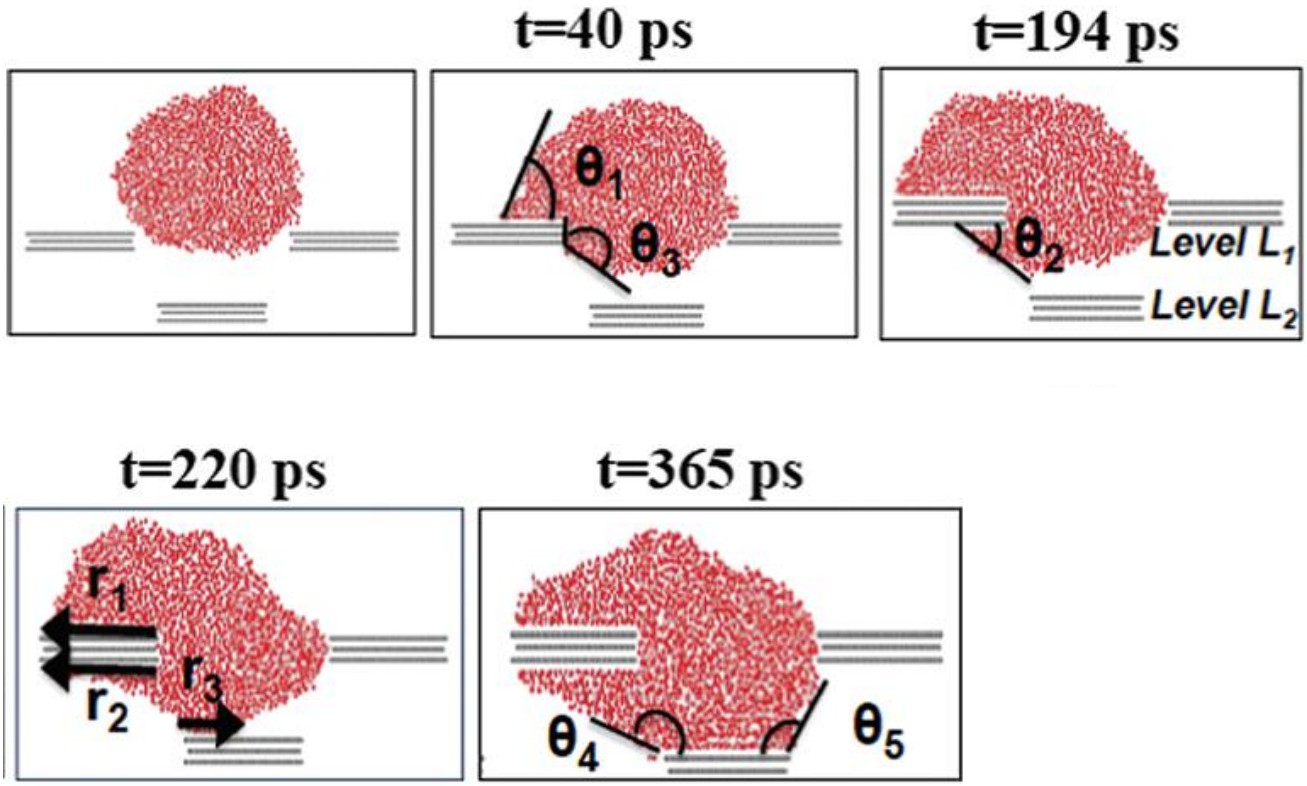

Fig. 4.11 Drop imbibition in a holey graphene structure for lateral ISS (δ) of 6 nm and vertical ISS (d) of 2.5 nm (see Fig. 4.1 and 4.4. for the definitions of δ and d). MD simulation snapshots showing drop dynamics at different time instants.

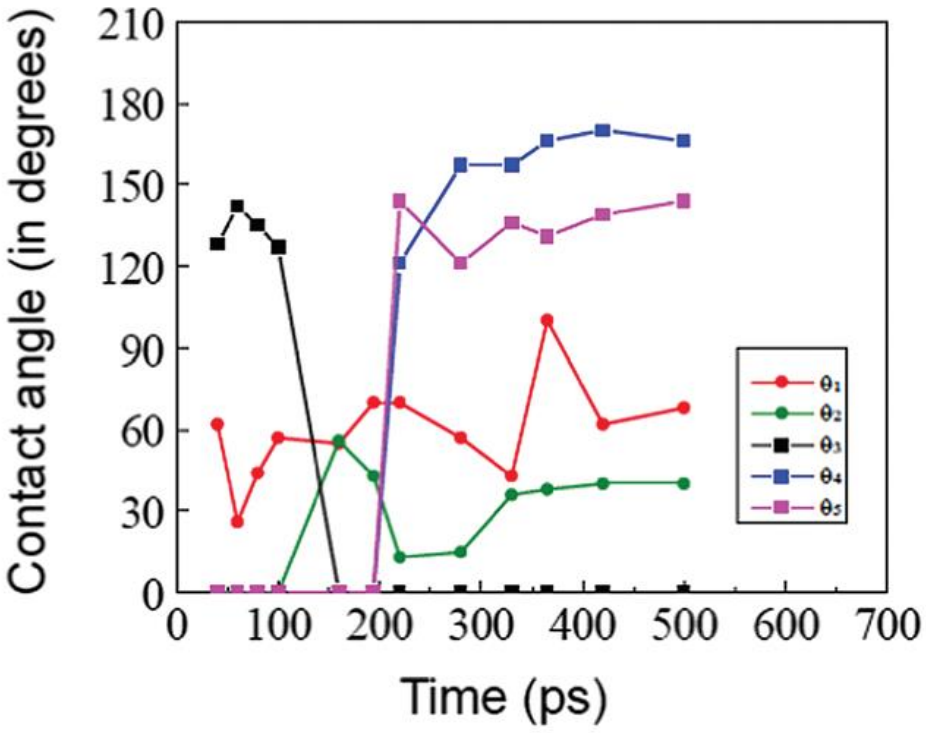

Fig. 4.12 Drop imbibition in a holey graphene structure for lateral ISS (δ) of 6 nm and vertical ISS (d) of 2.5 nm (see Fig. 4.1 and 4.4 for the definitions of δ and d). Time variation of contact angles θ_1, θ_2, θ_3, θ_4, and θ_5 identified in Fig. 4.11.

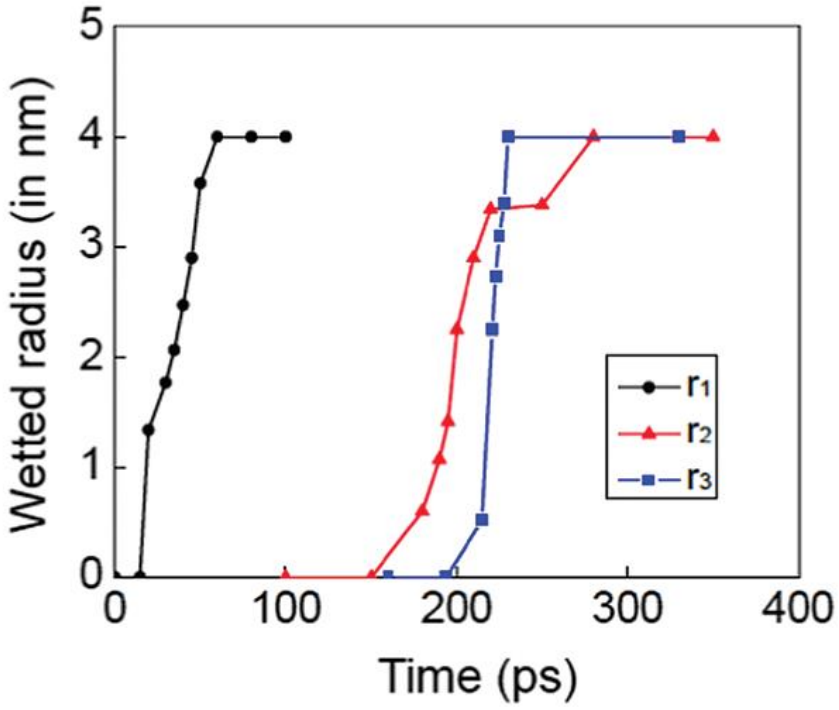

Fig. 4.13 Drop imbibition in a holey graphene structure for lateral ISS (δ) of 6 nm and vertical ISS (d) of 2.5 nm (see Fig. 4.1 and 4.4 for the definitions of δ and d). Time variation of contact radii r_1, r_2 and r_3 identified in Fig. 4.11.

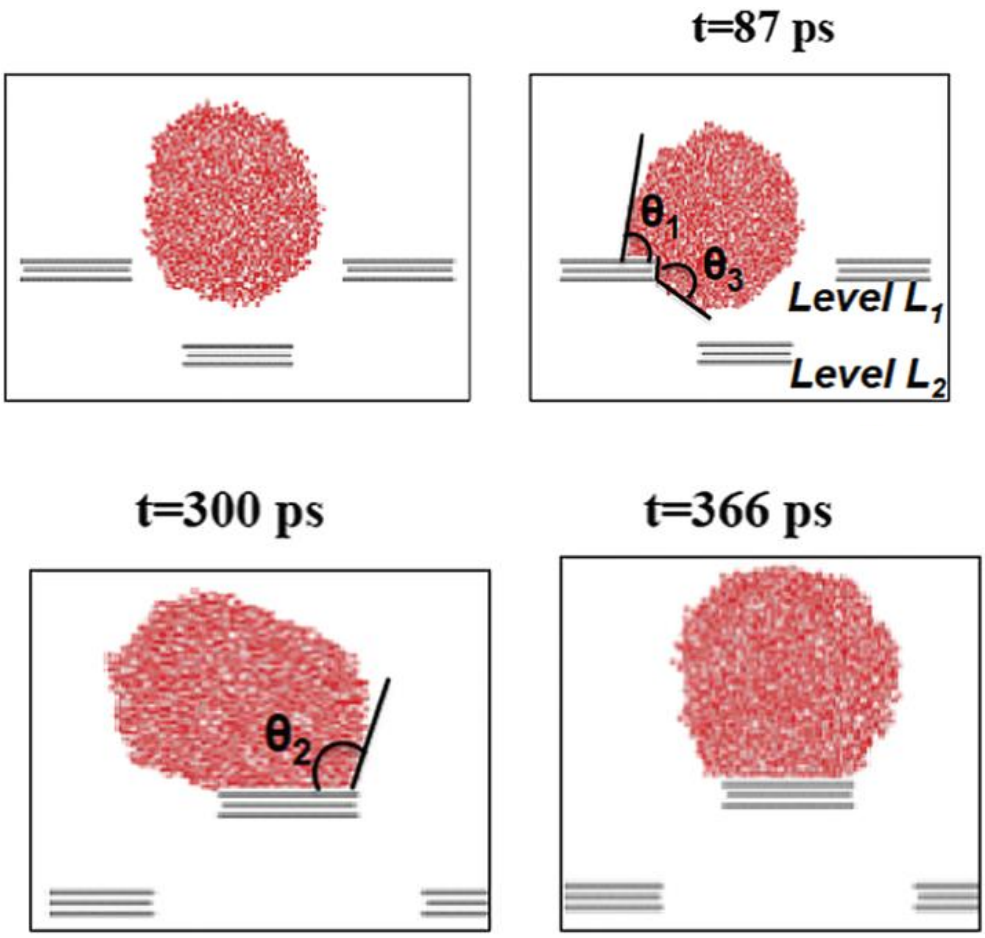

Fig. 4.14 Drop imbibition in a holey graphene structure for lateral ISS (δ) of 8 nm and vertical ISS (d) of 2.5 nm (see Fig. 4.1 and 4.4 for the definitions of δ and d). MD simulation snapshots showing drop dynamics at different time instants.

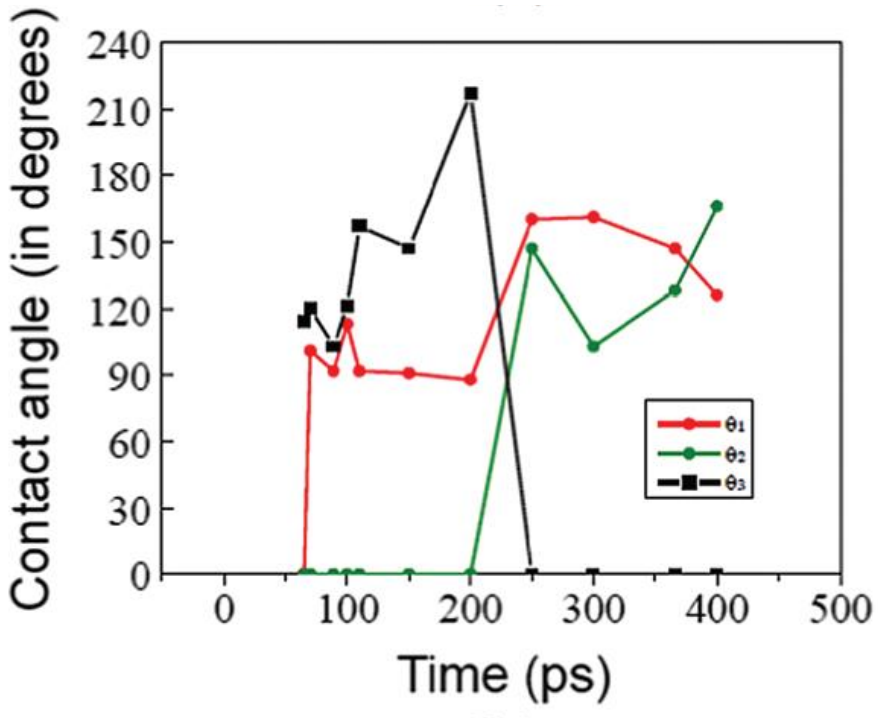

Fig. 4.15 Drop imbibition in a holey graphene structure for lateral ISS (δ) of 8 nm and vertical ISS (d) of 2.5 nm (see Fig. 4.1 and 4.4 for the definitions of δ and d). Time variation of contact angles θ_1, θ_2, and θ_3 identified in Fig. 4.14.

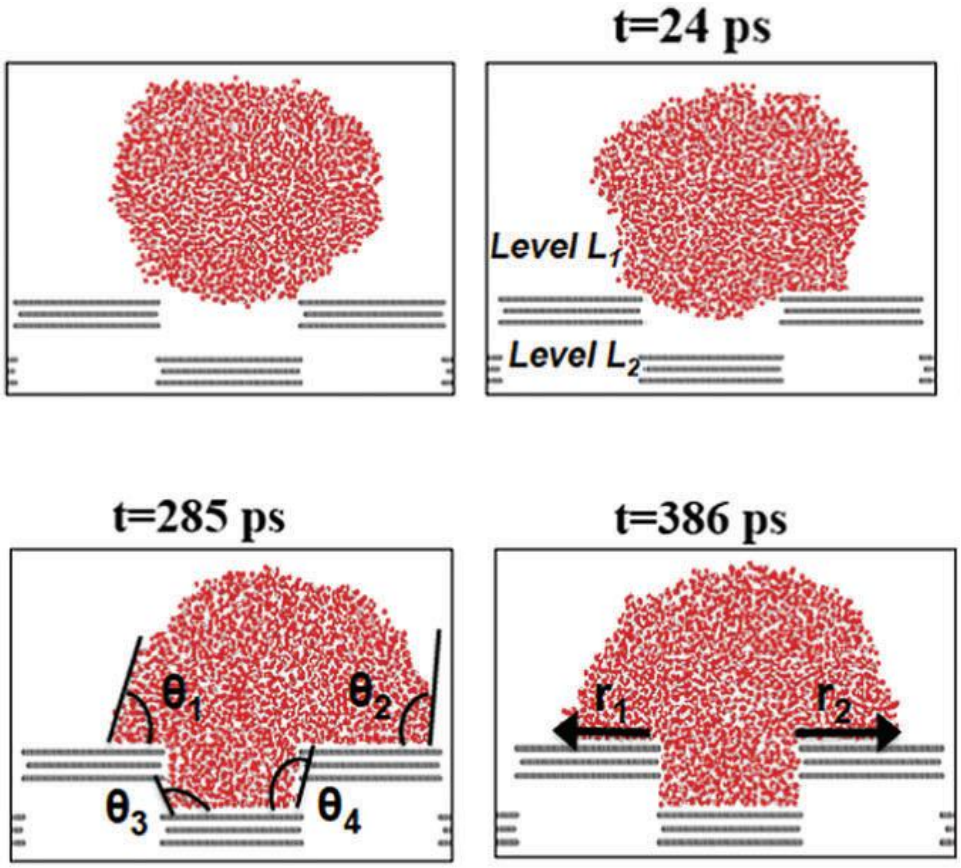

Fig. 4.16 Drop imbibition in a holey graphene structure for lateral ISS (δ) of 4 nm and vertical ISS (d) of 1 nm (see Fig. 4.1 and 4.4 for the definitions of δ and d). MD simulation snapshots showing drop dynamics at different time instants.

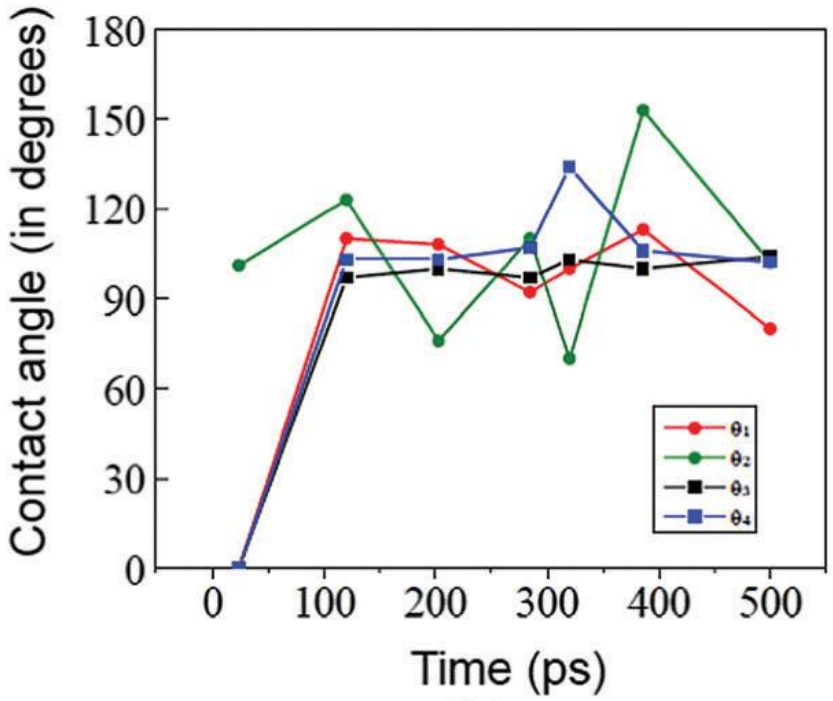

Fig. 4.17 Drop imbibition in a holey graphene structure for lateral ISS (δ) of 4 nm and vertical ISS (d) of 1 nm (see Fig. 4.1 and 4.4 for the definitions of δ and d). Time variation of contact angles θ_1, θ_2, θ_3, and θ_4 identified in Fig. 4.16

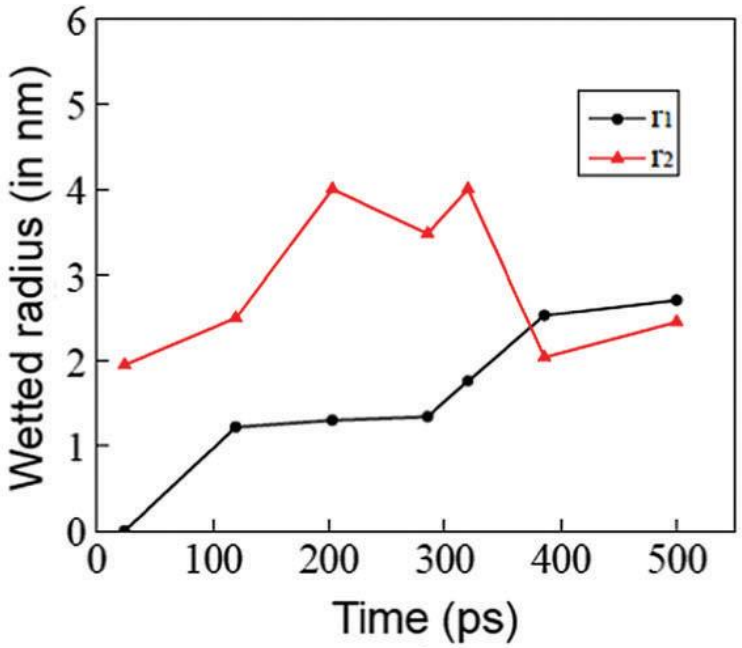

Fig. 4.18 Drop imbibition in a holey graphene structure for lateral ISS (δ) of 4 nm and vertical ISS (d) of 1 nm (see Fig. 4.1 and 4.4 for the definitions of δ and d). Time variation of contact radii r_1 and r_2 identified in Fig. 4.16.

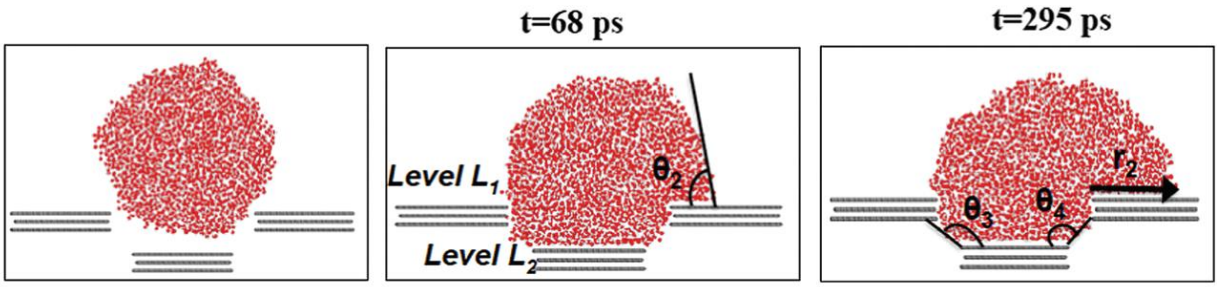

Fig. 4.19 Drop imbibition in a holey graphene structure for lateral ISS (δ) of 6 nm and vertical ISS (d) of 1 nm (see Fig. 4.1 and 4.4 for the definitions of δ and d). MD simulation snapshots showing drop dynamics at different time instants.

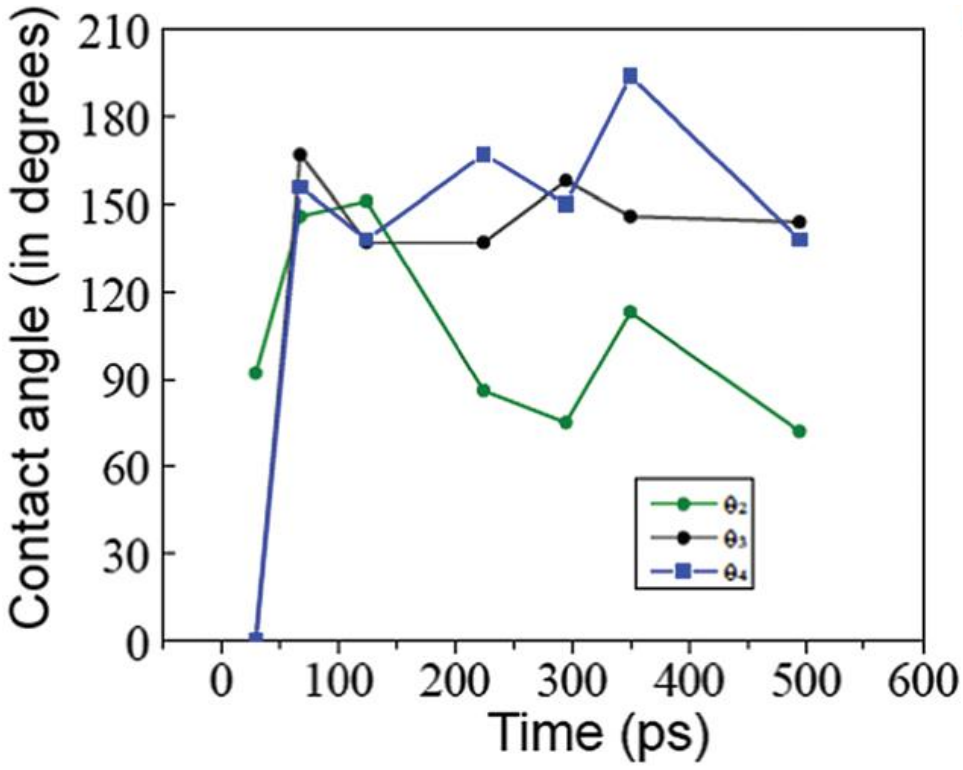

Fig. 4.20 Drop imbibition in a holey graphene structure for lateral ISS (δ) of 6 nm and vertical ISS (d) of 1 nm (see Fig. 4.1 and 4.4 for the definitions of δ and d). Time variation of contact angles θ_2, θ_3, and θ_4 identified in Fig.4.19.

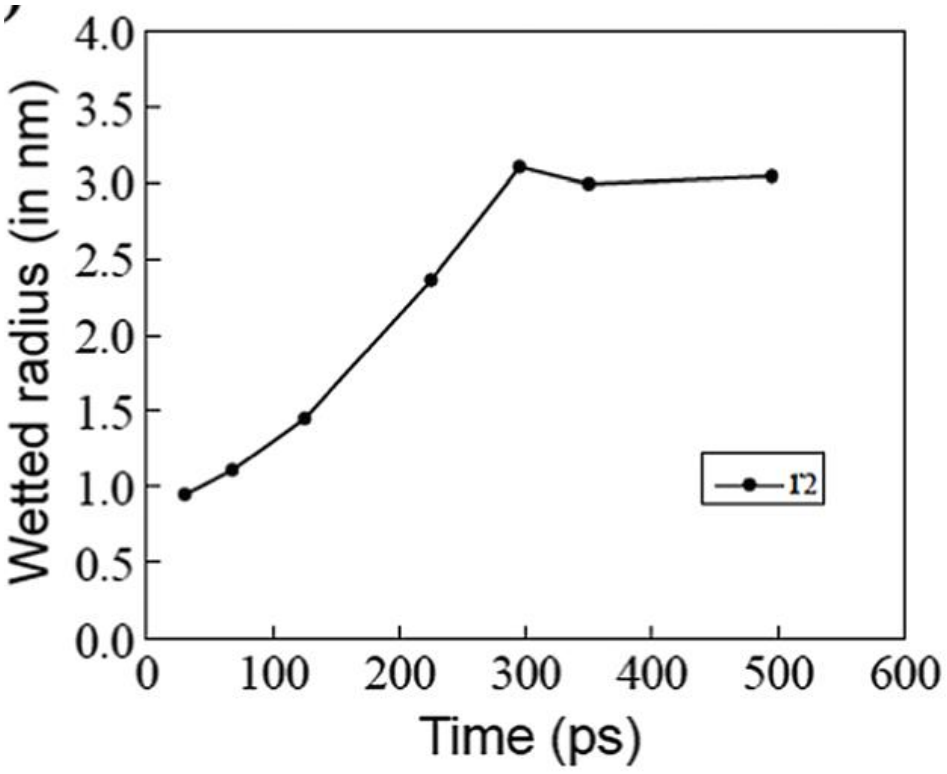

Fig. 4.21 Drop imbibition in a holey graphene structure for lateral ISS (δ) of 6 nm and vertical ISS (d) of 1 nm (see Fig. 4.1 and 4.4 for the definitions of δ and d). Time variation of the contact radius r_2 identified in Fig.4.19.

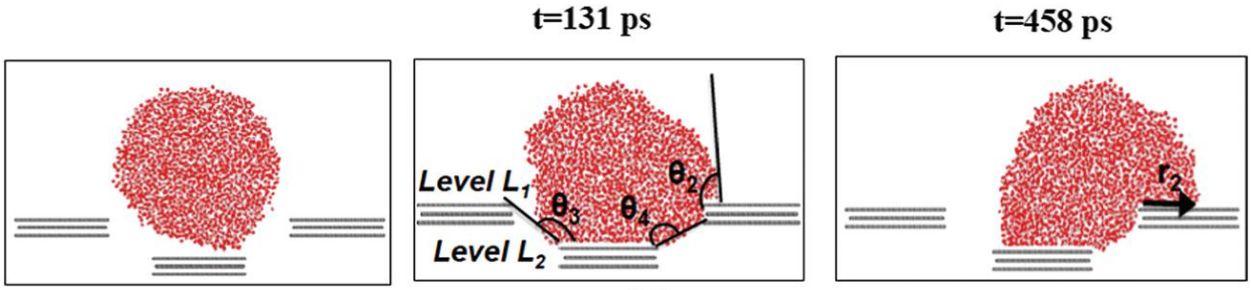

Fig. 4.22 Drop imbibition in a holey graphene structure for lateral ISS (δ) of 8 nm and vertical ISS (d) of 1 nm (see Fig. 4.1 and 4.4 for the definitions of δ and d). MD simulation snapshots showing drop dynamics at different time instants.

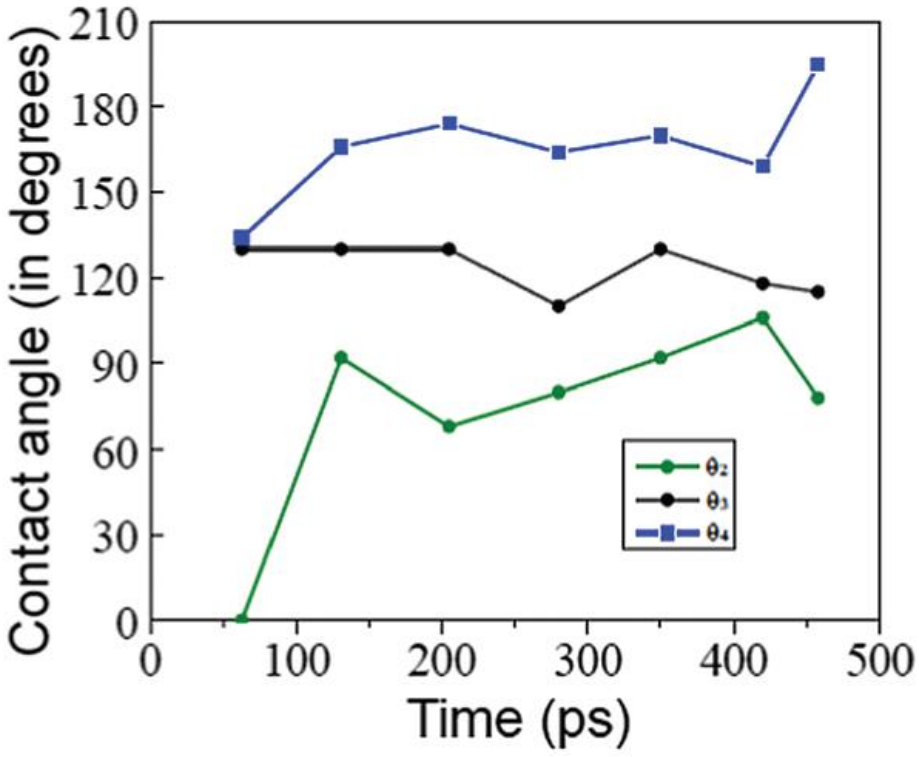

Fig. 4.23 Drop imbibition in a holey graphene structure for lateral ISS (δ) of 8 nm and vertical ISS (d) of 1 nm (see Fig. 4.1 and 4.4 for the definitions of δ and d). Time variation of contact angles θ_2, θ_3, and θ_4 identified in Fig. 4.22.

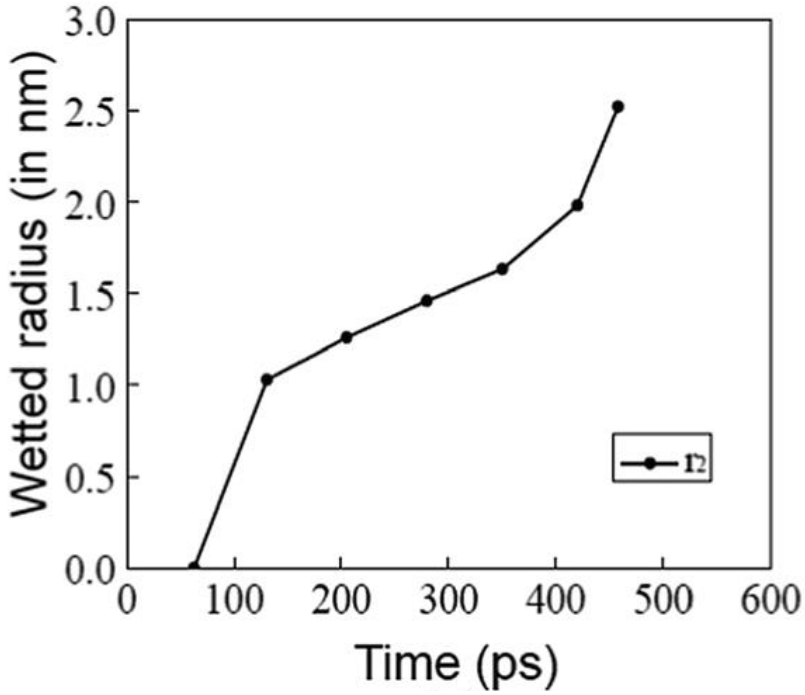

Fig. 4.24 Drop imbibition in a holey graphene structure for lateral ISS (δ) of 8 nm and vertical ISS (d) of 1 nm (see Fig. 4.1 and 4.4 for the definitions of δ and d). Time variation of contact radius r_2 identified in Fig. 4.22.

4.3 Results

Summary of results

In this study, we report MD findings of the combined no-force spreading–imbibition dynamics of the water nanodrop in holey graphene architecture as a function of vertical ISS (d) and lateral ISS (δ) characterizing the architecture. The entire spectra of imbibition and spreading behavior of the drop, governed by d–δ phase space, have been summarized in Fig. 4.25 and 4.26, respectively. Fig. 4.1-4.24 provide detailed temporal dynamics of the nanodrop for different combinations of δ and d, and Fig. 4.25 and 4.26 summarize these findings in a d–δ phase-space representation. Fig. 4.25 summarizes the three main types of imbibition events, namely (a) no imbibition, (b) partial imbibition, and (c) metastable imbibition. On the other hand, Fig. 4.26 summarizes the five main types of spreading events, which are related, through corresponding d–δ dependence, to the corresponding imbibition events. These spreading events are (a) wetted upper surfaces of two laterally separated graphene stacks in level L_1, (b) wetted upper surface of single graphene stack in level L_1, (c) wetted upper and lower surfaces of a given graphene stack in level L_1 and wetted upper surface of a graphene stack in level L_2,(d) wetted upper surfaces of two laterally separated graphene stacks in level L_1 and wetted upper surface of a graphene stack in level L_2, and (e) wetted upper surfaces of a single graphene stack in level L_1 and wetted upper surface of a graphene stack in level L_2.

4.3.1 Case 1: combined spreading–imbibition dynamics for large vertical inter-stack separation (ISS).

Herein, we consider a vertical ISS of 4 nm, as shown in Fig. 4.1-4.3. We keep this vertical ISS constant and vary the lateral separation to values of 4 nm, 6 nm, and 8 nm (see Fig. 4.1–4.7). We start with the case of the least lateral separation (4 nm), which also implies the least size of the holes. In Fig. 4.1, we provide snapshots from our MD simulations illustrating water nanodrop dynamics at different time instants for this case with lateral separation of 4 nm. As the drop comes in contact with the uppermost level (L_1) of the graphene stacks, the water molecules are in much closer proximity to the graphene layers of this upper level of the stack as compared to graphene layers of the stack at a lower vertical level (L_2). As a consequence, the relative influence of downward attraction on the water nanodrop from the graphene layers at level L_2 is negligible, and hence, the water drop localizes entirely in the upper level of the graphene stacks. Furthermore, given the relatively small lateral separation of these two stacks, the drop spreads simultaneously on the upper layer of these two stacks at level L_1. We describe this simultaneous spreading behavior by studying time variation of the dynamic contact angles θ_1 and θ_2 [see Fig.4.2]. Most remarkably, we find that θ_1 oscillates vigorously about a contact angle (~110^o) that is much larger than the equilibrium contact angle (~90^o) of a water drop on tri-layer unsupported graphene. On the other hand, θ_2 oscillates about this equilibrium value (~90^o). Therefore, although spreading occurs simultaneously on the upper surfaces of the two laterally separated graphene stacks of level L_1, there is a distinct asymmetry in spreading. We can explain this asymmetry by noting that unequal mass of liquid gets distributed on these two laterally separated graphene stacks. Another way to confirm this asymmetric spreading is to study the time variation

of the corresponding spreading radii r_1 and r_2 showing distinct asymmetry [see Fig. 4.3]; the fact that $r_1 < r_2$ is commensurate with $\theta_2 > \theta_2$.

While water remains mostly confined on the top surfaces of the laterally separated graphene stacks in level L_1, ensuring virtually no imbibition, there is wetting of the sides of the graphene layers. In other words, water indeed percolates in the space between the two laterally separated graphene stacks; yet, we consider no imbibition, since the water drop does not wick beyond the upper level of the graphene stack [see Fig.4.1]. The wetting behavior of the percolated part of the water drop can be quantified by noting the time variation of the contact angles θ_3 and θ_4, both of which are hydrophobic. However, unlike θ_1 and θ_2, they demonstrate very similar values over the time period of spreading. This confirms that unlike spreading on the upper layer of the graphene stack in level L_1, wetting of the sides of the graphene stack remains similar. To summarize, for this d–δ combination (lateral ISS δ of 4 nm and vertical ISS d of 4 nm) while imbibition is absent, the water nanodrop exhibits a myriad of wetting states, wetting multiple surfaces and demonstrating wide ranges of equilibrium contact angle values.

We next consider the case where this lateral separation is increased to 6 nm. The MD simulation snapshots for different times are shown in Fig. 4.4. Here too, water remains confined in the uppermost level L_1 of the graphene stacks on account of relatively weak attraction from the graphene layers of the lower level L_2. Therefore, for this case too, there is no inception of imbibition. A key difference with respect to the previous case (described in Fig. 4.1-4.3), however, is that here wetting occurs only on a single stack and not on two adjacent and laterally separated stacks. This obviously stems from the relatively larger lateral separation (6 nm) for this case. This equilibration of the drop on a single stack gives rise to several interesting wetting scenarios. In case the drop equilibrates on a continuous stretch of a 3-layer-graphene stack (*i.e.*,

when there are no holes), it will form an equilibrium contact angle of ~90º and the value of its wetted radius will be r_w. In the present study, $r_s < r_w$, where r_s is lateral dimension of a graphene stack. As a consequence, the drop contact angle is substantially larger than the equilibrium angle (~90º) and is in the superhydrophobic regime [see the time variation of θ_1 and θ_2 in Fig.4.5]. Of course, retention of the drop in this superhydrophobic state is ensured by exertion of a large pinning force on the three-phase contact line along the edge of the stack. This large pinning force, which is possibly similar to that of the well-known Gibbs pinning experienced by liquid menisci in contact with surfaces with sharp edges (*e.g.*, nanoedge of the holey graphene in the present case),[130] also ensures that the drop does not spill over and wet the sides of the graphene stack; therefore, angle θ_2 starts to evolve only when angle θ_3 has ceased to exist (θ_3 quantifies the wetting of the sides of the stack by the drop) [see Fig.4.5]. Hence, herein, like in the previous case, we find negligible imbibition, although development of wetting states is distinctly different.

We finally study the case of a very large lateral ISS (8 nm) with this vertical ISS (4 nm). The MD simulated snapshots at different times are shown in Fig.4.6. Herein, unlike the other two cases, the drop indeed starts to imbibe, i.e., some significant portion of the drop indeed goes beyond the uppermost graphene layer L_1. However, this imbibition is highly metastable, and the drop fails to reach the lower layer L_2 and gets pinned to one of the lateral graphene stacks of the upper layer L_1. Subsequently, the drop spins back and settles on the top of this graphene stack in layer L_1. Here too $r_s < r_w$, and accordingly, one witnesses large contact angles [see the variation of θ_1, θ_2 in Fig. 4.7] with the corresponding contact lines remaining pinned along the edges of the graphene stack. In addition, like in the previous case (see Fig. 4.4-4.5), the drop is eventually confined entirely on the top surface of the stack L_1 without wetting the sides of the graphene stack. This is established by noting that similar to the previous case (see Fig. 4.4-4.5), θ_2 starts to

evolve only when angle θ_3 has ceased to exist. It is worthwhile to mention here that pinning witnessed here as well as those that will be described later occur due to interaction of the water-nanodrop contact line with sharp nanoedges of holey graphene; therefore, like in the previous case, pinning behavior is possibly similar to well-known Gibbs pinning.[130,131]

To summarize, while we encounter several intriguing drop wetting dynamics as a function of interplay of lateral and vertical separations, we invariably witness that the liquid drop fails to demonstrate stable imbibition even beyond the graphene stacks at the uppermost level L_1.

4.3.2 Case 2: combined spreading–imbibition dynamics for intermediate vertical inter-stack separation (ISS).

For this case, we study drop imbibition dynamics in the holey graphene structure for a smaller vertical ISS of 2.5 nm for three separate cases with lateral ISSs of 4 nm, 6 nm, and 8 nm. For the case of lateral ISS of 4 nm, the behavior is exactly identical to that in the previous case (see Fig. 4.1-4.3). The corresponding MD simulation snapshots for this case are provided in Fig.4.8. Therefore, for this case too, vertical ISS of the graphene stacks is large enough (in comparison to lateral ISS) to ensure that water molecules are in much closer proximity to the graphene layers in the uppermost level (L_1) compared to the graphene layers in the lower level (L2). Therefore, just like in the previous case, the drop fails to imbibe and remains localized on the uppermost layer (L_1). Furthermore, the lateral ISS being small, the drop equilibrates by spreading on the two laterally separated stacks. In addition, like in the previous case, the description of wetting is completed by studying the time evolution of the contact angles θ_1, θ_2, θ_3, and θ_4 [see Fig.4.9] and the spreading radii r_1 and r_2 [see Fig. 4.10].

We next consider the case where the lateral ISS is 6 nm and the vertical ISS 2.5 nm. The MD simulation snapshots are revealed in Fig.4.11. Unlike in the previous case (see Fig. 4.4-4.5), the graphene layers of the lower level L_2 are in close enough proximity of the waterdrop, ensuring that they can exert significant attraction on the water nanodrop, thus triggering imbibition action. As a consequence, the drop simultaneously spreads on the graphene stack on the upper level (L_1) and imbibes towards the lower level (L_2). During this imbibition, a most remarkable situation arises. There is a greater number of water molecules that are closer to the bottom side of the graphene stack in level L_1 compared to the top side graphene stack at the lower level L_2. Therefore, the drop starts to spread on the former, while imbibing towards the latter. Eventually, the drop hits the graphene stacks at level L_2 and starts to spread. Therefore, we end up with several most interesting wetting scenarios: (a) a single drop wets four different surfaces (3 sides of the graphene stack at level L_1 and the stack at level L_2), (b) a single graphene stack is wetted on both top and bottom, and (c) there is a distinct time lag in the onset of spreading at different layers [see Fig.4.13]. Here too the description of wetting is completed by noting the time evolution of the contact angles θ_1, θ_2, θ_3, θ_4 and θ_5 [see Fig.4.12] as well the spreading radii r_1, r_2, and r_3 (r_1 is the spreading radius on the top surface of graphene stack at level L_1, r_2 is the spreading radius on the bottom surface of graphene stack at level L_1, and r_3 is the spreading radius on the top surface of graphene stack at level L_2) [see Fig. 4.13]. Very intriguingly, we witness superhydrophobic values for contact angles θ_4 and θ_5 (i.e., the contact angles made by the drop on the upper surface of the graphene stack at lower level L_2), but much smaller values for the contact angles θ_1 and θ_2. For the present case, imbibition beyond level L_1 being favored, significant amount of water moves beyond L_1 and distributes between the lower surface of the stack at level L_1 and the upper surface of the stack at L_2. This distribution is unequal, and more

amount of liquid goes towards the upper surface of the stack at L_2. However, the smallness of the lateral extent of the graphene layer in stack at L_2 ultimately results in the attainment of a hydrophobic contact angle (θ_3 and θ_4) [see Fig. 4.12] supported by a significantly large pinning force imparted by the edge of the graphene stack at level L_2. Please note that here imbibition occurs only up to the graphene stacks at level L_2 and the water drop does not imbibe beyond level L_2. Therefore, this can be considered to be an example of partial imbibition.

We finally consider the case where the lateral ISS is 8 nm and the vertical ISS is 2.5 nm. The MD simulation snapshots for this case are provided in Fig. 4.14. For this case, the behavior is very similar to that in the corresponding situation where the vertical separation is 4 nm (see Fig. 4.6-4.7). Therefore, here too the drop starts to imbibe, but fails to reach the lower level L_2. In the process, the drop gets pinned to one of the lateral graphene stacks of the upper level L_1. This pinning, coupled with the finite imbibing velocity of the drop, imparts a spinning action on the drop that forces the drop to spin back and settle

on the top of this graphene stack at level L_1. Furthermore, the fact that $r_s < r_w$ enforces much larger values of contact angles θ_1 and θ_2 [see Fig. 4.15]. In addition, like in the previous case (see Fig. 4.6-4.7), θ_2 appears only after the disappearance of θ_3.

To summarize, for this particular vertical ISS, we witness a plethora of imbibition behavior that involves no-imbibition, metastable imbibition, and stable partial imbibition.

4.3.3 Case 3: combined spreading–imbibition dynamics for small vertical inter-stack separation (ISS).

We finally consider a much smaller vertical ISS of 1 nm. We first study the case of lateral ISS of 4 nm [the corresponding MD snapshots are provided in Fig.4.16]. The significantly small vertical ISS implies that the drop senses the lower level L_2 at the start of imbibition, and accordingly, it simultaneously imbibes and spreads. This spreading occurs on the two laterally separated graphene stacks at the upper level L_1 and on the graphene stack at level L_2. Therefore, we witness the following highly interesting wetting scenarios: a single drop wets five different surfaces, namely the upper and side surfaces of each of the two graphene stacks at level L_1 and the upper surface of the graphene stack at level L_2. Like in the previous cases, the time variation of the contact angles θ_1, θ_2, θ_3 and θ_4 [see Fig.4.17] and the spreading radii r_1 and r_2 [see Fig. 4.18] are provided to complete the description of the imbibition process. Key to note here is that imbibition is restricted only to layer L_2 and the drop does not move below this layer. Therefore, this is the case of partial imbibition only and the drop fails to imbibe through the entire thickness of the holey graphene structure.

We next consider the case where the lateral ISS is 6 nm and the vertical ISS is 1 nm [see Fig. 4.19 for MD simulation snapshots]. Here too the proximity of the imbibing water drop to the graphene stack at level L_2 ensures that imbibition and spreading occur simultaneously. Spreading occurs on one graphene stack each at levels L_1 and L_2. The interesting wetting states witnessed here are as follows: (a) a single drop wetting four different surfaces and (b) the drop exhibits equilibrium angles ($\theta_2 \sim 90^o$) on the graphene stack at level L_1 [see Fig. 4.19], but demonstrates contact angles (θ_3 and θ_4) that are much larger on the graphene stack at level L_2 [see Fig. 4.20]. Such augmented contact angles on the lower stack can be explained by arguing that a larger

volume of liquid imbibes in the lower level (as compared to the case depicted in Fig. 4.16-4.18), leading to the attainment of this large contact angle (on the top surface of the graphene stack at level L_2) supported by a large pinning force from the edges of the graphene stack. We also study the evolution of the spreading radius r_2 [see Fig. 4.20] in order to complete the description of this combined spreading–imbibition dynamics. Like in the previous case (see Fig. 4.16-4.18), here too imbibition is only a partial one since the drop does not imbibe beyond the graphene layers at level L_2.

Lastly, we consider the case where the lateral ISS is 8 nm and the vertical ISS is 1 nm [see Fig. 4.22 for corresponding MD simulation snapshots]. In this case, unlike in the previous cases of lateral ISS of 8 nm (see Fig. 4.6-4.8 and 4.14-4.15), the drop can successfully imbibe and wet the graphene layer at level L_2. Therefore, there is simultaneous spreading and imbibition, with spreading occurring on the graphene stacks at levels L_1 and L_2. Of course, the drop exhibits equilibrium angles (~90^o) on the graphene stack at level L_1 but demonstrates a contact angle that is much larger on the graphene stack at level L_2 [see Fig. 4.23]. The reason is same as that for the case studied in Fig. 4.19-4.21 – imbibition of larger fluid mass, which is supported by the attainment of this hydrophobic contact angle in presence of a large pinning force imparted by the edges of the graphene stack at level L_2. Here too we study the evolution of the spreading radius r_1 [see Fig. 4.24] in order to complete the description of this combined spreading–imbibition dynamics. Like in the previous cases (see Fig. 4.16-4.18 and 4.19-4.21), imbibition here does not occur beyond level L_2, and hence, it is only partial imbibition.

To summarize, for this very small value of vertical ISS, we indeed witness partial imbibition regardless of the value of the lateral graphene ISS, although the associated spreading and wetting behaviors are indeed dictated by the lateral ISS.

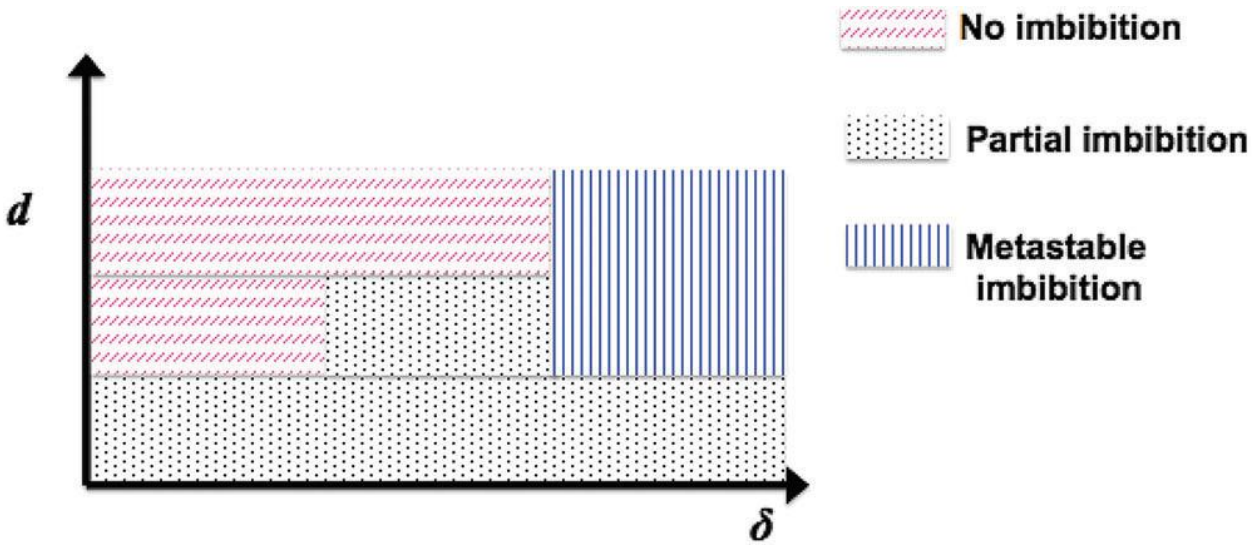

Fig. 4.25 *d*–*δ* phase space summarizing imbibition behavior of water nanodrop interacting with a multilevel holey graphene structure.

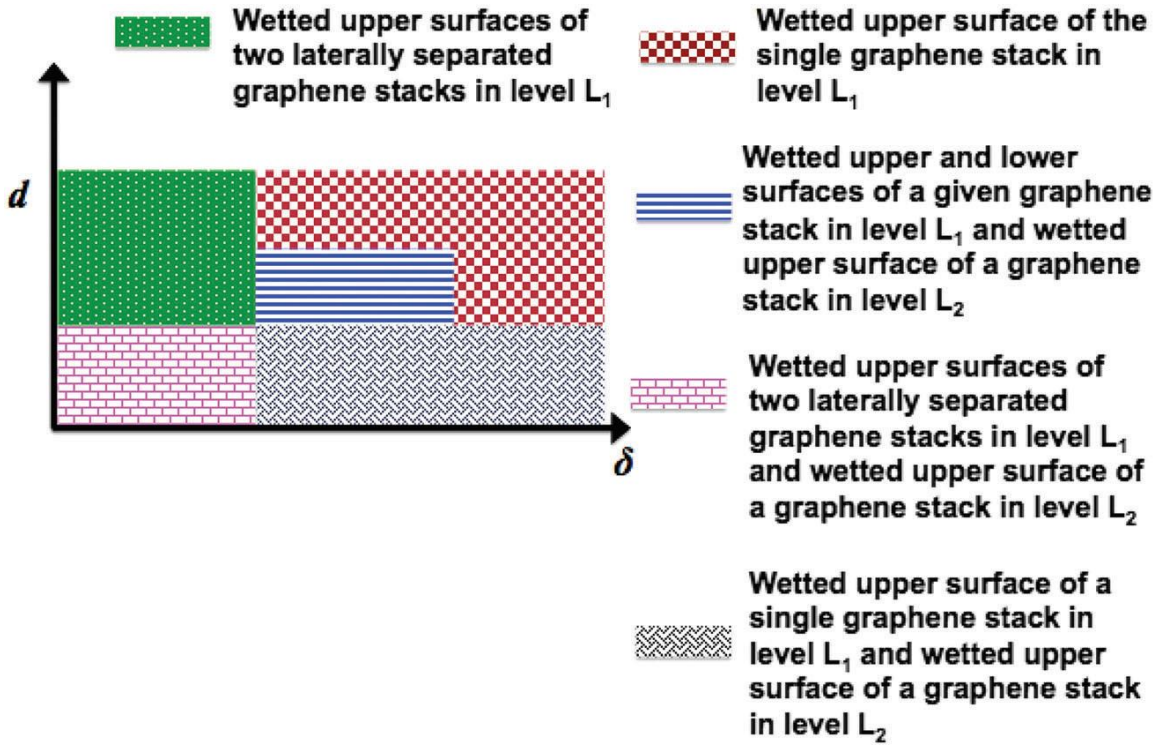

Fig. 4.26 *d*–*δ* phase space summarizing equilibrium wetting behavior of water nanodrop interacting with a multilevel holey graphene structure.

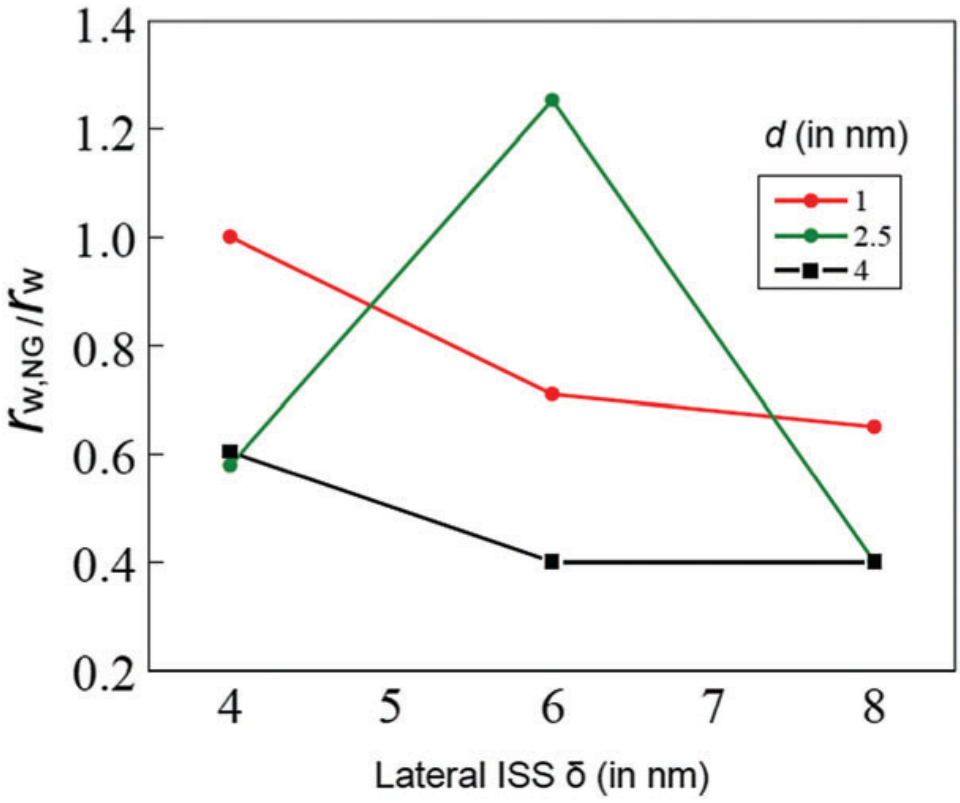

Fig. 4.27 Variation in $r_{w,NG}/r_w$ as a function of lateral ISS δ for different values of vertical ISS d during water–holey graphene interactions.

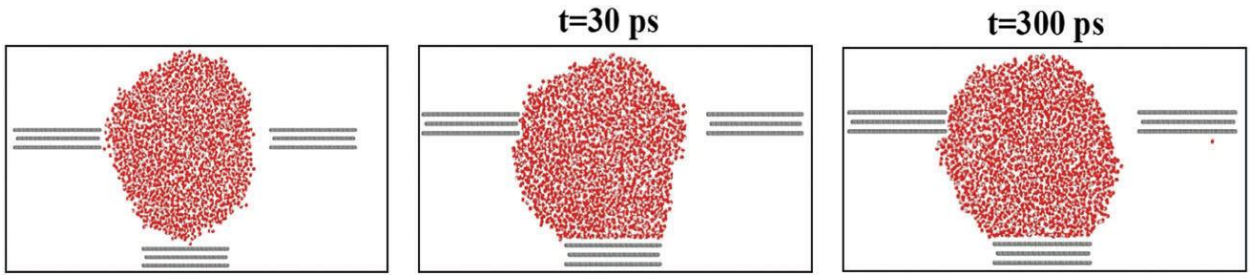

Fig. 4.28 Drop imbibition in a holey graphene structure for lateral ISS (d) of 8 nm and vertical ISS (d) of 4 nm (see Fig. 4.1 and 4.4 for the definitions of d and d). The same geometry has been used as in Fig. 4.6-4.7. However, here the drop starts from a location between the graphene stacks at levels L_1 and L_2, while in Fig. 4.6-4.7, the drop starts from above the graphene stacks at level L_1 (see Fig. 4.1 and 4.4 for the definitions of levels L_1 and L_2). As can be seen from the figure, very little change in drop configuration occurs between t = 30 ps and t = 300 ps, indicating that the drop attains its final configuration rather quickly.

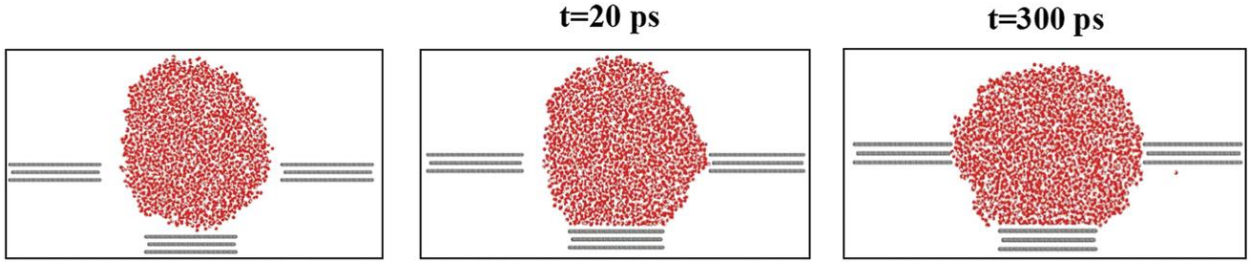

Fig. 4.29 Drop imbibition in a holey graphene structure for lateral ISS (d) of 8 nm and vertical ISS (d) of 2.5 nm (see Fig. 3.1 and 3.2 for the definitions of d and d). The same geometry has been used as in Fig. 4.14-4.15. However, here the drop starts from a location between the graphene stacks at levels L_1 and L_2, while in Fig. 4.14-4.15, the drop starts from above the graphene stacks at level L_1 (see Fig. 4.1 and 4.4 for the definitions of levels L_1 and L_2). As can be seen from the figure, not a significant amount of change in drop configuration is noted between t = 20 ps and t = 300 ps, indicating that the drop attains its final configuration rather quickly.

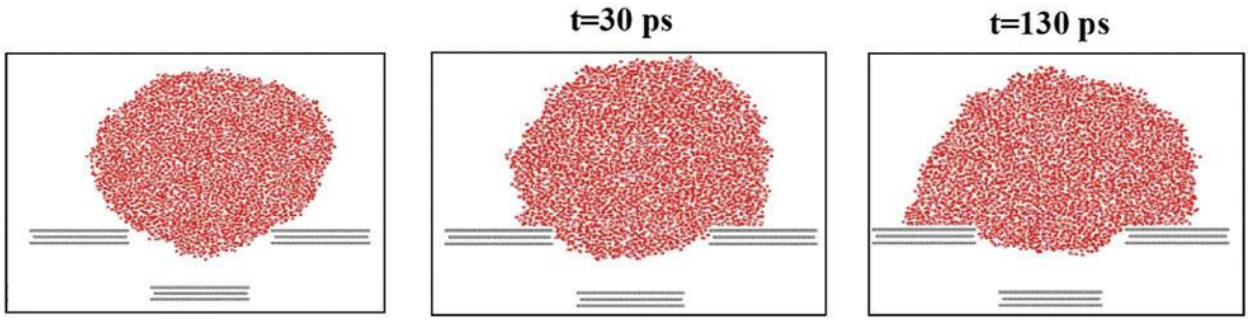

Fig. 4.30 Drop imbibition in a holey graphene structure for lateral ISS (δ) of 6 nm and vertical ISS (d) of 2.5 nm (see Fig. 4.1 and 4.4 for the definitions of δ and d). The same geometry has been used as in Fig. 4.14-4.15. However, here we consider a much larger drop containing N = 5000 molecules, while for all other simulations, we use N = 3000 molecules.

4.4 Discussions

4.4.1 Phase space for imbibition and wetting states

In Fig. 4.25, we summarize through a d–δ phase space, the key imbibition behaviors witnessed in our simulations. For substantially small d (the vertical ISS), we witness imbibition of the water drop (or a part of the water drop) from graphene layer at the upper level L_1 to the graphene layers at the lower level L_2. Of course, the drop ceases to move beyond the graphene layers at L_2. Therefore, for this small value of d, one witnesses partial imbibition regardless of the value of lateral separation δ (see Fig. 4.16–4-24). Such partial imbibition, albeit with the generation of completely non-trivial wetting states (discussed later), is also witnessed for slightly larger d and larger δ (see Fig. 4.11-4.13). Increase in d enforces imbibition events to disappear. This disappearance can be in the form of no imbibition at all when the drop does not wick beyond the graphene layers at level L_1 or in the form of metastable imbibition when a large part of the drop can only momentarily wick beyond L_1 in an unstable fashion only to be pushed back to the top of layer L_1. The no-imbibition events are typically witnessed for smaller values of δ (4, 6 nm) (see Fig. 4.1-4.3, 4.4-4.5 and 4.8-4.10), while metastable imbibition is observed for larger δ (8 nm) (see Fig. 4.6-4.8 and 4.14-4.15).

The retarded imbibition behavior summarized in Fig. 4.25 is invariably associated with a wide plethora of wetting behaviors, as summarized in the corresponding d– δ phase space of the wetting states (see Fig. 4.26). For small d, where there is always partial imbibition (see Fig. 4.25), graphene stacks at both levels L_1 and L_2 are wetted (see Fig. 4.26). Of course, the drop wets two laterally separated surfaces at level L_1 for small δ (see Fig. 4.16-4.18), but wets only one surface at level L_1 for larger δ (see Fig. 4.19-4.21 and 4.22-4.24). Interestingly, for the case

with larger δ, more volume of liquid wicks to the graphene stack at level L_2, ensuring attainment of large hydrophobic contact angles on the upper surface of the graphene stacks at level L_2 supported by appropriate pinning force from the edges of the graphene sheets at level L_2 (see Fig. 4.19-4.21 and 4.22-4.24). For large d, where there is either no imbibition or at best metastable imbibition, only graphene stack(s) at level L_1 is wetted. Here too, two laterally separated stacks are wetted for smaller δ (see Fig. 4.1-4.3 and 4.8-4.10), while only one stack is wetted for larger δ (see Fig. 4.4-4.5, 4.6-4.7 and 4.14-4.15). For the latter case, tendency to confine the water drop on a single stack enforces attainment of large hydrophobic contact angles supported by pinning forces from the edges of the graphene stacks at level L_1. The most interesting wetting state is witnessed for intermediate values of d and δ (d = 6 nm and δ = 2.5 nm). For that case, the water-drop wicks towards the graphene stacks at level L_2; however, the drop not only wets the top surfaces of the stacks at levels L_1 and L_2, but also wets the bottom surface of the stack at level L_1. Therefore, we encounter an unprecedented wetting scenario where a graphene stack consisting of several graphene layers experiences a fiber-like wetting behavior and, virtually, the entire stack is engulfed. This particular fiber-like wetting ensures wetting of a larger surface area of graphene, as evident in Fig. 4.27. In this figure, we study the ratio of wetted lengths in water–graphene wetting interactions in the presence and absence of holes in the graphene structure. For the case with no holes, we consider a continuous stretch of an unsupported graphene trilayer and the wetted length is denoted as r_w. On the other hand, this wetted length for nanoporous or holey graphene structure is denoted as $r_{w,NG}$. We clearly witness $r_{w,NG} > r_w$ for the case of d = 6 nm and δ = 2.5 nm. This finding of attainment of a larger wetting length compared to that of non-porous graphene (i.e., $r_{w,NG} > r_w$) establishes the significance of the present study for realistic applications. Nanoporous graphene, to date, has been typically used

for two broad classes of applications. For the first class of applications, 3-D porosity introduced by the nanoporous nature of holey graphene is leveraged to create greater ion-accessible surface area, thereby leading to applications ranging from efficient capacitive energy storage[97–100] to enhanced chemical reactions.[101,102] In the second class of applications, the porous nature of holey graphene allows it to be used as a nanoscopic filter, leading to applications such as in desalination,[14–16,104,105,132] and water–ethanol separation.[106] The present study opens up a new domain of applications of holey graphene. Studying water imbibition dynamics through holey graphene (please note that this is for the first time that such a study on no-force water imbibition through holey graphene has been conducted; all previous studies involved pressure-driven transport of water through holey graphene) leads to wetting states where for the first time holey graphene ensures an enhancement in water-accessible surface area. In other words, previously, holey graphene was primarily shown to enhance ion-accessible surface area; herein, we take it one step forward and show that holey graphene can lead to enhancement of water-accessible surface area. Therefore, just as standard holey graphene leads to improvement in all applications where enhanced ion accessibility is preferred, our study conceives the use of holey graphene in all applications that will be benefitted by enhanced water-accessible surface area. Some such applications are carbon-based electrical double layer or EDL capacitors (the effect of EDL, which is formed at water–carbon interface, will get enhanced by enhancement of available water–carbon surface area),[114] graphite- based compact heat exchangers (enhanced water–graphene surface area will allow even greater compaction of heat exchangers without reducing performance),[115] and ensuring a faster freezing of water with much less subcooling in presence of holey graphene nanoflakes introduced into bulk water (enhanced water–holey graphene

interaction area ensures water freezing with even lesser subcooling as compared to non-holey graphene nanoflakes).[116]

4.4.2 Comparison of results of the present study with those of pressure-driven transport across single- or few-layer nanoporous graphene

There has been extensive research on pressure-driven transport of water across single- or few-layer nanoporous graphene, unraveling tremendous potential of nanoporous graphene to help in desalination.[14–16,104,105,132] The present study differs from these well-researched problems on two key accounts. First, we consider the case of no-applied-force-driven imbibition. Second and more important, holey graphene architecture is slightly different from that of standard nanoporous single- or few-layer graphene typically used in desalination. This architecture, as evident from recent experiments[96,97] and mimicked in our simulations, consists of vertically and laterally separated stacks of multi-layered nano- porous graphene. Such vertical and lateral spacing is absent in standard single- or few-layer nanoporous membrane used for water desalination. Clearly, the presence of such finite spacing, coupled with the consideration of no-applied-force imbibition, makes the role of water–graphene capillary interactions extremely significant. Such a significant influence of capillary interactions is not relevant for standard water desalination studies where pressure-driven water transport ensues across single- or few-layer nanoporous graphene. Consequently, these studies never report the several new combined wetting–imbibition phenomena that we witnessed in our study. To iterate, some of these capillarity- driven new phenomena include (a) engulfment of a complete graphene stack by the water drop (leading to a fiber-like wetting state and a significant increase in water–accessible graphene surface area), (b) simultaneous wetting of multiple surfaces of multiple graphene

stacks, and (c) wetting with pinned and unpinned contact lines on vertically separated graphene layers.

4.2.3 History and drop-size dependence of nanodrop imbibition– spreading dynamics of holey graphene

In Fig. 4.28 and 4.29, we show the manner in which nanodrop imbibition–spreading dynamics depends on the history (or initial position) of the drop. In the case for both these figures, we choose δ = 8 nm, but choose d = 4 nm for the case shown in Fig. 4.28 and d = 2.5 nm for the case shown in Fig. 4.29. Therefore, the case in Fig. 4.28 shows the same geometry as that in Fig. 4.6-4.7, while the case in Fig. 4.29 shows the same geometry as that in Fig. 4.16-4.18. Of course, the difference is that while in the case shown in Fig. 4.6-4.7 and 4.14-4.15, the drop starts from the top of the graphene stacks at level L_1, in Fig. 4.28 and 4.29, the drop starts between the graphene stacks at levels L_1 and L_2.

As shown in both Fig. 4.28 and 4.29, the drop fails to go beyond the graphene stacks at level L_2. In other words, they fail to go beyond the first layer of the graphene stack that they encounter. This is similar to the cases reported in Fig. 4.6-4.7 and 4.14-4.15, where the water drop fails to go beyond the first graphene stack (namely the stack at level L_1) that the drop encounters. Of course, the change in initial position ensures that the drop shown in Fig. 4.6-4.7 and 4.14-4.15 undergoes initial metastable imbibition, which is missing for the drop shown in Fig. 4.28 and 4.29. Furthermore, the absence of metastable imbibition, as shown in Fig. 4.28 and 4.29, implies that the drops in these figures attain their final equilibrium state much faster than those shown in Fig. 4.6-4.7 and 4.14-4.15. In Fig. 4.30, we show nanodrop imbibition for much larger sized

drops (containing 5000 water molecules compared to 3000 molecules with which the other simulations have been conducted). For this case, we consider δ = 6 nm and d = 2.5 nm. Hence, the geometry is identical to the case studied in Fig. 4.11-4.13. However, unlike in Fig. 4.11-4.13, we find no imbibition beyond the graphene stacks at level L_1 and hence no fiber-like wetting is observed. However, on a closer look, we find that drop behavior in Fig. 4.30 is very much similar to that in Fig. 4.8-4.10 (δ = 4 nm, d = 2.5 nm); similar to the drop shown in Fig. 4.8-4.10, as shown in Fig. 4.30, the drop fails to go beyond the graphene stacks at level L_1 and only shows a slight bulging in the gap between the two laterally separated graphene stacks and gradual spreading on topmost graphene layers on the laterally separated stacks at level L_1 (compare the snapshots corresponding to t = 30 ps and 130 ps in Fig. 4.30). It is easy to explain this similarity in drop behavior shown in Fig. 4.8-4.9 and 4.30. For a larger sized drop (N = 5000), a larger lateral separation (δ = 6 nm) has a similar effect as a smaller lateral separation (d = 4 nm) would have on a smaller drop (N = 3000).

4.5 Conclusions

In this study, we investigate for the first time no-applied-force dynamics of a water nanodrop in contact with a multilevel holey graphene structure, whose architecture is built up by horizontally and vertically separated graphene stacks consisting of unsupported graphene trilayers. We demonstrate remarkable combined imbibition–spreading dynamics dictated by interplay of lateral and vertical ISSs. The dynamics spans a multitude of imbibition conditions and wetting states. In fact, it may even lead to case(s) where water–graphene contact zone is enhanced compared to water–graphene contact corresponding to continuous graphene sheets. Given that

existing studies have invariably considered pressure-driven transport of water through a multi-layer holey graphene structure (conceived as a nanoporous graphene membrane) for water purification and desalination applications, the present study sheds light on a hitherto unprobed physical situation of no-force water interaction with a holey graphene structure. We anticipate that our findings will not only shed light on hitherto unknown new water–holey graphene wetting and imbibition states, but will also provide useful insights into newer uses of holey graphene in significantly enhancing graphene–water interaction area for applications ranging from energy storage to heat transfer.[114–116] As a part of future research, we plan to extend the understanding developed through this study to cases where graphene nanoedges undergo oxygen terminations when these edges come in contact with water nanodrops, elucidating the role of applied electric field to improve water transport through porous graphene (in a manner similar to that achieved for nanoporous gold[130]

Chapter 5: Dynamics of a Water Nanodrop through a Holey Graphene Matrix: Role of Surface Functionalization, Capillarity, and Applied Forcing

5.1 Introduction

Nanoporous graphene, where continuous graphene sheets are made discontinuous by the presence of holes created on account of missing of certain C bonds,[133] has seen exceedingly growing recent interest in a multitude of applications, such as supercapacitors and batteries,[134,135] hydrogen production,[136,137] water desalination and filtration,[15,17,24,104,138–141] molecular sieving[142] water−ethanol separation,[106,143] ion selection,[144,145] DNA sequencing,[146] and many more. Holey graphene (HG) is a particular form of nanostructured graphene where multilayers of nanoporous graphene layers are organized in the form of stacks[95–101,147–150] and has been employed in several of the above applications that are benefitted by the presence of a large ion-accessible graphene surface area that the HG system offers. However, unlike the case of a single layer of nanoporous graphene, a HG system, possibly for having a thickness much larger than a single-layer nanoporous graphene, has never been utilized for membrane- like applications, such as water desalination, separation of water from a liquid−liquid mixture, *etc*. Central to these applications involving water is the manner, in which the interplay of an applied force, the capillary effects, and the nature of functionalization of the edges of the graphene holes dictates the water−HG interactions. Recently, the present authors have unveiled several important aspects of the no-force-driven wetting dynamics of a water nanodrop in contact with (a) monolayer and

multilayers of supported and unsupported, non-porous graphene layers[76] and (b) surfaces with graphene nanopillars.[77]

In this chapter, we employ molecular dynamics (MD) simulations to probe the force-driven dynamics of a water drop through a HGA. The edges of the holes of the HG are functionalized with either -H termination (we denote it as hydrophobic functionalization or HOF) or -OH termination (we denote it as hydrophilic functionalization or HIF). This functionalization saturates the unsaturation created by the removal of the C atoms during the formation of the holes. We study in detail the dynamics of a water drop through this HGA under different magnitudes of the applied forcing (on the water drop). We consider forces varying from 0.005 to 1 kcal/molÅ. Forces of the order of 0.1 kcal/molÅ and larger are often so large that they enforce such a hastened transport that we fail to single out ant time interval where one can witness a constant time-independent flux (this issue is discussed further later in this section). Therefore, we provide a detailed analysis of the drop dynamics for forces that are significantly smaller. For such forces, the capillary effects become significant given that we are considering a water drop and not a *slab of water*. Moreover for such forces the dominant influence of capillarity ensures a progressive increase in the flux with an increase in the applied force for HG with both HOF and HIF, while for larger forces the flux saturates and stops increasing with an increase in the force. On the other hand, large attractions between water and the HIF ensure (a) arresting of the dewetting effects enforcing retention of the water molecules within the graphene stacks and (b) slowing down of the transport of the water molecules past the graphene edges (see Fig. 5.1 a,b). As a consequence, the HGA with HOF demonstrates both augmented flux and an augmented volume of the permeated water for most of the force values for forces less than 0.1 kcal/molÅ. Finally, we pinpoint a time interval when the flux of water coming out of the HG with either HOF or HIF is constant. As already indicated, for

forces larger than or equal to 0.1 kcal/molÅ, we do not witness any such time interval where the flux is constant. Identification of this time interval where the flux is constant for smaller forces, allows us to attempt a Darcy's Law like description of the flux for such forces – we witness that capillarity enforces a breakdown of the Darcy's Law with flux becoming proportional to F^{α}, where α=1.3 and 1.7 for HG with HIF and HOF, respectively.

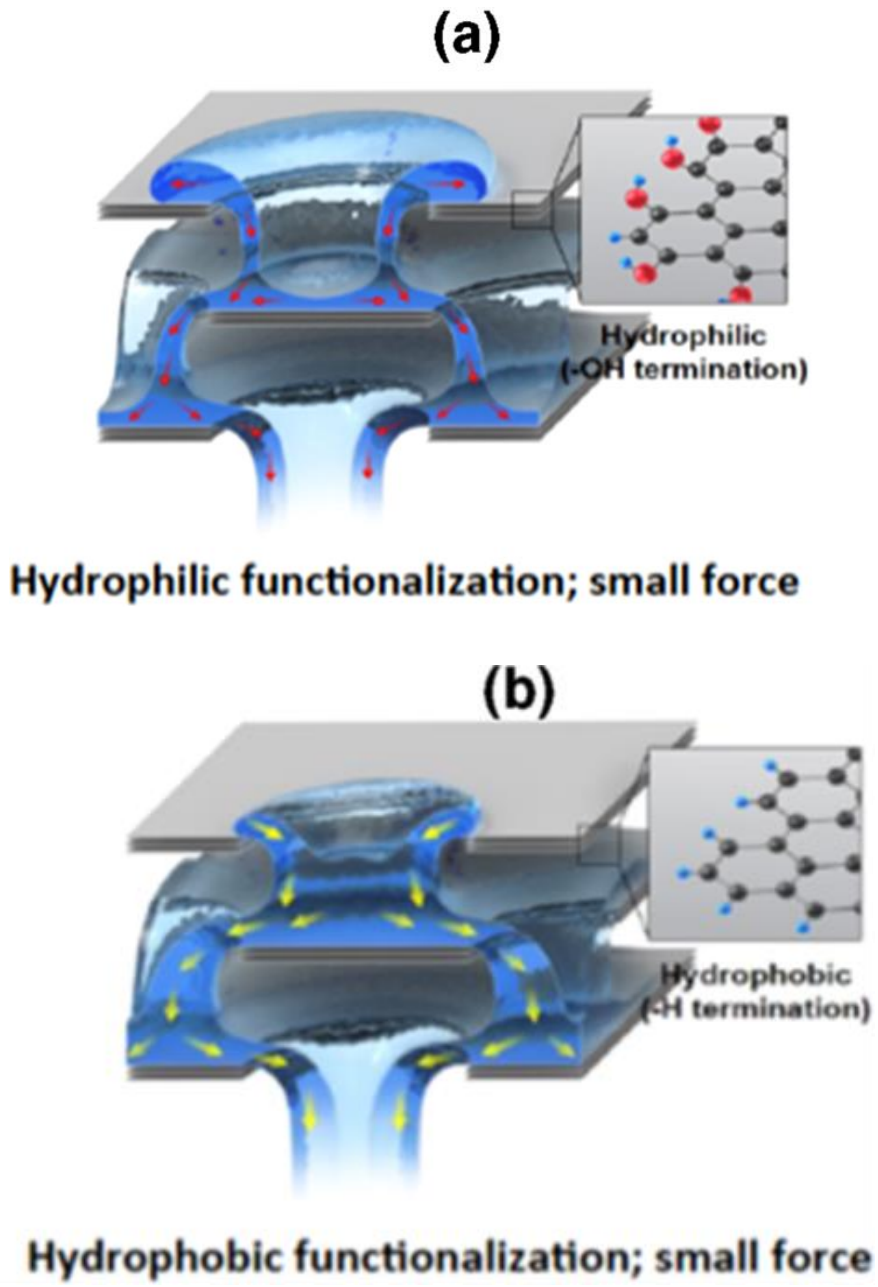

Figure 5.1. Schematic of the nanodrop dynamics in HGA with different functionalizations of the hole. The stack levels L_1–L_3 are the upper, middle, and lower stacks, with each stack consisting of three layers of graphene. Figure 5.5 identifies these stacks as well as the lateral interstack separation or ISS (δ) and vertical ISS (d) in a two-dimensional (2-D) representation. (a, b) Nanodrop dynamics for small forces (F < 0.1 kcal/(mol Å)) in HG with (a) hydrophilic functionalization (HIF) and (b) hydrophobic functionalization (HOF). The process is dominated by (i) the retention of water due to arrested dewetting for HG with HIF (see the larger water mass on graphene stacks in level L_1 for HG with HIF) and (ii) reduced flow rate and hence reduced flux due to HIF-water attraction (see the thinner velocity arrows near the graphene edges for graphene stacks in level L_3 for the HG with HIF).

5.2 Materials and Methods

The water nanodrop trajectories within the HGA are simulated in 2-D setup using the Large-scale Atomic/Molecular Massively Parallel Simulator (LAMMPS) software package. The water is modeled using TIP4P/2005 model, whereas the graphene architecture is constructed by considering each graphene stack to be made up of three graphene layers with specified vertical and lateral separations between the stacks and appropriate functionalization of the graphene edges. Appropriate post-processing of the water trajectories is carried out to obtain the different parameters that quantify the process.

5.2.1 System description

We carefully choose a quasi-2D geometry as described in the previous studies[77] to eliminate the tremendous line tension effect on the observed drop contact angle (θ) and the resulting wetting effects, which are critical to probe the nanodroplet-HGA interactions. Accordingly, the simulation box is set as 450 Å in x-axis direction, 20 Å in y-axis direction and 500 Å in z-axis direction. Periodic boundary condition is applied to all directions. Each stack of the graphene matrix (three layers graphene with 40 Å in length and 20 Å in width) represents the graphene sheets in between two holes, and the diameter of the holes are set as 60 Å (see Fig. 5.2). The vertical inter-stack separation between two holey graphene stacks is set as 25 Å. The holes (reflected as the lateral ISSs) are created by removing the C atoms; consequently both the edges of the graphene sheets have a zigzag shape ending with hydrogen (-H functionalization) or hydroxyl (-OH functionalization) terminations. The hole diameter and interlayer distance is selected by following the current experimental result, where the hole diameters mostly appear

around 5 nm.[151] And interlayer distance can be tuned in a range of 0.5-7 nm.[108] Fig. 5.2 provides a detailed view of the HG matrix.

Simulation model

Simulations have been carried out using the Large-scale Atomic/Molecular Massively Parallel Simulator (LAMMPS) software package. Water has been modeled using the Tip4p/2005 model.[152] This model allows accounting for the dipole-dipole interactions between water molecules and the partly charged terminations. Furthermore, in this model, the non-bonded interactions between distinct species (which are water molecules, C atoms, and the functionalization groups) consists of the Lennard–Jones (LJ) 12-6 potential (with a cut off distance of 10 angstroms) and columbic interaction. The parameters are calculated through Lorentz-Berthelot mixing rules[15] and summarized in Table 5.1. The carbon atoms in the graphene are fixed at their initial position, as there is no significant impact of graphene flexibility on the wetting behavior. Finally, in this model we incorporate the CHARMM36 force field potential file[153]into the LAMMPS for attributing the inner molecular interaction of hydroxyl terminations, which contains C-O and O-H bonds, C-O-H and C-C-O angles, and C-C-O-H dihedral motions. For hydrogen terminations, the C-H bond is set as fixed.

Performing simulation

All simulations are performed on a canonical ensemble (NVT) with temperature controlled by a Nose´–Hoover thermostat at 300 K. The time step is 1 fs. The simulations start by equilibrating water drops significantly away from the HG matrix. This will ensure that we consider the

interaction between a water nanodrop and a HG (and not “bulk-water”-nanoporous-graphene interaction). In Fig. 5.3, we show the equilibration process. 3000 water molecules (this number of water molecules leads to a drop of 6.5 nm diameter) transfer from solid phase to liquid phase by when the system temperature is increased from 1K to 300K in 50K increments. All the intermediate temperatures are held constant for 50 ps and the final 300K is kept constant for 200 ps to ensure that the equilibrium phase has been achieved.

Post equilibrium, a force (~kcal/mol-Å) is applied to every individual water molecule in the drop in order to make the drop permeate across the HGA (a representative snapshot is shown in Fig. 5.4). We use a large simulation box as compared to the water droplet size to ensure that the drop is not affected by its neighbors. As a result, only a small area (140×20 Å^2, see Fig. 5.4) of the matrix interacts with water and we use this area information to convert the applied force to a pressure (for the present dimensions, where F and pressure are linearly related, F=1 kcal/mol Å is equivalent to a pressure of 22 GPa), which helps the results to tally better with the experiments.

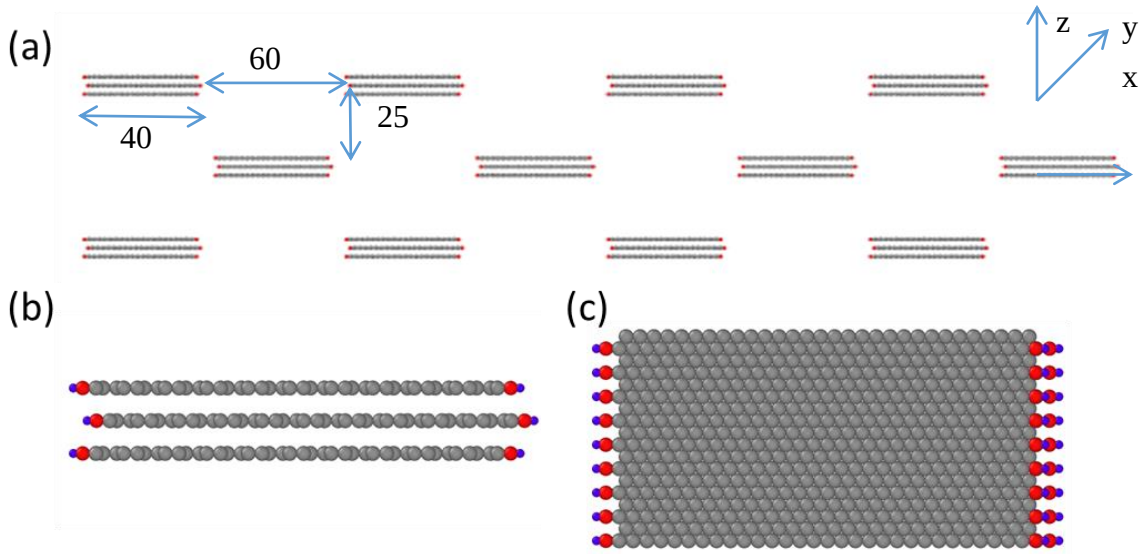

Figure 5.2. (a) Side view of the holey graphene matrix with hydroxyl terminations. Magnified (b) side and (c) top view of a representative of holey graphene sheets in between the two holes.

Table 5.1: LJ and charge parameters used in the simulations

Elements	**ε(kcal/mol)**	***σ* (Å)**	**q(e)**
C(sp2)	0.0859	3.3997	0
C_{COH}	0.0703	3.55	0.2
H_{COH}	0	0	0.44
O_{COH}	0.155	3.07	-0.64
C_{CH}	0.046	2.985	-0.155
H_{CH}	0.0301	2.42	0.115
H_w	0	0	0.5242
O_w	0.16275	3.16435	-1.0484

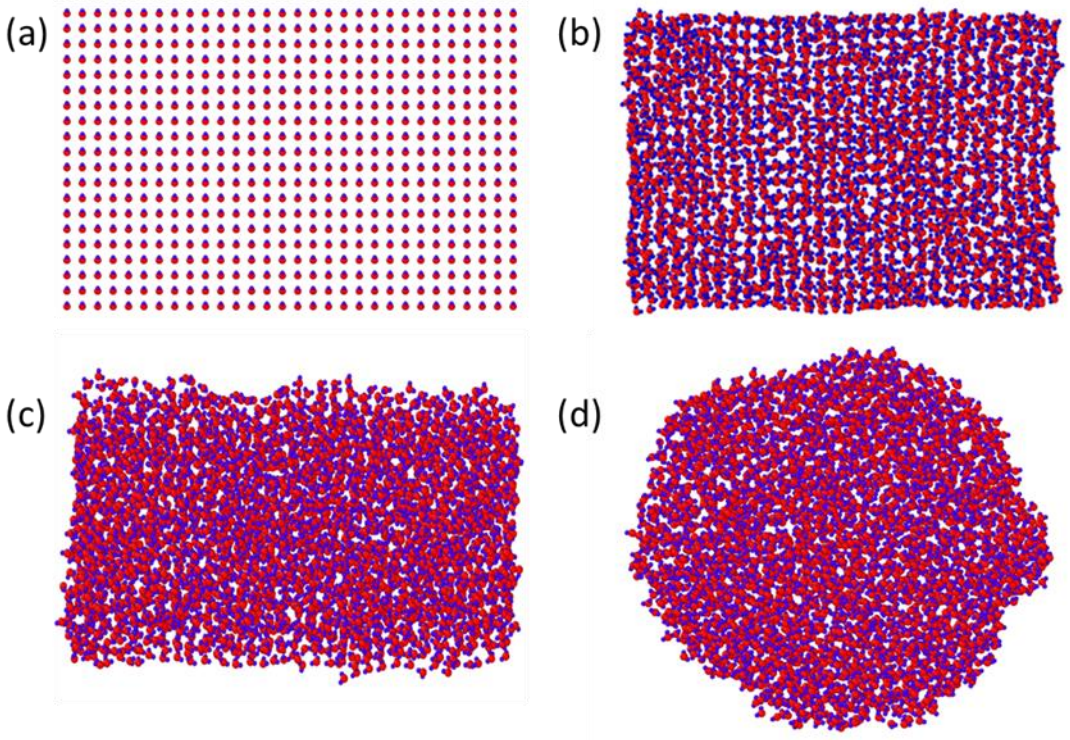

Figure 5.3. (a) Side view of 3000 water molecules at their initial position at 0k. (b) 50K. (c) 150K. (d) 300K.

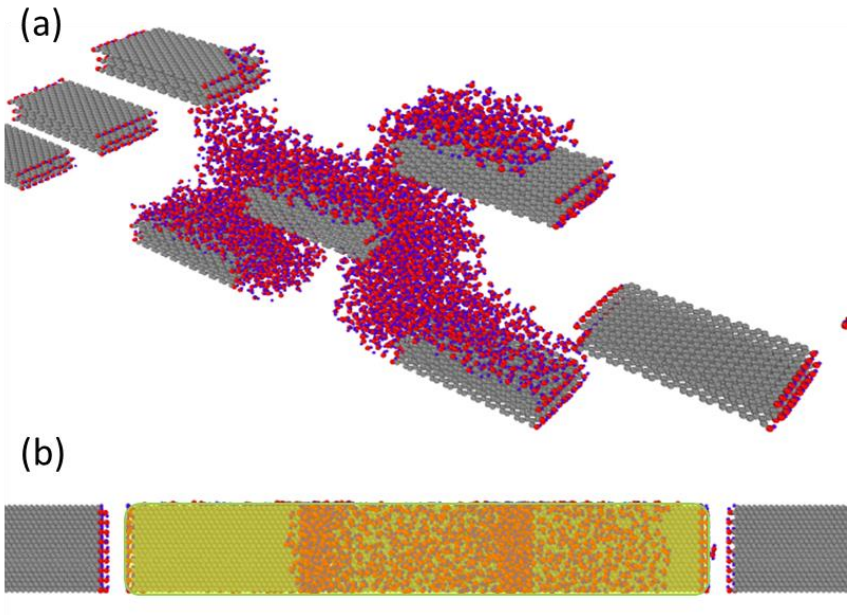

Figure 5.4. (a) Perspective view of the water molecules permeating the holey graphene matrix at 300k. (b) Top view of the matrix with the equivalent pressure calculation zone highlighted.

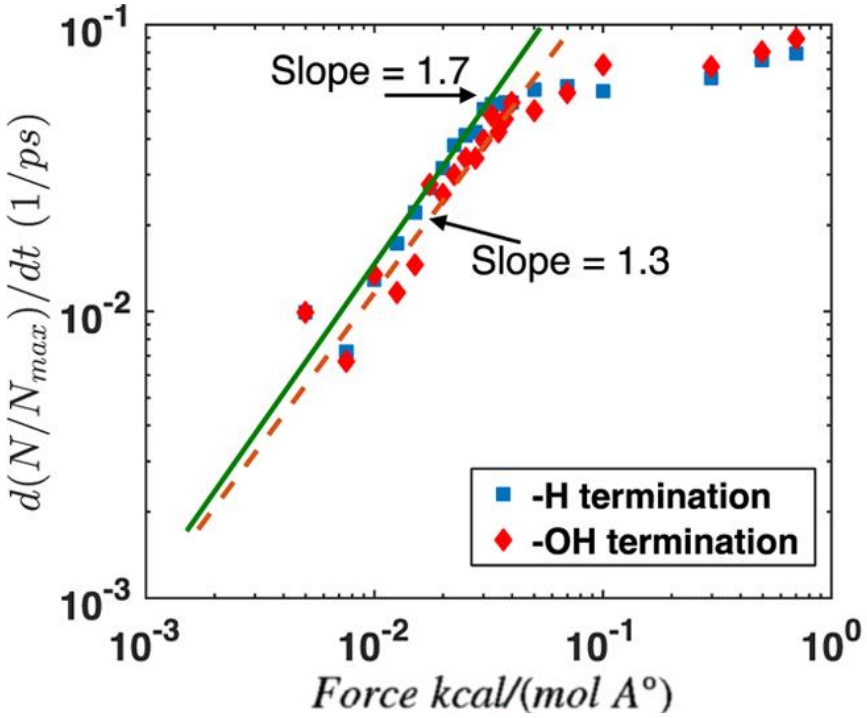

Figure 5.5. Flux-vs-force variation for the HGA with HIF and HOF. In the figure, we demonstrate *dN/dt* ~ F^{α} (where α_{HIF} = 1.3 and α_{HOF} = 1.7) from small force values.

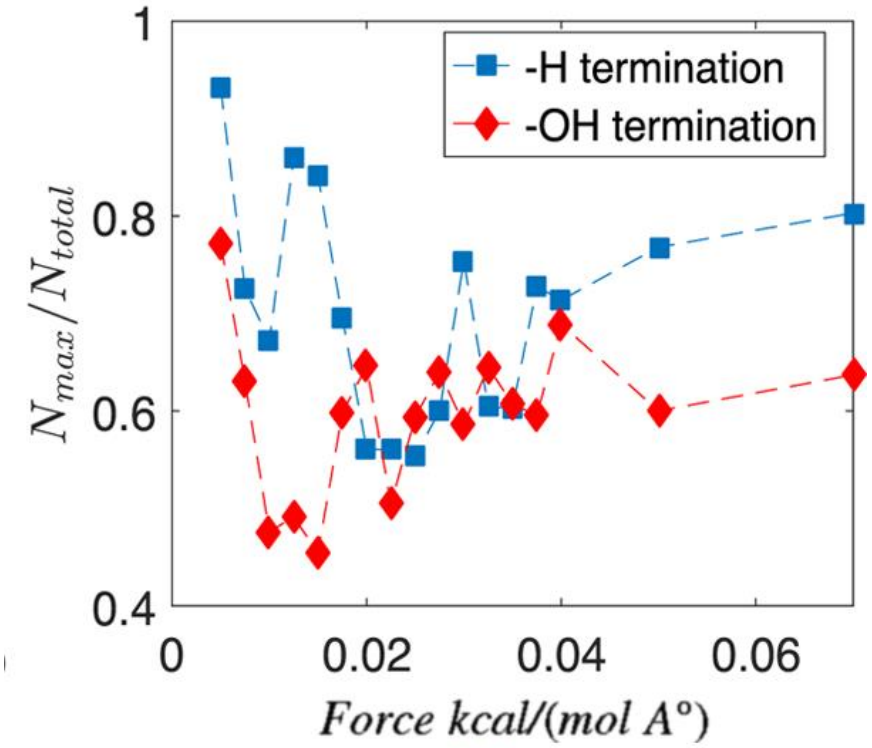

Figure 5.6. N_{max}/N_{total}-vs-force variation for the HGA with HIF and HOF. Here, N_{max} is the maximum amount of water molecules that leaves the HG, whereas N_{total} is the number of water molecules present in the water nanodrop.

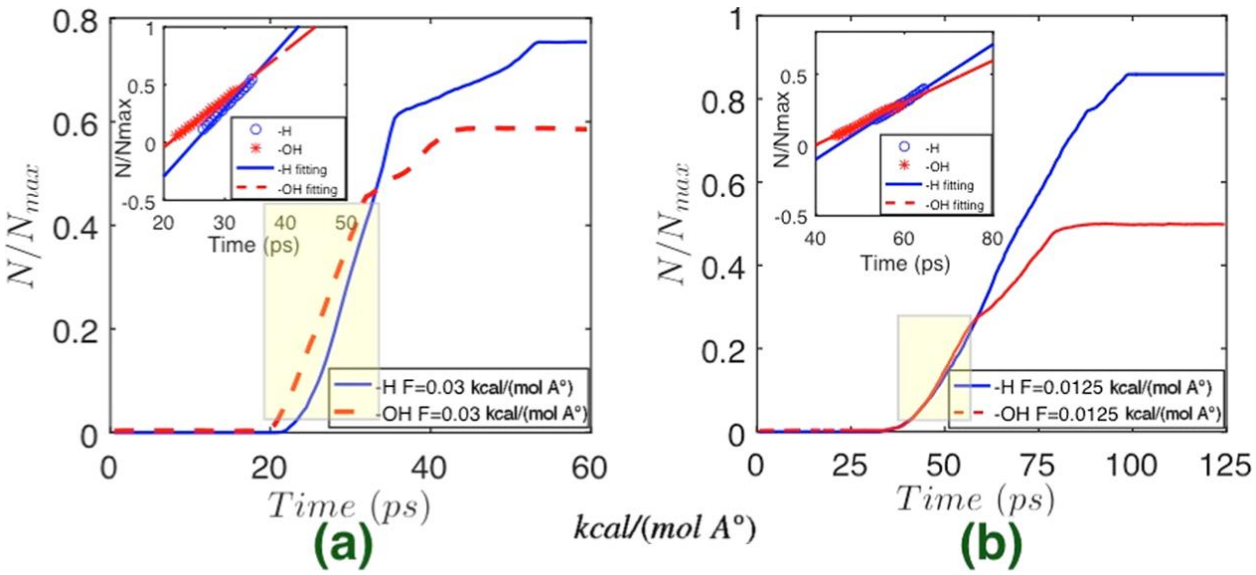

Figure 5.7 Time variation of the cumulative number of water molecules *N* leaving the HGA for (a) HG with HIF and (b) HG with HOF. In the inset of each of (a) and (b), we zoom the region of linear slope of the *N*-vs-t curve [this region is highlighted in (a) and (b)], clearly depicting how the flux (*dN/dt*) is larger for the HG with HOF.

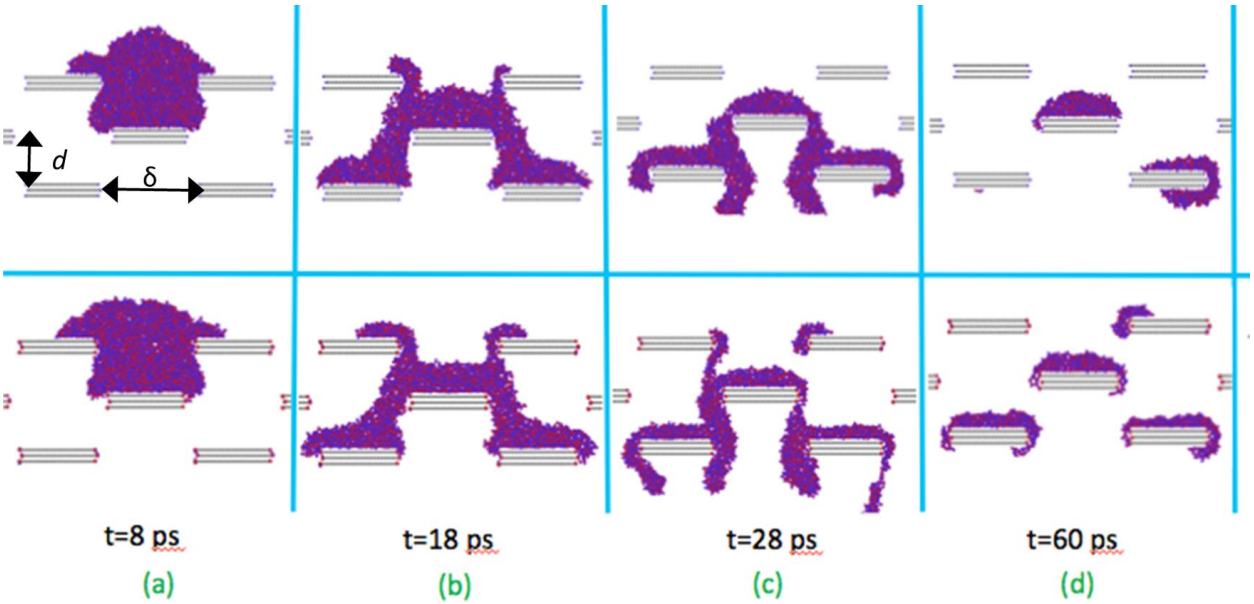

Figure 5.8 Time snapshots showing the dynamics of water drop through the HG system for (top) HOF and (bottom) HIF. The time corresponding to these snapshots are identified in the figure. We consider an applied force of F = 0.03 kcal/(mol Å) for this case.

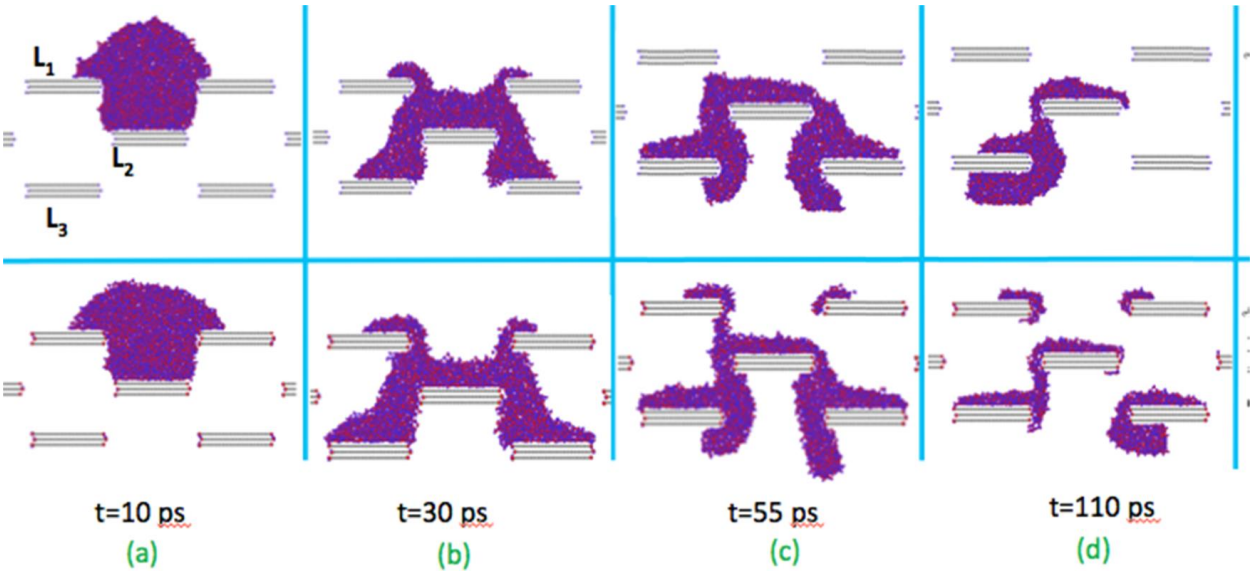

Figure 5.9. Time snapshots showing the dynamics of water drop through the HG system for (top) HOF and (bottom) HIF. The time corresponding to these snapshots are identified in the figure. We consider an applied force of F = 0.0125 kcal/(mol Å) for this case.

5.3 Results and Discussion

5.3.1 Flux and Volume of the Transported Water

Figure 5.5 shows the flux (quantified by *dN/dt*, here $N = N(t)$ denotes the total number of water molecules that have left the HGA at time t) as a function of the applied force for the HG with both HIF and HOF. We show the results for both the small and large forces. We clearly witness a slightly enhanced flux for the HG with the HOF. Figure 5.6 provides the variation of the total volume of the permeated water as a function of the applied force. Here too we witness a distinct increase for the case of HOF for most of the force values less than 0.1 kcal/(mol Å).

To better analyze the flux behavior for force values less than 0.1 kcal/(mol Å), we study the time variation of N (whichprovides the permeation rate or the flux) for different forces (see Figure 5.7a,b). Given that N denotes the number of water molecules leaving the HGA, we find $N = 0$ immediately after the drop enters the HGA. However, N gradually increases and attains a linear slope for certain time interval (see the magnified figures in the inset of Figure 5.7 a,b). This implies a constant dN/dt for this time interval, leading to the case of a steady flow because $\dot{m} = \rho A v \Rightarrow K(dN/dt) = \rho A v \Rightarrow v =$ constant (here $\dot{m}$ is the mass flow rate, which is proportional to dN/dt, v is the velocity, ρ is the density of water, and A is the effective passage area for the water to come out of the HGA). This increase in N with time is soon arrested and we witness saturation in the value of N, signaling that there is no further elimination of water from the HGA. Of course, this saturation value is larger for the HOF indicating a greater amount of permeated volume.

Identification of the time domain where the flow (or the flux) is steady allows us to attempt a Darcy's law-like description of the flux-versus-force behavior (Figure 5.5). The strong influence of capillarity leads to a breakdown of Darcy's law. In other words, flux-versus-force variation is no longer linear; rather $\left(\frac{dN}{dt}\right)_{HIF} \sim F^{1.3}$ (hence $\kappa_{HIF} \propto F^{0.3}$) and $\left(\frac{dN}{dt}\right)_{HOF} \sim F^{1.7}$ (hence $\kappa_{HOF} \propto F^{0.7}$). Consequently, the permeability κ (where $\kappa \propto \left(\frac{dN}{dt}\right)/F$) is force-dependent and is expressed as $\kappa_{HIF} \propto F^{0.3}$ and $\kappa_{HOF} \propto F^{0.7}$. As capillarity dominates here, any increase in force increases the influence of the applied force much more as compared to what happens for larger forces. This justifies this nonlinear behavior of the flux with respect to the applied force or equivalently a force-dependent permeability. Furthermore, the fact that $\kappa_{HOF} > \kappa_{HIF}$ can be justified by a significant retardation of the water transport past the graphene edges for the HIF on account of an enhanced water- hydrophilic-edge attraction. Figure 5.1 provides the schematic, Figures 5.8 and 5.9 provide the actual MD simulation snapshots. It should be noted that this steep nonlinear increase of the flux with the force for both types of functionalization is arrested for larger *F*. For such *F*, the flux effectively becomes constant and independent of *F*.

The total volume or the total number of the permeated water molecules is invariably larger for the HG with HOF, regardless of the force magnitude (see Figure 5.6). This occurs since the hydrophilic edges attract the water enforcing a retarded dewetting of water from the wetted graphene layers in HG with HIF. It is to be noted here that for a few values of forces less than 0.1 kcal/ (mol Å), we witness the value of *N* for the HG with HIF to be comparable or slightly larger than *N* for the HG with HOF. Of course, as has been elucidated later (see Figures 5.10−5.14), this trend where the total volume of permeated water is larger for the HG with HOF persists for other combinations of system parameters (*e.g.*, different values of *d* and δ and different numbers of graphene layers constituting the graphene stack).

5.3.2 Time-Dependent Water Trajectories through the HG Architecture.

Two mutually interconnected processes dictate the transport through the HGA: (a) vertical force imbibition (VFI) across the HGA and (b) wetting and dewetting across the graphene stacks at different levels (L_1– L_3, see Figure 5.8). Below we analyze this transport behavior for two different force values and attempt to explain the variation of flux and the permeated water volume as a function of the force (see Figures 5.5, 5.6) for different types of hole functionalization.

Transport for F = 0.03 kcal/(mol Å)

The simulation snapshots provided in Fig. 5.8 elucidate the drop dynamics for the cases of the HG with HIF and HOF, respectively (top panel: HG with HOF and bottom panel: HG with HIF). As the drop starts to penetrate the HGA, it contacts the graphene stacks at the uppermost level (level L_1) and starts to spread on the two laterally separated graphene stacks. This spreading dynamics is very similar for both the cases of HG with HIF and HG with HOF (see Figure 5.8 a-top,bottom) because only a very little fraction of the drop hits the functionalized edges during the onset of the spreading process. As a part of the water drop spreads, the rest of the drop undergoes the VFI across the graphene stack. Subsequently, this penetrating mass of water hits the center of the stack on the intermediate level (level L_2) and spreads on that stack identically for both the cases of HG with HIF and HG with HOF (see Figure 5.8a-top,bottom). Post this spreading, for HG with both types of functionalization, some water gets retained on this stack, whereas the rest

of the water penetrates further and hits and spreads on the two laterally separated stacks at the lowermost level or level L_3 (see Figure 5.8b-top,bottom). In the meantime, the spreading on the uppermost stacks (at level L_1) ceases and the dewetting starts. For the HG with HIF, a strong attraction between the water and the hydrophilic graphene edges retards the dewetting, thereby ensuring some water molecules fail to come out of the graphene stacks (compare Figure 5.8 b-top and 5.8 b-bottom). Such retarded dewetting driven retention of water molecules decreases the total volume of permeated water for the HG with HIF for F = 0.003 kcal/(mol Å) (see Figure 5.6). The water molecules that have wetted the stacks at the lowermost level (level L_3) overshoot the graphene layer and eventually leave the HG system. However, this overshooting enforces the water molecules to again come into contact with the functionalized graphene edges. The hydrophilic edge attracts the water molecules, which opposes the tendency of the water molecules to overshoot and leave the graphene stack. As a consequence, the time needed for the water molecules to come out of the HGA significantly increases for the HG with HIF. On the contrary, the HG with HOF does not impart such attraction, enforcing a much faster escape of the water molecules. This justifies the smaller flux for the HG with HIF for F = 0.003 kcal/(mol Å) (see Figure 5.5). The reduced flux ensures the presence of a much larger water within the HG with HIF (see the snapshots corresponding to t = 28 ps in Figure 5.8c and t = 60 ps in Figure 5.8d).

Transport for F = 0.0125 kcal/(mol Å)

Here, we consider drop dynamics for a much smaller force (F = 0.0125 kcal/(mol Å)) (see Figure 5.9). The simulations elucidate the drop dynamics for the cases of the HG with HIF and HOF. Very much similar to the case of F =0.03 kcal/(mol Å), here too we witness for both the cases of HG with HIF and HG with HOF (a) spreading and subsequent dewetting on graphene stacks in

level L_1, (b) VFI of the remaining water molecules to wet the graphene stacks at levels L_2 and L_3, and (c) escaping from the HGA following the wetting of the graphene stacks in level L_3. However, there are two key differences as compared to the case of F = 0.03 kcal/ (mol Å). For example, here the dewetting from the stacks in level L_1 is even more retarded for the HG with HIF leading to the retainment of a much large amount of water in the stacks. This stems from the fact that the force being lower, the dominant effects of capillarity is experienced even more pronouncedly leading to such an augmented hydrophilic- water-attraction mediated enhanced retention of water on graphene stacks in level L_1. The second difference is the manner in which the water exits the HGA. Firstly, the low applied force implies that the water molecules do not overshoot the graphene stack in level L_3. Consequently, the lowering of the velocity of the exiting water molecules for the HGA with HIF is witnessed as the water passes by the graphene edge (of the graphene stacks in level L_3) that is nearer to the wetted graphene stacks in level L_2. Most importantly, for the HGA with HOF the repulsion of the water molecules from the hydrophobic edges and the fact that the driving force remains small allows the water molecules to coalesce and exit the HGA as nearly a single mass of water. Of course, the gross behavior of augmented retention of water by the HG with HIF (and hence an increased value of permeated volume of water for the HG with HOF) and an augmented flux for the HG with HOF is witnessed here too.

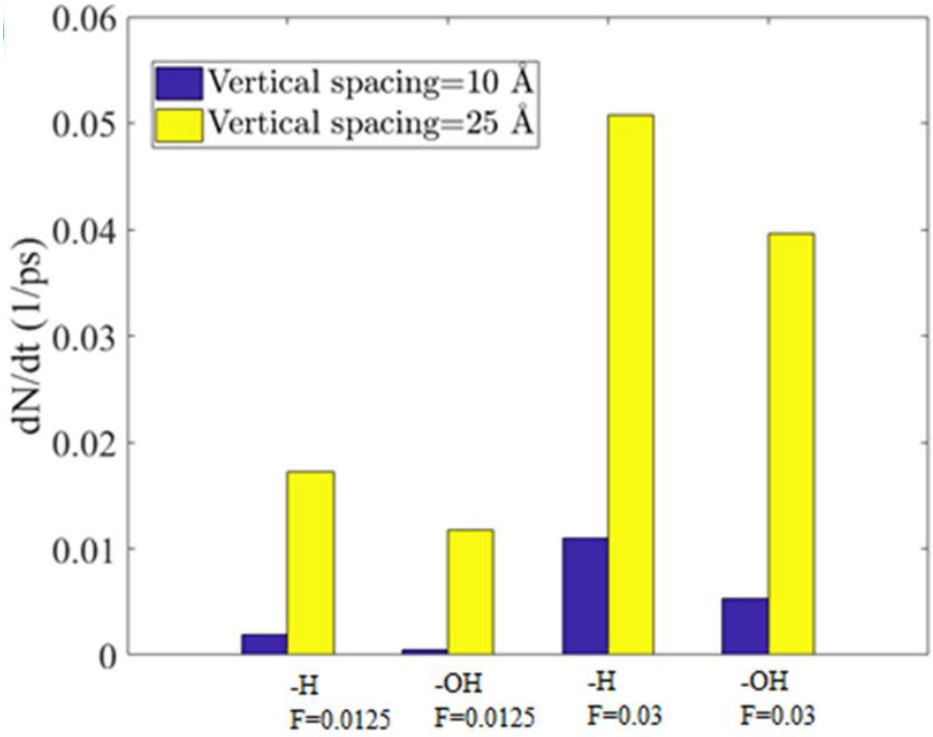

Figure 5.10. Variation of the flux for different values of the vertical spacing d (see Figure 5.8 for the definition) for two force levels (F = 0.03, 0.0125 kcal/(mol Å)) and for HG with both HOF and HIF. All other parameters are same as that in Figures 5.5−5.9.

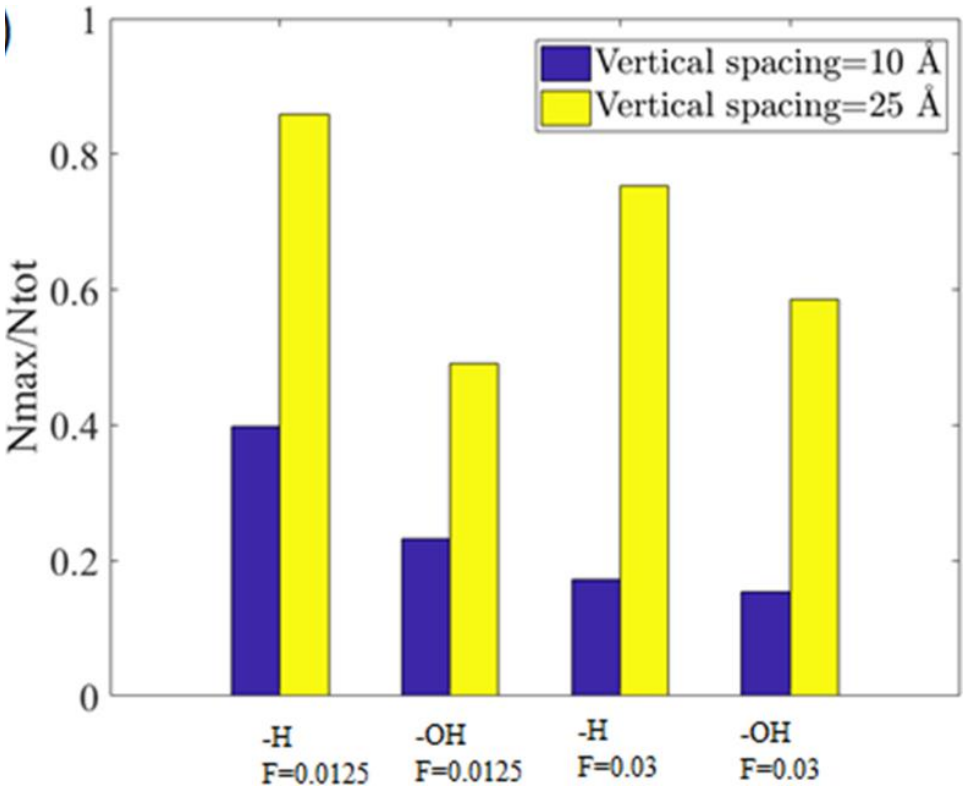

Figure 5.11 (a) Variation of the flux and (b) variation of N_{max}/N_{total} for different values of the vertical spacing d (see Figure 5.8 for the definition) for two force levels (F = 0.03, 0.0125 kcal/(mol Å)) and for HG with both HOF and HIF. All other parameters are same as that in Figures 5.5−5.9.

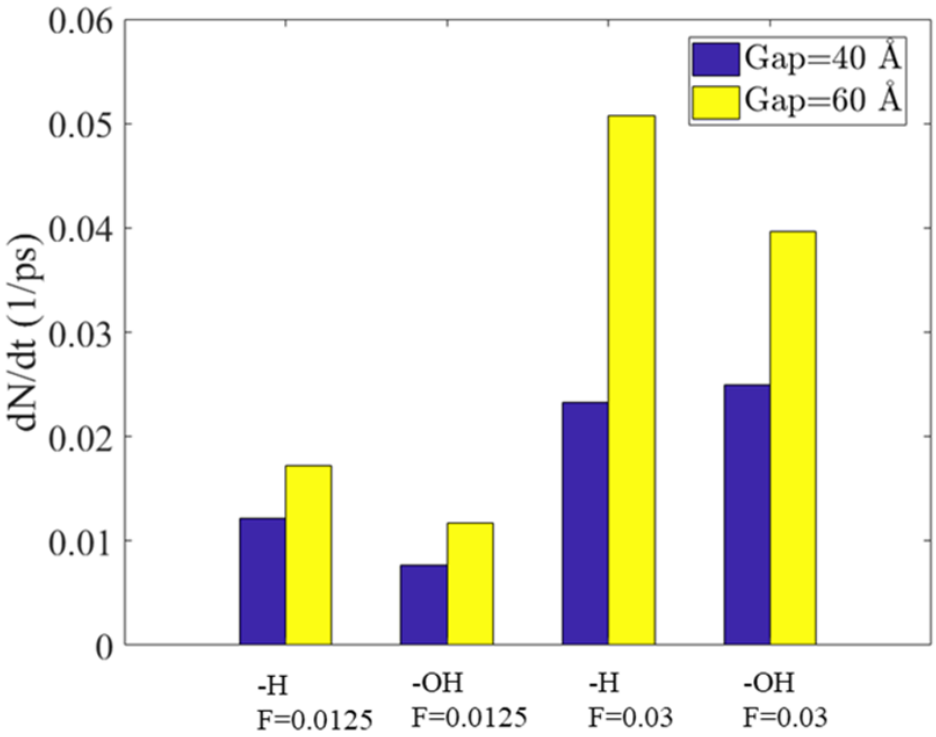

Figure 5.12 (a) Variation of the flux and (b) variation of N_{max}/N_{total} for different values of the hole dimension (which is also the horizontal gap δ between the graphene stacks, see Figure 5.8 for the definition of δ) for two force levels (F = 0.03, 0.0125 kcal/(mol Å)) and for HG with both HOF and HIF. All other parameters are same as that in Figures 5.5−5.9.

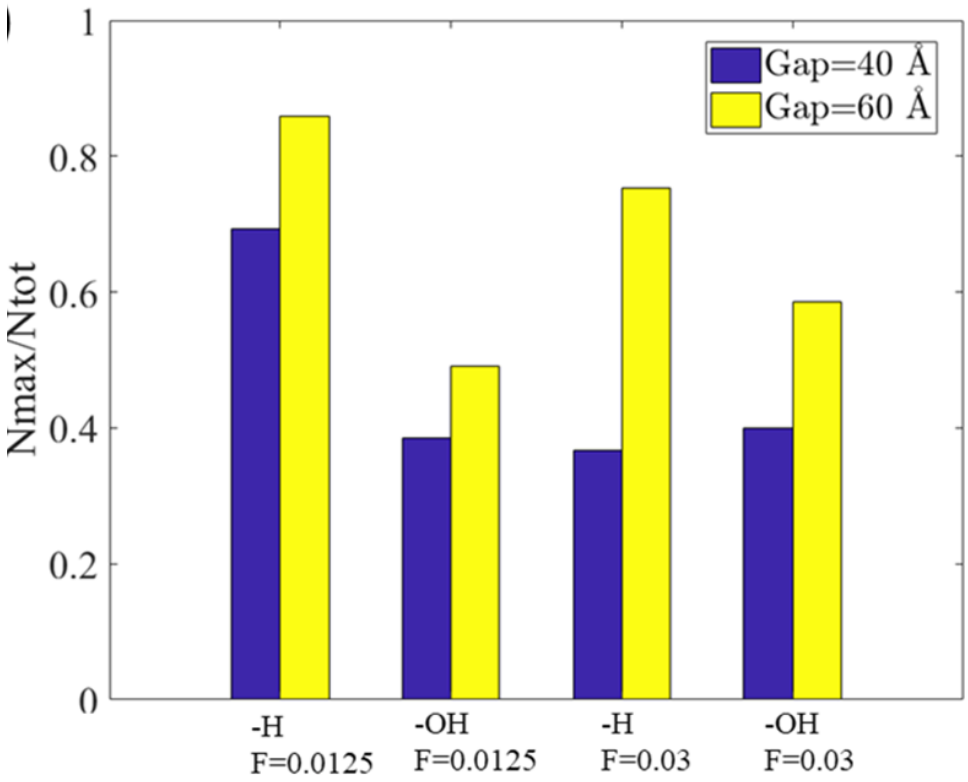

Figure 5.13 (a) Variation of the flux and (b) variation of N_{max}/N_{total} for different values of the hole dimension (which is also the horizontal gap δ between the graphene stacks, see Figure 5.8 for the definition of δ) for two force levels (F = 0.03, 0.0125 kcal/(mol Å)) and for HG with both HOF and HIF. All other parameters are same as that in Figures 5.5−5.9.

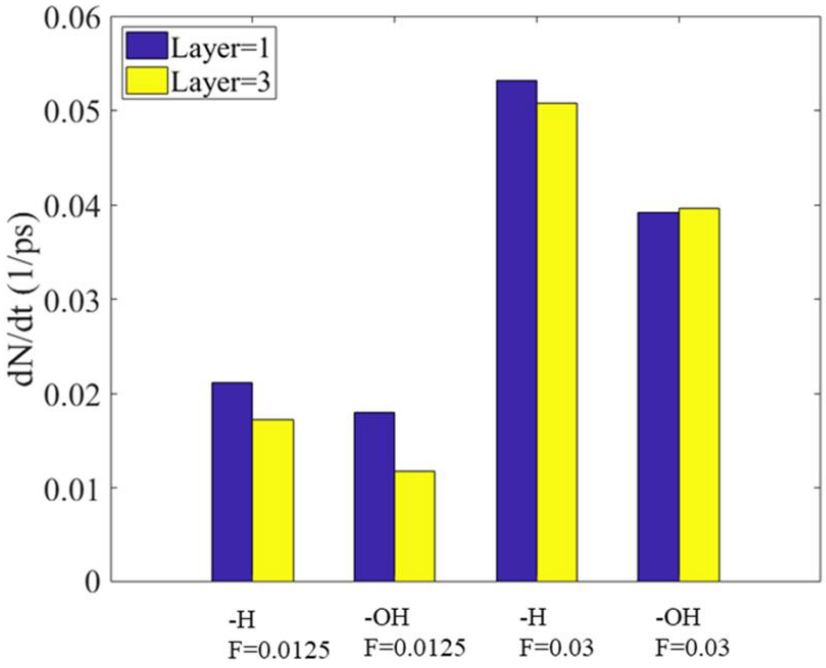

Figure 5.14 Variation of the flux for different number of graphene layers constituting each graphene stack for two force levels (F = 0.03, 0.0125 kcal/(mol Å)) and for HG with both HOF and HIF. All other parameters are same as that in Figures 5.5−5.9.

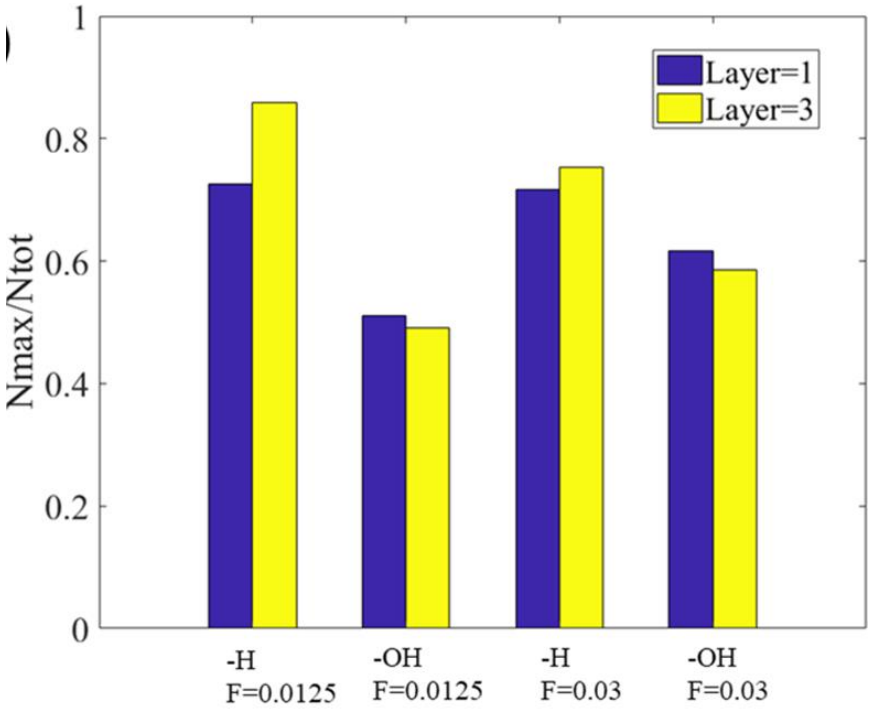

Figure 5.15 Variation of N_{max}/N_{total} for different number of graphene layers constituting each graphene stack for two force levels (F = 0.03, 0.0125 kcal/(mol Å)) and for HG with both HOF and HIF. All other parameters are same as that in Figures 5.5−5.9.

5.3.3 Effect of the System Parameters.

Effect of Variation of the Vertical Spacing d between the Graphene Stacks on the Drop Dynamics

We carry out separate simulations for a smaller vertical spacing d (between the graphene stacks, see Figure 5.8) of 10 Å and compare the results with those from our simulations with d = 25 Å (see Figure 5.5-5.9). We conduct simulations for two force levels (F = 0.03, 0.0125 kcal/(mol Å)) and for HG with both HOF and HIF.

We provide simulations showing the dynamics for both HOF and HIF for F = 0.03 kcal/(mol Å). The basic drop dynamics for both the force levels as well as both types of functionalization remain the same for this case as well. The drop follows the same pattern of interactions with the HGA: it first hits and spreads on the two top layers (stacks in level L_1, see Figure 5.8 for definition of L_1), then penetrates and hits the graphene stacks at level L_2 (see Figure 5.8 for definition of L_2), and finally hits and slides along the graphene stacks at level L_3. More importantly, for this value of d as well, the values of dN/dt and N_{max}/N_{total} are more for the HOF than HIF (see Figure 5.10). The most important issue, however, is that both these quantities get drastically reduced in comparison to the case of d = 25 Å (see Figures 5.10, 5.11). Significantly lower vertical separation between the graphene stacks would imply that the water drop prefers more lateral wetting and spreading than vertical forced imbibition leading to these significantly smaller values of dN/dt and N_{max}/N_{total}.

Effect of Variation of the Vertical Spacing d between the Hole Dimension δ on the Drop Dynamics

We carry out simulations for a different value of the hole dimension δ (see Figure 5.8 for the definition of δ), namely δ = 40 Å. Our previous simulations (Figures 5.5-5.8) were for δ = 60 Å. For this case as well, we consider two force levels (F = 0.03, 0.0125 kcal/(mol Å)) and HG with both HOF and HIF. In simulations, we show the corresponding dynamics for HG with HOF and HIF for F =0.03 kcal/(mol Å). Here too the basic drop dynamics, i.e., the manner, in which the drop wets the graphene stacks at the different levels (L_1–L_3), remain very similar to those for δ = 60 Å. The most important issue here is that the larger lateral proximity between the stacks (because δ is smaller) ensures that the water shows more enhanced wetting and spreading

tendency as compared to the case of δ = 60 Å (as evident in the simulations), and this is manifested in smaller values of dN/dt and N_{max}/N_{total} (see Figures 5.12,5.13). Of course, for this system as well dN/dt and N_{max}/N_{total} for the HG with the HOF is always more than the HG with the HIF.

Effect of Variation of the Number of Graphene Layers in Each Stack on the Drop Dynamics

The previous simulations (Figures 5.5-5.9) considered each graphene stack to consist of three graphene layers. Here, we repeat the simulations for the HG system where each graphene stack consists of only one graphene layer. Here too we consider two different forces (F = 0.03, 0.0125 kcal/(mol Å)) as well as HG with both HOF and HIF. We provide simulations elucidating the drop dynamics for the HG with HOF and HIF for F = 0.03 kcal/(mol Å). Here also, the drop dynamics is very similar to that for the case where each graphene stack consists of three graphene layers. More importantly, we do not see any noticeable trend in the drop- HG interactions that may affect the overall values of dN/dt and N_{max}/N_{total}. In fact, as revealed by Figures 5.14,5.15, there is hardly any difference between the cases with HG stacks of one and three graphene layers for a given force and given type of functionalization. Of course, here too we find that the HG with HOF shows distinctly larger values of dN/dt and N_{max}/ N_{total} as compared to the case of the HG with HIF.

5.3.4 Graphene Stacking Stability in an Aqueous Environment

As we mentioned in this chapter, one of the most important motivations to investigate the transport properties of graphene-based stockings is its application on seawater desalination.

Due to graphene's robust nature, graphene can possible sustain high pressure gradients. However, to the best of our knowledge, none of the previous work has carefully examined whether the graphene stacking structure is stable is water, i.e., Could the vertical interlayer distance of graphene stacking immersed in water be stable at a value that allow water to penetrate but reject ions (Fig. 5.16)? Without getting an answer to this issue, many reports simply fix or constrain carbon atoms to their initial locations. Here, we systematically investigate the stability of graphene stackings under various conditions.

Compared to the model using fixed carbon atoms, we employ the Dreiding force field to allow graphene to deform, and only the center of mass of graphene sheet is sampled during the simulations. The potential of mean force (PMF) curve using the interlayer distance as a reaction coordinate is mapped to reveal the stability of graphene stackings in an aqueous environment.

Fig 5.17 indicates that the two metastable states have very small energy barriers that are easily to be overcame by the thermal fluctuations, regardless the presence of pressure gradient or solutes. It is worthy to extend the dissuasions on the role pressure gradient plays in the stability. The hydrophobic effect between two graphene sheets is so strong that make water almost impossible to enter its interlayer spacing, or in the other words, the recombination of two free-standing graphene sheets in water is inevitable. But how would pressure change the game? As a pressure gradient is added to the system, water molecules are constantly pushed through the membrane, however, due to the finite maximum flux limit, a graphene stacking would respond to the exceed water flux by spontaneously wider the interlayer spacing. Would this factor be large enough to overcome the energy barrier to separate the recombined graphene sheets? The PMF shows that instead of opening the interlayer spacing, the pressure gradient helps the graphene

sheets recombine as the pressure increase the probability to bring these two sheets close enough to recombine. Therefore, pristine graphene stacking is not able to form stacking in water with a interlayer distance larger than 0.33 nm, half of the lattice constant along stacking direction.

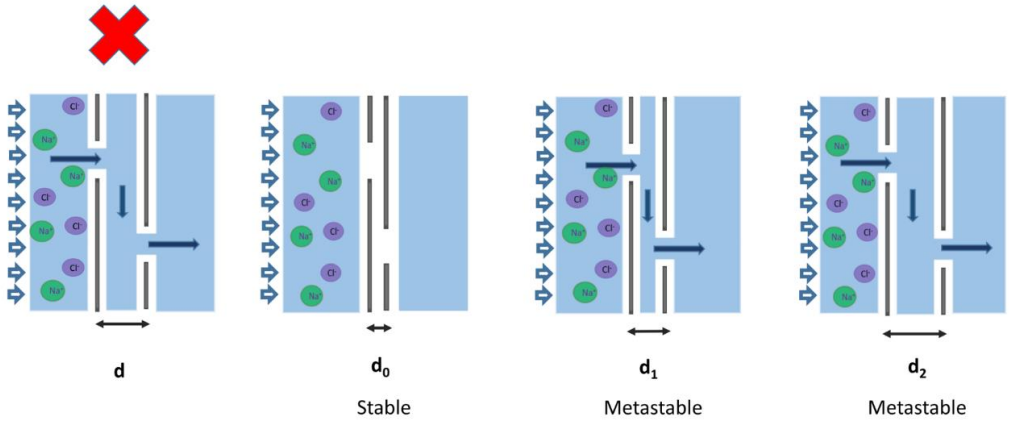

Figure 5.16 (a) the interlayer distance *d* is arbitrarily chosen in previous research. (b) the graphene stacking is most stable without accommodating any water molecules. (c-d) graphene stackings reach metastable states when there are one-layer or two-layers water in between graphene sheets.

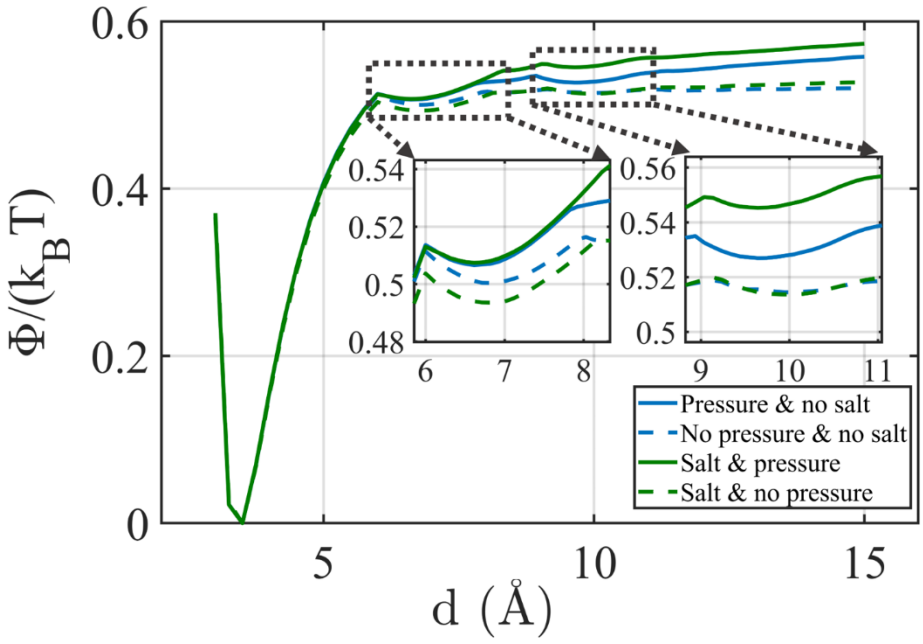

Figure 5.17. Normalized PMF(Φ) curve of graphene stacking using the interlayer distance *d* as a reaction coordinate, in four different environments: pure water without pressure gradient, ionic solution without pressure gradient, pure water with pressure gradient, and ionic solution with pressure gradients.

5.4 Conclusions

In this paper, we unravel that the force-driven dynamics of a water nanodrop through a HG matrix, characterized by parameters, such as the nature of functionalization of the edges of the HG and the dimensions of the holes and the vertical spacing separating the different graphene stacks, depend on the intricate interplay of the capillary effects and the impact of the driving force. For significantly lower forces, it is possible to attempt a Darcy law-like description of the water transport only to witness that the flux varies nonlinearly with the employed forcing with the extent of nonlinearity being much more severe in HG with HOF. The HG with the HOF also demonstrates a larger value of the total permeated water volume and we ascribe both these enhanced flux and enhanced permeation to the repulsive interactions between the hydrophobic edges and the water molecules. We also carry out an extended parametric analysis of the problem

and witness that this tendency of the HG with HOF to enhance the flux and the permeated water volume remain intact.

At the end, it is worthwhile to briefly discuss the connection of the present study to a more extensively studied problem of water transport through graphene oxide (GO) or reduced graphene oxide (rGO) laminate films.[148,154,155] These films are in the form of submicron thick membranes, and the graphene stacks/flakes are often separated by as small a gap as $d = 4$ Å (please see Figure 5.1c of ref 155 for the schematic). On the other hand, the lateral dimension (L) of the graphene flakes can be hundreds of nanometers making $L/d \sim 1000$. Under such circumstances, the laminate graphene membrane has a significantly larger tortuosity than the HG architecture that we consider here, enforcing the water molecules in such laminate films to undergo a much larger traversal distance inside the laminate membrane as compared to the case of HG. Therefore, the experimentally motivated[94,96] HG structure that we consider is significantly different from that of the graphene laminate membrane and therefore deserves to be investigated in terms of its properties in permeating water despite the significant number of earlier efforts in the investigation of water transport phenomena in a GO/rGO laminate structure.

In addition, we carefully investigate the stability of graphene sheets in aqueous environments, with or without the presence of pressure gradient or solutes by mapping the PMF curve using the interlayer distance as the reaction coordinate. The four PMF (free energy) shows very similar trend, which the graphite state (d=0.33nm) is the most stable phase and one-layer and two-layer water states are metastable. Moreover, the system strongly prefers the graphite state without a large enough barrier to separate the two metastable states from the stable graphite state. The results suggest that the pristine graphene stacking with any separation other than 0.33nm is

intrinsically energetically unfavorable and get little influence from other factors like the presence of ions and pressure.

Chapter 6: Water−Holey-Graphene Interactions: Route to Highly Enhanced Water-Accessible Graphene Surface Area

6.1 Introduction

Nanoporous graphene represents a particular type of structurally defective graphene.[133,156,157] These defects, appearing in the form of pores or holes, are a type of point defect. When many lattice atoms are removed from a small area on a layer of a graphene, the formation of such holes (with often unsaturated bonds) is preferred over the corresponding reconstruction that may necessitate bending or warping of the layer. These holes are characterized by unsaturation at the edges, which get saturated by hydrophobic or hydrophilic functionalization.[158] There has been massive interest in understanding the physics, chemistry, and material science of nanoporous graphene owing to its extensive use in a large number of applications such as desalination,[15,24,104,138,139,158–160] dialysis,[159] water−ethanol separation,[143,161] DNA sequencing,[158,161] oxygen reduction,[162,163] selective molecular and ion sieving,[13,17,164–167] fabrication of supercapacitors[168] and fuel cells,[169] and many more. Holey-graphene (HG) is an interesting variant of the nanoporous graphene, where unlike the typical case of single or few layers of nanoporous graphene, one witnesses a periodically spaced (having a spacing of one to several nanometers, *i.e.*, much larger than the typical graphene interlayer distances) graphene stack, where each stack consists of a single or a few layers of nanoporous graphene.[94–101,149,170–175] HG is a relatively recent discovery that has kindled the imagination of material scientists and chemists alike providing most notably a mechanism to significantly enhance the ion-accessible surface area of graphene. Such a capability of HG has been extensively used for applications such as fabrication of ultracapacitors and supercapacitors,[96,98–100,114,175] ultrahigh-rate energy

storage,[149] promoting chemical reactions[101,170,171] and atomic adosprtion,[172] improving the functioning of Li-ion batteries,[173,174] *etc*.

The significant number of investigations employing atomistic simulations to probe the interaction of water with a single or a few layers of nanoporous graphene have invariably considered a "bulk" mass of water (in the form of a cube or a rectangular parallelepiped) and neglected any detailed wetting or capillary interactions between water and nanoporous graphene.[15,24,104,138] On the other hand, the very structure of HG (see Figure 6.1) necessitates consideration of a framework that appropriately accounts for the water−graphene wetting interactions stemming from the apparently unavoidable role of the three phase contact line in dictating the water−HG interactions. Therefore, unlike the previous MD simulation studies, in the present study, we consider the interaction between an appropriately equilibrated water drop and the HG architecture (or HGA). In a recent study,[176] we have employed MD simulations to probe the *imbibition behavior of a water nanodrop in an HGA in the absence of any externally imposed force on the drop.* Our simulation setup considered HG dimensions predicted by the experiments.[96,108,113] Our results in that paper,[176] in addition to pinpointing different novel spreading and wetting states, also pointed to the development of a fiberlike wetting state where the drop wetted multiple surfaces of the HGA, eventually ensuring a wetting area ratio $r_{w,HG}/r_{w,G} > 1$ (where $r_{w,HG}$ is the graphene−water wetted area for the HGA and $r_{w,G}$ is the equilibrium graphene−water wetted area for the a water drop resting on a nonporous graphene substrate).

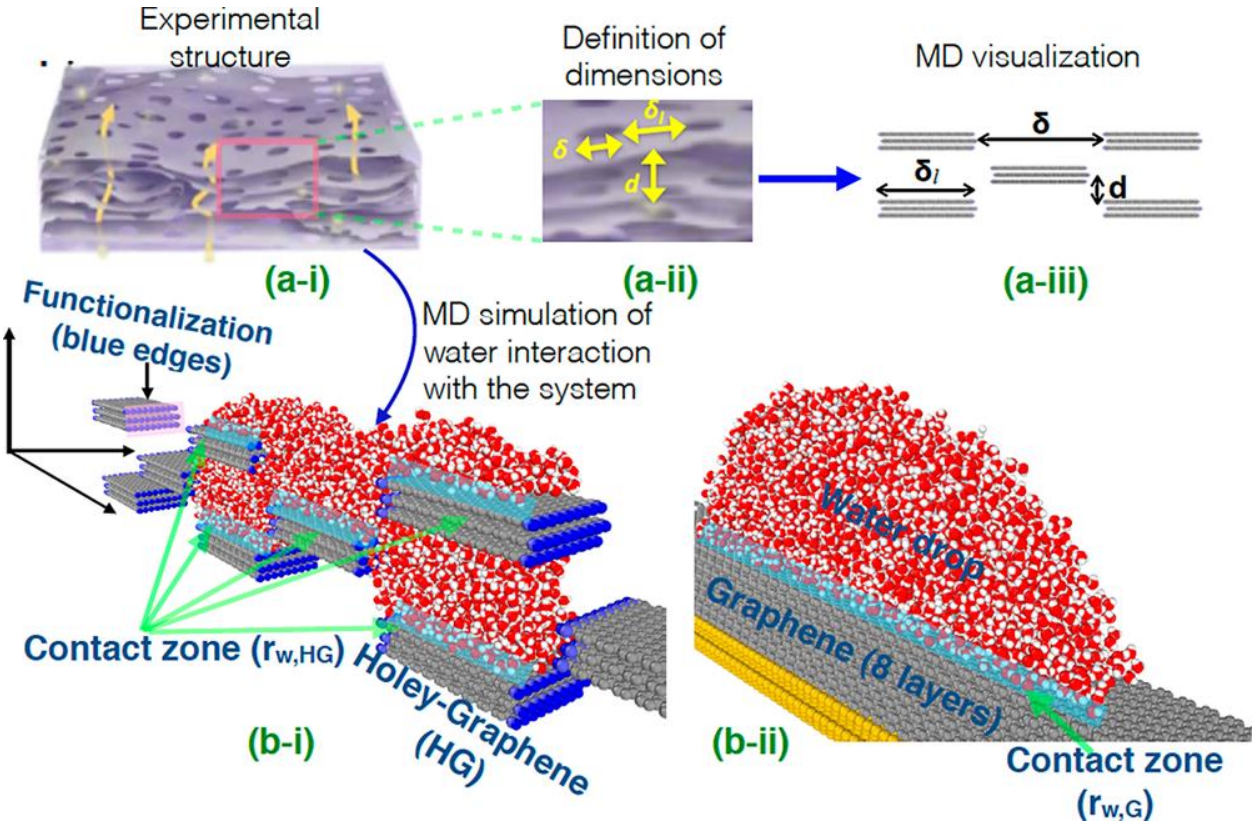

Figure 6.1. (a-i) Schematic of the actual experimentally fabricated holey-graphene architecture (Reprinted with permission from ref 98. Copyright © 2014 Nature Publishing Group.). The yellow arrows in the picture represent the direction of ion transport through the HG (see ref 66). (a-ii) Magnified section of this HG system that we attempt to simulate. (a-iii) Schematic representation of our simulation geometry trying to represent the magnified section in a-ii in a two-dimensional setting. (Reprinted with permission from ref 181. Copyright © 2017 PCCP Owner Societies). The HG is characterized by the dimensions δ (lateral separation between graphene stacks), δl (horizontal span of the graphene stack), and d (vertical separation between graphene stacks) [kindly compare a-ii and a-iii]. (b-i) Schematic of the generation of wetting states that ensure enhanced water-accessible graphene surface area by the interaction between water and HG. This enhanced water−graphene surface area is represented by the contact area ($r_{w,HG}$) over which water and HG surfaces interact and is compared (see b-ii) with respect to the contact area ($r_{w,G}$) of water on nonporous graphene. $r_{w,G}$ is the contact area achieved when a water nanodrop spreads on nonporous graphene. Given that the nonporous graphene is impenetrable, $r_{w,G}$ remains unchanged regardless of whether the drop interacts with the nonporous surface in the presence or absence of a force as long as the drop does not break down into smaller parts. For the HG, the edges of the graphene holes are colored in order to represent the presence of the functional groups (either−OH or −H) that saturate the unsaturation at the holes. For the nonporous graphene, we choose eight layers of graphene as the substrate, which ensures that it behaves as graphite and there is no chance of any change in the contact area due to the wetting translucency effect of graphene.[5,69,176–179]

In the present study, we first modify the architecture of our previous study by accounting for

−OH (*i.e.*, hydrophilic functionalization or HIF) and −H (i.e., hydrophobic functionalization or

HOF) termination of the edges of the graphene holes. Of course, very much like the previous paper, we consider a 2D representation of the system so that the water drop is represented as a cylindrical slab, while the HGA is represented as a system of periodic graphene stacks with vertical and lateral separations. Most importantly, in this study, we subject the water drop to a finite force (F) that drives it deep inside the HGA. The current problem is motivated to study a variant of the problem of force-driven interaction of water with nanoporous graphene membrane[17,104,138,139,158,167] with a finite contribution of capillary effects therefore, the origin of this force that drives the water−HG interaction is the same as that in water−nanoporous-graphene-membrane interactions, namely the suction pressure.[17,104,138,139,158,167] In the present case, this force F is applied for a time t that is less than the minimum time ($t_{F,0}$) needed to drive any amount of water out of the HGA. Our results demonstrate that the interplay of F and t, the dimensions of the HG matrix, and the nature of the surface functionalization lead to hitherto unknown combined capillarity and force driven imbibition dynamics of the water drop in the HGA leading to the generation of a plethora of novel transient and equilibrium wetting states. These different wetting states, apart from shedding light on the rich physics associated with the water−HG wetting interactions, are specially significant as they ensure an enhanced water-HG (or nanostructured graphene in general), namely the generation of extremely enhanced (often more than two times as compared to a nonporous graphene) water−graphene surface areas. Porous graphene has been known to provide a platform for water filtration and water desalination; in this paper, for the first time we have established that the porous graphene can be equally important for providing a highly stable and highly enhanced water−graphene surface area. Of course, a plethora of other methods attempting to enhance the water−graphene contact area have been attempted (see the Discussions section);

however, given the relative ease of ensuring a highly enhanced graphene−water surface area by simply adjusting the magnitude and the duration of the force with which water is made to interact with the HG (post the fabrication of HG), the present study signifies a much more facile mechanism of enhancing water−graphene surface area. This is the biggest novelty of the present paper in comparison to our previous study.[176] Such an enhancement in water− graphene surface area will be beneficial for applications involving larger graphene−water surface area such as graphene-based ultracapacitors,[97,180] graphene-based compact heat excahngers,[115] graphene-based techniques for water freezing with minimal subcooling,[116] etc. In fact, toward the end of the paper, we establish that this area enhancement would be equally true for an HG matrix with dimensions that exactly match the experimental results making our work appealing to the larger experimental community as well.

6.2 Molecular Dynamics Simulations

Here we discuss the key findings of the MD simulations of a well-equilibrated water nanodrop interacting with the HGA. We consider a 2D representation of the problem: as a consequence, the water drop is a cylindrical one while the HG is represented as stacks of graphene layers with specified vertical and lateral inter stack separations (ISSs). The vertical ISSs represent the vertical distance between the different stacks of graphene, while the lateral ISSs represent the dimensions of the graphene holes.

We have used the large-scale atomic/molecular massively parallel simulator (LAMMPS) package to simulate the 2D water nanodrop trajectories. For simulating the water drop, we use the TIP4P model. The holey graphene architecture (HGA) is made up of graphene stacks; where each

individual graphene stack consists of three layers of graphene. The graphene stacks have a specific vertical and lateral arrangement with proper functionalization (hydrogen and hydroxyl) present at its edges. Simulations have been carried out by varying a wide range of parameters, and we performed the post processing to find out various parameters dictating the water−HG interactions. Further details about the geometry, simulation, and post processing are provided.

6.2.1 System Description

The nanoporous graphene matrix is modeled in a 2D geometry to eliminate the tremendous line tension effect existing in any 3D nano-scale drop system.[181–183] Accordingly, the dimensions of the simulation box are set as 450, 20 and 500 Å in the X, Y and Z axis directions respectively. Each graphene stack consists of 3 layers of graphene assembled along Z axis direction, representing the graphene sheets left in between two neighboring pores. The lateral length of the stacks is set as approximately 40 Å and 60 Å, and the stacks end with a zigzag shape at both ends in X axis direction. Each carbon atom of stack edge is terminated by a Hydrogen atom or a Hydroxyl group. The horizontal gap between two stacks in the same X-Y plane stands for the diameter of the pores, and it is set as 60 Å. Two layers of graphene stacks are separated by a distance of 10 Å and 25 Å in the vertical direction, following the most current experimental result.[151,184] The detailed configurations of the HG matrix are shown in Figure 6.2.

6.2.2 Simulation Model

The system consists of 3000 TIP4P water and this water model is considered to be an appropriate approach to include the dipole-dipole interactions between water atoms and the partial charged terminations.[15] The non-bonded interaction between two atoms is described by the Lennard–Jones (LJ) 12-6 potential and the columbic interaction. The system temperature is controlled by applying a Nosé-Hoover thermostat to the water drop and set the carbon atoms fixed. All simulations are performed using Large-scale Atomic/Molecular Massively Parallel Simulator (LAMMPS) software package. The force field parameters used in this article are summarized here in Table 6.1. The water drop is made to move through the holey graphene matrix by employing a finite body force F to all the water molecules. The force is always applied only in the negative z direction (see Fig. 6.2 for the axes), i.e. in the direction perpendicular to the HG matrix. Of course, the constant force *F* is always present on the water molecules until the time when the force is switched off. At that point when the force is switched off, none of the water molecules are subjected to this force anymore. No external force is ever applied to the carbon atoms and other functional groups attached to the carbon atoms. This also implies that the HG matrix remain fixed in position during the entire simulation.

For a given set of parameters (i.e., a given set of d, δ, and δ_l values, given type of functionalization and given value of the applied forcing), we have played around with different values of the total time (Δt) for which the force has been applied. In the process, we have identified the corresponding critical value Δt_c; one witnesses the most enhanced value of the $r_{w,HG}/r_{w,G}$ ratios (both in terms of the temporal maximum as well as the equilibrium) when the force is applied for Δt_c. Typically, we find that this Δt_c is slightly larger than the time at which the wetting effect is maximum. All the results for a given set of parameters are provided for the case when the force is removed at $t=\Delta t_c$.

Obviously, depending on the combination of the parameters (e.g., HG dimensions, nature of hole functionalization, strength of the applied force), Δt_c varies. As we provide results for different combinations of the system parameters, the corresponding Δt_c also varies.

Such a simulation set up where force has been employed to all the water molecules have been extensively investigated before.[185–1877-9] There are also examples where liquid motion (or imbibition) has been studied by applying a pressure.[18810] However, such a set-up is applicable when one considers the imbibition of a slab of water.[18810] Consideration of a slab of water allows demarcating a well-defined boundary in contact with the water slab. Under such circumstances, a force can be applied to this boundary that translates into a pressure that drives the water slab. On the other hand, for a water drop one cannot define such well-identified boundary. Therefore, as has been done by Ref. 185, the force-driven transport of a water drop would necessitate the employment of a constant force on all the water molecules of the drop.

In this context, it is also important to point out a critical difference between our force model and that of Ref. 185. Both our model and Ref. 185 consider the triangular SPC/E water model. However, Ref. 185 applies force only to the oxygen atom, while we apply force to the oxygen as well as the hydrogen atoms. Such a step ensures that we eliminate the undesired *tumbling motion* of the water molecules that occurs when force is applied only to the oxygen atom of the SPC/E water molecule. This situation is represented in Fig. 6.3.

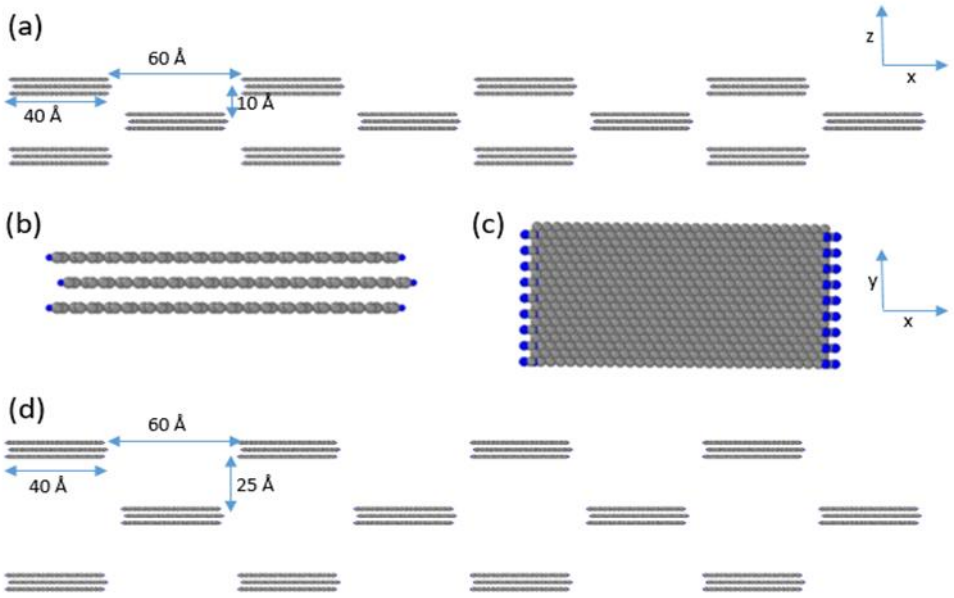

Figure 6.2 (a) Side view of the holey graphene matrix with hydrogen terminations and vertical gap 10 Å. Magnified (b) side and (c) top view of a representative of holey graphene sheets in between the two holes. (d) Side view of the holey graphene matrix with hydrogen terminations and vertical gap 25 Å.

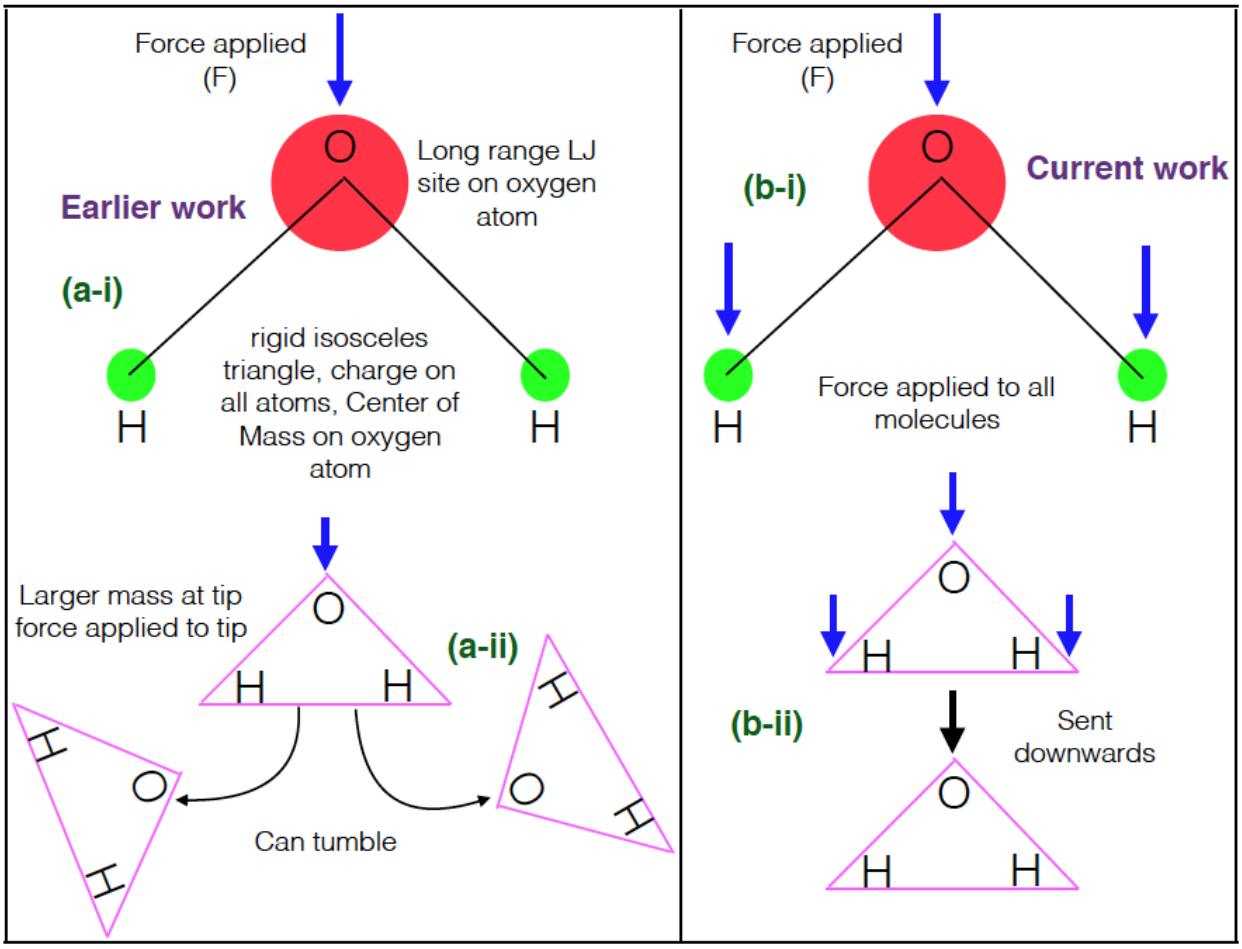

Figure 6.3 Comparison of the force model of the earlier work (Ref. 185) shown in (a) with our force model shown in (b). In Ref. 185, the force is applied only to the oxygen atom [see (a-i)], which would lead to a possible tumbling motion of the SPC/E water molecule [see (a-ii)]. On the other hand, in our model we employ the force on both the oxygen atom and the two hydrogen atoms [see (b-i)] ensuring that this tumbling motion has been arrested [as illustrated by comparing (a-ii) and (b-ii)].

Table 6.1 LJ and charge parameters used in the simulations

Elements	ε (kcal/mol)	σ (Å)	q
O_w	0.163	3.164	-1.048
H_w	0	0	0.524
C_{CH}	0.046	2.985	-0.115
H_{CH}	0.030	2.42	0.115
$C_{(sp2)}$	0.086	3.399	0
C_{COH}	0.070	3.55	0.2
H_{COH}	0	0	0.44
O_{COH}	0.155	3.07	-0.64

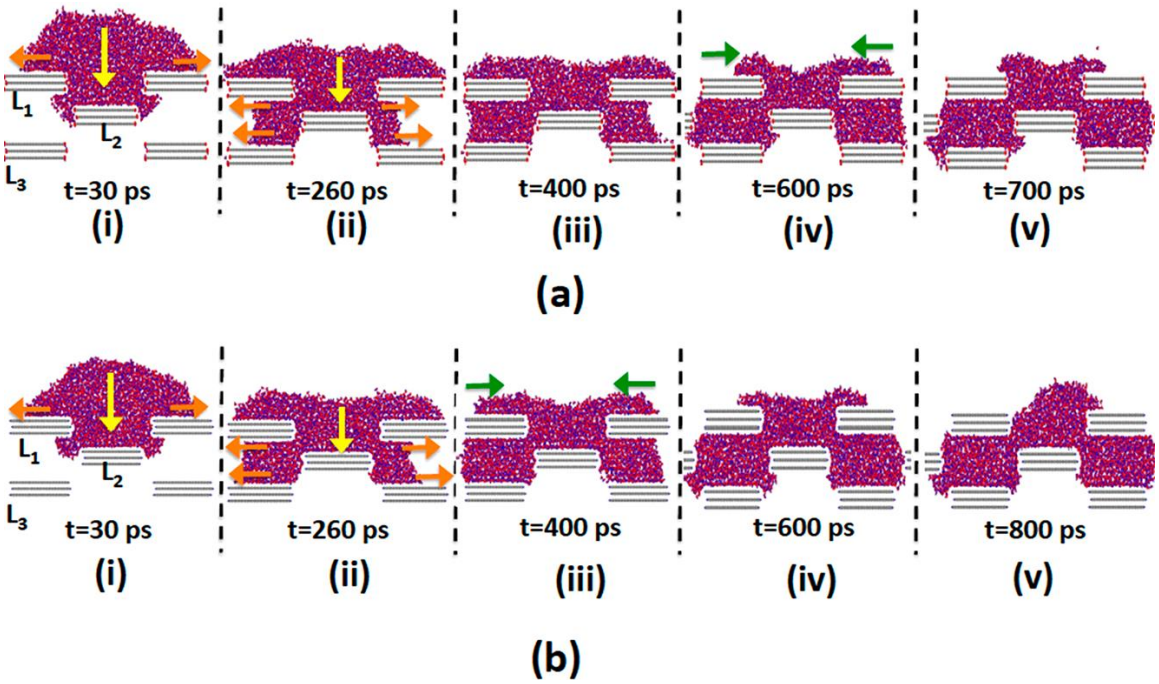

Figure 6.4 Snapshots elucidating the dynamics of the water nanodrop interacting with the HGA for −OH functionalization. In both a and b, i−v provides the snapshots corresponding to different times. Below each of these snapshots, the corresponding time is also noted. For both cases a and b, d = 1 nm, δ = 6 nm, and δ_1 = 4 nm, and we consider that a force of F = 0.005 kcal/mol·A is applied for t =600 ps.

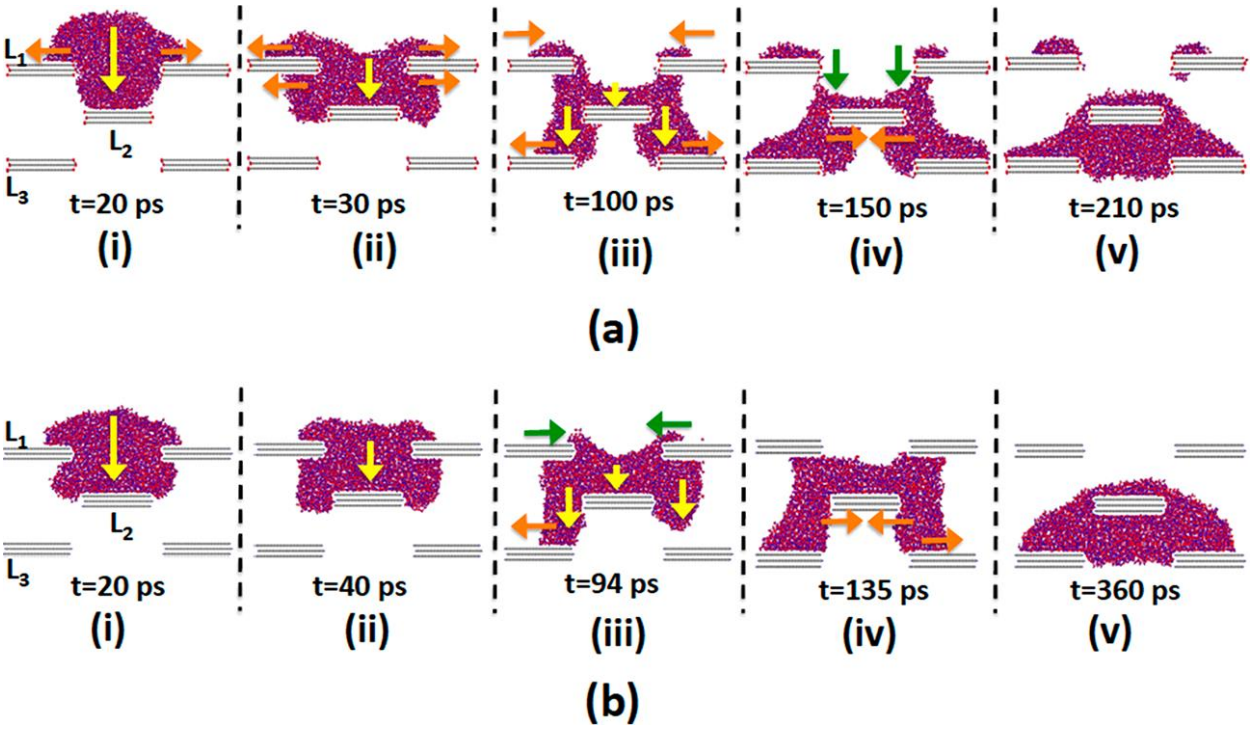

Figure 6.5 Snapshots elucidating the dynamics of the water nanodrop interacting with the HGA for −H functionalization. In both a and b, i−v provides the snapshots corresponding to different times. Below each of these snapshots, the corresponding time is also noted. For both a and b, d = 2.5 nm, δ = 6 nm, and δ_l = 4 nm, and we consider that a force of F = 0.005 kcal/mol·A is applied for t =200 ps for the case with HIF and for t = 300 ps for the case with HOF.

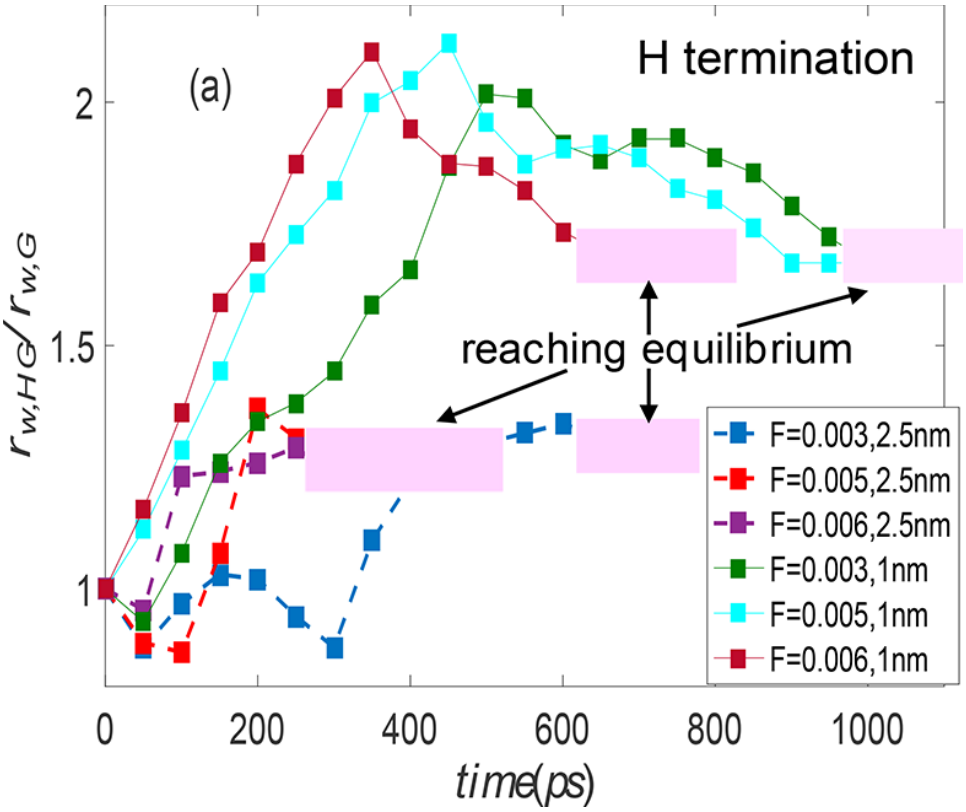

Figure 6.6 Variation of the $r_{w,HG}/r_{w,G}$ with time for different values of d and F for −H functionalization of the graphene holes. For a given d−F combination, the force is applied for a time t which ensures maximum value of $(r_{w,HG}/r_{w,G})_{transient}$ (for a given t) as well as maximum $(r_{w,HG}/r_{w,G})_{equilibrium}$. This value of t is summarized below (with F in kcal/mol·A): $(t)_{d=1nm,F=0.003,OH}$ = 700 ps, $(t)_{d=1nm,F=0.003,H}$ =700 ps, $(t)_{d=2.5nm,F=0.003,OH}$ = 450 ps, $(t)_{d=2.5nm,F=0.003,H}$ = 800 ps, $(t)_{d=1nm,F=0.005,OH}$ = 600 ps, $(t)_{d=1nm,F=0.005,H}$ = 600 ps, $(t)_{d=2.5nm,F=0.005,OH}$ = 200 ps, $(t)_{d=2.5nm,F=0.005,H}$ = 300 ps, $(t)_{d=1nm,F=0.006,OH}$ = 350 ps, $(t)_{d=1nm,F=0.006,H}$ = 350 ps, $(t)_{d=2.5nm,F=0.006,OH}$ = 200 ps, $(t)_{d=2.5nm,F=0.006,H}$ = 200 ps. Other dimensions are same as those in Figures 6.4 and 6.5. The transient wetting is characterized by the transient variation of $r_{w,HG}/r_{w,G}$; in other words, the duration of the transient wetting process is the period of time for which $r_{w,HG}/r_{w,G}$ varies with time before attaining equilibrium.

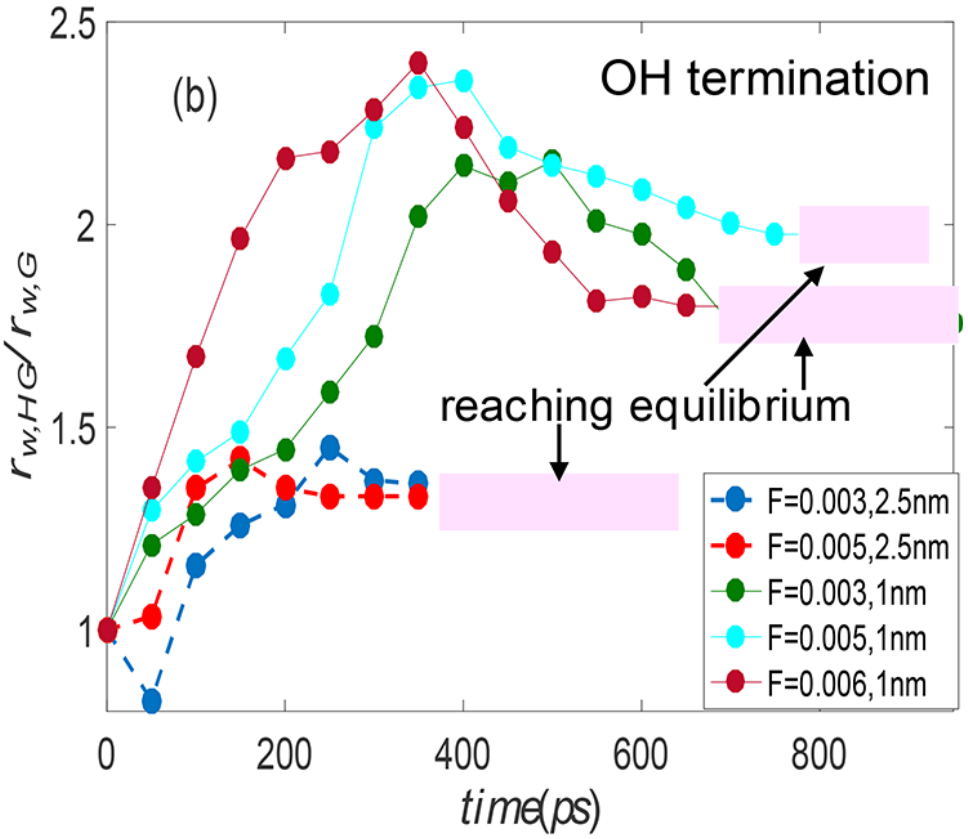

Figure 6.7 Variation of the $r_{w,HG}/r_{w,G}$ with time for different values of d and F for −OH functionalization of the graphene holes. For a given d–F combination, the force is applied for a time t which ensures maximum value of $(r_{w,HG}/r_{w,G})_{transient}$ (for a given t) as well as maximum $(r_{w,HG}/r_{w,G})_{equilibrium}$. This value of t is summarized below (with F in kcal/mol·A): $(t)_{d=1nm,F=0.003,OH}$ = 700 ps, $(t)_{d=1nm,F=0.003,H}$ =700 ps, $(t)_{d=2.5nm,F=0.003,OH}$ = 450 ps, $(t)_{d=2.5nm,F=0.003,H}$ = 800 ps, $(t)_{d=1nm,F=0.005,OH}$ = 600 ps, $(t)_{d=1nm,F=0.005,H}$ = 600 ps, $(t)_{d=2.5nm,F=0.005,OH}$ = 200 ps, $(t)_{d=2.5nm,F=0.005,H}$ = 300 ps, $(t)_{d=1nm,F=0.006,OH}$ = 350 ps, $(t)_{d=1nm,F=0.006,H}$ = 350 ps, $(t)_{d=2.5nm,F=0.006,OH}$ = 200 ps, $(t)_{d=2.5nm,F=0.006,H}$ = 200 ps. Other dimensions are same as those in Figures 6.4 and 6.5. The transient wetting is characterized by the transient variation of $r_{w,HG}/r_{w,G}$; in other words, the duration of the transient wetting process is the period of time for which $r_{w,HG}/r_{w,G}$ varies with time before attaining equilibrium.

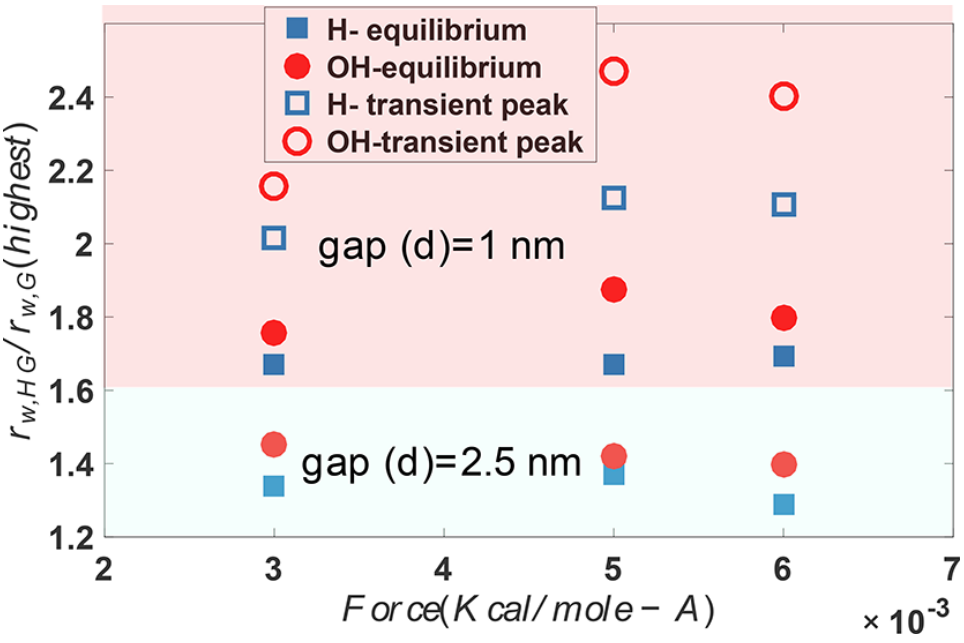

Figure 6.8 Summary of the $(r_{w,HG}/r_{w,G})_{transient,peak}$ [i.e., the maximum value of $(r_{w,HG}/r_{w,G})_{transient}$] and $(r_{w,HG}/r_{w,G})_{equilibrium}$ values for different combinations of d, F (expressed in kcal/mol·A), and hole functionalization. For a given d–F combination, the force is applied for a time t which ensures maximum value of $(r_{w,HG}/r_{w,G})_{transient,peak}$ (for a given t) as well as maximum $(r_{w,HG}/r_{w,G})$equilibrium. We provide $(r_{w,HG}/r_{w,G})_{transient,peak}$ only for d = 1 nm since we do not witness any significant peak in the $(r_{w,HG}/r_{w,G})_{transient,peak}$ variation for d = 2.5 nm (see Figure 6.6-6.7). Other dimensions are same as those in Figures 6.4 and 6.5.

6.3 Results

The drop dynamics on the HG matrix with different dimensions and functionalization are elucidated in Figure 6.4 and 6.5. Figure 6.4a shows the dynamics of the water nanodrop interacting with the HGA with −OH functionalization. We consider d = 1 nm. Hence the vertically separated graphene stacks are significantly closer to one another. Therefore, the drop, immediately after contacting the graphene stacks in level L_1, undergoes a spreading on the laterally separated stacks in level L_1 [shown by the orange arrows on graphene stacks in level L_1; see Figure 6.4a,i] and encounter a downward motion [shown by the yellow arrow; see Figure 6.4a,i] that wets the upper surface of the graphene stack in level L_2. As the drop (or all the molecules constituting the water drop) is under the applied force until 600 ps, this vertically downward translation of the drop continues, and the drop simultaneously spreads on the bottom part of the graphene stacks in level L_1 and (b) the upper part of the graphene stacks in level L_3 (see Figure 6.4a,ii]. This spreading is shown by orange arrows in Figure 6.4a,ii. Two events are responsible for such a spreading behavior. First, the height of the puddle-like portion of the drop on the top of the graphene stacks in levels L_1 decreases in the presence of the applied force. Second, the water that is released as a result [shown by a yellow arrow in Figure 6.4a,ii] wets and spreads on the bottom of the graphene stacks in levels L_1 and top of the graphene stacks in level L_3. Therefore, Figure 6.4a,ii shows how the water simultaneously wets as many as seven horizontal surfaces. In fact this wetting progresses and reaches a maximum around 400 ps (see Figure 6.4a,iii). This dynamic wetting state (at t ~400 ps) is the one that corresponds to the maximum value of $(r_{W,HG}/r_W)_{transient}$ (see Figure 6.7). The force is continued to be applied even after t = 400 ps, and as a consequence, gradually after t = 400 ps, there is dewetting (shown by green arrows) from the top surface of the graphene stacks at level L_1 (see Figure 6.4a,iv). These

additional water molecules leaving the graphene stacks at level L_1 due to dewetting do not wet any new stack; rather they accumulate in the space between the different vertically separated stacks. As a consequence, there is a gradual decrease in the wetted area (see Figure 6.7) for $t >$ 400 ps. The force is removed at t = 600 ps; hence very soon after that the water drop attains an equilibrium configuration (see Figure 6.4a,v), as also indicated by the attainment of an equilibrium of the ratio ($r_{w,HG}/r_{w,G}$) (see Figure 6.7).

Figure 6.4b shows the dynamics of the water drop interacting with the HG matrix (with d = 1 nm) with HOF of its holes. The major part of the dynamics (e.g., force driven simultaneous spreading on as many as seven horizontal surfaces, a gradual decrease in the height of the puddle accumulated on the top of the graphene stacks in levels L_1, attaining a maximum extent of spreading at $t \sim 400$ ps, etc.) remains very similar to that for the case of HIF (see Figure 6.4a). The only main difference between the cases of HG with the HOF and the HIF is the manner in which the enhanced attraction between the HIF and water reduces dewetting (as discussed above), which is not witnessed for the case of HG with the HOF. As a result, the dewetting on the graphene stacks in level L_1 starts much earlier for the HG with HOF. Therefore, at $t \sim 400$ ps, i.e., at a time when the wetting of the bottom of the graphene stacks in level L_1 and the top of the graphene stacks in level L_3 attains a maximum, the dewetting from the top of the graphene stacks in level L_1 has already started. This has been illustrated by green arrows in Figure 6.4b,iv. Accordingly, the maximum value of $(r_{w,HG}/r_{w,G})_{transient}$ [or $(r_{w,HG}/r_{w,G})_{transient,peak}$] that is attained for the case of HG with HOF is less than that for the case of HG with HIF (compare Figure 6.6 and 6.7). Also, such an enhanced dewetting for the case of HG with HOF would imply that at equilibrium, very little water is present on the top of the graphene stacks at the level L_1 (see Figure 6.4b,v). Here the attainment of equilibrium is slightly delayed (occurs at $t \sim 800$ ps,

while the force was removed at t = 600 ps) as compared to the case of the HIF (where equilibrium occurs at $t \sim 700$ ps). The enhanced dewetting for the case of HG with HOF leads to a maximum possible removal of water fromm the upper surface of the graphene stacks in level L_1, which in turn ensures that a much larger time is needed for attaining the equilibrium. Figure 6.5a probes the dynamics of interactions between the water nanodrop and the HG matrix with −OH functionalization and d = 2.5 nm. At the beginning, very much like the case of d = 1 nm, the drop spreads on the graphene stacks in level L_1 (as shown by orange arrows) and there is a vertically downward migration of the drop wetting the graphene stack in level L_2 (see Figure 6.5a,i). Subsequently, the bottom of the stacks at level L_1 (see Figure 6.5a,ii) gets wetted. However, the presence of the large vertical separation between the graphene stacks implies that in the presence of the applied vertical force, water only wets a portion of the graphene stacks in level L_3 and that too when the puddle of water that has accumulated on top of the graphene stacks in level L_1 has got sufficiently thinned (see Figure 6.5a,iii). Therefore, here too the water simultaneously wets seven horizontal surfaces (see Figure 6.5a,iii); however the large vertical distance between the graphene stacks implies that only a part of these surfaces get wetted. This is reflected in the significantly smaller value of $(r_{w,HG}/ r_{w,G})_{transient}$ at any time t for this case as compared to the case of d = 1 nm (see Figure 6.7). More importantly, the significant resistance to dewetting imparted by the strong attraction between water and the HIF implies that while the puddle accumulated in the lateral space between the graphene stacks at level L_1 thins down, there is still a significant amount of water left on the upper surface of the graphene stacks in level L_1 (see Figure 6.5a,iii). In fact, this water on the upper surface of the graphene stacks at level L_1 stays there while the applied force drives the rest of the water away from the graphene stacks at level L_1 (see Figure 6.5a,iv). In the process, the drop attains an equilibrium state where (a) the

water completely engulfs the graphene stack in level L_2, while the top of the graphene stacks in level L_3 gets wetted and (b) there are isolated islands of water on the laterally separated graphene stacks at level L_1 (see Figure 6.5a,v). This equilibrium (see Figure 6.5a,v) is attained at $t \sim 210$ ps, i.e., almost instantly after the removal of the force at $t = 200$ ps. In Figure 6.5b we study the interaction of the water nanodrop with the HG matrix with HOF of its holes. Here too we consider $d = 2.5$ nm. The significantly large value of d ensures that the wetting of the bottom surfaces of the graphene stacks in level L_1 and the top surfaces of the graphene stacks in level L_3 necessitates significant thinning of the puddle of the water that has accumulated in the space between the laterally separated graphene stacks in level L_1 (see Figure 6.5b,ii and iii). However, this thinning of the puddle is also associated with a significantly enhanced dewetting of the water from the top of the graphene stacks in level L_1. Such a dewetting behavior is not witnessed for the case of HG with HIF (see Figure 6.5a) due to the large attraction between the HIF and water. As a consequence, the water only wets five horizontal surfaces together (see Figure 6.5b,iv), i.e., the water has completely dewetted the top of the graphene stacks in level L_1. This also explains as to why even for $d = 2.5$ nm, one witnesses a smaller value of $(r_{w,HG}/ r_{w,G})_{transient}$ for any t for the case of HG with HOF as compared to the case of HG with HIF. In fact, such enhanced dewetting induced complete removal of the water from graphene stacks in level L_1 implies that at equilibrium, water exists as a single mass that completely engulfs the graphene stacks at level L_2 and wets the top surface of the graphene stacks at level L_3 (see Figure 6.5b,v). This equilibrium is reached at $t \sim 360$ ps, i.e., shortly after the removal of the force at $t = 300$ ps. Since this equilibrium state, unlike the equilibrium state corresponding to the case with the HIF (see Figure 6.5a,v), does not contain water wetting the top of the graphene stacks in level L_1, we find $(r_{w,HG}/ r_{w,G})_{equilibrium,HOF,d=2.5\text{ nm}} < (r_{w,HG}/ r_{w,G})_{equilibrium,HIF,d=2.5\text{ nm}}$ (compare Figures 6.6 and 6.7).

Figure 6.6-6.7 summarizes the time evolution of the area ratio $r_{w,HG}/r_{w,G}$ for different d and F combinations for (a) −H functionalization and (b) −OH functionalization. As discussed before, for a given d−F combination, we choose that value of t (i.e., the time for which the force is applied, identified in the caption of Figure 6.6-6.7) that ensures a maximum value of the peak in the $r_{w,HG}/r_{w,G}$ variation (i.e., $(r_{w,HG}/r_{w,G})_{transient,peak}$) as well as maximum equilibrium value of $r_{w,HG}/r_{w,G}$. As evident from the detailed analysis of the drop dynamics in Figures 6.4 and 6.5, for smaller d, the presence of a much smaller space between two vertically separated graphene stacks ensure that a given volume of water is able to simultaneously access and wet multiple number of graphene stacks, thereby enabling a larger $(r_{w,HG}/ r_{w,G})_{transient}$ (at a given t) as well as a larger $(r_{w,HG}/r_{w,G})_{equilibrium}$. Most interestingly, the effect of the force in dictating either $(r_{w,HG}/ r_{w,G})_{peak}$ or $(r_{w,HG}/ r_{w,G})_{equilibrium}$ for a given d is not massively significant. The reason is that for a given F, we choose the corresponding t (i.e., the time for which the force is applied) in a manner such that we obtain the highest possible value $(r_{w,HG}/ r_{w,G})_{transient,peak}$ and $(r_{w,HG}/ r_{w,G})_{equilibrium}$ corresponding to that particular F. Hence this combination of F and t ensures that the key role of F is to ensure an optimal positioning of the drop (or the deformed drop) inside the HG matrix. Of course, the effect of the force is witnessed in the overall dynamics; accordingly, the peak in the $r_{w,HG}/r_{w,G}$ variation (for d = 1 nm) as well as the attainment of $(r_{w,HG}/ r_{w,G})_{equilibrium}$ always occurs for a much lesser time for a larger F. Finally, the −OH termination ensures a slightly larger value of $(r_{w,HG}/r_{w,G})_{transient}$ at a given t, primarily associated with the tendency of reduced dewetting (due to the attraction of the water molecules to the HIF) that allows the retainment of the wetted water molecules within the graphene stacks for a longer duration of time. functionalization. This is the central result of the paper elucidating the manner in which a controlled interaction between

water and HG unravels the remarkable capability of HG in generating wetting states that ensure highly enhanced water−graphene wetting area. Of course, from Figure 6.6 we can clearly witness the following main results, which have been already discussed while probing the drop dynamics in details (see Figures 6.4−6.7): (a) $(r_{w,HG}/r_{w,G})_{equilibrium}$ is always larger for a smaller d for a given F and d (for reasons explained above), increase in F has a relatively less effect in altering $(r_{w,HG}/r_{w,G})_{transient,peak}$ and $(r_{w,HG}/r_{w,G})_{equilibrium}$ values (for reasons explained above), and (c) $(r_{w,HG}/r_{w,G})_{transient,peak}$ for d = 1 nm is enhanced for −OH functionalization due to the effect of arrested dewetting on account of enhanced attraction between water and hydrophilic functionalization.

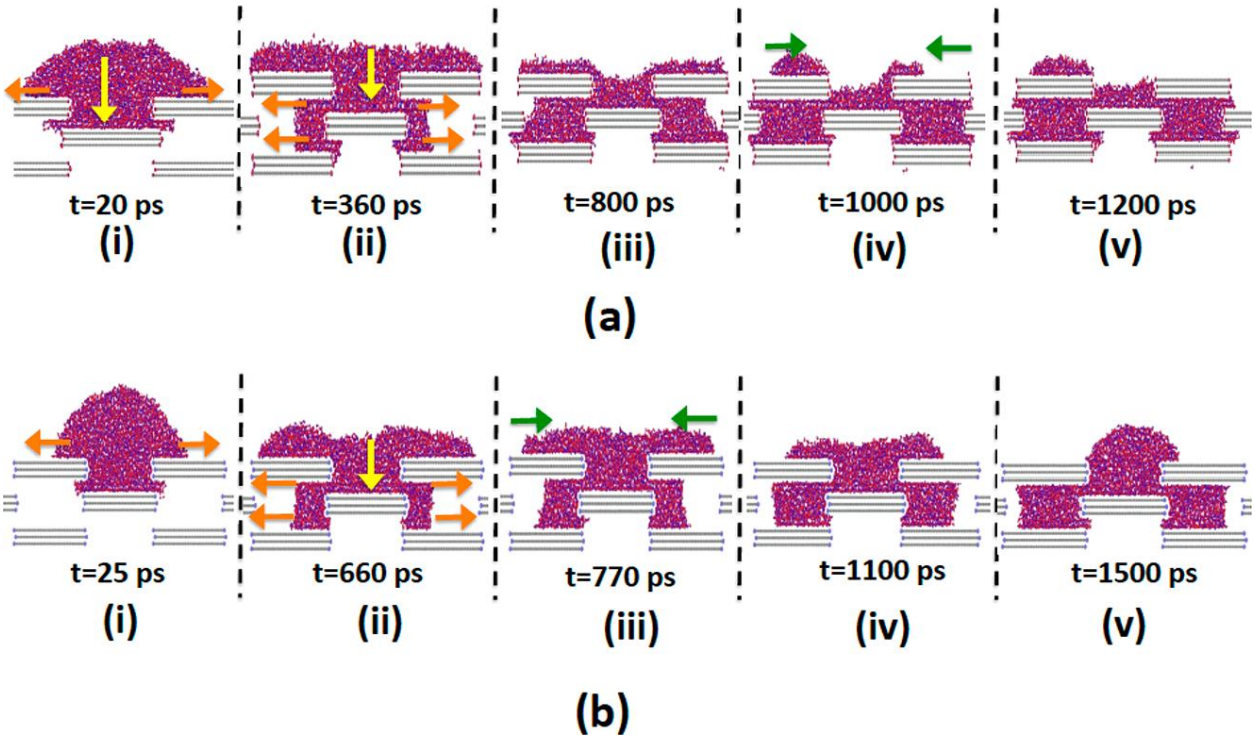

Figure 6.9 Snapshots elucidating the dynamics of the water nanodrop interacting with the HGA for −OH functionalization. In both a and b, i−v provides the snapshots corresponding to different times. Below each of these snapshots, the corresponding time is also noted. For both a and b, d = 1 nm, δ = 5.9 nm, and δ_l = 6.2 nm, and we consider that a force of F = 0.005 kcal/mol·A is applied for t = 1000 and 1100 ps for the HG with HIF and HOF, respectively.

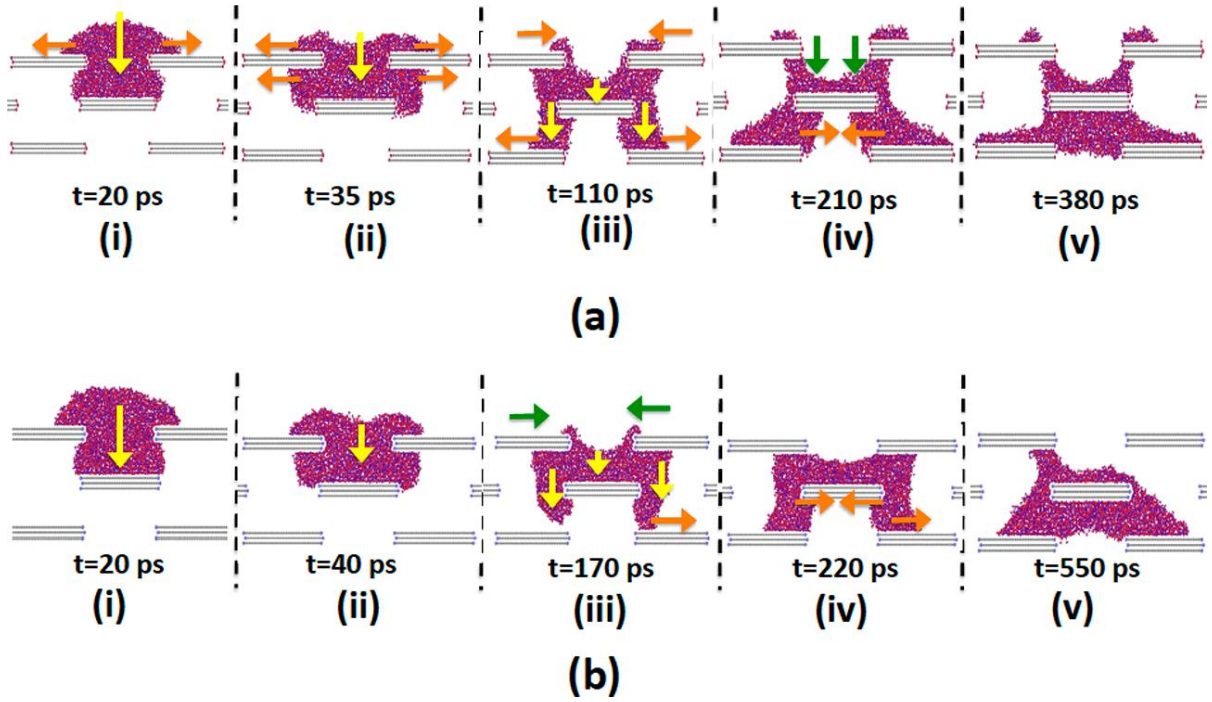

Figure 6.10 Snapshots elucidating the dynamics of the water nanodrop interacting with the HGA for −H functionalization. In both a and b, i−v provides the snapshots corresponding to different times. Below each of these snapshots, the corresponding time is also noted. For both a and b, d = 2.5 nm, δ = 5.9 nm, and δ_l = 6.2 nm, and we consider that a force of F = 0.005 kcal/(mol·A) is applied for t =330 and 420 ps for the HG with HIF and HOF, respectively.

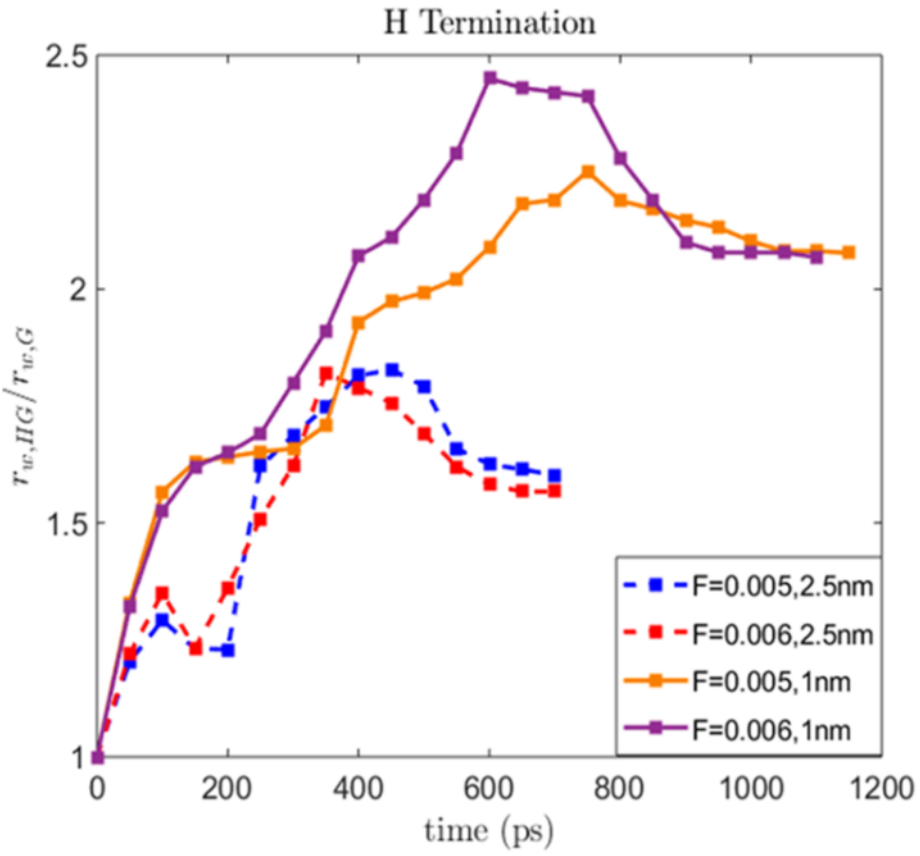

Figure 6.11 Variation of the $r_{w,HG}/r_{w,G}$ with time for different values of d and F (expressed in kcal/mol·A) (other dimensions are same as those in Figures 6.9 and 6.10) for −H functionalization of the graphene holes. For a given d−F combination, the force is applied for a time t which ensures maximum value of $(r_{w,HG}/r_{w,G})_{transient}$ (for a given t) as well as maximum $(r_{w,HG}/r_{w,G})_{equilibrium}$. This value of t is summarized below (with F in kcal/mol·A): $(t)_{d=1nm,F=0.005,OH}$ = 1000 ps, $(t)_{d=1nm,F=0.005,H}$ = 1100 ps, $(t)_{d=2.5nm,F=0.005,OH}$ = 330 ps, $(t)_{d=2.5nm,F=0.005,H}$ =420 ps, $(t)_{d=1nm,F=0.006,OH}$ = 900 ps, $(t)_{d=1nm,F=0.006,H}$ = 980 ps, $(t)_{d=2.5nm,F=0.006,OH}$ = 220 ps, $(t)_{d=2.5nm,F=0.006,OH}$ = 380 ps. The transient wetting is characterized by the transient variation of the $r_{w,HG}/r_{w,G}$; in other words, the duration of the transient wetting process is the period of time for which $r_{w,HG}/r_{w,G}$ varies with time before attaining equilibrium.

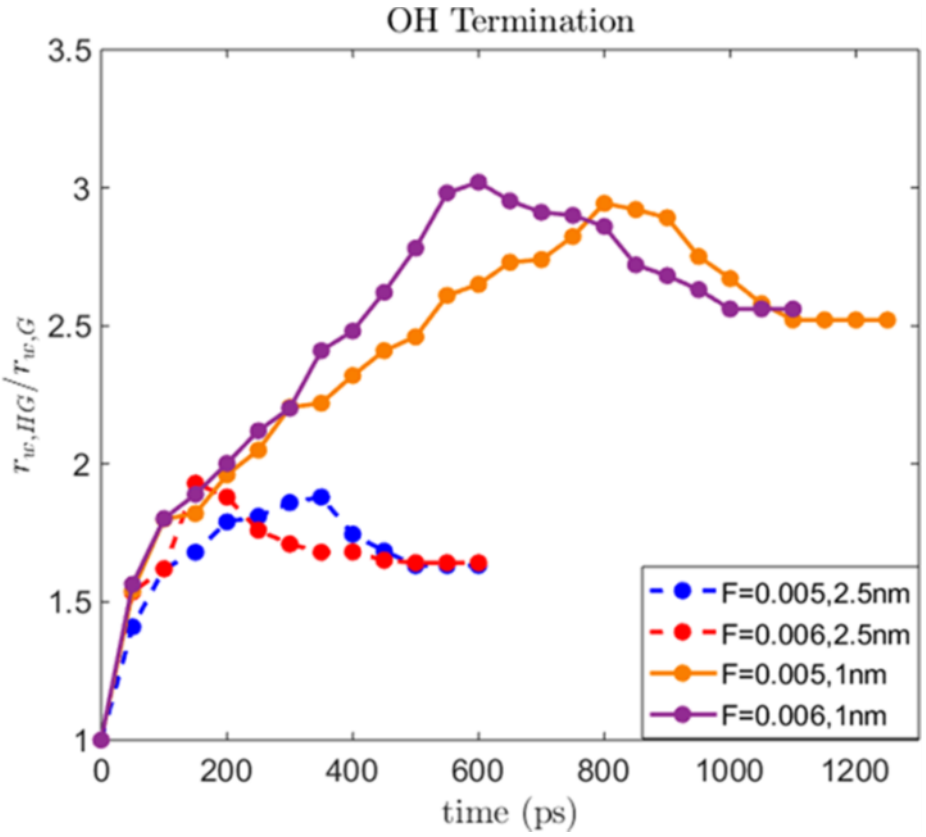

Figure 6.12 Variation of the $r_{w,HG}/r_{w,G}$ with time for different values of d and F (expressed in kcal/mol·A) (other dimensions are same as those in Figures 6.9 and 6.10) for −OH functionalization of the graphene holes. For a given *d*−*F* combination, the force is applied for a time t which ensures maximum value of $(r_{w,HG}/r_{w,G})$transient (for a given t) as well as maximum $(r_{w,HG}/r_{w,G})$equilibrium. This value of t is summarized below (with *F* in kcal/mol·A): $(t)_{d=1nm,F=0.005,OH}$ = 1000 ps, $(t)_{d=1nm,F=0.005,H}$ = 1100 ps, $(t)_{d=2.5nm,F=0.005,OH}$ = 330 ps, $(t)_{d=2.5nm,F=0.005,H}$ =420 ps, $(t)_{d=1nm,F=0.006,OH}$ = 900 ps, $(t)_{d=1nm,F=0.006,H}$ = 980 ps, $(t)_{d=2.5nm,F=0.006,OH}$ = 220 ps, $(t)_{d=2.5nm,F=0.006,OH}$ = 380 ps. The transient wetting is characterized by the transient variation of the $r_{w,HG}/r_{w,G}$; in other words, the duration of the transient wetting process is the period of time for which $r_{w,HG}/r_{w,G}$ varies with time before attaining equilibrium.

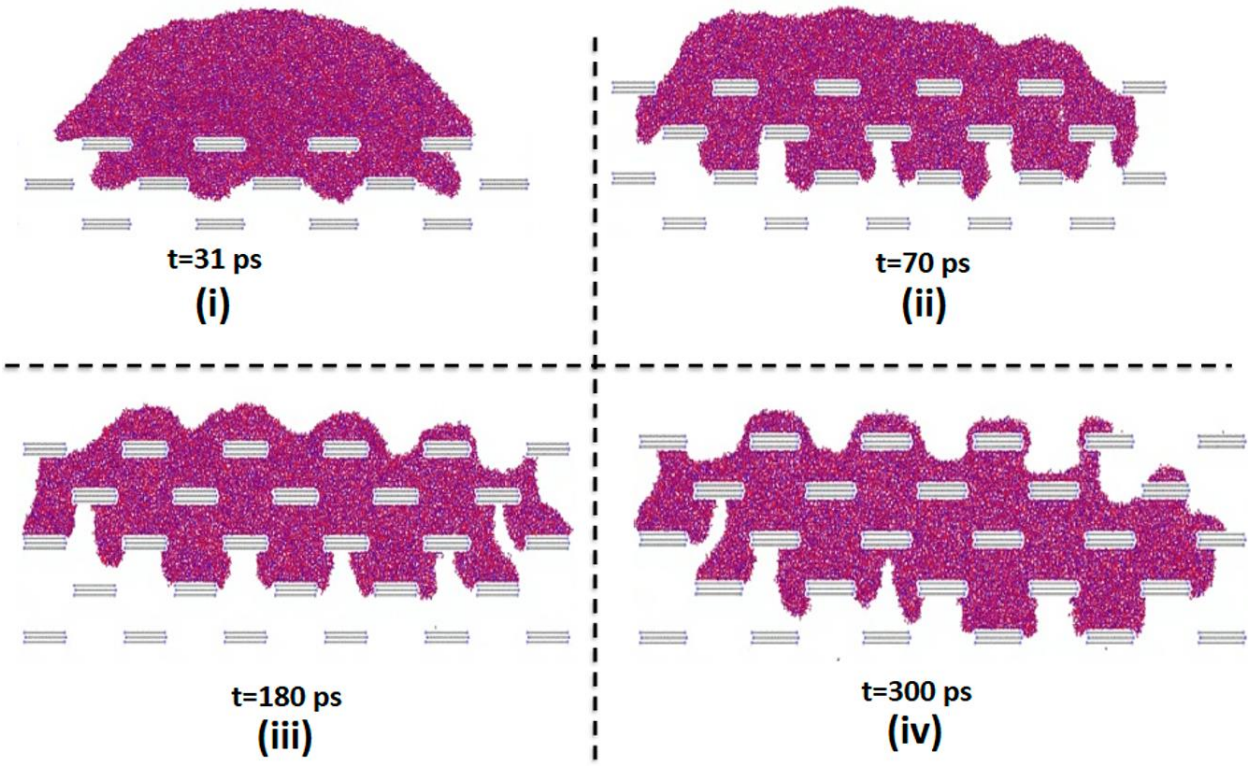

Figure 6.13 Snapshots elucidating the dynamics of a large water nanodrop (N = 30 000, while for all other simulations we use N = 3000) interacting with the HGA for H functionalization (or HOF). Parts i−iv provide the snapshots corresponding to different times. Below each of these snapshots, the corresponding time is also noted. Other parameters are d = 2.5 nm, δ = 6 nm, and δ_l = 4 nm, and we consider that a force of F = 0.005 kcal/mol·A. The force is maintained throughout the time the simulation is run.

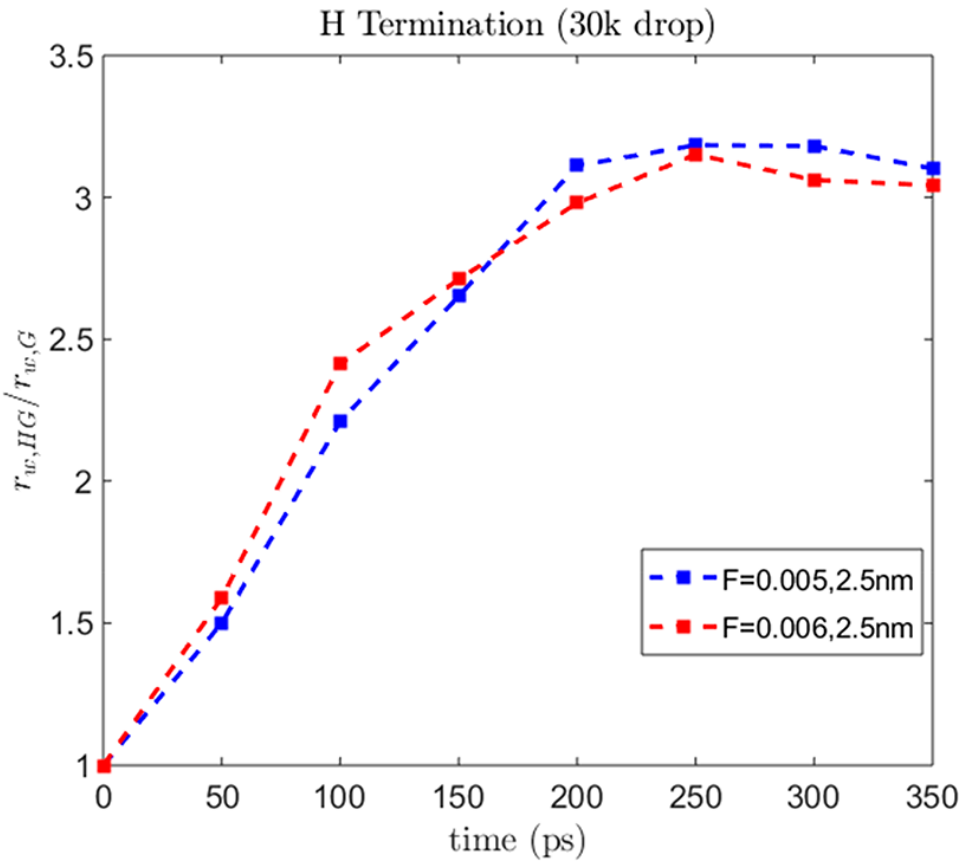

Figure 6.14 Variation of the $r_{w,HG}/r_{w,G}$ with time for different values of F (expressed in kcal/mol·A) for a large water drop passing through the HG matrix (see Figure 6.13 for the parameters of the HG matrix).

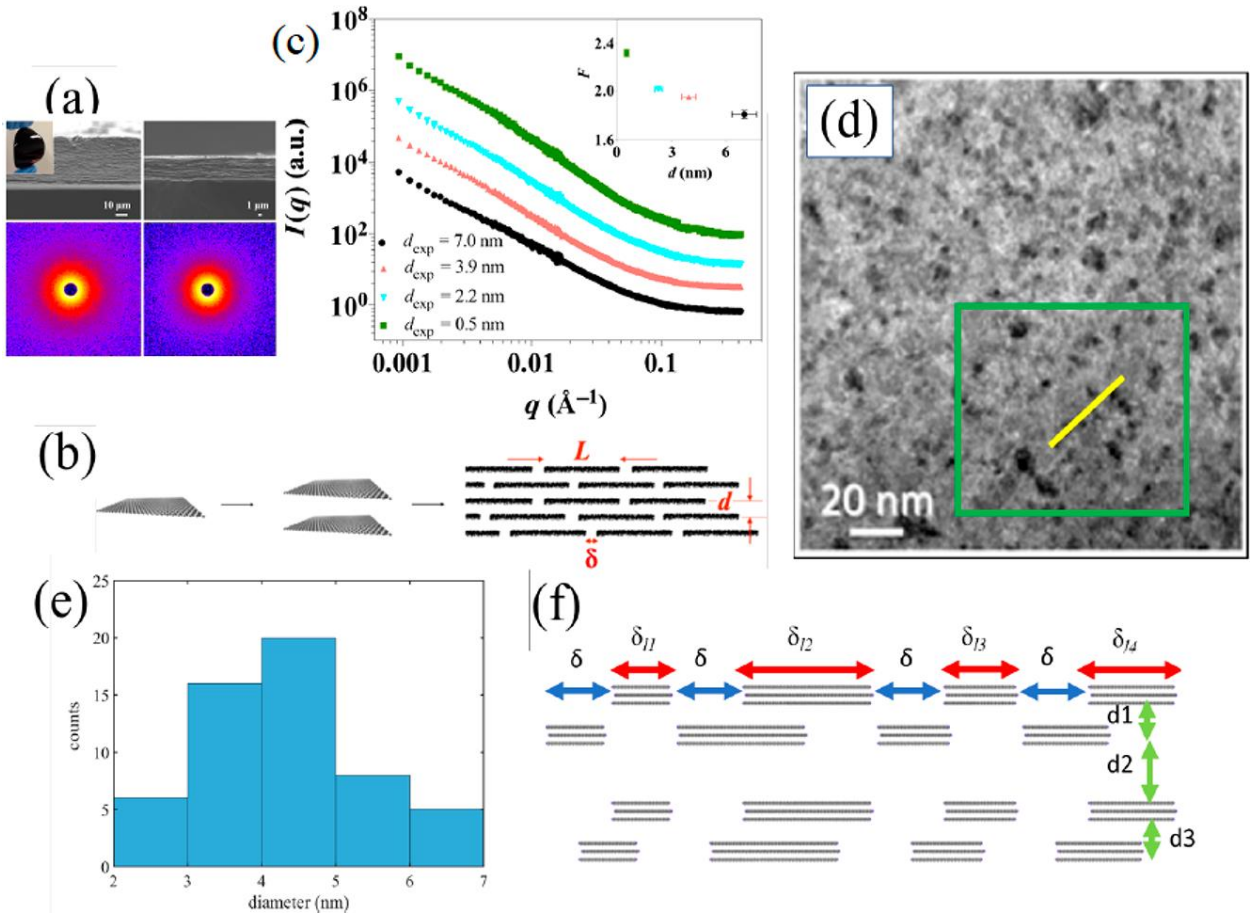

Figure 6.15 (a top) Scanning electron microscopy images depicting the cross-section of the layered graphene gel (LGG) membranes with interlayer separation of 3.2 nm (left) and 0.5 nm (right), respectively. (upper left corner) Actual LGG membrane. (bottom) Corresponding SANS patterns. (b) Schematic showing the manner in which the LGG membrane may be represented as parallel stacking of graphene nanosheets with dimensions L (equivalent to δ_l for our considered HG architecture), d, and δ (the dimensions d and δ have the same implications in our considered architecture as well). (c) Reduced 1D SANS data showing the existence of different possible values of the interlayer separation (namely 0.5, 2.2, 3.9, and 7 nm) (Parts a–c are reprinted with permission from ref [108]. Copyright © 2016 American Association for the Advancement of Science). (d) Microscopic image showing the top view of a nanoporous graphene. (Reprinted with permission from ref [189]. Copyright © 2011 American Association for the Advancement of Science). (e) Histogram analysis of the pore size distribution in part d. (f) Side view of the HG structure that we consider. The HG matrix is dictated by the dimensions $d_1 = d_3 = 1$ nm, $d_2 = 2.5$ nm, $\delta = 4$ nm, $\delta_{l1} = 3$ nm, $\delta_{l2} = 7.5$ nm, $\delta_{l3} = 4$ nm, and $\delta_{l4} = 5$ nm. In the text, we discuss in detail how these dimensions are directly obtained from the experiments.

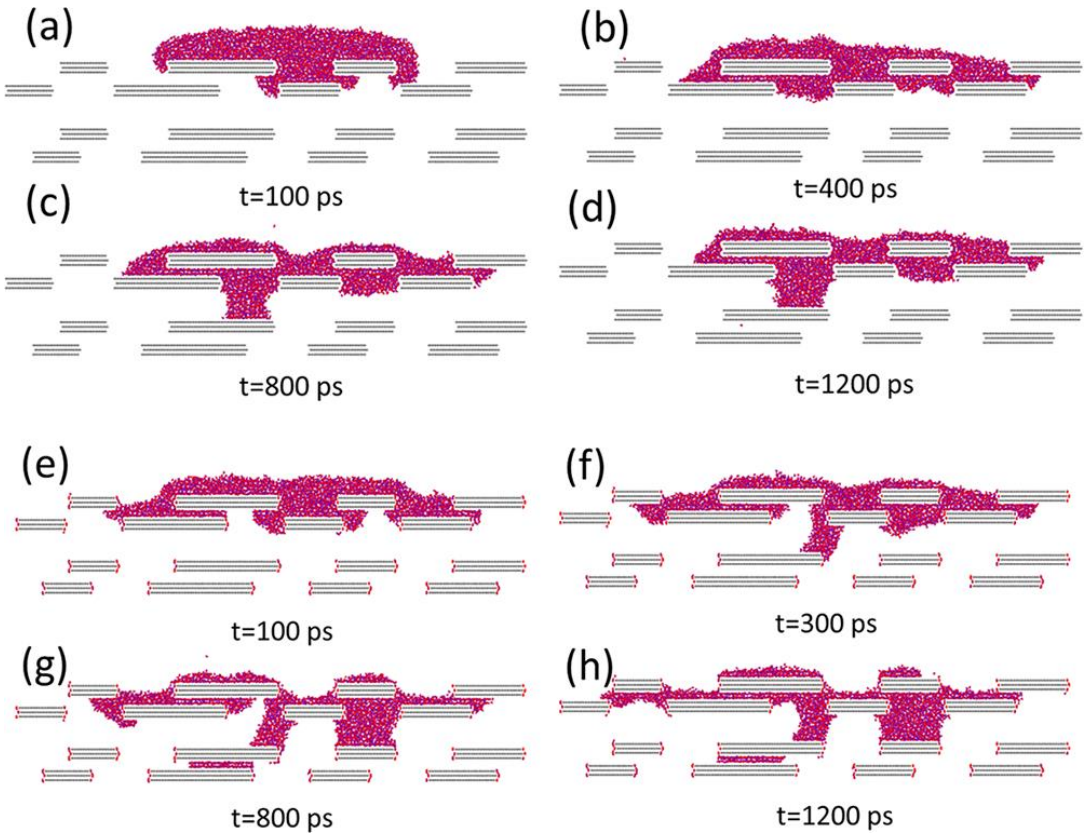

Figure 6.16 Snapshots elucidating the dynamics of the drop in the holey graphene matrix (shown in Figure 6.15f) with both −H termination (a−d) and −OH termination (e−h). For both of the cases, the water drop consists of 4000 water molecules and is subjected to a constant force of F = 0.006 kcal/(mol·Å), which is removed after t = 400 ps.

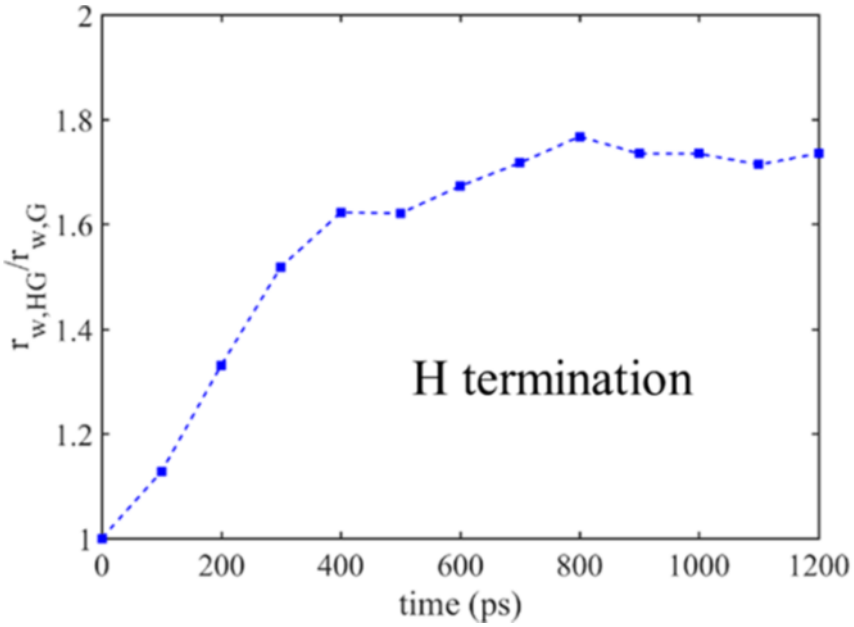

Figure 6.17 Variation of $r_{w,HG}/r_{w,G}$ with time for the HG architecture described in Figure 6.15f. Results are shown for both the −H termination. For both of the cases, the water drop consists of 4000 water molecules and is subjected to a constant force of F =0.006 kcal/mol·Å, which is removed after t = 400 ps.

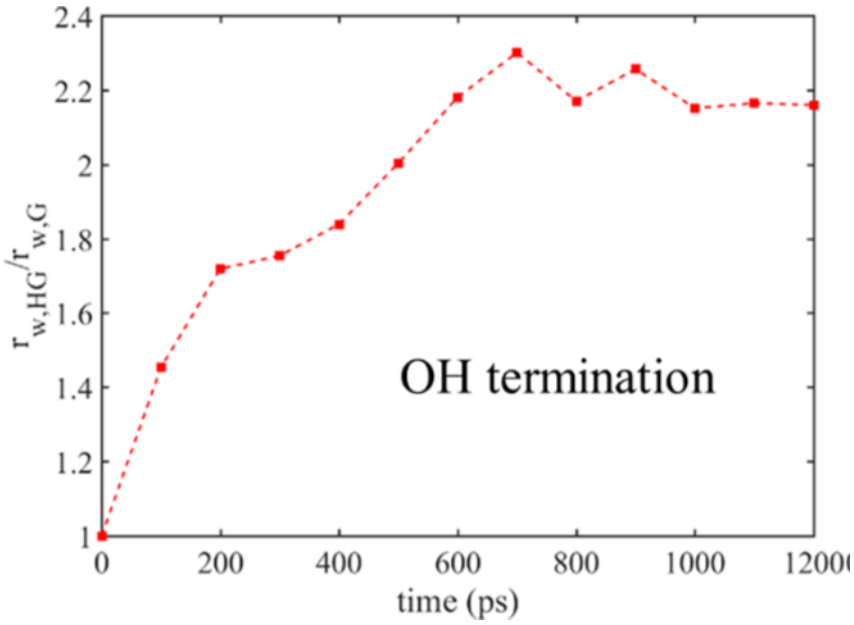

Figure 6.18 Variation of $r_{w,HG}/r_{w,G}$ with time for the HG architecture described in Figure 6.15f. Results are shown for both the −OH termination. For both of the cases, the water drop consists of 4000 water molecules and is subjected to a constant force of F =0.006 kcal/mol·Å, which is removed after t = 400 ps.

6.4 Discussions

6.4.1 Applications of Generating Enhanced Water-Accessible Graphene Surface Area Using HG

Sophisticated techniques like laser scribing has been employed to reduce graphene oxide films to graphene having very large specific surface area, which enables its use as excellent electrochemical capacitors in the presence of aqueous electrolyte solvents such as H_3PO_4.[113] Other examples of the deployment of sophisticated techniques to fabricate graphene based materials with large specific surface area that can interact with aqueous electrolyte and lead to the fabrication of highly effcient ultracapacitors include (a) chemical activation of exfoliated graphene,[180] (b) preparation of nanocomposites using graphene sheets and graphene foams,[190–193] (c) fabrication of porous graphene-based carbons containing hierarchical pores,[194] and many more. Through this chapter, on the other hand, we establish for the first time that generation of an increased water-accessible (or aqueous-electrolyte-accessible) surface area which is paramount in fabricating graphene-based ultracapacitors, is afforded by the force-driven water−HG interactions without necessitating the use of such sophisticated fabrication techniques.

Graphene with large specific surface areas and capable of interacting with water has also been routinely used for developing nanohybrids (e.g., graphene−cobalt−oxide nano-hybrid,[195] carbon nitride−aromatic diimide graphene nanohybrids,[196] NiS_x−catalyst−graphene nanohybrid,[197] cuprous oxide/graphene nanohybrids[198]) that enable enhanced chemical reactions such as water splitting,[195,197,198] generating hydrogen peroxide from water,[198] etc. This chapter by elucidating the possibility of enhancing water-accessible graphene surface by using HG will provide a

possible design alternative where such graphene-based nanohybrids can be fabricated using a HG platform for enhancing different chemical reactions.

We would like to re-emphasize here that in comparison to the different methods described above, the use of the HG is a much simpler approach to enhance the water-graphene wetting areas. The above statement does not imply that the fabrication procedure of HG is easier than that of the processes like laser scribing,[113] chemical activation of exfoliated graphene,[164] fabrication of nanocomposites using graphene sheets and foams,[190–193] etc.; rather it implies that, once we have a HG matrix, we can ensure very large and stable water−graphene surface area by simply triggering an interaction between water and this HG in the presence of a force whose magnitude and the duration of application is carefully controlled. Of course, one can conceive of even simpler approach than the use of HG for generating enhanced water−graphene wetting area. For example, one can enhance the water−graphene wetting area by merely squeezing a water drop between two different graphene plates or between a square nanochannel whose all the four walls are of graphene. For such cases, the area enhancement would be due to the formation of the *liquid capillary bridges*.[199,200] However, the big challenge of such a design is that it cannot be easily employed (possibly as a coating to surfaces) in a manner that allows the utilization of the enhanced water−graphene surface area for some applications. For example, consider the case where one would like to use this enhanced water−graphene surface area to achieve an enhanced heat transfer from the heated metal pipes by employing a nanoscale coating of graphene. It is much easier to employ a coating of HG (which is very easy to fabricate) on such metal pipes than to ensure a coating that has such square nanochannel (with four graphene walls). Once such HG coating is applied to metal pipes, a much faster conductive heat loss can be ensured by virtue

of the fact that water can access large area of the heated graphene (which has been heated by conduction from the hot metal pipe).

Therefore, the use of HG not only ensures a facile approach for generating enhanced water−graphene wetting areas but also ascertains an easy employability for actual practical applications.

6.4.2 Results for Other Combinations of the System Parameters

In addition to the results provided here, we have also carried out extensive MD simulations for other combinations of HG dimensions as well as a significantly larger drop size. For example, we carried out simulations for d = 1,2.5 nm, δ = 5.9 nm, and δ_l = 6.2 nm, i.e., we now consider a HG architecture where the length of the graphene stack is slightly larger than the hole dimensions (see Figures 6.9−6.12). This is in sharp contrast to the cases discussed in Figures 6.4−6.8, where we had considered d = 1, 2.5 nm, δ = 6 nm, and δ_l = 4 nm. Figure 6.9a shows the drop dynamics for the HG with HIF and d = 1 nm, δ = 5.9 nm, and δ_l = 6.2 nm with the drop being subjected to a force of F = 0.005 kcal/(mol·Å). The basic wetting mechanism (in terms of how the graphene stacks at different vertical levels L_1−L_3 get wetted) remains very similar to that studied in Figure 6.4a. However, the main difference lies in the fact that for this case the overall time of wetting the graphene stacks at different layers is much longer. This can be directly attributed to the fact that here the length of the graphene stack is larger than the hole dimension and a larger amount of fluid gets involved in wetting, which in turn makes less water available in the horizontal space between the graphene stacks enforcing a much slower depthwise forced vertical imbibition of the water molecules through the HG matrix. For example, after the initial wetting

of the graphene stacks at level L_1 (see Figure 6.4a,i for the definition of level L_1) and the subsequent penetration of the drop to the stack at level L_2 (see Figure 6.9a,i), the water mass takes a significantly longer time (t = 360 ps as compared to t = 260 ps in Figure 6.4a,ii) to start wetting the bottom of the graphene stacks at level L_1 and the top of the graphene stacks at level L_3 (see Figure 6.9a,ii). This is entirely due to the reduced speed of the forced vertical imbibition, as identified above. Such a reduction also means that the maximum wetted area is achieved at $t \sim$ 800 ps (see Figure 6.9a,iii) as compared to t ~ 400 ps in Figure 6.4a,iii. Of course, at a slightly later time ($t \sim$ 1000 ps), the dewetting from upper level of graphene stacks starts (see Figure 6.9a,iv); such dewetting is also witnessed in Figure 6.4a,iv but at a much earlier time (t = 600 ps). Finally, the force is removed at t = 1000 ps and the drop attains an equilibrium configuration at t= 1200 ps (see Figure 6.9a,v), which is distinctly larger than t =800 ps, i.e., the time when the drop in the system studied in Figure 6.4a,v attained equilibrium.

In Figure 6.9b, we repeat these simulations but for graphene edges with HOF. Here too the overall drop dynamics remain similar to that reported in Figure 6.4b, albeit the process occurs much more slowly. Here the reason for the slow vertical imbibition is the fact that the edge of the graphene stack from an upper level (say level L_1) protrudes over the graphene stack at the level immediately below (level L_2). Such an arrangement would imply that for the vertical imbibition (say from level L_1 to L_2), the water molecules would be bound to come in contact with the hydrophobic graphene edges thereby severely slowing down the imbibition. Therefore, for this chosen geometry, the water transport in HG with both HIF and HOF gets slowed down, but for different physical reasons. Such slow down ensures, as evident in Figure 6.9b,ii, the wetting of the bottom of the graphene stacks in levels L_1 and the top of the graphene stacks in level L_3 starts much later (i.e., t = 660 ps as compared to t = 260 ps in Figure 6.4b,ii). Also such slow

down ensures that the maximum wetted area is achieved at t = 770 (as compared to t = 400 ps in Figure 6.4b,iii) (see Figure 6.9b,iii). The HOF also ensures that dewetting from the graphene stacks in level L_1 starts early (see Figure 6.9b,iii and iv and compare it to Figure 6.9a,iv). Finally, the force is removed at t = 1100 ps and the equilibrium is attained significantly later at t = 1500 ps (see Figure 6.9b,v).

In Figure 6.10a,b, we study the drop dynamics for HG with HIF and HOF for d = 2.5 nm, δ = 5.9 nm, and δ_l = 6.2 nm for the case when the drop is subjected to F = 0.005 kcal/mol·Å. Here too, the dynamics remain similar (in terms of the progression of wetting of the different stacks) to that reported in Figure 6.5a,b, albeit slowed down due to the same reasons (separate for HOF and HIF), as illustrated in the discussions for Figures 6.9a,b. Of course, larger value of d would imply that vertical imbibition of the drop from level L_1 to L_2 would be only possible when the water mass in the horizontal space between the graphene stacks in level L_1 has suffciently thinned out (see Figure 6.10 a,ii, iii, and iv and b,ii, iii, and iv). This is true for the HG with both HIF and HOF. The relatively slow nature of this vertical imbibition is evident by comparing the times of Figure 6.10 a,iv with Figure 6.5a,iv and Figure 6.10 b,iv with Figure 6.5 b,iv. Of course, for the HG with the HIF even at the equilibrium stage (reached at t = 380 ps after the force was removed at t = 330 ps, see Figure 6.10 a,v some water molecules are found to wet the graphene stacks in level L_1, while for the HG with HOF at the equilibrium stage (reached at t = 550 ps after the force was removed at t = 420 ps, see Figure 6.10 b,v) none of the water molecules are found to wet the top surface of the graphene stacks in level L_1.

In Figure 6.11-6.12, we provide the time variation of the ratio $r_{w,HG}/ r_{w,G}$ for the cases studies in Figures 6.9a,b and 6.10a,b as well as for the case where the HG system is identical to that in Figures 6.9a,b and 6.10a,b, but the drop is subjected to a force F = 0.006 kcal/mol·Å. Results

show very similar qualitative behavior as reported in Figure 6.6 in the sense that the ratio $r_{w,HG}/r_{w,G}$ (for any value of d, any type of functionalization, or any value of the force) first increases with time, attains a maximum value of much more than one, and then decreases and equilibrates to a value more than unity. Also similar to Figure 6.6-6.7, this maximum as well as the equilibrium value of $r_{w,HG}/r_{w,G}$ is always larger for the case of smaller d and the case of the HG with HIF. In Figure 6.11-6.12 we report the results for the case where the length of the graphene stack is larger but the size of the graphene hole remains same (in comparison to the case for which we report the results in Figure 6.6-6.7). Therefore, the water encounters the same passage area to imbibe, but a larger surface area to wet. This ensures that $r_{w,HG}/r_{w,G}$ values (for a given value of the applied force and given type of surface functionalization) is larger in Figure 6.11-6.12 than in Figure 6.6-6.7.

Finally, we study the interaction of the drop with the HG for a drop that is ten times larger than the drop considered so far the drop consists of 30 000 water molecules, while previous simulations (Figures 6.4, 6.5, 6.9, and 6.10) all considered 3000 water molecules. The drop dynamics is depicted in Figure 6.13, and the large drop ensured simultaneous coverage of a large number of graphene stacks. In fact, such an action even led to a significantly larger near equilibrium value of $r_{w,HG}/r_{w,G}$, as evident in Figure 6.14. In principle, the mechanism of the drop interacting with the HG is same regardless of the size of the water drop. Here too the drop first wets a few of the graphene stacks (larger drop wets a larger number of stacks) on the upper level and simultaneously imbibe through the HG matrix wetting graphene stacks at lower levels. Of course, this behavior (along with those witnessed for smaller water drop) is characteristic of the case where there are several adjacent holes. In case there is just one hole (similar to the case

studied by ref 15), there exists no graphene stack at lower levels and accordingly the overall wetting effect would be reduced.

6.4.3 Simulation Results for the HG Architecture with Experimentally Motivated

Dimensions. As indicated in Figure 6.1a-iii, three dimensions dictate the HG architecture: *d* or the vertical gap between the different stacks, δ or the dimension of the holes, and δ_l or the lateral length of the graphene stack. In this subsection, we shall provide the simulation results for the water−HG interactions for the HG architecture where we use direct experimental results to choose the values of *d*, δ, and δ_l. Cheng et al.[108] successfully fabricated layered graphene gel (LGG) with an architecture very similar to the HG architecture that we use (see Figure 6.15a,b). Cheng et al.[108] employed SANS (small angle neutron scattering) analysis to establish that the interlayer vertical distance characterized the LGG may vary from 0.5 to 7 nm (see Figure 6.15c). Although the SANS analysis clearly indicated that there was an ordering in the vertical direction, there is no direct evidence showing the local variation of the interlayer distance *d*. Therefore, in the HG architecture that we construct (please see Figure 6.15f), we use a combination of two values (1 and 2.5 nm) that fall within this range of 0.5−7 nm. Accordingly, our constructed HG matrix consists of four horizontal layers of graphene stacks with vertical interstack separation distance *d* varying as 1 nm (d_1), 2.5 nm (d_2), and 1 nm (d_3), respectively (see Figure 6.15f). The next important issue is the choice of the pore size (which will determine δ) and the separation between the pores (which will determine δ_l). There are several state-of-the-art methods for fabricating nanoporous or holey graphene, such as the KOH activation method[189] and the air

annealing method.[94] The results shown in these papers indicate that the pore size/diameter can be precisely controlled within a small range by carefully adjusting the experimental parameters. We obtain the diameter distribution from the marked section (in the green rectangle) of the microscopic image taken from ref 197 (see Figure 6.15d) and the hole diameter distribution peaks around 4 nm (see Figure 6.15e). Therefore, we choose $\delta = 4$ nm in our constructed HG matrix. Unlike the pore size, the distance between the pores (which determines the parameter δ_l) is much more random and nonuniform. Therefore, an appropriate accounting of this situation would necessitate the consideration of the HG architecture where unlike our chosen HG architecture (in Figures 6.4, 6.5, 6.9, 6.10, 6.13), the value of δ_l cannot be constant and should vary randomly. In order to obtain the experimentally supported values of δ_l, we randomly select a cross-section labeled by yellow line in the green box (see Figure 6.15d). Along this yellow line, four values of δ_l (separated by the pores) are witnessed: 3 nm (δ_{l1}), 7.5 nm (δ_{l2}), 4 nm (δ_{l3}), and 5 nm (δ_{l4}). In our constructed HG architecture, we use these four values to ascribe randomness to the values of δ_l: accordingly, we have $\delta_{l1} = 3$ nm, $\delta_{l2} = 7.5$ nm, $\delta_{l3} = 4$ nm, and $\delta_{l4} = 5$ nm (please see Figure 6.15f). These randomly chosen δ_l values are repeated for all the four rows of the graphene stacks constituting the HG architecture (see Figure 6.15f). In summary, therefore, we construct the HG architecture with dimensions finalized using a thorough analysis of the experimental results.

We study the interactions between a water drop (consisting of 4000 water molecules) and this HG architecture with dimensions motivated by experimental results (described in Figure 6.15f). Like our previous simulations, the water drop is first brought to equilibrium at 300 K slightly away from the HG matrix. Subsequently, an external force of 0.006 kcal/mol· Å is applied to all the water molecules of the water drop and the water drop is made to move into the HG matrix.

Finally, the force field is removed at t = 400 ps allowing the water molecules to attain a final equilibrium state within the HG matrix. The drop dynamics within the HG matrix with dimensions specified in Figure 6.15f and both −H and −OH terminations are elucidated in Figure 6.16 a−d and e and f, respectively.

The enhancement in the area ratio, quantified by $r_{w,HG}/r_{w,G}$, is shown in Figure 6.17. The time-vs-$r_{w,HG}/r_{w,G}$ variation (Figure 6.17) is very similar qualitatively to those witnessed for the HG matrix with uniform dimensions (please see Figures 6.6-6.7 and 6.11-6.12). In other words, $(r_{w,HG}/r_{w,G})_{transient}$ attains a maximum (this maximum value is 1.8 at t = 800 ps for the HG matrix with −H termination and 2.3 at t = 700 ps for the HG matrix with −OH termination) and then decreases and attains a slightly reduced value at equilibrium (this equilibrium value is 1.7 for the HG matrix with −H termination and 2.1 for the HG matrix with−OH termination). Two more critical observations emerge if we compare Figure 6.17-6.18 with Figures 6.6-6.7 and 6.11-6.12. First, both $(r_{w,HG}/r_{w,G})_{transient,maximum}$ and $(r_{w,HG}/r_{w,G})_{equilibrium}$ are larger for the HG matrix with −OH termination. As evident from Figures 6.6-6.7 and 6.11-6.12, the parameter that has the largest influence on deciding the $r_{w,HG}/r_{w,G}$ is the value of the vertical interstack separation d. A smaller d (d = 1 nm) leads to a larger value (both transient maximum and equilibrium) of $r_{w,HG}/r_{w,G}$ as compared to a larger d (d = 2.5 nm). Given that for case studied here (architecture depicted in Figure 6.15f), d varies between 2.5 and 1 nm, both the transient maximum and equilibrium values of $r_{w,HG}/r_{w,G}$ are intermediate to those witnessed for cases with uniform values of d (either d = 2.5 nm or d = 1 nm, see Figure 6.11-6.12). Figures 6.15−18 therefore establish that we witness very similar wetting and area enhancement effect during the water− HG matrix interactions with the dimensions of the HG matrix being chosen by a thorough analysis of the experimental results.

6.5 Conclusions

To summarize, in this paper, we carry out extensive MD simulations to shed light on a completely new capillarity-driven wetting physics associated with water−HG interactions. We unravel that such interactions dictated by a plethora of factors such as the duration and magnitude of the applied forcing, nature of functionalization of the edges of the graphene holes, and the dimensions of the HG matrix ensure generation of novel transient and equilibrium water−graphene wetting states. Development of such wetting states, which are also scalable (i.e., witnessed even for a drop as large as ten times the original drop size) are associated with a significant enhancement of the water-accessible surface area of graphene. This enhanced area ratio has a transient maximum value or a slightly reduced equilibrium value. Both the numbers (the one representing the transient peak and the one representing the equilibrium) are important. The equilibrium value represents the ability of the holey graphene (HG) matrix to ensure a stable and time- independent enhancement of the area ratio. On the other hand, the transient maximum, which is invariably larger than the equilibrium, indicates a window of time where certain applications that require transient but very large graphene surface area (e.g., certain kinds of chemical reactions with molecules intercalated within the graphene layers) can be carried out.

It is well-known that a variety of functional groups can be found at a defected graphene surface (e.g., the edge of a graphene hole). These functional groups can be hydroxyl, carbonyl, carboxyl, etc. As we are studying the interactions of water with such holey graphene, we are mostly interested to study representative examples of hydrophobic and hydrophilic functional groups. Accordingly, we choose the −H termination (representing the hydrophobic case) and the −OH

termination (representing the hydrophilic case). Of course, for our simulations we could have chosen other functional groups as well, representing such disparate cases of hydrophobic and hydrophilic functionalization, or could have used a model where a given HG matrix had a distribution of −OH and –H functionalization of the graphene edges. These simulations would have ensured an even more extensive accounting of the effect of the system parameters, albeit the central findings would have still been very much the same qualitatively.

Chapter 7

Ion at Air−Water Interface Enhances Capillary Wave Fluctuations: Energetics of Ion Adsorption

7.1 Introduction

The problem of ion adsorption at air−water (a/w) interface is significant to better understand a large number of events ranging from Hoffmeister effects in protein chemistry,[201] light-induced conversion of hailde ions to halogen atoms on the surface of a water drop,[202,203] use of the a/w interface for promoting certain reactions,[204,205] regulating the size and composition of atmospheric aerosols that play a critical role in thunderstorm activity, lightning production, and precipitation,[206,207] hydrolysis of SO_2 in cloud droplets responsible for producing acid rain,[208] oxidation of chloride ion to chlorine gas contributing to the ozone formation in the polluted marine boundary layer,[209,210] dictating the preferential ion adsorption to proteins at the air−water interface,[211] improving the efficiency of the fabrication of semiconductor thin-film transistors,[212] and many more. Extensive studies over the past couple of decades have opened up a large number of issues that dictate the preferential adsorption/desorption of a variety of different ions at the air water interface.[213–230] Several of these studies attempted to provide a comprehensive understanding of the ion adsorption/desorption process by specifically studying the changes in the internal energy, enthalpy, and entropy, and the resulting changes in the Helmholtz and Gibbs free energy as the ion moves from the bulk to the interface.[218–222] Two key inferences emerge from these analyses: (a) The presence of the ions at the interface dampens the fluctuations of the

capillary waves (CWs) thereby decreasing the entropy (i.e., $\Delta S < 0$);[220] (b) The ion at the interface displaces the weakly interacting surface and ion-solvating water molecules to the bulk where the water molecules can form stronger water−water bonds thereby decreasing the overall enthalpy (i.e., $\Delta H < 0$).[220] Obviously, these two effects compete with each other and regulate the overall Gibbs free energy change $\Delta G = \Delta H - T\Delta S$ to decide if at all the ion adsorption at the a/w interface is favorable or not.

Here we present results from extensive atomistic simulations that contradict these inferences about the physical origins of the different energy components that dictate the ion adsorption at the a/w interface. First and foremost, we discover that the fluctuations of the capillary wave are enhanced and not reduced with the ion at the a/w interface. The existing studies[220] reported a suppression of the CWs as they considered too small a size of the simulation box that led to a pinning of the CWs. We also obtain the wave characteristics of these enhanced CW fluctuations to confirm that a single mode associated with the longest wavelength dominates these enhanced fluctuations, which causes a large decrease in the pressure−volume (or PV) work and hence the enthalpy with the ion at the interface. In parallel, we also demonstrate that the enthalpy change associated with the ion- at-interface mediated displacement of the weakly interacting surface and coordinated water molecules to bulk is extremely small. This enables us to infer that $\Delta H_{\text{ion-at-interface}} < 0$ is primarily associated with the PV work dictated by the properties of the enhanced fluctuations of the CWs with the ion at the interface. Therefore, here too, we contradict the key inference of the existing studies: The ion-at-interface mediated decrease in enthalpy is not due to the resulting redistribution of the water molecules but is due to the resulting change in the pressure volume work associated with the modified CW fluctuations. Given that the presence of the ion at the interface enhances the capillary wave fluctuations, what happens to the

entropy change? We establish that the entropy change is negative just as reported by the existing studies, and we associate such a change to the corresponding predominance of a single mode in the enhanced fluctuations of the CW. We carry out all the simulations using the interaction potential used by Venkateswaran et al.;[221] therefore, the overall variations in ΔG, ΔH, and $-T\Delta S$ are exactly similar to those predicted by ref 221. Despite this, the appropriate choice of the simulation box size allows us to pinpoint the actual physical causes that dictate the variation of the energy components and that is where our study counters and contradicts the existing simulation studies and points to a new understanding of the energetics of ion adsorption at the a/w interface.

7.2 Materials and Methods

All the simulations are carried out in a system having a simulation cell size of x × y × z = 52 Å × 52 Å × 200 Å. A periodic boundary condition is applied in all the three Cartesian directions. The simulations are performed by using the molecular dynamics (MD) simulation package LAMMPS.[81] A total of 5780 SPC/E water molecules and one cation (σ = 0.44 nm, ϵ = 0.85 kJ/mol, q = 1.2 e) are introduced in the system. A layer of hydroxyl group is attached to the bottom of the simulation box to help the solution slab remain cubic. The simulations are initially carried out in the canonical ensemble (NVT) for 1 ns at 300 K to reach an equilibrium. At equilibrium, the liquid phase occupies a continuous space starting from the bottom of the simulation box and the corresponding global Gibbs dividing surface (indicating the liquid−vapor interface) is located at approximately z = 64 Å from the bottom of the simulation box. This leaves out the rest of the simulation box for the vapor phase. Once the equilibrium has been

reached, the simulations are carried out using the microcanonical ensemble (NVE) for another 5 ns. Data is collected from this simulation of additional 5 ns, and this methodology ensures that the influence of the thermostat on the capillary wave (CW) hydrodynamics is eliminated. Furthermore, the kinetic energy fluctuations during the data collection are also carefully monitored to prevent the status shifts from the equilibrium. The interaction between water (treated with the SPC/E model) and ion is calculated using the short-range Lennard-Jones (LJ) potential and long-range electrostatic potential: The LJ parameters (σ_{ij}, ε_{ij}) between two different species are obtained by Lorentz−Berthelot rules,[15] and the Columbic interactions are solved by using the particle−particle particle-mesh (PPPM) solver.[231]

The potential of mean force (PMF) for all the systems is calculated by employing the umbrella sampling with the ion placed in the simulation box. The z location for the ion is constrained at 12 different values (ranging from 57 to 68 Å from the bottom of the simulation box) by employing a bias potential with a spring constant of K_{bias} = 836.8 kJ/mol/nm^2 along the z direction. Therefore, our energy data are obtained for 12 values of the z location for the ion. The system internal energy and liquid phase pressure are collected directly from the simulation output, while the liquid phase volume is generated using Voronoi Tessellation algorithm. Finally, all the error bars are provided based on the standard error (SE) calculated from the standard deviation (SD).

7.2.1 Justifications of simulations

The simulation set-up of the system used in this study is largely different from those used in pervious literature. For example, the cross-section area is set to be 16 times of σ_{water}, which is significantly more than the correlation range in the simulations. In other words, using this set-up

can prevent the system to have unnecessary interaction due to the periodic boundary conditions. However, the consequences of using this set-up are not clear, as it has not been studied thoroughly. For example, it is not clear that the NVT ensemble is still valid or not. How would the system react to the ion approaching to the interface? Here, I would like to include the justification of the system to support the idea of using a larger simulation system.

Liquid Phase Volume

The volume of the simulation slab is generated using the Voronoi Tessellation algorithm, which shows negligible change as the ion moves from the bulk to the a/w interface (see Fig. 7.1). This negligible variation also allows us to define an average value of the volume of the simulation box, which is later used to calculate the PV work.

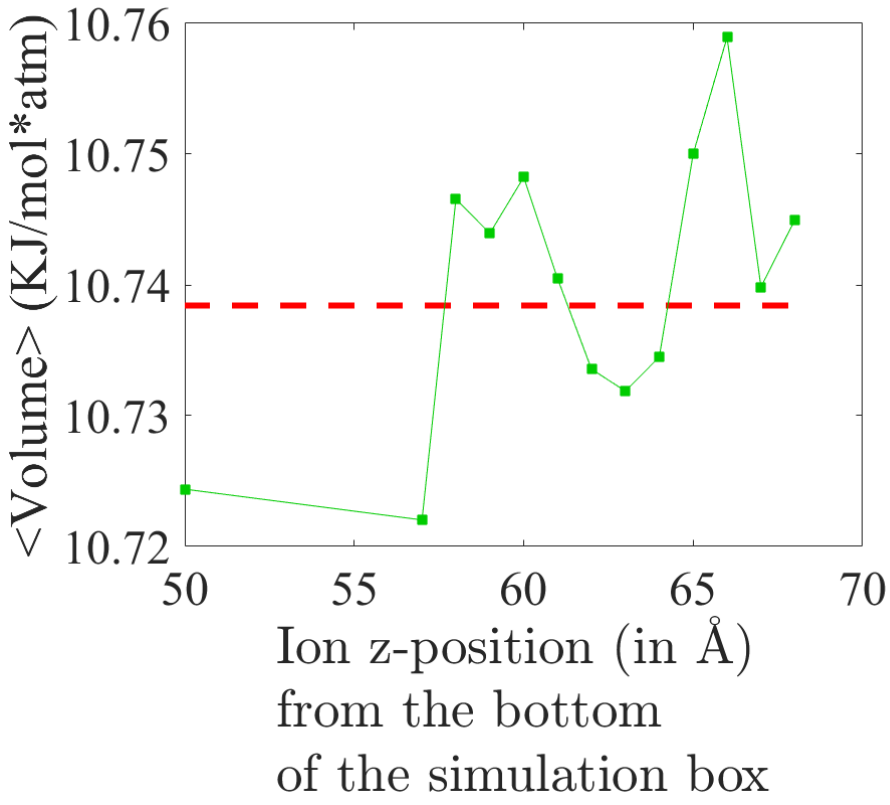

Figure 7.1: Variation of the volume of the simulation slab as the ion moves from the bulk (quantified by the ion z position with z≤62 Å) to the a/w interface (quantified by the ion z position with z≥66 Å). We find very little variation in the volume as the ion moves from the bulk to the interface. Therefore, we ascribe an average value (shown by red dotted line) to this volume, which is used while calculating the PV work.

Liquid-Phase Pressure

Unlike the volume, the pressure of the system shows a dramatic reduction as the ion moves from the bulk to the a/w interface (see Fig. 7.2). This is attributed to the fact that the CWs with the ion at the a/w interface is dominated by a single mode of longest wavelength leading to a significant lowering of the pressure.

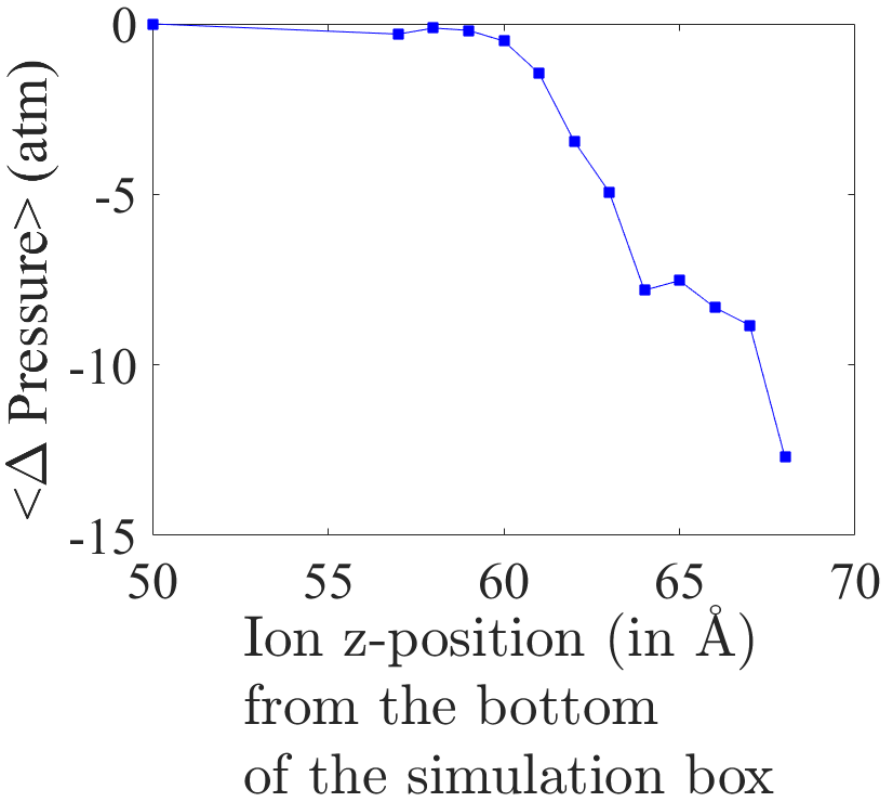

Figure 7.2: Variation of the pressure change within the simulation slab as the ion moves from the bulk (quantified by the ion z position with z≤62 Å) to the a/w interface (quantified by the ion z position with z≥66 Å).

7.2.2. Measurement of fluctuations

The simulation system is equilibrated using the NVE ensemble for 1 ns and in the process, we evaluate the surface fluctuations. For this simulation, we constrain the ion motion only along the z direction, setting the ion free to move in the x-y plane (see Fig.7.3). During the sampling period, the ion travels across the simulation boundary freely and covers a wide range of the simulation box (see Fig. 7.4), allowing the surface to present multiple corrugation configurations. The surface water molecules are separated from the water slab using the coarse-grain density

method. Subsequently, the root-mean-square height difference between the surface water and the global Gibbs dividing surface $h(GDS)$ is collected to obtain the surface fluctuations.

$$\delta h(x) = h(x) - h(GDS), \qquad (7.1)$$

where $\delta h(x)$ is the collection of global fluctuations of the surface, and $h(x)$ is the collection of surface water height within a bin defined by x.

By this sampling method, a quantitatively averaged surface fluctuation is obtained, instead of having a fluctuation peak around the ion location.

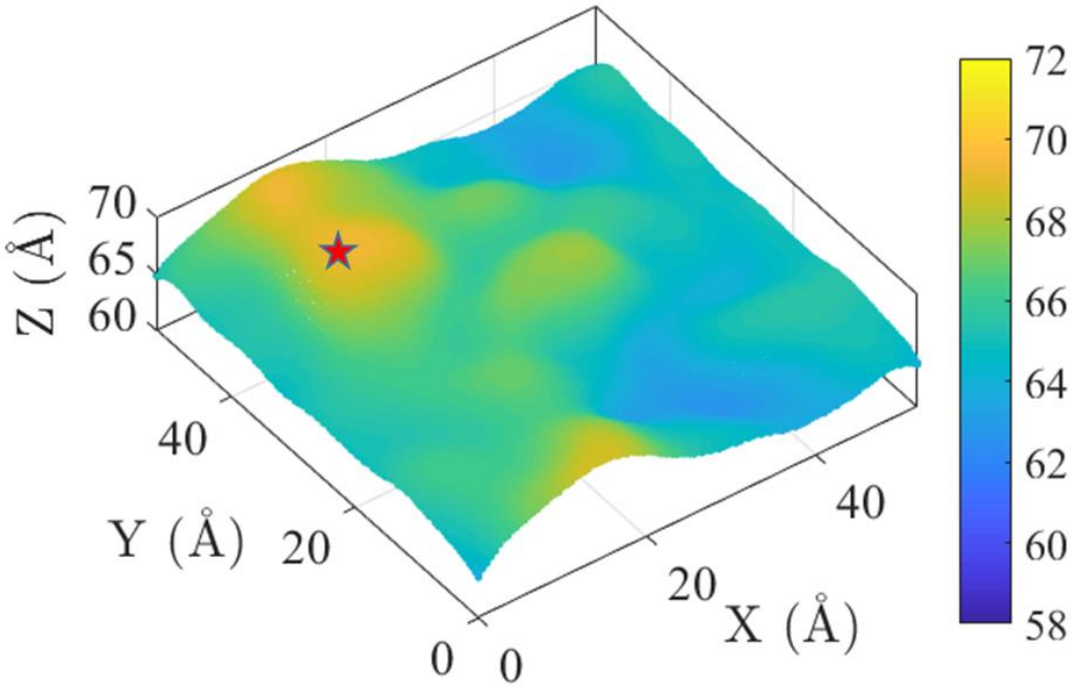

Figure 7.3: A 3D view of a liquid-vapor interface with an ion location shown by the red star.

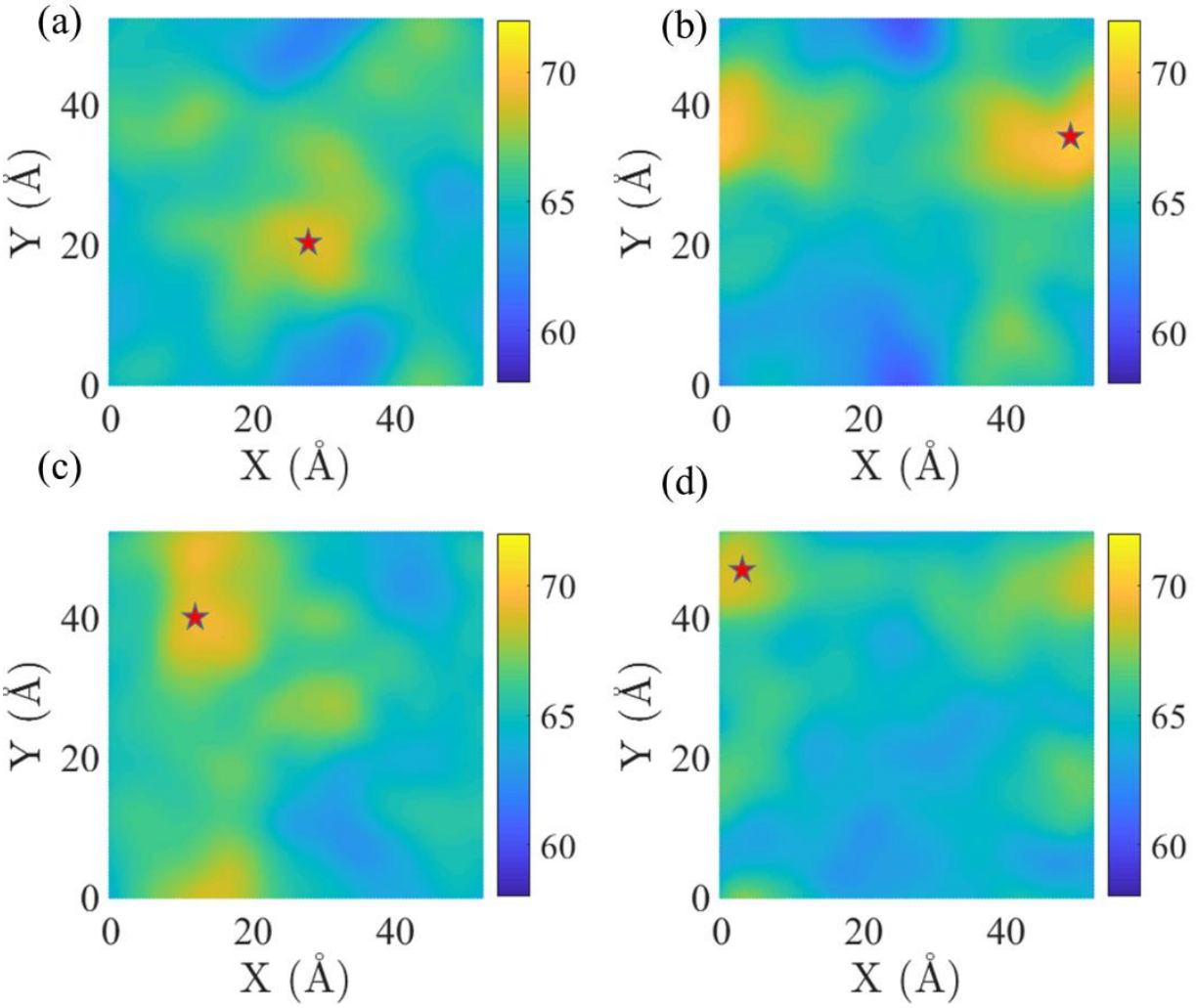

Figure 7.4: A series of 2D views of liquid-vapor interface with ion locations shown by the red stars.

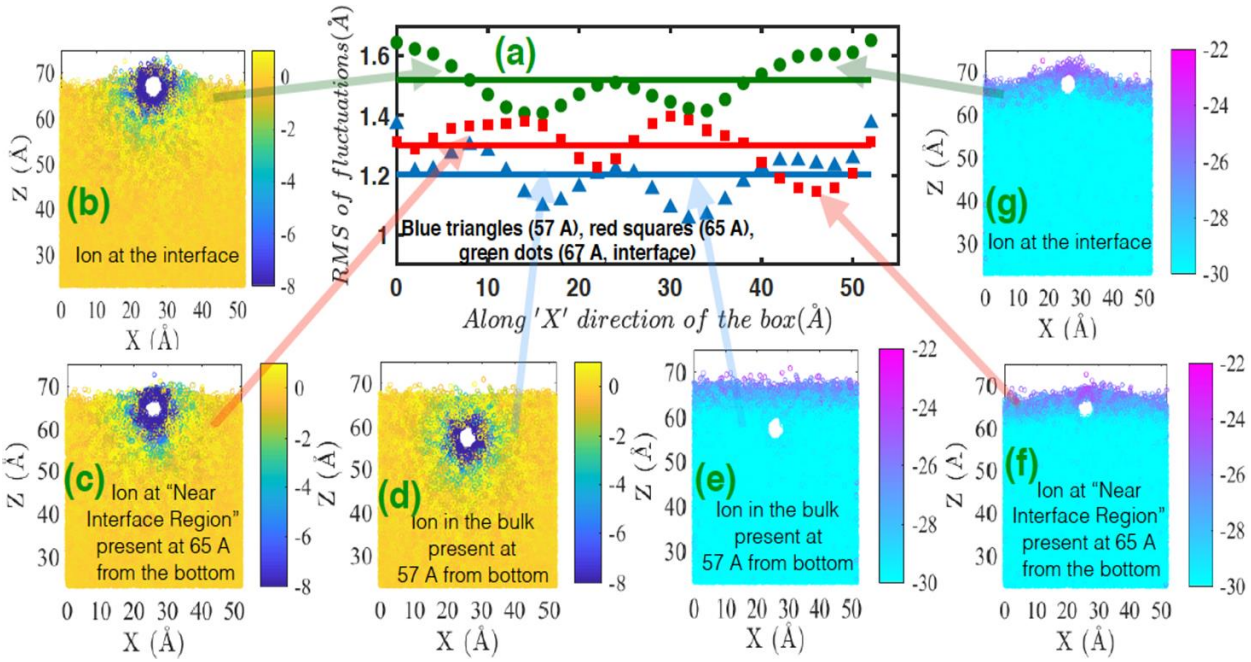

Figure 7.5 (a) Root mean square (RMS) of the CW fluctuations with the cation at three different locations [green circles: cation at the a/w interface, i.e., at z = 67 Å; red squares: cation at the NIR (please see the text for the definition of NIR or near-interface region), i.e., z = 65 Å; blue triangles: cation in the bulk, i.e., z = 57 Å]. The lines parallel to the horizontal axis denote the average of the fluctuations. (b−d) Distribution of the water molecules distinguished in terms of their interaction energies with the cation for (b) cation at the a/w interface, (c) cation at the NIR, and (d) cation in the bulk. (e−g) Distribution of the water molecules distinguished in terms of their interaction energies with the other water molecules for (e) cation in the bulk, (f) cation at the NIR, and (g) cation at the a/w interface.

7.3 Results

7.3.1 Evidence of the Increase in CW Fluctuations with Ion at the Air−Water Interface

Figure 7.5a quantifies the fluctuations of the CWs with the cation being positioned at the three different locations with respect to the a/w interface (see section 7.2.2 for the techniques to quantify the CW fluctuations). These three different locations are (a) the a/w interface [see Figure 7.5b,g], (b) the near-interface region (or NIR) [see Figure 7.5c,f], which refers to the

region up to which the influence of the CWs are experienced (in other words, the width of this region is approximately twice the amplitude of the long wavelengths constituting the CWs), and (c) the bulk [see Figure 7.5d,e]. Here we shall study the interactions between a cation and the a/w interface. We have also carried out simulations to study the interactions between an anion and the a/w interface. We do not witness any distinct qualitative variation in the different inferences. Therefore, we refrain from discussing the results when the ion is an anion. Furthermore, henceforth in this paper the term "ion" will be synonymously used to imply a cation. In Figure 7.5a, we clearly witness an increase in the fluctuations of the CWs with the ion at the interface, and the magnitude of these fluctuations decreases as the ion gradually moves from the interface to the bulk through the NIR. This finding is completely opposite of that reported by the existing studies,[220,221] which claim that the ion at the interface must always reduce the CW fluctuations. We associate this finding of ref 220 to the consideration of a significantly small size of the simulation box. For example, Otten et al.[220] considered a simulation volume (20 Å × 20 Å × 20 Å) that is small enough to cause a pinning of the CWs, which dampens the CW fluctuations. It is well-established that the simulation box size must be significantly larger than at least 10σ (i.e., 31.6 Å considering σ = 3.16 Å for water) to avoid periodic boundary conditions artificially impacting the simulation results.[232,233] Therefore, we believe that the notion of these papers[220–222] that the dampening of the CWs occur due to the presence of the ion at the interface is inappropriate; a dampening of the CWs is witnessed not due to the presence of the ions at the a/w interface but rather to the selection of too small a size of the simulation box[220] that leads to a pinning of the CWs. Of course, in our simulations, we considered a much larger system size of 52 Å × 52 Å × 65 Å, which is distinctly larger than the cut off of 10σ = 31.6 Å. Therefore, our simulation system is a suffciently large box of water with a single

ion (see Figure 7.1). Other relevant details of our simulation are summarized in the "Materials and Methods" section (section 7.2).

In order to reaffirm our hypothesis that the ion-at-interface mediated suppression of the CW fluctuations reported by the previous studies[220–222] is due to the consideration of a reduced size of the simulation box,[220] we carry out extensive simulations for significantly small simulation box size and indeed witness that the CW fluctuations are reduced as the ion moves from the bulk to the a/w interface (the details have been provided in section 7.4.3 towards the end of this chapter).

It is worthwhile to discuss ref 220 in more detail here. The box size used in ref 220 is larger (in $x \times y$ directions) than 10σ ($x \times y$ = 3.5 nm × 3.46 nm as well as $x \times y$ = 7 nm × 7 nm). However, ref 220 does not provide any explicit result showing the variation of the CW fluctuations with the ion position. Therefore, we have no clue what would be their corresponding prediction of the CW fluctuations and if that would affect their prediction of the factors responsible for the energy changes. We still refer to ref 220 while identifying papers that have neglected the role of appropriate capture of the CW fluctuations since ref 220 supports the predicted mechanisms (for ion adsorption) of ref 222. It is also noteworthy that ref 220 despite being a study of much wider scope (studying the behavior of both single ion and ion pair) does not provide answers to the following questions: How would free energies, enthalpy, and entropy of ion adsorption be affected by the consideration of larger simulation box? How would PV work compete with the change in the internal energy for dictating ΔH? Are the CW fluctuations dampened or enhanced, and what accordingly would be the factors contributing to the entropy change? The lack of answers to these questions ensures that the actual physical mechanisms responsible for the

behavior of a single ion and an ion pair, governed by the appropriate capturing of the CWs, have not been unravelled in ref 220. In contrast, our study considers and responds to all these above questions for a single ion (as will be evident from the results later). Our simulations consider the potentials used in ref 220 and therefore (as will be evident later) produce very similar ΔG (as in ref 220) for the adsorption of a single ion for both large and small simulation boxes [compare the red curves between Figures 7.5]. However, unlike ref 220, an analysis of the corresponding ion−CW interactions help us to dissect the physical factors that contribute to these variations of ΔG, ΔH and ΔS.

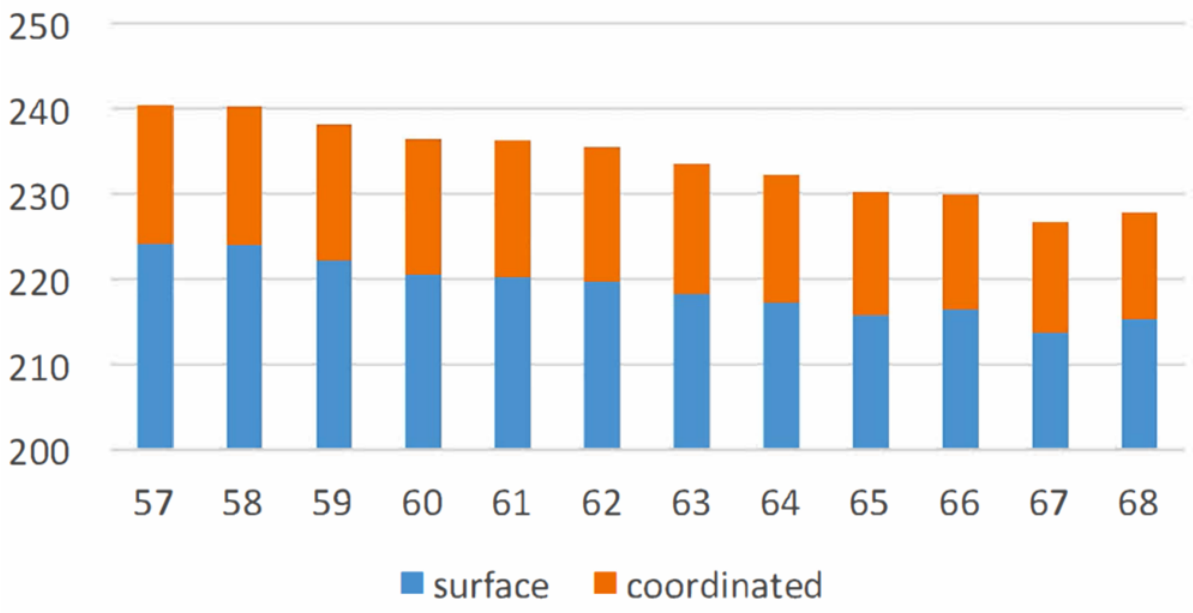

Figure 7.6 Variation of the average number of surface and coordinated water molecules for different distances of the cation (measured in Å) from the bottom of the simulation box. A distance of 66−68 Å represents the cation at the a/w interface and a distance of <63 Å represents the cation in the bulk. For this plot, we first identify what differentiates between the different types of water molecules (surface, coordinate, and bulk). The bulk and the surface water molecules are identified by studying the corresponding local number densities ρ_{local} around these water molecules. A water molecule is considered a bulk water molecule if $\rho_{local} = 0.032/Å^3$ and a surface water molecule if $\rho_{surface\ water} = 0.016/Å^3$. In contrast, a coordinated water molecule is the water molecule at a radial distance of 5 Å from the ion center.

7.3.2 Energy Map of the Water Molecules, Ion Enforced Redistribution of Water Molecules, and the Resulting Δ*H*

Figure 7.5b−g provides the energy map of the water molecules (in kJ/mol) with the ion at different locations (with respect to the a/w interface). The detailed analysis, which has been developed following Otten et al.,[220] considers the energy of interaction of a water molecule with the ion [Figure 7.5b−d] and other water molecules [Figure 7.5e−g]. Following Otten et al.,[220] we can relate the energy of a water molecule to the energies $\bar{e}_j$ corresponding to three different environments, namely the (a) the a/w interface, (b) the coordinate region (i.e., the solvation

shell of the ion), and (c) the bulk. Consequently, the change in the local internal energy as the ion moves from the bulk to the interface can be expressed as[220]

$$\Delta U_{local} = \left(\bar{e}_{cord} - \bar{e}_{bulk}\right)\Delta n_{cord} + \left(\bar{e}_{surf} - \bar{e}_{bulk}\right)\Delta n_{surf}, \qquad (7.2)$$

where Δn_{cord} and Δn_{surf} denote the change in the number of water molecules in the coordinate region and the surface (or the a/w interface) as the ion moves from the bulk to the a/w interface. Otten et al.[220] provided explicit numbers for $\bar{e}_{cord} - \bar{e}_{bulk}$ and $\bar{e}_{surf} - \bar{e}_{bulk}$. In contrast, we calculate Δn_{cord} and Δn_{surf} (see Figure 7.6). As evident from Figure 7.6 as well as ref 220, as the ion moves from the bulk to the interface, there is a small change, Δn_{cord}, in the number of the coordinated water molecules, while there is a slightly larger change (or decrease) Δn_{surf} in the number of surface water molecules. Once we know the energy differences $\bar{e}_{cord} - \bar{e}_{bulk}$ and $\bar{e}_{surf} - \bar{e}_{bulk}$ and Δn_{cord} and Δn_{surf}, eq 7.2 can be employed to obtain the change in the local internal energy associated with the ion moving from the bulk to the a/w interface. Otten et al.[220] hypothesized that this local internal energy change is approximately equal to the global internal energy change, which in turn became equal to the global enthalpy change (associated with the ion transfer from the bulk to the a/w interface) since the *PV* (pressure− volume) work is negligible in the presence of damped CW fluctuations triggered by the consideration of too small a simulation volume. Of course, even if $\Delta H_{\mathrm{global}} \approx \Delta U_{\mathrm{global}} \approx \Delta U_{\mathrm{local}}(z)$, then the values of Δn_{cord} and Δn_{surf} are so low (see Figure 7.6) that the large negative value of $\Delta H_{\mathrm{global}}$ that is hypothesized to be associated with the ion transfer from the bulk to the interface is never achieved. Therefore, we directly contradict the inference of the previous papers[220,221] that the decrease in the enthalpy caused by the movement of the ion from the bulk to the a/w interface can be associated with the resulting redistribution of the water molecules.

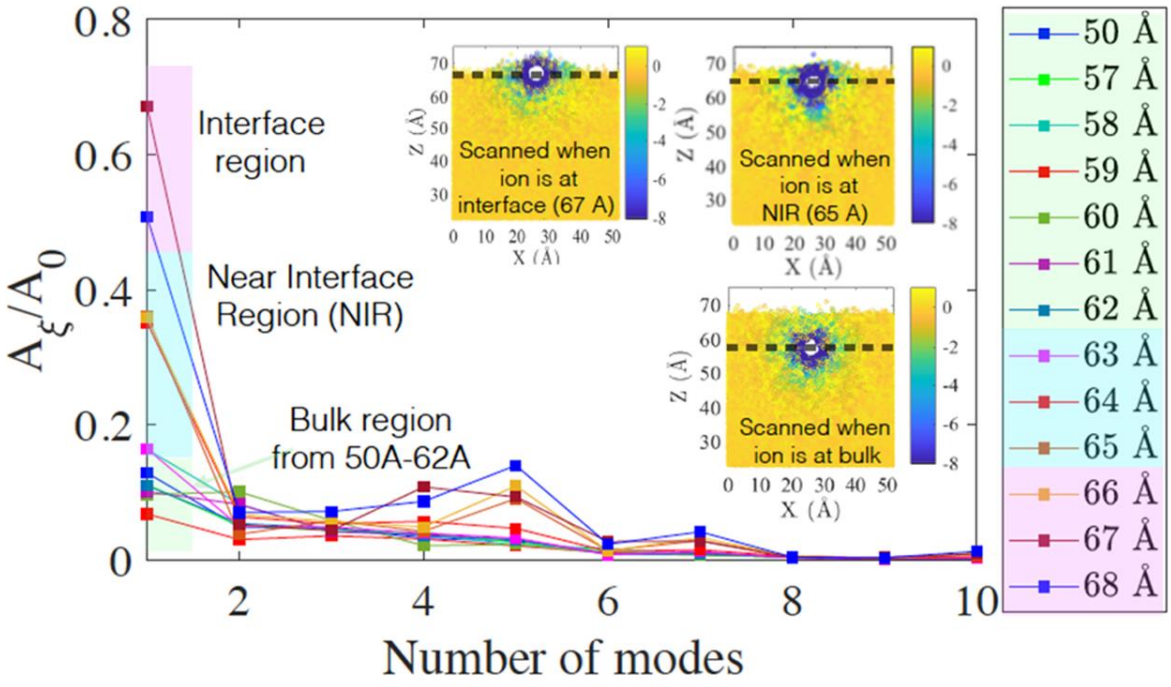

Figure 7.7 Variation of the parameter A_ξ/A_0 associated with a given mode for the different modes constituting the CWs for different ion positions. This parameter A_ξ/A_0 dictates the contribution of a given mode in the CW. The physical interpretation of A_ξ and A_0 are provided in the main text.

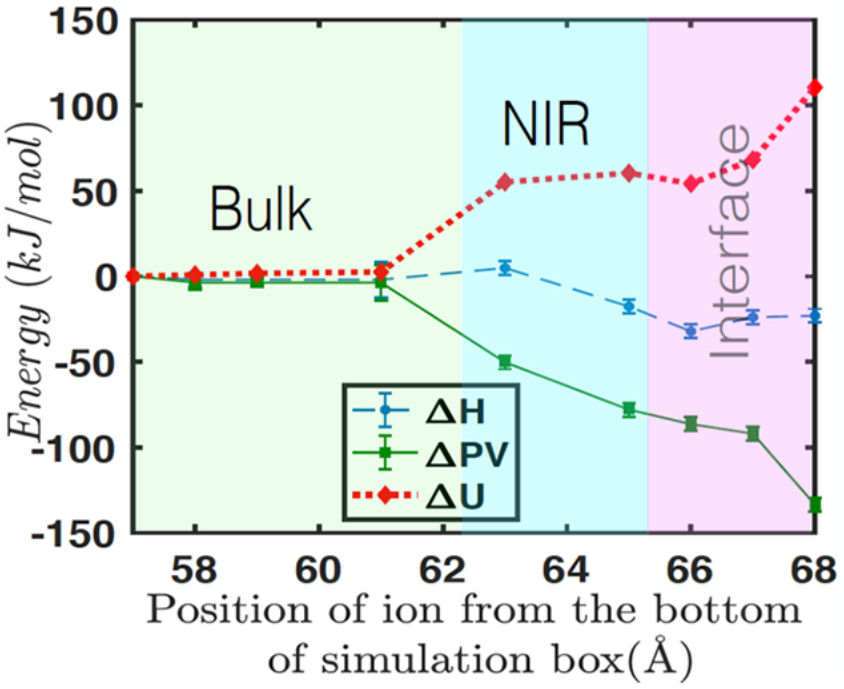

Figure 7.8 Variation of ΔU (change in internal energy), P−V work [or Δ(PV)], and ΔH with respect to the cation distance from the bottom of the simulation box.

7.3.3 Wave Characteristics of the Capillary Waves in the Presence of the Ion and the Resulting PV Work and the Change in Enthalpy

In order to pinpoint the actual cause for the significantly high negative enthalpy change associated with the ion transfer from the bulk to the interface, following the procedure elucidated in refs,[233,234] we first investigate the surface structure (or the wave characteristics) of the CWs fluctuations for different ion positions. The CW is composed of several modes (namely, 1−10) with mode 1 having the longest wavelength [or equivalently, representing the lower wavevector cutoff][234] allowed by the size of the simulation box. The contribution of each mode (or the

wavevector) to the CW is quantified in terms of the corresponding value of the dimensionless ratio A_ξ/A_0 associated with a given mode. Here A_ξ represents the surface area associated with a particular wavelength, accounting for all the roughness associated with the CW fluctuations,[234] and A_0 represents the projection area. We provide the detailed method to compute A_ξ. For the ion at the a/w interface, the CW (with augmented fluctuations, see Figure 7.5a) is dominated by only one mode (mode 1) associated with the longest wavelength (see Figure 7.7); this is evident from the fact that with the ion at the a/w interface the A_ξ/A_0 value for this mode is significantly higher than those associated with the other modes. Additionally, we study the ion-oxygen (oxygen of the water molecule) cylindrical radial distribution function $g(r)$ for two different locations of the ion (one in the bulk and one at the interface). As long as the value of this RDF is larger than unity, we can infer that the presence of the ions is affecting the water molecules, and from there, we can quantify the length scale l_{ion} over which the ion affects the water molecules. We witness $l_{ion,ion\text{-}at\text{-}interface} \gg l_{ion,ion\text{-}in\text{-}bulk}$, and $l_{ion,ion\text{-}at\text{-}interface} \approx 2.3$ nm signifies the length scale that dictates the range of influence of the ions on the water molecules with the ion at the interface. Given that $l_{ion,ion\text{-}at\text{-}interface}$ provides the radius of this zone of influence, the total length/diameter of the zone of influence l_{zone} should be twice this length, i.e., ~4.6 nm. l_{zone} provides a cut off that dictates the size of the simulation box, i.e., the simulations must be conducted in box such that $l \gg 10\sigma$ and $l > l_{zone}$. For the present case, we satisfy this condition by choosing $l = 5.2$ nm (see the "Materials and Methods" section or section 7.2), and obviously, the longest wavelength that dictates the ion−CW interactions is ~l. Given that the periodic boundary condition of the system would always imply that a second ion is present at a distance of l from the first ion, in which case $l < l_{zone}$, the water molecules within the simulation box would be influenced by this second ion yielding a wrong estimate of all the quantities.

Predominance of the contribution of a mode of a given wavelength (see Figure 7.7) ensures that the pressure fluctuations characterizing the CWs are significantly reduced with the ion at the interface. This is established, showing a much smaller (quantified by a larger negative value) of ΔP as the ion approaches the a/w interface. However, the CWs with the ion in the bulk have a uniform distribution of the contribution from the constituting modes (in other words, there is a uniform distribution of A_ξ/A_0 ratio corresponding to different modes with the ion in the bulk) (see Figure 7.7). This results in a larger value of pressure fluctuations, as evidenced by a larger value of ΔP with the ion in the bulk. This large difference in ΔP as the ion approaches the a/w interface from the bulk causes a significant lowering of the pressure−volume work $\Delta(PV) = V\Delta P + P\Delta V \approx V\Delta P$ (since the change in volume is negligible as the ion moves from the bulk to the a/w interface). This significantly negative $\Delta(PV)$ ensures a negative (or favorable) enthalpy change, i.e., $\Delta H = \Delta U + \Delta(PV) < 0$ with the ion at the interface (see Figure 6.4) despite a very large unfavorable (or positive) change in the internal energy (U). Therefore, we can make the second important inference of the paper: The negative (or favorable) ΔH witnessed here and in the previous papers[220,221] as the ion moves from the bulk to the interface is primarily due to the change in the pressure volume work associated with the wave structure of the CW fluctuations and not due to the redistribution of the water molecules. Also note that the ΔU appearing in Figure 7.8 which is the global ΔU and computed directly using LAMMPS is significantly different than the ΔU_{local} (discussed above) stemming from the fact that the consideration of an appropriate simulation volume (in our case) allows for (a) a less relative change (with respect to the total number of water molecules) of the number of surface water molecules and (b) for the ion-position-dependent change in dielectric constant.[235]

From the detailed wave-structure analysis of the CWs, we can paint a physical picture of how the ion at the interface triggers the CW fluctuations. As the ion approaches the interface, it deforms it locally. Such local interface deformation is energetically unfavorable, and the system tries to nullify it by smoothing the interface. The most energetically preferred mechanism for such smoothing is to develop a CW of longest possible wavelength supported by the simulation box size. This is the reason why with the ion at the interface one witnesses a predominance of A_ξ/A_0 associated with the mode with the longest wavelength.

It is useful to discuss here how this smoothing happens when the ion approaches the a/w interface for a small simulation box. Of course, exactly the same mechanism of smoothing will develop where the wave with the long wavelength would try to smooth the ion-induced local deformation of the a/w interface. Therefore, for this case of small simulation box as well, we witness a divergence of A_ξ/A_0 value with an increase in the wavelength or a decrease in the mode number. However, there is a very important difference between the cases corresponding to large and small simulation box sizes. If we integrate all the different values of A_ξ/A_0 for the different wave numbers and obtain the total area associated with the CW fluctuations (i.e., A/A_0), then we find that for the large simulation box A/A_0 ratio increases as the ion approaches the interface, whereas for the small simulation box A/A_0 ratio decreases as the ion approaches the interface. This can be directly associated with the fact that the overall CW fluctuations, which also directly dictate this integrated area ratio A/A_0, increase with the ion at the interface for large simulation box but get suppressed (due to pinning) with the ion at the interface for the small simulation box [in fact, for small simulation box, at a given mode number, $(A_\xi/A_0)_{\text{ion-at-interface}} < (A_\xi/A_0)_{\text{ion-in-bulk}}$].

Such weakened A/A_0 ratio with the ion at the interface for small simulation box leads to such variations of ΔH ($\Delta H > 0$) [Figure 7.9 below] and $-T\Delta S$ ($-T\Delta S < 0$) [Figure 7.9 below] that are

not commensurate with the ion adsorption process. In summary, therefore, even though the diverging nature of the CW amplitude with the wavelength is retained even for the small simulation box size, its impact needs to be quantified in terms of the variation of the overall integrated area, and these things are drastically different for the large and small simulation boxes.

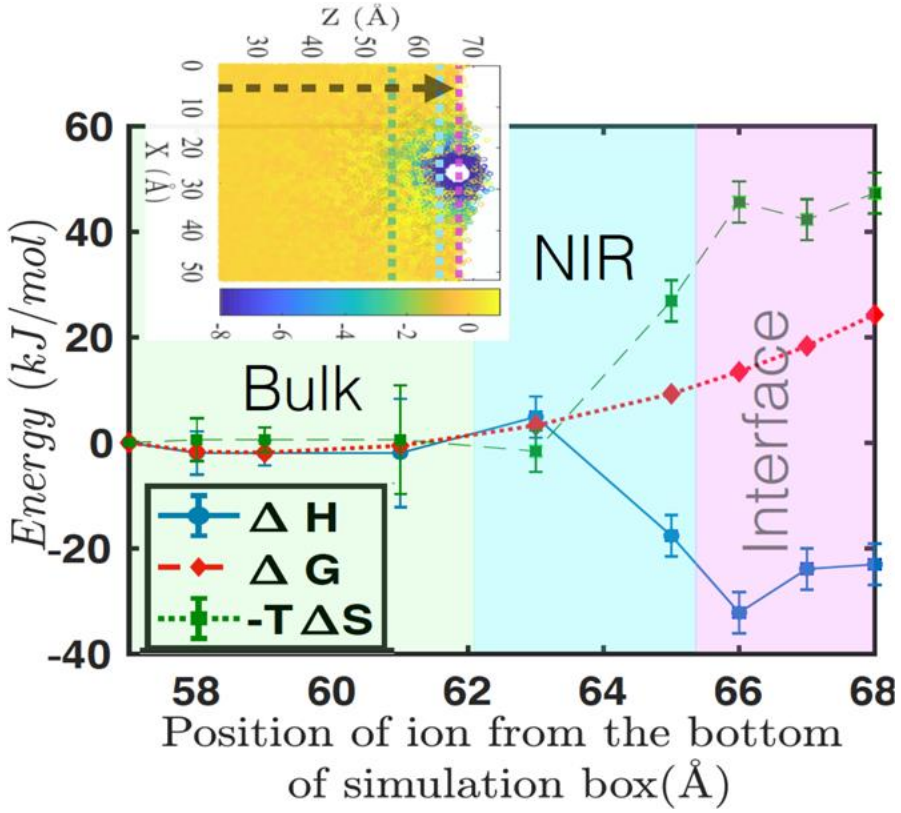

Figure 7.9 Variation of ΔH, −TΔS, and ΔG with respect to the cation distance from the bottom of the simulation box

7.3.4 Variation of the Enthalpy, Entropy, and Gibbs Free Energy

Finally, in Figure 7.9, we show the variation of ΔG and ΔH and the resulting $-T\Delta S = \Delta G - \Delta H$. The variations of these different energy components in Figure 7.9 are identical to those predicted in ref 221, as we use the same interaction potentials as ref 221. Critically, here very much like ref 221, we witness a decrease in entropy. However, ref 221 and other papers associated this entropy decrease to the ion-at-interface mediated dampening of CWs,[220,222] while we establish that the ion-at-interface actually augments the CW fluctuations [Figure 7.5a]. Thus, the question

is what reduces the entropy? Entropy reduction can be associated with the fact that with the ion at the interface the enhancement of the CW fluctuations is dominated by a single mode associated with longest wave- length, while with ion-at-bulk, the CW fluctuations are constituted by modes of multiple wavelengths (see Figure 7.7). Presence of the modes of multiple wavelengths enhances the mixing entropy for the case with the ion in the bulk, justifying the decrease in the entropy as the ion moves from the bulk to the a/w interface. We provide the detailed calculation procedure for the entropy change. This discovery of the physical cause of the entropy reduction is the third important inference of the paper: the negative (or unfavorable) ΔS witnessed here and previous papers,[220,221] as the ion moves from the bulk to the interface, is primarily due to the change in the mixing entropy of the different modes dictating with the wave structure of the CW fluctuations and not due to the suppression of the CW fluctuations.

7.4 Discussions

7.4.1 Importance of the Present Study in the Context of the Experiments Studying Ion Adsorption/Desorption at the Air−Water Interfaces

The behaviors of the ions at the interfaces have been attracting the attention of the research community for more than a century (see some of the excellent reviews on this topic in refs 214, 223-224). The initial interest in the topic was raised by the experimental findings that the surface tension of the aqueous salt solutions is larger than that of the pure water.[236] A depletion of ions (inorganic) from the a/w interface was associated with this increase.[237] For a major part of the previous century, such a depletion of inorganic ions from the a/w interface was a universally accepted notion. It is only in the past two decades that the researchers started to challenge this

idea and proposed highly sophisticated experimental techniques and atomistic simulations that established that there could be several inorganic ions that show propensity toward the a/w interface. These sophisticated experimental strategies, including vibrational sum frequency generation spectroscopy (VSFG),[238–243] second harmonic generation (SHG) spectroscopy,[244,245] high-pressure VUV photoelectron spectroscopy,[246] and X-ray photoelectron spec- troscopy,[247,248] provide significantly more comprehensive under- standing (as compared to the indirect strategies such as the measurement of the surface tension or surface potential of an electrolyte solution or using the evidence from hypothesized chemical reactions at the a/w interface) suggesting the preference (or the lack of it) of the ions toward the a/w interface. These sophisticated approaches have been able to confirm an attraction/repulsion of the ions toward the a/w interface and in the process validate the corresponding predictions from the MD simulations pinpointing the behavior of the ions toward the a/w interface. Combined experimental and simulation approaches confirm that certain ions are indeed attracted toward the a/w interface, while others are repelled.

In Table 7.1, we summarize the adsorption/desorption behaviors of different ions as revealed by these sophisticated spectroscopic experimental techniques and the corresponding MD simulations.

The extensive progress in determining if a given ion would adsorb at the a/w interface or not has shifted attention to the question: What are the physical mechanisms (driving forces) that dictate ion adsorption at the a/w interface?[224] Use of the MD simulations seems to be an ideal approach to answer this question; however, the force fields to be used for such MD simulations should be connected to the experimental findings. For example, the use of SHG spectroscopy allows quantification of the Gibbs free energy (ΔG) of the ion adsorption process by fitting the

Langmuir isotherm to the SHG response.[220,222,249] The force fields for the MD simulations should be chosen so that the corresponding ΔG predicted from the MD simulations should be close to the experimental result. This ΔG, thus obtained from the MD simulations, would of course help determine if the ion is attracted or repelled from the a/w interface. More importantly, it can be dissected to bring out the relative contributions of the enthalpy and the entropy changes in determining the overall ΔG (i.e, the overall ion adsorption/desorption process).[219,220,222] Our present paper becomes important at this dissection stage, or in other words, to provide the answer to this question: What are the physical mechanisms (driving forces) that dictate ion adsorption at the a/w interface? We establish the need to carry out the MD simulations with an appropriately large simulation box size that forbids the suppression of the CWs (as occurs in ref 220) and in the process helps to delineate the factors that contribute to the enthalpy and the entropy changes responsible for causing the ion adsorption/desorption at the a/w interface. Therefore, our work would ensure a better use of the experimental findings (e.g., the quantification of the ΔG for ion adsoprtion using the SHG approach) to develop the MD framework that is more capable of pinpointing the right driving forces needed for the ion adsorption/desorption. This is the central connection of our paper to the larger experimental community investigating the interactions between ion and a/w interface.

Table 7.1: Experiments on adsorption/desorption of inorganic ions at the air-water interface and supporting MD Simulations

Reference	Studied Ion and interface	Experimental Method	Main conclusions from experiments	Findings from the MD simulations
Otten et al.[220]	SCN^- at air-water interface	Resonance-enhanced second harmonic generation (SHG) spectroscopy	ΔG_{ads} is negative indicating a favorable adsorption at the air-water interface	MD simulations support the findings by providing a substantially negative value of ΔG (or ΔE) (where *E* is the Helmholtz free energy and $\Delta G = \Delta E$, as PV work is neglected) supporting such ion adsorption.
Peterson and Saykally [250]	Tetrabutyl-ammonium cation at air-water interface	Resonance-enhanced second harmonic generation (SHG) spectroscopy	ΔG_{ads} is negative indicating a favorable adsorption at the air-water interface	MD simulations in a different study confirms the observations.[251]

Perrine et al.[218]	K^+ and Li^+ ion at the air-water interface	X-ray photoelectron experiments	Li^+ ion shows a propensity to adsorb while K^+ ion does not at the air-water interface	MD simulations (218) support the findings
Tian et al.[252]	I^-, NO_3^-, NH_4^+, Cl^-, K^+, Na^+, and SO_4^{2-} ions at the air-water interface	Phase-sensitive sum-frequency vibrational spectroscopy	Relative tendencies of these different ions to accumulate at the air-water rank as (in decreasing order): I^-, NO_3^-, NH_4^+, Cl^-, K^+, Na^+, SO_4^{2-}	MD simulations (252) support these observations, except for the adsorption tendency of the NO_3^- and NH_4^+ ions.
Piatkowski et al.[216]	I^- and Cl^- ions at the air-water interface	Surface-specific femtosecond vibrational spectroscopy	Both I^- and Cl^- ions have large tendency to adsorb at the air-water interface, with I^- ion showing a much larger tendency	This paper does not carry our MD simulations; but previous MD papers have confirmed this observation qualitatively. (253)
Liu et al.[242]	Halide ions (from the sodium halide salts) at the air-	Vibrational sum frequency generation spectroscopy	Bromide and iodide ions have a greater propensity to absorb at the air-water interface as compared to the	MD simulations by Jungwirth and Douglas (254) and Caleman et al. (253) reproduce these findings on the relative

	water interface		Fluoride and Chloride ions; however, no quantification based on the bcorresponding Gibbs free energy of adsorption was provided	preference of the halide ions at the air-water interface
Raymond and Richmond [243]	Halide ions (from the sodium halide salts) at the air-water interface	Vibrational sum frequency generation spectroscopy	Very similar inferences as that of Liu et al. (242)	MD simulations by Jungwirth and Douglas (254) and Caleman et al. (253) reproduce these findings on the relative preference of the halide ions at the air-water interface
Mucha et al[253]	Halide ions from the acidic halides and Na^+ cations from the NaOH	Vibrational sum frequency generation spectroscopy	H_3O^+ and heavier halide ions are attracted while OH^- and Na^+ ions are repelled from the interface	MD simulations (255) confirm these observations

Gopalakrishnan et al.[254]	SO_4^{2-} and NH_4^+ ions	Vibrational sum frequency generation spectroscopy	SO_4^{2-} ions are repelled from the air-water interface and NH_4^+ ions approach the interface more closely than the Na^+ ions	MD simulations of previous papers (257) and this paper (256) confirm these observations.
Petersen and Saykally[244]	Azide (N_3^-) ion	Second harmonic generation (SHG) spectroscopy	Azide ions adsorb strongly to the air-water interface	MD simulations by Yang et al. (258) confirm this observation.
Petersen et al.[245]	Iodide (I^-) ion	Second harmonic generation (SHG) spectroscopy	Iodide ions adsorb strongly to the air-water interface	MD simulations (254) confirm this observation.
Petersen et al.[255]	SCN^- ion	Second harmonic generation (SHG) spectroscopy	SCN^- adsorb strongly to the air-water interface	MD simulations (259) confirm this observation.

Bohm et al.[256]	F^- ion from the CsF salt	Photoelectron spectroscopy	F^- ion is depleted from the air-water interface	MD simulations on the F^- ion obtained from the NaF salt confirms this observation (254)
Winter et al.[251]	Tetrabutyl ammonium ion and Iodide ion	Photoelectron spectroscopy	Both Tetrabutyl ammonium ion and Iodide ion are attracted to the air-water interface	MD simulations (251) confirm these observations
Ghosal et al.[247]	Bromide and Iodide ions from KBr and KI salts	X-ray photoelectron spectroscopy	Concentration of both bromide and iodide ions are enhanced at the air-water interface	MD simulations (247) confirm these observations
Cheng et al.[248]	Cl^- ion obtained from the NaCl and RbCl salts	X-ray photoelectron spectroscopy	Cl^- ions obtained from the NaCl showed a greater tendency to get attracted to the air-water interface as compared to the Cl^- ions obtained from the RbCl	MD simulations (248) confirm these observations

7.4.2 Significance of the Present Study: Technical and Broader Perspective

The purpose of this paper is to show how the appropriate accounting of the simulation system size is essential to understand the detailed mechanisms that dictate the adsorption of an ion at an a/w interface. The adsorption process is quantified from the corresponding variation of the Gibbs free energy, enthalpy, entropy, and internal energy.[219,220,222] These quantities depend on the parameters of the model used for the MD simulations. In contrast, a correct accounting of the simulation box size, which in turn allows us to capture the influence of the CWs appropriately, ensures that we pinpoint the right physical factors that dictate these changes. For example, in the present paper, we identify that with the ion at the interface, the *PV* work (and not the redistribution of the interfacial water molecules, as proposed by ref 220) is the main cause of the enthalpy change, while the lowering of mixing entropy (and not the suppression of the CW fluctuations, as proposed by ref 220) is the main cause of the entropy decrease. Therefore, our paper provides a generic framework that would serve as the microscope to analyze and dissect the fundamental forces that dictate the adsorption of the ions and other moieties at the a/w interface.

In Table 7.2, we list a large number of papers that have conducted the MD simulations of inorganic ions, inorganic gas molecules, organic molecules (some of which are known atmospheric pollutants, e.g., phenol), and nanoparticles interacting with the a/w interface using a simulation box size that is less than 10σ. The CW fluctuations, which are intrinsic to any a/w interface, are invariably suppressed in these calculations, thereby creating a situation where there might be an inappropriate prediction of the factors that dictate the ion (or other moiety)

adsorption/desorption at the a/w interface. All these studies need to be reanalyzed by considering a larger simulation box size and an appropriate accounting of the influence of the CWs (this is what our paper proposes a framework for) in order to pinpoint the appropriate physical mechanisms that dictate the interactions of the ions and other moieties with the a/w interface. Therefore, from a purely technical standpoint, our paper raises the issue of how to better capture the key physical principles that govern the behavior of ions, biomolecules, colloids, and so on at the a/w interface.

From the perspective of broader impact, our paper will contribute to a better understanding and analysis of all those phenomena where the adsorption/interaction of ion(s) with the a/w interface becomes important. These phenomena include the problems of (a) environmental chemistry [e.g., hydrolysis of SO_2 and N_2O_5 in cloud droplets leading to the formation of acid rain,[208] reaction of Cl^- ion with the sea salt aerosols (SSA) to form the Cl_2 gas in the marine troposphere leading to the depletion of the ozone layer,[209,257] uptake of OH^- ion by the SSA eventually catalyzing the formation of the environmentally hazardous sulfate particles,[204,258–261] nocturnal and tropospheric release of the Cl_2 gas caused by the reaction of the Cl^- with the nitrate radicals,[210,262] production of Br_2 gas by the reaction of the Br^- ion with the SSA[263] which can lead to an "ozone hole" in stratosphere,[264] and triggering foam

formation by the interaction of NaCl with the a/w interface in seawater],[265] (b) biology and chemical engineering [e.g., differential reaction probability of the kosmotropic and chaotropic ions with the proteins adsorbed at the a/w interface thereby dictating the protein dynamics at the a/w interface,[211] adosprtion of the ionic surfactants at the a/w interface dictating the processes such as detergency, emulsification, dispersion, coating, wetting, floatation, and oil recovery, and adsorption of EDL-supporting colloids at a/w interfaces for various applications, etc.], and (c)

fabrication of the semi- conductor thin-film transistors by using ionic liquids.[212,266] We provide detailed discussions on how these different applications will be potentially benefitted from a better physical understanding of the interactions between ions (and other moieties) with the a/ w interface, which our paper intends to do.

Table 7.2: List of Papers that have conducted MD simulations for the interactions of ions (and other moieties) with the air-water interface using a simulation box of size less than 10σ

Reference	Ion (or Other Moieties) simulated	Simulation box Size
Tuma et al. [267]	Cl^-, Br^-, I^-, and Na^+ generated from the Sodium halide salts	$x \times y \times z$ = 18.6Å×18.6Å×50Å
Jungwirth and Tobias[268]	F^-, Cl^-, Br^-, I^-, and Na^+ ions generated from the Sodium halide salts	$x \times y \times z$ = 30Å×30Å×100Å
Winter *et al.* [251]	Tetrabutylammonium and Iodide ion	$x \times y \times z$ = 31Å×31Å×100Å
Salvador *et al.* [269]	NO_3^- ion	$x \times y \times z$ = 26.4Å×26.4Å×100Å
Yang *et al.* [270]	Azide (N_3^-) ion	$x \times y \times z$ = 26.4Å×26.4Å×100Å
Jungwirth and Tobias[271]	Na^+ and Cl^- ions from the NaCl salt	$x \times y \times z$ = 30Å×30Å×100Å
Mucha *et al.* [253]	H_3O^+, Cl^-, Br^-, Na^+, OH^-, and I^- ions	$x \times y \times z$ = 30Å×30Å×100Å
Gopalakrishnan *et al.*[254]	SO_4^{2-} and NH_4^+ ions	$x \times y \times z$ = 30Å×30Å×100Å
Petersen *et al.* [255]	Na^+ and SCN^- ions	$x \times y \times z$ = 30Å×30Å×150Å
Roeselova *et al.* [272]	OH^- ion and O_3 species	$x \times y \times z$ = 30Å×30Å×100Å
Brown *et al.* [273]	Na^+ and I^- ions from the NaI salt	$x \times y \times z$ = 30Å×30Å×160Å
McCaffrey *et al.* [222]	SCN^- ion	$x \times y \times z$ = 21.3Å×19.7Å×40Å
Otten *et al.* [274]	SCN^- ion	$x \times y \times z$ = 20Å×20Å×40Å

Stern *et al.* [275]	I^- ion	$x \times y \times z$ = 15Å×15Å×70Å
Tse *et al.*[276]	Hydrated Excess Protons and Hydroxide Anions	$x \times y \times z$ = 31Å×31Å×100Å
Horinek *et al.* [277]	F^-, Cl^-, Br^-, I^-, Li^+, Na^+, K^+, and Cs^+ ions	$x \times y \times z$ = 30Å×30Å×90Å
Baer *et al.* [278]	H_3O^+ and OH^- ions	$x \times y \times z$ = 15Å×15Å×71.44Å
Wick *et al.* [279]	Na^+ and OH^- ions generated from NaOH	$x \times y \times z$ = 23.6Å×23.6Å×23.6Å
Wick *et al.* [280]	H_3O^+ ion	$x \times y \times z$ = 26Å×26Å×120Å
Roeselova *et al.* [281]	OH^- ion	$x \times y \times z$ = 30Å×30Å×100Å
Vieceli *et al.* [282]	OH^- ion and O_3 species	$x \times y \times z$ = 26.3Å×26.3Å×76.3Å
Minofar *et al.*[283]	CH_3COO^-, NO_3^-, and Mg^{2+} ions	$x \times y \times z$ = 30Å×30Å×100Å
Hrobárik *et al.* [284]	Choline, tetraalkylammonium (TAA), and Na^+ cations, and SO_4^{2-} and Cl^- anions	$x \times y \times z$ = 31Å×31Å×100Å
Dang *et al.*[285]	H_3O^+ ion	$x \times y \times z$ = 26.3Å×26.3Å×26.3Å
Petersen *et al.*[286]	H_3O^+ ion	$x \times y \times z$ = 31.2Å×31.2Å×75Å
Yiapanis *et al.* [287]	Graphitic nanoparticles	$x \times y \times z$ = 400Å×25.5Å×100Å
Baer *et al.* [288]	SO_2 molecule	$x \times y \times z$ = 15Å×15Å×71.44Å
Murdachaew *et al.*[289]	NO_2 molecule	$x \times y \times z$ = 15Å×15Å×71.44Å
Kusaka *et al.* [290]	Phenol (as an example of a neutral amphiphilic organic compound)	$x \times y \times z$ = 25Å×25Å×150Å

Martins-Costa *et al.* [291]	Formaldehyde, acetaldehyde, benzaldehyde	$x \times y \times z$ = 24.7Å×24.7Å×130Å
Vacha *et al.*[292]	Polycyclic aromatic hydrocarbons like naphthalene, anthracene, and phenanthrene	$x \times y \times z$ = 23.5Å×23.5Å×200Å
Vacha *et al.*[292]	Polycyclic aromatic hydrocarbons like benzene and naphthalene	$x \times y \times z$ = 18.6Å×18.6Å×388Å
Chen *et al.*[293]	Dimethyl Sulfoxide and Methanesulfonic Acid	$x \times y \times z$ = 30Å×30Å×100Å
Blower *et al.*[294]	Malonic acid	$x \times y \times z$ = 30Å×30Å×30Å

7.4.3 Results for the simulation in a smaller simulation box

We perform a new set of simulations to evaluate the effect of the size of the simulation box. We consider a simulation box size x × y × z = 20 Å × 20 Å × 100 Å in the canonical ensemble (NVT) at 300 K. In total, the simulation consists of 288 SPC/E water molecules and one cation, occupying a volume of 20 Å × 20 Å × 20 Å at equilibrium (i.e., the z height of the equilibrated water mass is 20 Å from the bottom of the simulation box) [see Fig. 7.10(a)]. Here too the same interaction potentials are used for calculating the interactions between the different species . Also, the potential of mean force (PMF) for all the systems are calculated by employing the umbrella sampling with the ion placed in the simulation box. The z-location for the ion is constrained at 6 different values (ranging from 15 Å to 25 Å from the bottom of the simulation box) by employing a bias potential with a spring constant of K_{bias}=836.8 kJ/mol/nm^2 along z direction. Therefore, our energy data are obtained for 6 values of the z location for the ion. The error bar is obtained following the same procedure as employed in the simulations that use a large simulation box size (see section 7.2).

In Fig. 7.10(b), we provide the variation of Δ(PV), ΔH, and ΔU for different ion positions obtained from the simulations for this small simulation box. We witness that Δ(PV) is not sufficient to change the sign of ΔH, making it positive as ΔU is also large and positive. Furthermore in Fig. 7.10(c), we provide the variation of ΔH, −TΔS, and ΔG for different ion positions obtained from the simulations for this small simulation box. Most surprisingly, we witness negative –TΔS, i.e.,the entropy change (as ion moves from the bulk to the interface) is positive. Therefore, the variation in the entropy and the enthalpy associated with the ion

movement from the bulk to the interface is just the opposite to what has been reported previously (7-9) and we associate that to the consideration of an erroneous simulation box size. Finally, we attempt to understand the role of the small simulation box on the CW fluctuations. When periodic boundary condition is applied to a water/vapor interface simulation, the corrugation at each end along one direction (X or Y) must match. In other words, the two red lines in Fig. 7.11a must have the same profile as would the two black lines (see Fig. 7.11a). The

overlapping of these two set of profiles results in an unnatural height profile at each corner (labeled as red boxes, see Fig. 7.11 b,c). In a significantly smaller simulation box ($L \approx 6\sigma$), the capillary wave is not able to develop fully, thereby ensuring that the detrimental impact of this unnatural height profile at each corner (associated with a periodic boundary condition) is extremely significant [see Fig. 7.11c]. On the other hand, in a larger simulation box ($L \approx 16\sigma$), this impact of this unnatural height profile at each corner is relatively small so that the capillary

wave is able to develop out of the corner region [see Fig. 7.11b]. Comparing the two cases of purewater surface corrugations obtained by both smaller and larger simulation boxes, we can infer that the relatively larger significance of the unnatural height profile at each corner caused by the periodic boundary conditions ensure that much of the surface fluctuation information is missing for the simulation that uses a smaller simulation box. Fig. 7.12 shows the dependence of surface fluctuation on the ion locations for the simulations carried out using a small simulation box. One can clearly see that the consideration of a small simulation box leads to a dampening of the CW fluctuations as the ion moves from the bulk to the interface. Fig. 7.12 is in complete contrast to what we report for larger simulation box size and firmly establishes our hypothesis that the dampening of the CW fluctuations (as proposed previously, see Refs. 276-278) can solely be attributed to the selection of too small a simulation box.

Finally in Fig. 7.13(a), we provide the variation of the ratio A_ξ/A_0 , characterizing the amplitude of the CWs, with the number of modes for the simulations conduced in this small simulation box. We find that for this case as well the A_ξ/A_0 diverges with the wavelength (i.e., has the highest values for mode 1). However, the overall area A/A_0, characterizing the CW fluctuations and obtained by integrating/summing A_ξ/A_0 for different modes, decreases as the ion approaches the interface [see Fig. 7.13(b)]. This is in sharp contrast to what happens for the case of large simulation box and can be attributed to the artificial pinning of the CWs in a small simulation box.

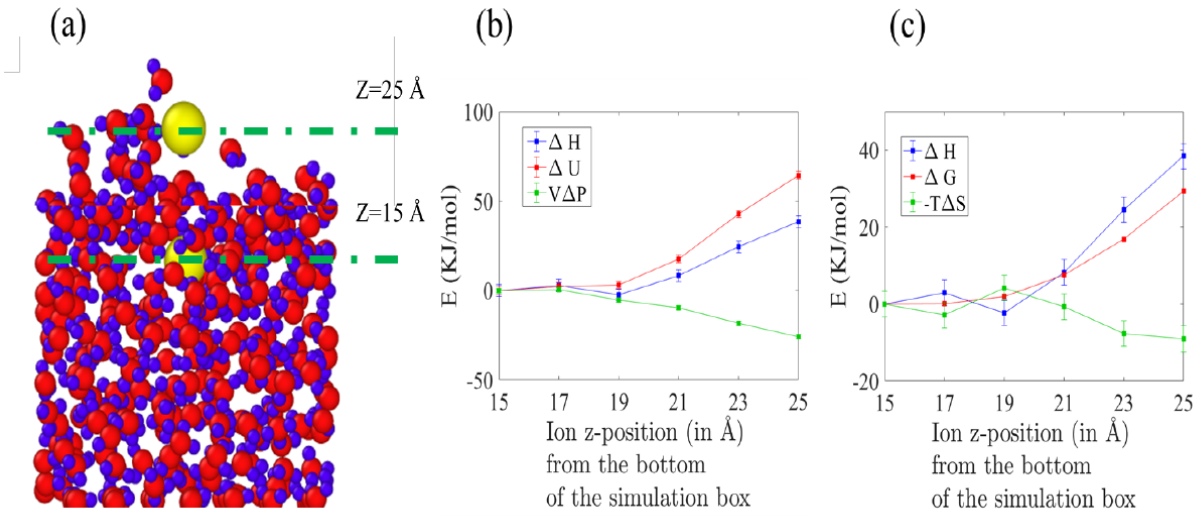

Figure 7.10: (a) The simulation set up with small simulation box size. (b) Variation of Δ(PV), ΔH, and ΔU for different ion positions obtained from the simulations for this small simulation box. (c) Variation of ΔH, −TΔS, and ΔG for different ion positions obtained from the simulations for this small simulation box. In (b) and (c), we consider the movement of the ion from the bulk (quantified by the ion z position with z<16 Å) to the a/w interface (quantified by the ion z position with z≥20 Å).

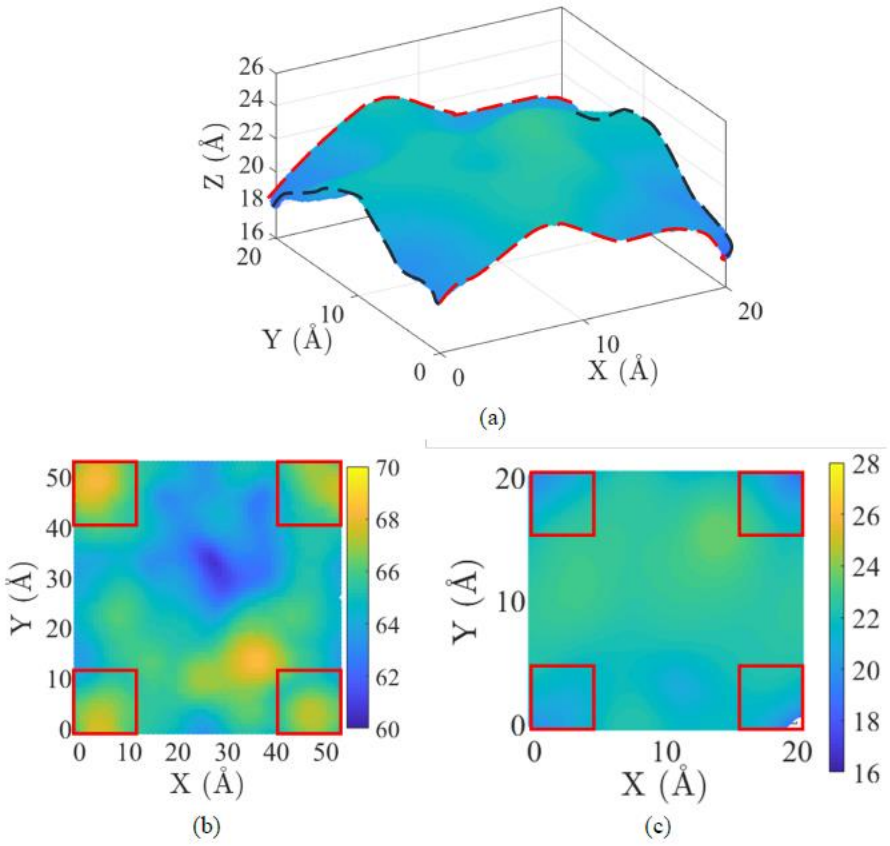

Figure 7.11: (a) A 3D view of a liquid-vapor interface showing the effect of the periodic boundary conditions on the corrugations at the boundaries. A schematic of unphysical surface corrugation due to the application of the periodic boundary condition to a system with (b) a large simulation volume and (c) a small simulation volume.

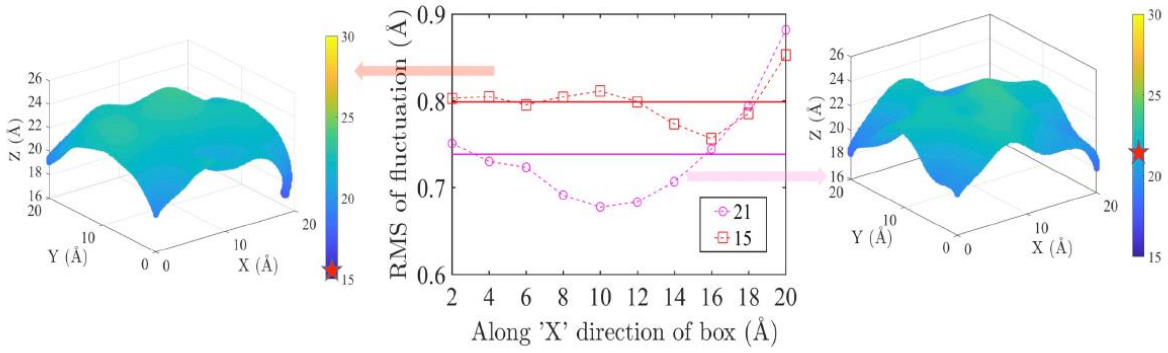

Figure 7.12: The RMS (Root Mean Square) of the CW fluctuations with the cation at two different Z locations (in Å) for simulations using a small simulation box: Z=15 Å represents the ion in the bulk, while Z= 21 Å represents the ion at the interface.

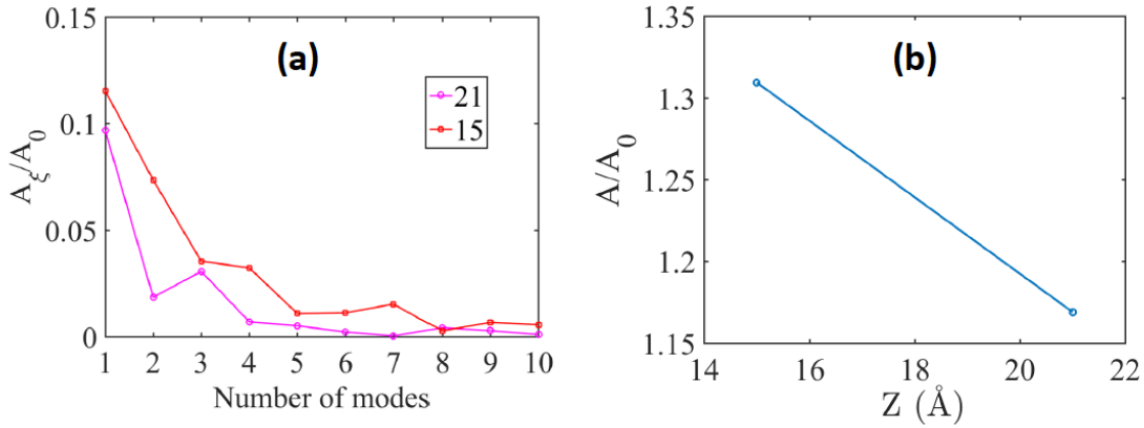

Figure 7.13: (a) Variation of the ratio Aξ / A0 characterizing the amplitude of the CWs, with the number of modes for two different Z values (in Å) of the ion (Z=15 Å represents the ion in the bulk, while Z= 21 Å represents the ion at the interface). (b) Ratio of A/A0 (where A represents the sum of A_ξ corresponding to all the modes) as a function of the ion position.

7.5 Conclusions

We provide atomistic simulations-based evidence that establishes that the fluctuations of the CWs are enhanced as the ion moves from the bulk to the a/w interface. Further analyses establish

that wave structure of the CWs with the ion at the interface is dominated by the mode with the longest wavelength. This leads to a drastic reduction in the pressure and the pressure−volume work, leading to the drastic enthalpy reduction. Finally, we also establish that the structural features of the CWs ensures a significant decrease in the mixing entropy with the ion at the interface and is the primary cause of the entropy reduction.

Our simulations are carried out with a generic cation and generic anion (results not reported). However, we anticipate that our simulation approach that emphasizes on the appropriate selection of the simulation volume and a subsequent analysis of the wave structure of the CWs would be critical to quantify the interaction of specific cations and anions with the a/w interface. Furthermore, the presented simulation methodology will also be useful to better under- stand more involved systems such as the system studying interaction of a pair of similar and oppositely charged ions with the a/w interface,[221] system studying the ion-a/w interaction in the presence of a solid substrate,[222] and so on.

8. Conclusions and outlook

8.1 Thesis summary

This dissertation focuses on providing new insights on various thermodynamic and dynamic properties of multiple water-ion-2D materials related phenomena, including, wetting, water flow, and ion adsorption. All these physioco-chemical problems occur at the liquid-graphene and liquid-air interfaces and are probed over a nanometer scale. Molecular dynamics simulations methods have been accordingly employed to investigate these problems. These conduced simulations have shed light on understanding these problems, including (1) the wetting dynamics of nano-structured graphene (see Chapter 3), (2) the water permeation through holey-graphene membrane with and without the present of external pressure gradient (see Chapter 4-6), and (3) energetics analysis of the ion adsorption at the air/water interface (see Chapter 7). By solving those problems, his dissertation improves our understandings on utilizing newly emerging 2D materials as functionalized surfaces. In this dissertation, besides the water wetting and permeation behaviors, ion-water and ion-ion correlations are specifically considered. The following sections summarize the key findings of the thesis and also provide some outlooks that pinpoint the future directions.

8.2 Key scientific findings and future directions

8.2.1 Wetting dynamics of nano-structured graphene (Chapter 3)

This chapter focused on the spreading of a droplet on a nano-structured graphene sheet. . Microscale experiments report that when a liquid drop rolls on the superhydrophobic (SH) surface (consisting of microscale pillars), the drop three-phase contact line (TPCL) remains pinned on the pillar edges and the rolling occurs by the bending of the air-water interface of the drop to an angle that can exceed 180°. Our detailed nanoscale MD simulations confirmed the exact same mechanism of drop dynamics on a SH surface: we considered drop spreading (instead of rolling) and the spreading occurred by the bending of the air-water interface of the liquid drop with the TPCL remaining pinned on the nanopillars of the SH surface. This finding confirmed the universal mechanism of drop dynamics on SH surface that transcends the length scale as well as the nature of the drop motion.

8.2.2 Water interactions with holey-graphene membrane (Chapter 4-6)

Nano-porous graphene, or holey-graphene, is proposed to be able to serve as a membrane for reverse osmosis desalination. This dissertation first explored the possibility of utilizing holey graphene as a catalysis carrier in an aqueous environment chemical reaction. Accordingly, the dissertation established that a droplet could exhibit imbibition behavior when it is placed on top of a holey-graphene membrane. Certain combinations of the structure parameters enhanced the effective wetting area, which improved the catalysis kinetics and showed that holey graphene membrane could be an ideal material in many related fields. Second, the permeation of water flow through the holey graphene was studied in details for the first time. Multiple levels of

pressure were applied to drive the flow through the membrane, and it was found that the flow was controlled by the capillary force during the penetration in the channel created by two adjacent holey-graphene sheets; accordingly, the flow did not follow the Darcy's law.. Lastly, the wetting enhancement of holey graphene membrane was found to be even more effective when a pressure was added to the system and removed shortly afterwards. In other words, in presence of the external force perturbation, the droplet imbibition in a holey graphene membrane was found to be much more stable and effective.

8.2.3 Ion adsorption at the air-water interface (Chapter 7)

The problem of ion removal from seawater using a nano-porous membrane revealed that the ion-water and ion-ion correlations have been typically ignored or treated without care. However, the ion hydration and dehydration processes are very complicated and affect the understanding of the desalination process. The ion is not likely to fully dehydrate in an aqueous environment. However, the situation could be different at the air/water or solid/water interface. In this dissertation, we discover significant flaws in the current understanding of the thermodynamics of ion adsorption at the air-water interface. We discovered that when an ion was partially dehydrated near the Gibbs dividing surface, it caused a large energy penalty. Meanwhile, the pressure of the system decreased, while the volume remained the same: the consequent reduction in the pressure-volume work is the essential factor that balanced the energy penalty due to the ion dehydration. During the analysis, it was discovered found that the ion at the air-water interface enhanced the capillary waves, while previous studied reported an ion-adsorption-induced suppression of the capillary waves at the air-water interface. Furthermore, the ion

merely enhanced the longest allowed wave mode, which reduced the system mixing entropy. The observations offered a new perspective to revisit the thermodynamics of the well-established ion adsorption behaviors.

8.3 Outlook

In this dissertation, I have investigated the ion-water-2D materials interactions to demonstrate the potential of 2D materials when they are involved in a series of physical and chemical effects. Through this dissertation, hope it provide useful information and perspectives to experimentalists to thoroughly understand the controlling mechanisms involved in several effects pertaining to water-2D-Materials-ion interactions. Meanwhile, there are several related problems worth mentioning. For example, the ion-water correlation at the solid/liquid interface of other 2D materials. Solid/liquid interface is intrinsically different from the air/liquid interface and this becomes particularly interesting at the interfaces of non-graphene 2D materials (e.g., hexagonal boron nitride, MoS_2, black phosphorous, MXene, etc.). Other interesting problems can be probing the air-water adsorption of other ions, ion-pairs, organic molecules, nanoparticles, polymers, etc. I hope the different methods and insights developed in this dissertation will be critical in probing these problems.

Reference

(1) Nicholson, D.; Quirke, N. Ion Pairing in Confined Electrolytes. **2003**, No. January. https://doi.org/10.1080/0892702031000078427.

(2) Roy, S.; Baer, M. D.; Mundy, C. J.; Schenter, G. K. Supporting Information : Marcus Theory Of. No. 1.

(3) Phys, J. C.; Fyta, M.; Netz, R. R.; Fyta, M.; Netz, R. R. Ionic Force Field Optimization Based on Single-Ion and Ion-Pair Solvation Properties : Going beyond Standard Mixing Rules Ionic Force Field Optimization Based on Single-Ion and Ion-Pair Solvation Properties : Going beyond Standard Mixing Rules. **2013**, *124103* (February 2012). https://doi.org/10.1063/1.3693330.

(4) Li, D.; Kaner, R. B. Graphene-Based Materials. **2008**, *320* (May), 1170–1172.

(5) Rafiee, J.; Mi, X.; Gullapalli, H.; Thomas, A. V; Yavari, F.; Shi, Y.; Ajayan, P. M.; Koratkar, N. A. Wetting Transparency of Graphene. *Nat. Mater.* **2012**, *11*, 217.

(6) Li, Z.; Wang, Y.; Kozbial, A.; Shenoy, G.; Zhou, F.; McGinley, R.; Ireland, P.; Morganstein, B.; Kunkel, A.; Surwade, S. P.; et al. Effect of Airborne Contaminants on the Wettability of Supported Graphene and Graphite. *Nat. Mater.* **2013**. https://doi.org/10.1038/nmat3709.

(7) Jiang, D. E.; Cooper, V. R.; Dai, S. Porous Graphene as the Ultimate Membrane for Gas Separation. *Nano Lett.* **2009**. https://doi.org/10.1021/nl9021946.

(8) Sun, B.; Huang, X.; Chen, S.; Munroe, P.; Wang, G. Porous Graphene Nanoarchitectures: An Efficient Catalyst for Low Charge-Overpotential, Long Life, and High Capacity

Lithium-Oxygen Batteries. *Nano Lett.* **2014**. https://doi.org/10.1021/nl500397y.

(9) O'Hern, S. C.; Stewart, C. A.; Boutilier, M. S. H.; Idrobo, J. C.; Bhaviripudi, S.; Das, S. K.; Kong, J.; Laoui, T.; Atieh, M.; Karnik, R. Selective Molecular Transport through Intrinsic Defects in a Single Layer of CVD Graphene. *ACS Nano* **2012**. https://doi.org/10.1021/nn303869m.

(10) Xiao, J.; Mei, D.; Li, X.; Xu, W.; Wang, D.; Graff, G. L.; Bennett, W. D.; Nie, Z.; Saraf, L. V.; Aksay, I. A.; et al. Hierarchically Porous Graphene as a Lithium-Air Battery Electrode. *Nano Lett.* **2011**. https://doi.org/10.1021/nl203332e.

(11) Rollings, R. C.; Kuan, A. T.; Golovchenko, J. A. Ion Selectivity of Graphene Nanopores. *Nat. Commun.* **2016**. https://doi.org/10.1038/ncomms11408.

(12) O'Hern, S. C.; Jang, D.; Bose, S.; Idrobo, J. C.; Song, Y.; Laoui, T.; Kong, J.; Karnik, R. Nanofiltration across Defect-Sealed Nanoporous Monolayer Graphene. *Nano Lett.* **2015**. https://doi.org/10.1021/acs.nanolett.5b00456.

(13) Sint, K.; Wang, B.; Král, P. Selective Ion Passage through Functionalized Graphene Nanopores. *J. Am. Chem. Soc.* **2008**. https://doi.org/10.1021/ja804409f.

(14) Surwade, S. P.; Smirnov, S. N.; Vlassiouk, I. V; Unocic, R. R.; Veith, G. M.; Dai, S.; Mahurin, S. M. Water Desalination Using Nanoporous Single-Layer Graphene. *Nat. Nanotechnol.* **2015**. https://doi.org/10.1038/nnano.2015.37.

(15) Cohen-Tanugi, D.; Grossman, J. C. Water Desalination across Nanoporous Graphene. *Nano Lett.* **2012**. https://doi.org/10.1021/nl3012853.

(16) Cohen-Tanugi, D.; McGovern, R. K.; Dave, S. H.; Lienhard, J. H.; Grossman, J. C.

Quantifying the Potential of Ultra-Permeable Membranes for Water Desalination. *Energy Environ. Sci.* **2014**. https://doi.org/10.1039/c3ee43221a.

(17) Wang, E. N. Water Desalination: Graphene Cleans up Water. *Nature Nanotechnology*. 2012. https://doi.org/10.1038/nnano.2012.153.

(18) A, B.; Hummer, G.; Rasaiah, J. C.; Noworyta, J. P. Water Conduction through the Hydrophobic Channel of a Carbon Nanotube. **2001**, *414* (November), 188–190.

(19) Holt, J. K.; Park, H. G.; Wang, Y.; Stadermann, M.; Artyukhin, A. B.; Grigoropoulos, C. P.; Noy, A.; Bakajin, O. Sub – 2-Nanometer Carbon Nanotubes. **2006**, *312* (May), 1034–1038.

(20) Phys, J. C. How Fast Does Water Flow in Carbon Nanotubes ? **2014**, *094701* (October 2012). https://doi.org/10.1063/1.4793396.

(21) Falk, K.; Sedlmeier, F.; Joly, L.; Netz, R. R.; Lyon, D. Molecular Origin of Fast Water Transport in Carbon Nanotube Membranes : Superlubricity versus Curvature Dependent Friction. **2010**, 4067–4073. https://doi.org/10.1021/nl1021046.

(22) Secchi, E.; Marbach, S.; Niguès, A.; Stein, D.; Siria, A.; Bocquet, L. Massive Radius-Dependent Flow Slippage in Carbon Nanotubes. *Nat. Publ. Gr.* **2016**, *537* (7619), 210–213. https://doi.org/10.1038/nature19315.

(23) Cohen-Tanugi, D.; Grossman, J. C. Water Permeability of Nanoporous Graphene at Realistic Pressures for Reverse Osmosis Desalination. *J. Chem. Phys.* **2014**. https://doi.org/10.1063/1.4892638.

(24) Cohen-Tanugi, D.; Grossman, J. C. Mechanical Strength of Nanoporous Graphene as a

Desalination Membrane. *Nano Lett.* **2014**. https://doi.org/10.1021/nl502399y.

(25) Anand, A.; Unnikrishnan, B.; Mao, J. Y.; Lin, H. J.; Huang, C. C. Graphene-Based Nanofiltration Membranes for Improving Salt Rejection, Water Flux and Antifouling–A Review. *Desalination*. 2018. https://doi.org/10.1016/j.desal.2017.12.012.

(26) Aghigh, A.; Alizadeh, V.; Wong, H. Y.; Islam, M. S.; Amin, N.; Zaman, M. Recent Advances in Utilization of Graphene for Filtration and Desalination of Water: A Review. *Desalination*. 2015. https://doi.org/10.1016/j.desal.2015.03.024.

(27) Hummer, G.; Pratt, L. R.; Garcia, A. E. Free Energy of Ionic Hydration. *J. Phys. Chem.* **1996**. https://doi.org/10.1021/jp951011v.

(28) Hummer, G.; Pratt, L. R.; García, A. E. Hydration Free Energy of Water. *J. Phys. Chem.* **1995**. https://doi.org/10.1021/j100038a062.

(29) Åqvist, J. Ion-Water Interaction Potentials Derived from Free Energy Perturbation Simulations. *J. Phys. Chem.* **1990**. https://doi.org/10.1021/j100384a009.

(30) Shirts, M. R.; Pande, V. S. Solvation Free Energies of Amino Acid Side Chain Analogs for Common Molecular Mechanics Water Models. *J. Chem. Phys.* **2005**. https://doi.org/10.1063/1.1877132.

(31) Straatsma, T. P.; Berendsen, H. J. C. Free Energy of Ionic Hydration: Analysis of a Thermodynamic Integration Technique to Evaluate Free Energy Differences by Molecular Dynamics Simulations. *J. Chem. Phys.* **1988**. https://doi.org/10.1063/1.455539.

(32) Zwanzig, R. *Nonequilibrium Statistical Mechanics*; Oxford University Press, 2001.

(33) Barthlott, W.; Neinhuis, C. Purity of the Sacred Lotus, or Escape from Contamination in

Biological Surfaces. *Planta* **1997**, *202* (1), 1–8. https://doi.org/10.1007/s004250050096.

(34) Gao, X.; Jiang, L. Water-Repellent Legs of Water Striders. *Nature* **2004**, *432* (7013), 36. https://doi.org/10.1038/432036a.

(35) Deng, X.; Mammen, L.; Butt, H.-J.; Vollmer, D. Candle Soot as a Template for a Transparent Robust Superamphiphobic Coating. *Science (80-.).* **2012**, *335* (6064), 67 LP – 70. https://doi.org/10.1126/science.1207115.

(36) Blossey, R. Self-Cleaning Surfaces — Virtual Realities. *Nat. Mater.* **2003**, *2* (5), 301–306. https://doi.org/10.1038/nmat856.

(37) Zheng, Y.; Bai, H.; Huang, Z.; Tian, X.; Nie, F.-Q.; Zhao, Y.; Zhai, J.; Jiang, L. Directional Water Collection on Wetted Spider Silk. *Nature* **2010**, *463*, 640.

(38) Zhang, X.; Shi, F.; Niu, J.; Jiang, Y.; Wang, Z. Superhydrophobic Surfaces: From Structural Control to Functional Application. *J. Mater. Chem.* **2008**. https://doi.org/10.1039/b711226b.

(39) Yang, Y.; Wang, P.; Zhang, Z.; Liu, H.; Zhang, J.; Zhuang, J.; Wang, X. Nanowire Membrane-Based Nanothermite: Towards Processable and Tunable Interfacial Diffusion for Solid State Reactions. *Sci. Rep.* **2013**, *3*, 1694.

(40) Zhu, J.; Hsu, C.-M.; Yu, Z.; Fan, S.; Cui, Y. Nanodome Solar Cells with Efficient Light Management and Self-Cleaning. *Nano Lett.* **2010**, *10* (6), 1979–1984. https://doi.org/10.1021/nl9034237.

(41) de Gennes, P. G. Wetting: Statics and Dynamics. *Rev. Mod. Phys.* **1985**, *57* (3), 827–863. https://doi.org/10.1103/RevModPhys.57.827.

(42) Bonn, D.; Eggers, J.; Indekeu, J.; Meunier, J.; Rolley, E. Wetting and Spreading. *Rev. Mod. Phys.* **2009**, *81* (2), 739–805. https://doi.org/10.1103/RevModPhys.81.739.

(43) Snoeijer, J. H.; Andreotti, B. Moving Contact Lines: Scales, Regimes, and Dynamical Transitions. *Annu. Rev. Fluid Mech.* **2013**, *45* (1), 269–292. https://doi.org/10.1146/annurev-fluid-011212-140734.

(44) Dussan, E. B.; Dussan, V. E. B. On the Spreading of Liquids on Solid Surfaces: Static and Dynamic Contact Lines. *Annu. Rev. Fluid Mech.* **1979**. https://doi.org/10.1146/annurev.fl.11.010179.002103.

(45) Voinov, O. V. Hydrodynamics of Wetting. *Fluid Dyn.* **1976**, *11* (5), 714–721. https://doi.org/10.1007/BF01012963.

(46) Tanner, L. H. The Spreading of Silicone Oil Drops on Horizontal Surfaces. *J. Phys. D. Appl. Phys.* **1979**, *12* (9), 1473–1484. https://doi.org/10.1088/0022-3727/12/9/009.

(47) Cox, R. G. The Dynamics of the Spreading of Liquids on a Solid Surface. Part 1. Viscous Flow. *J. Fluid Mech.* **1986**, *168*, 169–194. https://doi.org/DOI: 10.1017/S0022112086000332.

(48) EGGERS, J.; STONE, H. A. Characteristic Lengths at Moving Contact Lines for a Perfectly Wetting Fluid: The Influence of Speed on the Dynamic Contact Angle. *J. Fluid Mech.* **2004**, *505*, 309–321. https://doi.org/DOI: 10.1017/S0022112004008663.

(49) Hocking, L. M. Rival Contact-Angle Models and the Spreading of Drops. *J. Fluid Mech.* **1992**, *239*, 671–681. https://doi.org/DOI: 10.1017/S0022112092004579.

(50) Eggers, J. Existence of Receding and Advancing Contact Lines. *Phys. Fluids* **2005**, *17* (8),

82106. https://doi.org/10.1063/1.2009007.

(51) Ngan, C. G.; Dussan V., E. B. On the Nature of the Dynamic Contact Angle: An Experimental Study. *J. Fluid Mech.* **1982**, *118*, 27–40. https://doi.org/DOI: 10.1017/S0022112082000949.

(52) Seebergh, J. E.; Berg, J. C. Dynamic Wetting in the Low Capillary Number Regime. *Chem. Eng. Sci.* **1992**, *47* (17–18), 4455–4464. https://doi.org/10.1016/0009-2509(92)85123-S.

(53) Sinha, S.; Padia, V.; Bae, K. Il; Chen, G.; Das, S. Effect of Electric Double Layer on Electro-Spreading Dynamics of Electrolyte Drops. *Colloids Surfaces A Physicochem. Eng. Asp.* **2017**, *514*, 209–217. https://doi.org/https://doi.org/10.1016/j.colsurfa.2016.11.031.

(54) Blake, T. D. The Physics of Moving Wetting Lines. *J. Colloid Interface Sci.* **2006**, *299* (1), 1–13. https://doi.org/https://doi.org/10.1016/j.jcis.2006.03.051.

(55) Blake, T. D.; Shikhmurzaev, Y. D. Dynamic Wetting by Liquids of Different Viscosity. *J. Colloid Interface Sci.* **2002**, *253* (1), 196–202. https://doi.org/https://doi.org/10.1006/jcis.2002.8513.

(56) Blake, T. D.; Haynes, J. M. Kinetics of Liquid Liquid Displacement. *J. Colloid Interface Sci.* **1969**. https://doi.org/10.1016/0021-9797(69)90411-1.

(57) Schneemilch, M.; Hayes, R. A.; Petrov, J. G.; Ralston, J. Dynamic Wetting and Dewetting of a Low-Energy Surface by Pure Liquids. *Langmuir* **2002**. https://doi.org/10.1021/la980476k.

(58) Snoeijer, J. H. Free-Surface Flows with Large Slopes: Beyond Lubrication Theory. *Phys.*

Fluids **2006**, *18* (2), 21701. https://doi.org/10.1063/1.2171190.

(59) Kistler, S. F. Hydrodynamics of Wetting. *Surfactant Sci. Ser.* **1993**.

(60) Bracke, M.; Voeght, F.; Joos, P. The Kinetics of Wetting: The Dynamic Contact Angle. In *Trends in Colloid and Interface Science III*; 2007. https://doi.org/10.1007/bfb0116200.

(61) Kim, J.-H.; Kavehpour, H. P.; Rothstein, J. P. Dynamic Contact Angle Measurements on Superhydrophobic Surfaces. *Phys. Fluids* **2015**, *27* (3), 32107. https://doi.org/10.1063/1.4915112.

(62) Mohammad Karim, A.; Kavehpour, H. P. Dynamics of Spreading on Ultra-Hydrophobic Surfaces. *J. Coatings Technol. Res.* **2015**, *12* (5), 959–964. https://doi.org/10.1007/s11998-015-9686-z.

(63) Butt, H.-J.; Gao, N.; Papadopoulos, P.; Steffen, W.; Kappl, M.; Berger, R. Energy Dissipation of Moving Drops on Superhydrophobic and Superoleophobic Surfaces. *Langmuir* **2017**, *33* (1), 107–116. https://doi.org/10.1021/acs.langmuir.6b03792.

(64) Tavakoli, F.; Kavehpour, H. P. Cold-Induced Spreading of Water Drops on Hydrophobic Surfaces. *Langmuir* **2015**, *31* (7), 2120–2126. https://doi.org/10.1021/la503620a.

(65) Yang, J.; Koplik, J.; Banavar, J. R. Molecular Dynamics of Drop Spreading on a Solid Surface. *Phys. Rev. Lett.* **1991**, *67* (25), 3539–3542. https://doi.org/10.1103/PhysRevLett.67.3539.

(66) De Coninck, J.; D'Ortona, U.; Koplik, J.; Banavar, J. R. Terraced Spreading of Chain Molecules via Molecular Dynamics. *Phys. Rev. Lett.* **1995**, *74* (6), 928–931. https://doi.org/10.1103/PhysRevLett.74.928.

(67) Winkels, K. G.; Weijs, J. H.; Eddi, A.; Snoeijer, J. H. Initial Spreading of Low-Viscosity Drops on Partially Wetting Surfaces. *Phys. Rev. E* **2012**, *85* (5), 55301. https://doi.org/10.1103/PhysRevE.85.055301.

(68) Andrews, J. E.; Sinha, S.; Chung, P. W.; Das, S. Wetting Dynamics of a Water Nanodrop on Graphene. *Phys. Chem. Chem. Phys.* **2016**. https://doi.org/10.1039/c6cp01936f.

(69) Andrews, J. E.; Wang, Y.; Sinha, S.; Chung, P. W.; Das, S. Roughness-Induced Chemical Heterogeneity Leads to Large Hydrophobicity in Wetting-Translucent Nanostructures. *J. Phys. Chem. C* **2017**, *121* (18), 10010–10017. https://doi.org/10.1021/acs.jpcc.7b02222.

(70) Chang, C.-C.; Sheng, Y.-J.; Tsao, H.-K. Wetting Hysteresis of Nanodrops on Nanorough Surfaces. *Phys. Rev. E* **2016**, *94* (4), 42807. https://doi.org/10.1103/PhysRevE.94.042807.

(71) Blake, T. D.; Clarke, A.; De Coninck, J.; de Ruijter, M. J. Contact Angle Relaxation during Droplet Spreading: Comparison between Molecular Kinetic Theory and Molecular Dynamics. *Langmuir* **1997**, *13* (7), 2164–2166. https://doi.org/10.1021/la962004g.

(72) Nieminen, J. A.; Abraham, D. B.; Karttunen, M.; Kaski, K. Molecular Dynamics of a Microscopic Droplet on Solid Surface. *Phys. Rev. Lett.* **1992**, *69* (1), 124–127. https://doi.org/10.1103/PhysRevLett.69.124.

(73) De Coninck, J.; Blake, T. D. Wetting and Molecular Dynamics Simulations of Simple Liquids. *Annu. Rev. Mater. Res.* **2008**, *38* (1), 1–22. https://doi.org/10.1146/annurev.matsci.38.060407.130339.

(74) Bertrand, E.; Blake, T. D.; Coninck, J. De. Influence of Solid–Liquid Interactions on Dynamic Wetting: A Molecular Dynamics Study. *J. Phys. Condens. Matter* **2009**, *21* (46),

464124. https://doi.org/10.1088/0953-8984/21/46/464124.

(75) Wu, X.; Phan-Thien, N.; Fan, X.-J.; Ng, T. Y. A Molecular Dynamics Study of Drop Spreading on a Solid Surface. *Phys. Fluids* **2003**, *15* (6), 1357–1362. https://doi.org/10.1063/1.1566751.

(76) Shen, Y.; Couzis, A.; Koplik, J.; Maldarelli, C.; Tomassone, M. S. Molecular Dynamics Study of the Influence of Surfactant Structure on Surfactant-Facilitated Spreading of Droplets on Solid Surfaces. *Langmuir* **2005**, *21* (26), 12160–12170. https://doi.org/10.1021/la051354c.

(77) HE, G.; HADJICONSTANTINOU, N. G. A Molecular View of Tanner's Law: Molecular Dynamics Simulations of Droplet Spreading. *J. Fluid Mech.* **2003**, *497*, 123–132. https://doi.org/DOI: 10.1017/S0022112003006839.

(78) Yang, J.; Koplik, J.; Banavar, J. R. Terraced Spreading of Simple Liquids on Solid Surfaces. *Phys. Rev. A* **1992**, *46* (12), 7738–7749. https://doi.org/10.1103/PhysRevA.46.7738.

(79) Gentili, D.; Chinappi, M.; Bolognesi, G.; Giacomello, A.; Casciola, C. M. Water Slippage on Hydrophobic Nanostructured Surfaces: Molecular Dynamics Results for Different Filling Levels. *Meccanica* **2013**, *48* (8), 1853–1861. https://doi.org/10.1007/s11012-013-9717-8.

(80) Schellenberger, F.; Encinas, N.; Vollmer, D.; Butt, H.-J. How Water Advances on Superhydrophobic Surfaces. *Phys. Rev. Lett.* **2016**, *116* (9), 96101. https://doi.org/10.1103/PhysRevLett.116.096101.

(81) Plimpton, S. Fast Parallel Algorithms for Short-Range Molecular Dynamics. *J. Comput. Phys.* **1995**, *117* (1), 1–19. https://doi.org/https://doi.org/10.1006/jcph.1995.1039.

(82) Stukowski, A. Visualization and Analysis of Atomistic Simulation Data with OVITO–the Open Visualization Tool. *Model. Simul. Mater. Sci. Eng.* **2009**, *18* (1), 15012. https://doi.org/10.1088/0965-0393/18/1/015012.

(83) Weijs, J. H.; Marchand, A.; Andreotti, B.; Lohse, D.; Snoeijer, J. H. Origin of Line Tension for a Lennard-Jones Nanodroplet. *Phys. Fluids* **2011**, *23* (2), 22001. https://doi.org/10.1063/1.3546008.

(84) Orsi, M. Comparative Assessment of the ELBA Coarse-Grained Model for Water. *Mol. Phys.* **2014**. https://doi.org/10.1080/00268976.2013.844373.

(85) Werder, T.; Walther, J. H.; Jaffe, R. L.; Halicioglu, T.; Koumoutsakos, P. On the Water−Carbon Interaction for Use in Molecular Dynamics Simulations of Graphite and Carbon Nanotubes. *J. Phys. Chem. B* **2003**, *107* (6), 1345–1352. https://doi.org/10.1021/jp0268112.

(86) Merabia, S.; Shenogin, S.; Joly, L.; Keblinski, P.; Barrat, J.-L. Heat Transfer from Nanoparticles: A Corresponding State Analysis. *Proc. Natl. Acad. Sci.* **2009**, *106* (36), 15113 LP – 15118. https://doi.org/10.1073/pnas.0901372106.

(87) Koishi, T.; Yasuoka, K.; Fujikawa, S.; Zeng, X. C. Measurement of Contact-Angle Hysteresis for Droplets on Nanopillared Surface and in the Cassie and Wenzel States: A Molecular Dynamics Simulation Study. *ACS Nano* **2011**, *5* (9), 6834–6842. https://doi.org/10.1021/nn2005393.

(88) Girit, Ç. Ö.; Meyer, J. C.; Erni, R.; Rossell, M. D.; Kisielowski, C.; Yang, L.; Park, C.-H.; Crommie, M. F.; Cohen, M. L.; Louie, S. G.; et al. Graphene at the Edge: Stability and Dynamics. *Science (80-.).* **2009**, *323* (5922), 1705 LP – 1708. https://doi.org/10.1126/science.1166999.

(89) Nose, S. Constant-Temperature Molecular Dynamics. *J. Phys. Condens. Matter* **1990**, *2* (S), SA115–SA119. https://doi.org/10.1088/0953-8984/2/s/013.

(90) Marchand, A.; Weijs, J. H.; Snoeijer, J. H.; Andreotti, B. Why Is Surface Tension a Force Parallel to the Interface? *Am. J. Phys.* **2011**, *79* (10), 999–1008. https://doi.org/10.1119/1.3619866.

(91) Khan, S.; Singh, J. K. Wetting Transition of Nanodroplets of Water on Textured Surfaces: A Molecular Dynamics Study. *Mol. Simul.* **2014**. https://doi.org/10.1080/08927022.2013.819578.

(92) Wilson, P. M.; Mbah, G. N.; Smith, T. G.; Schmidt, D.; Lai, R. Y.; Hofmann, T.; Sinitskii, A. Three-Dimensional Periodic Graphene Nanostructures. *J. Mater. Chem. C* **2014**. https://doi.org/10.1039/c3tc32277g.

(93) Liu, Z.; Ma, L.; Shi, G.; Zhou, W.; Gong, Y.; Lei, S.; Yang, X.; Zhang, J.; Yu, J.; Hackenberg, K. P.; et al. In-Plane Heterostructures of Graphene and Hexagonal Boron Nitride with Controlled Domain Sizes. *Nat. Nanotechnol.* **2013**, *8*, 119.

(94) Lin, Y.; Han, X.; Campbell, C. J.; Kim, J.-W.; Zhao, B.; Luo, W.; Dai, J.; Hu, L.; Connell, J. W. Holey Graphene Nanomanufacturing: Structure, Composition, and Electrochemical Properties. *Adv. Funct. Mater.* **2015**, *25* (19), 2920–2927. https://doi.org/10.1002/adfm.201500321.

(95) Lin, Y.; Liao, Y.; Chen, Z.; Connell, J. W. Holey Graphene: A Unique Structural Derivative of Graphene. *Mater. Res. Lett.* **2017**. https://doi.org/10.1080/21663831.2016.1271047.

(96) Han, X.; Funk, M. R.; Shen, F.; Chen, Y. C.; Li, Y.; Campbell, C. J.; Dai, J.; Yang, X.; Kim, J. W.; Liao, Y.; et al. Scalable Holey Graphene Synthesis and Dense Electrode Fabrication toward High-Performance Ultracapacitors. *ACS Nano* **2014**. https://doi.org/10.1021/nn502635y.

(97) Xu, Y.; Lin, Z.; Zhong, X.; Huang, X.; Weiss, N. O.; Huang, Y.; Duan, X. Holey Graphene Frameworks for Highly Efficient Capacitive Energy Storage. *Nat. Commun.* **2014**. https://doi.org/10.1038/ncomms5554.

(98) Zhang, J.; Yang, X.; He, Y.; Bai, Y.; Kang, L.; Xu, H.; Shi, F.; Lei, Z.; Liu, Z. H. δ-MnO2/Holey Graphene Hybrid Fiber for All-Solid-State Supercapacitor. *J. Mater. Chem. A* **2016**. https://doi.org/10.1039/c6ta02989b.

(99) Zhou, Q.; Zhang, M.; Chen, J.; Hong, J. D.; Shi, G. Nitrogen-Doped Holey Graphene Film-Based Ultrafast Electrochemical Capacitors. *ACS Appl. Mater. Interfaces* **2016**. https://doi.org/10.1021/acsami.6b05601.

(100) Yang, C. H.; Huang, P. L.; Luo, X. F.; Wang, C. H.; Li, C.; Wu, Y. H.; Chang, J. K. Holey Graphene Nanosheets with Surface Functional Groups as High-Performance Supercapacitors in Ionic-Liquid Electrolyte. *ChemSusChem* **2015**. https://doi.org/10.1002/cssc.201500030.

(101) Lv, X.; Lv, W.; Wei, W.; Zheng, X.; Zhang, C.; Zhi, L.; Yang, Q. H. A Hybrid of Holey Graphene and Mn 3 O 4 and Its Oxygen Reduction Reaction Performance. *Chem.*

Commun. **2015**. https://doi.org/10.1039/c4cc09930c.

(102) Chen, S.; Qiao, S. Z. Hierarchically Porous Nitrogen-Doped Graphene-NiCo2O4 Hybrid Paper as an Advanced Electrocatalytic Water-Splitting Material. *ACS Nano* **2013**. https://doi.org/10.1021/nn404444r.

(103) Chowdhury, S.; Balasubramanian, R. Holey Graphene Frameworks for Highly Selective Post-Combustion Carbon Capture. *Sci. Rep.* **2016**. https://doi.org/10.1038/srep21537.

(104) Cohen-Tanugi, D.; Lin, L. C.; Grossman, J. C. Multilayer Nanoporous Graphene Membranes for Water Desalination. *Nano Lett.* **2016**. https://doi.org/10.1021/acs.nanolett.5b04089.

(105) Konatham, D.; Yu, J.; Ho, T. A.; Striolo, A. Simulation Insights for Graphene-Based Water Desalination Membranes. *Langmuir* **2013**. https://doi.org/10.1021/la4018695.

(106) Gravelle, S.; Yoshida, H.; Joly, L.; Ybert, C.; Bocquet, L. Carbon Membranes for Efficient Water-Ethanol Separation. *J. Chem. Phys.* **2016**. https://doi.org/10.1063/1.4963098.

(107) Shi, Q.; He, Z.; Gupta, K. M.; Wang, Y.; Lu, R. Efficient Ethanol/Water Separation via Functionalized Nanoporous Graphene Membranes: Insights from Molecular Dynamics Study. *J. Mater. Sci.* **2017**, *52* (1), 173–184. https://doi.org/10.1007/s10853-016-0319-4.

(108) Cheng, C.; Jiang, G.; Garvey, C. J.; Wang, Y.; Simon, G. P.; Liu, J. Z.; Li, D. Nanotechnology: Ion Transport in Complex Layered Graphene-Based Membranes with Tuneable Interlayer Spacing. *Sci. Adv.* **2016**. https://doi.org/10.1126/sciadv.1501272.

(109) Bakli, C.; Chakraborty, S. Capillary Filling Dynamics of Water in Nanopores. *Appl. Phys.*

Lett. **2012**. https://doi.org/10.1063/1.4758683.

(110) Gravelle, S.; Ybert, C.; Bocquet, L.; Joly, L. Anomalous Capillary Filling and Wettability Reversal in Nanochannels. *Phys. Rev. E* **2016**. https://doi.org/10.1103/PhysRevE.93.033123.

(111) Ahadian, S.; Mizuseki, H.; Kawazoe, Y. On the Kinetics of the Capillary Imbibition of a Simple Fluid through a Designed Nanochannel Using the Molecular Dynamics Simulation Approach. *J. Colloid Interface Sci.* **2010**. https://doi.org/10.1016/j.jcis.2010.09.011.

(112) Oyarzua, E.; Walther, J. H.; Mejía, A.; Zambrano, H. A. Early Regimes of Water Capillary Flow in Slit Silica Nanochannels. *Phys. Chem. Chem. Phys.* **2015**. https://doi.org/10.1039/c5cp01862e.

(113) Yang, X.; Cheng, C.; Wang, Y.; Qiu, L.; Li, D. Liquid-Mediated Dense Integration of Graphene Materials for Compact Capacitive Energy Storage. *Science (80-.).* **2013**. https://doi.org/10.1126/science.1239089.

(114) Ji, H.; Zhao, X.; Qiao, Z.; Jung, J.; Zhu, Y.; Lu, Y.; Zhang, L. L.; MacDonald, A. H.; Ruoff, R. S. Capacitance of Carbon-Based Electrical Double-Layer Capacitors. *Nat. Commun.* **2014**. https://doi.org/10.1038/ncomms4317.

(115) Heltzel, A.; Mishra, C.; Ruoff, R. S.; Fleming, A. Analysis of an Ultrathin Graphite-Based Compact Heat Exchanger. *Heat Transf. Eng.* **2012**. https://doi.org/10.1080/01457632.2012.654727.

(116) Li, X.; Chen, Y.; Cheng, Z.; Jia, L.; Mo, S.; Liu, Z. Ultrahigh Specific Surface Area of Graphene for Eliminating Subcooling of Water. *Appl. Energy* **2014**.

https://doi.org/10.1016/j.apenergy.2014.02.032.

(117) Stukowski, A. Visualization and Analysis of Atomistic Simulation Data with OVITO-the Open Visualization Tool. *Model. Simul. Mater. Sci. Eng.* **2010**. https://doi.org/10.1088/0965-0393/18/1/015012.

(118) Leroy, F.; Liu, S.; Zhang, J. Parametrizing Nonbonded Interactions from Wetting Experiments via the Work of Adhesion: Example of Water on Graphene Surfaces. *J. Phys. Chem. C* **2015**. https://doi.org/10.1021/acs.jpcc.5b10267.

(119) Shi, B.; Webb, E. B. Self-Pinning of a Nanosuspension Droplet: Molecular Dynamics Simulations. *Phys. Rev. E* **2016**. https://doi.org/10.1103/PhysRevE.94.012614.

(120) Lu, G.; Hu, H.; Duan, Y.; Sun, Y. Wetting Kinetics of Water Nano-Droplet Containing Non-Surfactant Nanoparticles: A Molecular Dynamics Study. *Appl. Phys. Lett.* **2013**. https://doi.org/10.1063/1.4837717.

(121) Zhang, J.; Milzetti, J.; Leroy, F.; Müller-Plathe, F. Formation of Coffee-Stain Patterns at the Nanoscale: The Role of Nanoparticle Solubility and Solvent Evaporation Rate. *J. Chem. Phys.* **2017**. https://doi.org/10.1063/1.4978284.

(122) Koplik, J.; Maldarelli, C. Diffusivity and Hydrodynamic Drag of Nanoparticles at a Vapor-Liquid Interface. *Phys. Rev. Fluids* **2017**. https://doi.org/10.1103/PhysRevFluids.2.024303.

(123) Zhang, X.-X.; Chen, M. Icephobicity of Functionalized Graphene Surfaces. *J. Nanomater.* **2016**. https://doi.org/10.1155/2016/6731840.

(124) Wang, Y.; Andrews, J. E.; Hu, L.; Das, S. Drop Spreading on a Superhydrophobic

Surface: Pinned Contact Line and Bending Liquid Surface. *Phys. Chem. Chem. Phys.* **2017**. https://doi.org/10.1039/c7cp01777d.

(125) Liu, Q.; Xu, B. Wettability of Water Droplet on Misoriented Graphene Bilayer Sructure: A Molecular Dynamics Study. *AIP Adv.* **2015**. https://doi.org/10.1063/1.4923193.

(126) Ho, T. A.; Papavassiliou, D. V; Lee, L. L.; Striolo, A. Liquid Water Can Slip on a Hydrophilic Surface. *Proc. Natl. Acad. Sci.* **2011**. https://doi.org/10.1073/pnas.1105189108.

(127) Driskill, J.; Vanzo, D.; Bratko, D.; Luzar, A. Wetting Transparency of Graphene in Water. *J. Chem. Phys.* **2014**. https://doi.org/10.1063/1.4895541.

(128) Akaishi, A.; Yonemaru, T.; Nakamura, J. Formation of Water Layers on Graphene Surfaces. *ACS Omega* **2017**. https://doi.org/10.1021/acsomega.7b00365.

(129) Vanzo, D.; Bratko, D.; Luzar, A. Wettability of Pristine and Alkyl-Functionalized Graphane. *J. Chem. Phys.* **2012**. https://doi.org/10.1063/1.4732520.

(130) Xue, Y.; Markmann, J.; Duan, H.; Weissmüller, J.; Huber, P. Switchable Imbibition in Nanoporous Gold. *Nat. Commun.* **2014**. https://doi.org/10.1038/ncomms5237.

(131) Concus, P.; Finn, R. ON THE BEHAVIOR OF A CAPILLARY SURFACE IN A WEDGE. *Proc. Natl. Acad. Sci.* **2006**. https://doi.org/10.1073/pnas.63.2.292.

(132) Koh, D.-Y.; Lively, R. P. Membranes at the Limit. *Nat. Nanotechnol.* **2015**, *10*, 385.

(133) Banhart, F.; Kotakoski, J.; Krasheninnikov, A. V. Structural Defects in Graphene. *ACS Nano*. 2011. https://doi.org/10.1021/nn102598m.

(134) Zhang, J.; Guo, B.; Yang, Y.; Shen, W.; Wang, Y.; Zhou, X.; Wu, H.; Guo, S. Large Scale

Production of Nanoporous Graphene Sheets and Their Application in Lithium Ion Battery. *Carbon N. Y.* **2015**. https://doi.org/10.1016/j.carbon.2014.12.039.

(135) Sun, S.; Wang, P.; Wang, S.; Wu, Q.; Fang, S. Fabrication of MnO 2 /Nanoporous 3D Graphene for Supercapacitor Electrodes. *Mater. Lett.* **2015**. https://doi.org/10.1016/j.matlet.2015.01.061.

(136) Ito, Y.; Cong, W.; Fujita, T.; Tang, Z.; Chen, M. High Catalytic Activity of Nitrogen and Sulfur Co-Doped Nanoporous Graphene in the Hydrogen Evolution Reaction. *Angew. Chemie - Int. Ed.* **2015**. https://doi.org/10.1002/anie.201410050.

(137) Qiu, H. J.; Ito, Y.; Cong, W.; Tan, Y.; Liu, P.; Hirata, A.; Fujita, T.; Tang, Z.; Chen, M. Nanoporous Graphene with Single-Atom Nickel Dopants: An Efficient and Stable Catalyst for Electrochemical Hydrogen Production. *Angew. Chemie - Int. Ed.* **2015**. https://doi.org/10.1002/anie.201507381.

(138) Cohen-Tanugi, D.; Grossman, J. C. Nanoporous Graphene as a Reverse Osmosis Membrane: Recent Insights from Theory and Simulation. *Desalination* **2015**. https://doi.org/10.1016/j.desal.2014.12.046.

(139) Cohen-Tanugi, D.; Grossman, J. C. Water Permeability of Nanoporous Graphene at Realistic Pressures for Reverse Osmosis Desalination. *J. Chem. Phys.* **2014**. https://doi.org/10.1063/1.4892638.

(140) Wang, L.; Boutilier, M. S. H.; Kidambi, P. R.; Jang, D.; Hadjiconstantinou, N. G.; Karnik, R. Fundamental Transport Mechanisms, Fabrication and Potential Applications of Nanoporous Atomically Thin Membranes. *Nature Nanotechnology*. 2017. https://doi.org/10.1038/nnano.2017.72.

(141) Qin, Y.; Hu, Y.; Koehler, S.; Cai, L.; Wen, J.; Tan, X.; Xu, W. L.; Sheng, Q.; Hou, X.; Xue, J.; et al. Ultrafast Nanofiltration through Large-Area Single-Layered Graphene Membranes. *ACS Appl. Mater. Interfaces* **2017**. https://doi.org/10.1021/acsami.7b00504.

(142) Boutilier, M. S. H.; Jang, D.; Idrobo, J. C.; Kidambi, P. R.; Hadjiconstantinou, N. G.; Karnik, R. Molecular Sieving Across Centimeter-Scale Single-Layer Nanoporous Graphene Membranes. *ACS Nano* **2017**. https://doi.org/10.1021/acsnano.7b01231.

(143) Kommu, A.; Singh, J. K. Separation of Ethanol and Water Using Graphene and Hexagonal Boron Nitride Slit Pores: A Molecular Dynamics Study. *J. Phys. Chem. C* **2017**. https://doi.org/10.1021/acs.jpcc.7b00172.

(144) Sahu, S.; Zwolak, M. Ionic Selectivity and Filtration from Fragmented Dehydration in Multilayer Graphene Nanopores. *Nanoscale* **2017**. https://doi.org/10.1039/c7nr03838k.

(145) Li, Z.; Liu, Y.; Zhao, Y.; Zhang, X.; Qian, L.; Tian, L.; Bai, J.; Qi, W.; Yao, H.; Gao, B.; et al. Selective Separation of Metal Ions via Monolayer Nanoporous Graphene with Carboxyl Groups. *Anal. Chem.* **2016**. https://doi.org/10.1021/acs.analchem.6b02175.

(146) Heerema, S. J.; Dekker, C. Graphene Nanodevices for DNA Sequencing. *Nature Nanotechnology*. 2016. https://doi.org/10.1038/nnano.2015.307.

(147) Fan, Z.; Cheng, Z.; Feng, J.; Xie, Z.; Liu, Y.; Wang, Y. Ultrahigh Volumetric Performance of a Free-Standing Compact N-Doped Holey Graphene/PANI Slice for Supercapacitors. *J. Mater. Chem. A* **2017**, *5* (32), 16689–16701. https://doi.org/10.1039/C7TA04384H.

(148) Huang, K.; Liu, G.; Shen, J.; Chu, Z.; Zhou, H.; Gu, X.; Jin, W.; Xu, N. High-Efficiency

Water-Transport Channels Using the Synergistic Effect of a Hydrophilic Polymer and Graphene Oxide Laminates. *Adv. Funct. Mater.* **2015**. https://doi.org/10.1002/adfm.201502205.

(149) Sun, H.; Mei, L.; Liang, J.; Zhao, Z.; Lee, C.; Fei, H.; Ding, M.; Lau, J.; Li, M.; Wang, C.; et al. Three-Dimensional Holey-Graphene/Niobia Composite Architectures for Ultrahigh-Rate Energy Storage. *Science (80-.).* **2017**, *356* (6338), 599 LP – 604. https://doi.org/10.1126/science.aam5852.

(150) Kotal, M.; Kim, H.; Roy, S.; Oh, I. K. Sulfur and Nitrogen Co-Doped Holey Graphene Aerogel for Structurally Resilient Solid-State Supercapacitors under High Compressions. *J. Mater. Chem. A* **2017**. https://doi.org/10.1039/c7ta05237e.

(151) Han, X.; Funk, M. R.; Shen, F.; Chen, Y. C.; Li, Y.; Campbell, C. J.; Dai, J.; Yang, X.; Kim, J. W.; Liao, Y.; et al. Scalable Holey Graphene Synthesis and Dense Electrode Fabrication toward High-Performance Ultracapacitors. *ACS Nano* **2014**. https://doi.org/10.1021/nn502635y.

(152) Abascal, J. L. F.; Vega, C. A General Purpose Model for the Condensed Phases of Water: TIP4P/2005. *J. Chem. Phys.* **2005**. https://doi.org/10.1063/1.2121687.

(153) Huang, J.; Mackerell, A. D. CHARMM36 All-Atom Additive Protein Force Field: Validation Based on Comparison to NMR Data. *J. Comput. Chem.* **2013**. https://doi.org/10.1002/jcc.23354.

(154) Nair, R. R.; Wu, H. A.; Jayaram, P. N.; Grigorieva, I. V; Geim, A. K. Unimpeded Permeation of Water through Helium-Leak-Tight Graphene-Based Membranes. *Science (80-.).* **2012**. https://doi.org/10.1126/science.1211694.

(155) Lee, B.; Li, K.; Yoon, H. S.; Yoon, J.; Mok, Y.; Lee, Y.; Lee, H. H.; Kim, Y. H. Membrane of Functionalized Reduced Graphene Oxide Nanoplates with Angstrom-Level Channels. *Sci. Rep.* **2016**. https://doi.org/10.1038/srep28052.

(156) Yuan, W.; Chen, J.; Shi, G. Nanoporous Graphene Materials. *Materials Today*. 2014. https://doi.org/10.1016/j.mattod.2014.01.021.

(157) Yang, T.; Lin, H.; Zheng, X.; Loh, K. P.; Jia, B. Tailoring Pores in Graphene-Based Materials: From Generation to Applications. *Journal of Materials Chemistry A*. 2017. https://doi.org/10.1039/c7ta04692h.

(158) Wells, D. B.; Belkin, M.; Comer, J.; Aksimentiev, A. Assessing Graphene Nanopores for Sequencing DNA. *Nano Lett.* **2012**. https://doi.org/10.1021/nl301655d.

(159) Kidambi, P. R.; Jang, D.; Idrobo, J. C.; Boutilier, M. S. H.; Wang, L.; Kong, J.; Karnik, R. Nanoporous Atomically Thin Graphene Membranes for Desalting and Dialysis Applications. *Adv. Mater.* **2017**. https://doi.org/10.1002/adma.201700277.

(160) Jang, D.; Idrobo, J. C.; Laoui, T.; Karnik, R. Water and Solute Transport Governed by Tunable Pore Size Distributions in Nanoporous Graphene Membranes. *ACS Nano* **2017**. https://doi.org/10.1021/acsnano.7b04299.

(161) Merchant, C. A.; Healy, K.; Wanunu, M.; Ray, V.; Peterman, N.; Bartel, J.; Fischbein, M. D.; Venta, K.; Luo, Z.; Johnson, A. T. C.; et al. DNA Translocation through Graphene Nanopores. *Nano Lett.* **2010**. https://doi.org/10.1021/nl101046t.

(162) Lin, Z.; Waller, G. H.; Liu, Y.; Liu, M.; Wong, C. P. Simple Preparation of Nanoporous Few-Layer Nitrogen-Doped Graphene for Use as an Efficient Electrocatalyst for Oxygen

Reduction and Oxygen Evolution Reactions. *Carbon N. Y.* **2013**. https://doi.org/10.1016/j.carbon.2012.10.039.

(163) Ito, Y.; Qiu, H. J.; Fujita, T.; Tanabe, Y.; Tanigaki, K.; Chen, M. Bicontinuous Nanoporous N-Doped Graphene for the Oxygen Reduction Reaction. *Adv. Mater.* **2014**. https://doi.org/10.1002/adma.201400570.

(164) Li, H.; Song, Z.; Zhang, X.; Huang, Y.; Li, S.; Mao, Y.; Ploehn, H. J.; Bao, Y.; Yu, M. Ultrathin, Molecular-Sieving Graphene Oxide Membranes for Selective Hydrogen Separation. *Science (80-.).* **2013**. https://doi.org/10.1126/science.1236686.

(165) Celebi, K.; Buchheim, J.; Wyss, R. M.; Droudian, A.; Gasser, P.; Shorubalko, I.; Kye, J. Il; Lee, C.; Park, H. G. Ultimate Permeation across Atomically Thin Porous Graphene. *Science (80-.).* **2014**. https://doi.org/10.1126/science.1249097.

(166) Joshi, R. K.; Carbone, P.; Wang, F. C.; Kravets, V. G.; Su, Y.; Grigorieva, I. V; Wu, H. A.; Geim, A. K.; Nair, R. R. Precise and Ultrafast Molecular Sieving through Graphene Oxide Membranes. *Science (80-.).* **2014**. https://doi.org/10.1126/science.1245711.

(167) O'Hern, S. C.; Boutilier, M. S. H.; Idrobo, J. C.; Song, Y.; Kong, J.; Laoui, T.; Atieh, M.; Karnik, R. Selective Ionic Transport through Tunable Subnanometer Pores in Single-Layer Graphene Membranes. *Nano Lett.* **2014**. https://doi.org/10.1021/nl404118f.

(168) Yang, H.; Kannappan, S.; Pandian, A. S.; Jang, J. H.; Lee, Y. S.; Lu, W. Graphene Supercapacitor with Both High Power and Energy Density. *Nanotechnology* **2017**. https://doi.org/10.1088/1361-6528/aa8948.

(169) Palaniselvam, T.; Kashyap, V.; Bhange, S. N.; Baek, J.-B.; Kurungot, S. Nanoporous

Graphene Enriched with Fe/Co-N Active Sites as a Promising Oxygen Reduction Electrocatalyst for Anion Exchange Membrane Fuel Cells. *Adv. Funct. Mater.* **2016**. https://doi.org/10.1002/adfm.201504765.

(170) Qin, L.; Ding, R.; Wang, H.; Wu, J.; Wang, C.; Zhang, C.; Xu, Y.; Wang, L.; Lv, B. Facile Synthesis of Porous Nitrogen-Doped Holey Graphene as an Efficient Metal-Free Catalyst for the Oxygen Reduction Reaction. *Nano Res.* **2017**. https://doi.org/10.1007/s12274-016-1293-5.

(171) Lv, R.; Wang, H.; Yu, H.; Peng, F. Controllable Preparation of Holey Graphene and Electrocatalytic Performance for Oxygen Reduction Reaction. *Electrochim. Acta* **2017**. https://doi.org/10.1016/j.electacta.2017.01.024.

(172) Tromer, R. M.; Da Luz, M. G. E.; Ferreira, M. S.; Pereira, L. F. C. Atomic Adsorption on Nitrogenated Holey Graphene. *J. Phys. Chem. C* **2017**. https://doi.org/10.1021/acs.jpcc.6b10058.

(173) Qie, L.; Lin, Y.; Connell, J. W.; Xu, J.; Dai, L. Highly Rechargeable Lithium-CO2 Batteries with a Boron- and Nitrogen-Codoped Holey-Graphene Cathode. *Angew. Chemie - Int. Ed.* **2017**. https://doi.org/10.1002/anie.201701826.

(174) Wang, X.; Lv, L.; Cheng, Z.; Gao, J.; Dong, L.; Hu, C.; Qu, L. High-Density Monolith of N-Doped Holey Graphene for Ultrahigh Volumetric Capacity of Li-Ion Batteries. *Adv. Energy Mater.* **2016**. https://doi.org/10.1002/aenm.201502100.

(175) Luo, G.; Liu, L.; Zhang, J.; Li, G.; Wang, B.; Zhao, J. Hole Defects and Nitrogen Doping in Graphene: Implication for Supercapacitor Applications. *ACS Appl. Mater. Interfaces* **2013**. https://doi.org/10.1021/am403427h.

(176) Wang, Y.; Sinha, S.; Hu, L.; Das, S. Interaction between a Water Drop and Holey Graphene: Retarded Imbibition and Generation of Novel Water-Graphene Wetting States. *Phys. Chem. Chem. Phys.* **2017**. https://doi.org/10.1039/c7cp04411a.

(177) Shih, C. J.; Wang, Q. H.; Lin, S.; Park, K. C.; Jin, Z.; Strano, M. S.; Blankschtein, D. Breakdown in the Wetting Transparency of Graphene. *Phys. Rev. Lett.* **2012**. https://doi.org/10.1103/PhysRevLett.109.176101.

(178) Kim, D.; Pugno, N. M.; Buehler, M. J.; Ryu, S. Solving the Controversy on the Wetting Transparency of Graphene. *Sci. Rep.* **2015**. https://doi.org/10.1038/srep15526.

(179) Shih, C.-J.; Strano, M. S.; Blankschtein, D. Wetting Translucency of Graphene. *Nat. Mater.* **2013**. https://doi.org/10.1038/nmat3760.

(180) El-Kady, M. F.; Strong, V.; Dubin, S.; Kaner, R. B. Laser Scribing of High-Performance and Flexible Graphene-Based Electrochemical Capacitors. *Science (80-.).* **2012**. https://doi.org/10.1126/science.1216744.

(181) Andrews, J. E.; Sinha, S.; Chung, P. W.; Das, S. Wetting Dynamics of a Water Nanodrop on Graphene. *Phys. Chem. Chem. Phys.* **2016**. https://doi.org/10.1039/c6cp01936f.

(182) Rafiee, J.; Mi, X.; Gullapalli, H.; Thomas, A. V.; Yavari, F.; Shi, Y.; Ajayan, P. M.; Koratkar, N. A. Wetting Transparency of Graphene. *Nat. Mater.* **2012**. https://doi.org/10.1038/nmat3228.

(183) Weijs, J. H.; Marchand, A.; Andreotti, B.; Lohse, D.; Snoeijer, J. H. Origin of Line Tension for a Lennard-Jones Nanodroplet. *Phys. Fluids* **2011**. https://doi.org/10.1063/1.3546008.

(184) Cheng, C.; Jiang, G.; Garvey, C. J.; Wang, Y.; Simon, G. P.; Liu, J. Z.; Li, D. Nanotechnology: Ion Transport in Complex Layered Graphene-Based Membranes with Tuneable Interlayer Spacing. *Sci. Adv.* **2016**. https://doi.org/10.1126/sciadv.1501272.

(185) Speyer, K.; Pastorino, C. Droplet Transport in a Nanochannel Coated by Hydrophobic Semiflexible Polymer Brushes: The Effect of Chain Stiffness. *Langmuir* **2017**. https://doi.org/10.1021/acs.langmuir.7b02640.

(186) Wang, F. C.; Zhao, Y. P. Slip Boundary Conditions Based on Molecular Kinetic Theory: The Critical Shear Stress and the Energy Dissipation at the Liquid-Solid Interface. *Soft Matter* **2011**. https://doi.org/10.1039/c1sm05543g.

(187) Wei, N.; Peng, X.; Xu, Z. Breakdown of Fast Water Transport in Graphene Oxides. *Phys. Rev. E - Stat. Nonlinear, Soft Matter Phys.* **2014**. https://doi.org/10.1103/PhysRevE.89.012113.

(188) Muscatello, J.; Jaeger, F.; Matar, O. K.; Müller, E. A. Optimizing Water Transport through Graphene-Based Membranes: Insights from Nonequilibrium Molecular Dynamics. *ACS Appl. Mater. Interfaces* **2016**. https://doi.org/10.1021/acsami.5b12112.

(189) Tan, Z.; Chen, G.; Zhu, Y. Carbon-Based Supercapacitors Produced by the Activation of Graphene. In *Nanocarbons for Advanced Energy Storage*; 2015. https://doi.org/10.1002/9783527680054.ch7.

(190) Zhang, K.; Zhang, L. L.; Zhao, X. S.; Wu, J. Graphene/Polyaniline Nanofiber Composites as Supercapacitor Electrodes. *Chem. Mater.* **2010**. https://doi.org/10.1021/cm902876u.

(191) Wu, Q.; Xu, Y.; Yao, Z.; Liu, A.; Shi, G. Supercapacitors Based on Flexible

Graphene/Polyaniline Nanofiber Composite Films. *ACS Nano* **2010**. https://doi.org/10.1021/nn1000035.

(192) Chen, S.; Zhu, J.; Wu, X.; Han, Q.; Wang, X. Graphene Oxide-Mno2 Nanocomposites for Supercapacitors. *ACS Nano* **2010**. https://doi.org/10.1021/nn901311t.

(193) Dong, X. C.; Xu, H.; Wang, X. W.; Huang, Y. X.; Chan-Park, M. B.; Zhang, H.; Wang, L. H.; Huang, W.; Chen, P. 3D Graphene-Cobalt Oxide Electrode for High-Performance Supercapacitor and Enzymeless Glucose Detection. *ACS Nano* **2012**. https://doi.org/10.1021/nn300097q.

(194) Kim, T.; Jung, G.; Yoo, S.; Suh, K. S.; Ruoff, R. S. Activated Graphene-Based Carbons as Supercapacitor Electrodes with Macro- and Mesopores. *ACS Nano* **2013**. https://doi.org/10.1021/nn402077v.

(195) Mao, S.; Wen, Z.; Huang, T.; Hou, Y.; Chen, J. High-Performance Bi-Functional Electrocatalysts of 3D Crumpled Graphene-Cobalt Oxide Nanohybrids for Oxygen Reduction and Evolution Reactions. *Energy Environ. Sci.* **2014**. https://doi.org/10.1039/c3ee42696c.

(196) Kofuji, Y.; Isobe, Y.; Shiraishi, Y.; Sakamoto, H.; Tanaka, S.; Ichikawa, S.; Hirai, T. Carbon Nitride-Aromatic Diimide-Graphene Nanohybrids: Metal-Free Photocatalysts for Solar-to-Hydrogen Peroxide Energy Conversion with 0.2% Efficiency. *J. Am. Chem. Soc.* **2016**. https://doi.org/10.1021/jacs.6b05806.

(197) Kong, C.; Min, S.; Lu, G. Dye-Sensitized NiSx Catalyst Decorated on Graphene for Highly Efficient Reduction of Water to Hydrogen under Visible Light Irradiation. *ACS Catal.* **2014**. https://doi.org/10.1021/cs5006844.

(198) Kecsenovity, E.; Endrődi, B.; Tóth, P. S.; Zou, Y.; Dryfe, R. A. W.; Rajeshwar, K.; Janáky, C. Enhanced Photoelectrochemical Performance of Cuprous Oxide/Graphene Nanohybrids. *J. Am. Chem. Soc.* **2017**. https://doi.org/10.1021/jacs.7b01820.

(199) Dodds, S.; da Silveira Carvalho, M.; Kumar, S. Stretching and Slipping of Liquid Bridges near Plates and Cavities. In *Physics of Fluids*; 2009. https://doi.org/10.1063/1.3212963.

(200) Kusumaatmaja, H.; Lipowsky, R. Equilibrium Morphologies and Effective Spring Constants of Capillary Bridges. *Langmuir* **2010**. https://doi.org/10.1021/la102206d.

(201) Jungwirth, P.; Cremer, P. S. Beyond Hofmeister. *Nat. Chem.* **2014**. https://doi.org/10.1038/nchem.1899.

(202) Finlayson-Pitts, B. J. Reaction of NO2 with NaCl and Atmospheric Implications of NOCl Formation. *Nature* **1983**. https://doi.org/10.1038/306676a0.

(203) Finlayson-Pitts, B. J.; Ezell, M. J.; Pitts, J. N. Formation of Chemically Active Chlorine Compounds by Reactions of Atmospheric NaCl Particles with Gaseous N2O5 and ClONO2. *Nature* **1989**. https://doi.org/10.1038/337241a0.

(204) Laskin, A.; Gaspar, D. J.; Wang, W.; Hunt, S. W.; Cowin, J. P.; Colson, S. D.; Finlayson-Pitts, B. J. Reactions at Interfaces as a Source of Sulfate Formation in Sea-Salt Particles. *Science (80-.).* **2003**. https://doi.org/10.1126/science.1085374.

(205) Laskin, A.; Wang, H.; Robertson, W. H.; Cowin, J. P.; Ezell, M. J.; Finlayson-Pitts, B. J. A New Approach to Determining Gas-Particle Reaction Probabilities and Application to the Heterogeneous Reaction of Deliquesced Sodium Chloride Particles with Gas-Phase Hydroxyl Radicals. *J. Phys. Chem. A* **2006**. https://doi.org/10.1021/jp063263+.

(206) Tao, W. K.; Chen, J. P.; Li, Z.; Wang, C.; Zhang, C. Impact of Aerosols on Convective Clouds and Precipitation. *Rev. Geophys.* **2012**. https://doi.org/10.1029/2011RG000369.

(207) Jungwirth, P.; Rosenfeld, D.; Buch, V. A Possible New Molecular Mechanism of Thundercloud Electrification. *Atmos. Res.* **2005**. https://doi.org/10.1016/j.atmosres.2004.11.016.

(208) Calvert, J. G.; Lazrus, A.; Kok, G. L.; Heikes, B. G.; Walega, J. G.; Lind, J.; Cantrell, C. A. Chemical Mechanisms of Acid Generation in the Troposphere. *Nature* **1985**. https://doi.org/10.1038/317027a0.

(209) Knipping, E. M.; Lakin, M. J.; Foster, K. L.; Jungwirth, P.; Tobias, D. J.; Gerber, R. B.; Dabdub, D.; Finlayson-Pitts, B. J. Experiments and Simulations of Ion-Enhanced Interfacial Chemistry on Aqueous NaCl Aerosols. *Science (80-.).* **2000**. https://doi.org/10.1126/science.288.5464.301.

(210) Knipping, E. M.; Dabdub, D. Impact of Chlorine Emissions from Sea-Salt Aerosol on Coastal Urban Ozone. *Environ. Sci. Technol.* **2003**. https://doi.org/10.1021/es025793z.

(211) Yano, Y. F.; Kobayashi, Y.; Ina, T.; Nitta, K.; Uruga, T. Hofmeister Anion Effects on Protein Adsorption at an Air-Water Interface. *Langmuir* **2016**. https://doi.org/10.1021/acs.langmuir.6b02352.

(212) Algarni, S. A.; Althagafi, T. M.; Smith, P. J.; Grell, M. An Ionic Liquid-Gated Polymer Thin Film Transistor with Exceptionally Low “on” Resistance. *Appl. Phys. Lett.* **2014**. https://doi.org/10.1063/1.4875746.

(213) Duignan, T. T.; Baer, M. D.; Mundy, C. J. Ions Interacting in Solution: Moving from

Intrinsic to Collective Properties. *Current Opinion in Colloid and Interface Science*. 2016. https://doi.org/10.1016/j.cocis.2016.05.009.

(214) Manciu, M.; Ruckenstein, E. Ions at the Air/Water Interface. *J. Colloid Interface Sci.* **2006**. https://doi.org/10.1016/j.jcis.2006.09.034.

(215) Mamatkulov, S. I.; Allolio, C.; Netz, R. R.; Bonthuis, D. J. Orientation-Induced Adsorption of Hydrated Protons at the Air–Water Interface. *Angew. Chemie - Int. Ed.* **2017**. https://doi.org/10.1002/anie.201707391.

(216) Piatkowski, L.; Zhang, Z.; Backus, E. H. G.; Bakker, H. J.; Bonn, M. Extreme Surface Propensity of Halide Ions in Water. *Nat. Commun.* **2014**. https://doi.org/10.1038/ncomms5083.

(217) Levin, Y.; Dos Santos, A. P.; Diehl, A. Ions at the Air-Water Interface: An End to a Hundred-Year-Old Mystery? *Phys. Rev. Lett.* **2009**. https://doi.org/10.1103/PhysRevLett.103.257802.

(218) Perrine, K. A.; Parry, K. M.; Stern, A. C.; Van Spyk, M. H. C.; Makowski, M. J.; Freites, J. A.; Winter, B.; Tobias, D. J.; Hemminger, J. C. Specific Cation Effects at Aqueous Solution−vapor Interfaces: Surfactant-like Behavior of Li + Revealed by Experiments and Simulations . *Proc. Natl. Acad. Sci.* **2017**. https://doi.org/10.1073/pnas.1707540114.

(219) Caleman, C.; Hub, J. S.; van Maaren, P. J.; van der Spoel, D. Atomistic Simulation of Ion Solvation in Water Explains Surface Preference of Halides. *Proc. Natl. Acad. Sci.* **2011**. https://doi.org/10.1073/pnas.1017903108.

(220) Otten, D. E.; Shaffer, P. R.; Geissler, P. L.; Saykally, R. J. Elucidating the Mechanism of

Selective Ion Adsorption to the Liquid Water Surface. *Proc. Natl. Acad. Sci.* **2012**. https://doi.org/10.1073/pnas.1116169109.

(221) Venkateshwaran, V.; Vembanur, S.; Garde, S. Water-Mediated Ion-Ion Interactions Are Enhanced at the Water Vapor-Liquid Interface. *Proc. Natl. Acad. Sci.* **2014**. https://doi.org/10.1073/pnas.1403294111.

(222) McCaffrey, D. L.; Nguyen, S. C.; Cox, S. J.; Weller, H.; Alivisatos, A. P.; Geissler, P. L.; Saykally, R. J. Mechanism of Ion Adsorption to Aqueous Interfaces: Graphene/Water vs. Air/Water. *Proc. Natl. Acad. Sci.* **2017**. https://doi.org/10.1073/pnas.1702760114.

(223) Jungwirth, P.; Tobias, D. J. Specific Ion Effects at the Air/Water Interface. *Chem. Rev.* **2006**. https://doi.org/10.1021/cr0403741.

(224) Tobias, D. J.; Stern, A. C.; Baer, M. D.; Levin, Y.; Mundy, C. J. Simulation and Theory of Ions at Atmospherically Relevant Aqueous Liquid-Air Interfaces. *Annu. Rev. Phys. Chem.* **2013**, *64* (1), 339–359. https://doi.org/10.1146/annurev-physchem-040412-110049.

(225) Brini, E.; Fennell, C. J.; Fernandez-Serra, M.; Hribar-Lee, B.; Lukšič, M.; Dill, K. A. How Water's Properties Are Encoded in Its Molecular Structure and Energies. *Chem. Rev.* **2017**. https://doi.org/10.1021/acs.chemrev.7b00259.

(226) Zhao, Y.; Li, H.; Zeng, X. C. First-Principles Molecular Dynamics Simulation of Atmospherically Relevant Anion Solvation in Supercooled Water Droplet. *J. Am. Chem. Soc.* **2013**. https://doi.org/10.1021/ja407286t.

(227) D'Auria, R.; Tobias, D. J. Relation between Surface Tension and Ion Adsorption at the Air-Water Interface: A Molecular Dynamics Simulation Study. *J. Phys. Chem. A* **2009**.

https://doi.org/10.1021/jp810488p.

(228) Brandes, E.; Karageorgiev, P.; Viswanath, P.; Motschmann, H. Breaking the Symmetry of Ions at the Air-Water Interface. *J. Phys. Chem. C* **2014**. https://doi.org/10.1021/jp5045805.

(229) Tian, C.; Byrnes, S. J.; Han, H. L.; Shen, Y. R. Surface Propensities of Atmospherically Relevant Ions in Salt Solutions Revealed by Phase-Sensitive Sum Frequency Vibrational Spectroscopy. *J. Phys. Chem. Lett.* **2011**. https://doi.org/10.1021/jz200791c.

(230) Vazdar, M.; Pluhařová, E.; Mason, P. E.; Vácha, R.; Jungwirth, P. Ions at Hydrophobic Aqueous Interfaces: Molecular Dynamics with Effective Polarization. *J. Phys. Chem. Lett.* **2012**. https://doi.org/10.1021/jz300805b.

(231) Luty, B. A.; Van Gunsteren, W. F. Calculating Electrostatic Interactions Using the Particle-Particle Particle-Mesh Method with Nonperiodic Long-Range Interactions. *J. Phys. Chem.* **1996**. https://doi.org/10.1021/jp9518623.

(232) Willard, A. P.; Chandler, D. Instantaneous Liquid Interfaces. *J. Phys. Chem. B* **2010**. https://doi.org/10.1021/jp909219k.

(233) Chacón, E.; Tarazona, P.; Alejandre, J. The Intrinsic Structure of the Water Surface. *J. Chem. Phys.* **2006**. https://doi.org/10.1063/1.2209681.

(234) Bresme, F.; Chacón, E.; Tarazona, P. Molecular Dynamics Investigation of the Intrinsic Structure of Water-Fluid Interfaces via the Intrinsic Sampling Method. *Phys. Chem. Chem. Phys.* **2008**. https://doi.org/10.1039/b807437m.

(235) Kuznetsov, V. S.; Usol'tseva, N. V; Zherdev, V. P. Dielectric Permittivity in a Dense

Layer of the Hydration Shell of an Ion in a Strong-Electrolyte Solution. *Russ. J. Inorg. Chem.* **2014**. https://doi.org/10.1134/s0036023614060126.

(236) Heydweiller, A. Über Physikalische Eigenschaften von Lösungen in Ihrem Zusammenhang. II. Oberflächenspannung Und Elektrisches Leitvermögen Wässeriger Salzlösungen. *Ann. Phys.* **1910**, *338* (11), 145–185. https://doi.org/10.1002/andp.19103381108.

(237) Onsager, L.; Samaras, N. N. T. The Surface Tension of Debye-Hückel Electrolytes. *J. Chem. Phys.* **1934**. https://doi.org/10.1063/1.1749522.

(238) Baldelli, S.; Schnitzer, C.; Shultz, M. J. The Structure of Water on HCl Solutions Studied with Sum Frequency Generation. *Chem. Phys. Lett.* **1999**. https://doi.org/10.1016/S0009-2614(99)00094-9.

(239) Schnitzer, C.; Baldelli, S.; Shultz, M. J. Sum Frequency Generation of Water on NaCl, NaNO3, KHSO4, HCl, HNO3, and H2SO4 Aqueous Solutions. *J Phys Chem B*. 2000.

(240) Shultz, M. J.; Schnitzer, C.; Simonelli, D.; Baldelli, S. Sum Frequency Generation Spectroscopy of the Aqueous Interface: Ionic and Soluble Molecular Solutions. *International Reviews in Physical Chemistry*. 2000. https://doi.org/10.1080/014423500229882.

(241) Shultz, M. J.; Baldelli, S.; Schnitzer, C.; Simonelli, D. Aqueous Solution/Air Interfaces Probed with Sum Frequency Generation Spectroscopy. *J. Phys. Chem. B* **2002**. https://doi.org/10.1021/jp014466v.

(242) Liu, D.; Ma, G.; Levering, L. M.; Allen, H. C. Vibrational Spectroscopy of Aqueous

Sodium Halide Solutions and Air−Liquid Interfaces: Observation of Increased Interfacial Depth. *J. Phys. Chem. B* **2004**. https://doi.org/10.1021/jp036169r.

(243) Raymond, E. A.; Richmond, G. L. Probing the Molecular Structure and Bonding of the Surface of Aqueous Salt Solutions. *J. Phys. Chem. B* **2004**. https://doi.org/10.1021/jp037725k.

(244) Petersen, P. B.; Saykally, R. J. Confirmation of Enhanced Anion Concentration at the Liquid Water Surface. *Chem. Phys. Lett.* **2004**. https://doi.org/10.1016/j.cplett.2004.08.049.

(245) Petersen, P. B.; Johnson, J. C.; Knutsen, K. P.; Saykally, R. J. Direct Experimental Validation of the Jones-Ray Effect. *Chem. Phys. Lett.* **2004**. https://doi.org/10.1016/j.cplett.2004.08.048.

(246) Winter, B.; Weber, R.; Schmidt, P. M.; Hertel, I. V; Faubel, M.; Vrbka, L.; Jungwirth, P. Molecular Structure of Surface-Active Salt Solutions: Photoelectron Spectroscopy and Molecular Dynamics Simulations of Aqueous Tetrabutylammonium Iodide. *J. Phys. Chem. B* **2004**. https://doi.org/10.1021/jp0493531.

(247) Ghosal, S.; Hemminger, J. C.; Bluhm, H.; Mun, B. S.; Hebenstreit, E. L. D.; Ketteler, G.; Ogletree, D. F.; Requejo, F. G.; Salmeron, M. Electron Spectroscopy of Aqueous Solution Interfaces Reveals Surface Enhancement of Halides. *Science (80-.).* **2005**. https://doi.org/10.1126/science.1106525.

(248) Cheng, M. H.; Callahan, K. M.; Margarella, A. M.; Tobias, D. J.; Hemminger, J. C.; Bluhm, H.; Krisch, M. J. Ambient Pressure X-Ray Photoelectron Spectroscopy and Molecular Dynamics Simulation Studies of Liquid/Vapor Interfaces of Aqueous NaCl,

RbCl, and RbBr Solutions. *J. Phys. Chem. C* **2012**. https://doi.org/10.1021/jp205500h.

(249) Onorato, R. M.; Otten, D. E.; Saykally, R. J. Adsorption of Thiocyanate Ions to the Dodecanol/Water Interface Characterized by UV Second Harmonic Generation. *Proc. Natl. Acad. Sci.* **2009**. https://doi.org/10.1073/pnas.0904800106.

(250) Petersen, P. B.; Saykally, R. J. Probing the Interfacial Structure of Aqueous Electrolytes with Femtosecond Second Harmonic Generation Spectroscopy. *J. Phys. Chem. B* **2006**. https://doi.org/10.1021/jp0601825.

(251) Winter, B.; Weber, R.; Schmidt, P. M.; Hertel, I. V.; Faubel, M.; Vrbka, L.; Jungwirth, P. Molecular Structure of Surface-Active Salt Solutions: Photoelectron Spectroscopy and Molecular Dynamics Simulations of Aqueous Tetrabutylammonium Iodide. *J. Phys. Chem. B* **2004**. https://doi.org/10.1021/jp0493531.

(252) Tian, C.; Byrnes, S. J.; Han, H. L.; Shen, Y. R. Surface Propensities of Atmospherically Relevant Ions in Salt Solutions Revealed by Phase-Sensitive Sum Frequency Vibrational Spectroscopy. *J. Phys. Chem. Lett.* **2011**. https://doi.org/10.1021/jz200791c.

(253) Mucha, M.; Frigato, T.; Levering, L. M.; Allen, H. C.; Tobias, D. J.; Dang, L. X.; Jungwirth, P. Unified Molecular Picture of the Surfaces of Aqueous Acid, Base, and Salt Solutions. *J. Phys. Chem. B* **2005**. https://doi.org/10.1021/jp0445730.

(254) Gopalakrishnan, S.; Jungwirth, P.; Tobias, D. J.; Allen, H. C. Air-Liquid Interfaces of Aqueous Solutions Containing Ammonium and Sulfate: Spectroscopic and Molecular Dynamics Studies. *J. Phys. Chem. B* **2005**. https://doi.org/10.1021/jp0500236.

(255) Petersen, P. B.; Saykally, R. J.; Mucha, M.; Jungwirth, P. Enhanced Concentration of

Polarizable Anions at the Liquid Water Surface: SHG Spectroscopy and MD Simulations of Sodium Thiocyanide. *J. Phys. Chem. B* **2005**. https://doi.org/10.1021/jp050864c.

(256) Böhm, R.; Morgner, H.; Oberbrodhage, J.; Wulf, M. Strong Salt Depletion at the Surface of Highly Concentrated Aqueous Solutions of CsF, Studied by HeI-UPS. *Surf. Sci.* **1994**. https://doi.org/10.1016/0039-6028(94)90296-8.

(257) Oum, K. W.; Lakin, M. J.; DeHaan, D. O.; Brauers, T.; Finlayson-Pitts, B. J. Formation of Molecular Chlorine from the Photolysis of Ozone and Aqueous Sea-Salt Particles. *Science (80-.).* **1998**. https://doi.org/10.1126/science.279.5347.74.

(258) An Association between Air Pollution and Mortality in Six U.S. Cities. *Journal of Occupational and Environmental Medicine*. 1995. https://doi.org/10.1097/00043764-199502000-00008.

(259) Charlson, R. J.; Lovelock, J. E.; Andreae, M. O.; Warren, S. G. Oceanic Phytoplankton, Atmospheric Sulphur, Cloud Albedo and Climate. *Nature* **1987**. https://doi.org/10.1038/326655a0.

(260) Charlson, R. J.; Schwartz, S. E.; Hales, J. M.; Cess, R. D.; Coakley, J. A.; Hansen, J. E.; Hofmann, D. J. Climate Forcing by Anthropogenic Aerosols. *Science (80-.).* **1992**. https://doi.org/10.1126/science.255.5043.423.

(261) IPCC. Climate Change 2001: The Scientific Basis. *Intergov. Panel Clim. Chang. Cambridge Univ. Press* **2001**. https://doi.org/10.1256/004316502320517344.

(262) Weis, D. D.; Ewing, G. E. The Reaction of Nitrogen Dioxide with Sea Salt Aerosol. *J. Phys. Chem. A* **1999**. https://doi.org/10.1021/jp984488q.

(263) Yang, X.; Cox, R. A.; Warwick, N. J.; Pyle, J. A.; Carver, G. D.; O'Connor, F. M.; Savage, N. H. Tropospheric Bromine Chemistry and Its Impacts on Ozone: A Model Study. *J. Geophys. Res. Atmos.* **2005**. https://doi.org/10.1029/2005JD006244.

(264) Enami, S.; Vecitis, C. D.; Cheng, J.; Hoffmann, M. R.; Colussi, A. J. Global Inorganic Source of Atmospheric Bromine. *J. Phys. Chem. A* **2007**. https://doi.org/10.1021/jp074903r.

(265) Craig, V. S. J.; Ninham, B. W.; Pashley, R. M. The Effect of Electrolytes on Bubble Coalescence in Water. *J. Phys. Chem.* **1993**. https://doi.org/10.1021/j100141a047.

(266) Fujii, M. N.; Ishikawa, Y.; Miwa, K.; Okada, H.; Uraoka, Y.; Ono, S. High-Density Carrier-Accumulated and Electrically Stable Oxide Thin-Film Transistors from Ion-Gel Gate Dielectric. *Sci. Rep.* **2015**. https://doi.org/10.1038/srep18168.

(267) Tůma, L.; Jeníček, D.; Jungwirth, P. Propensity of Heavier Halides for the Water/Vapor Interface Revisited Using the Amoeba Force Field. *Chem. Phys. Lett.* **2005**. https://doi.org/10.1016/j.cplett.2005.06.009.

(268) Jungwirth, P.; Tobias, D. J. Molecular Structure of Salt Solutions: A New View of the Interface with Implications for Heterogeneous Atmospheric Chemistry. *J. Phys. Chem. B* **2001**. https://doi.org/10.1021/jp012750g.

(269) Salvador, P.; Curtis, J. E.; Tobias, D. J.; Jungwirth, P. Polarizability of the Nitrate Anion and Its Solvation at the Air/Water Interface. *Phys. Chem. Chem. Phys.* **2003**. https://doi.org/10.1039/b304537d.

(270) Yang, X.; Kiran, B.; Wang, X. Bin; Wang, L. S.; Mucha, M.; Jungwirth, P. Solvation of

the Azide Anion (N3-) in Water Clusters and Aqueous Interfaces: A Combined Investigation by Photoelectron Spectroscopy, Density Functional Calculations, and Molecular Dynamics Simulations. *J. Phys. Chem. A* **2004**. https://doi.org/10.1021/jp0496396.

(271) Jungwirth, P.; Tobias, D. J. Surface Effects on Aqueous Ionic Solvation: A Molecular Dynamics Simulation Study of NaCl at the Air/Water Interface from Infinite Dilution to Saturation. *J. Phys. Chem. B* **2000**. https://doi.org/10.1021/jp000941y.

(272) Roeselovà, M.; Jungwirth, P.; Tobias, D. J.; Gerber, R. B. Impact, Trapping, and Accommodation of Hydroxyl Radical and Ozone at Aqueous Salt Aerosol Surfaces. A Molecular Dynamics Study. *J. Phys. Chem. B* **2003**. https://doi.org/10.1021/jp030592i.

(273) Brown, E. C.; Mucha, M.; Jungwirth, P.; Tobias, D. J. Structure and Vibrational Spectroscopy of Salt Water/Air Interfaces: Predictions from Classical Molecular Dynamics Simulations. *J. Phys. Chem. B* **2005**. https://doi.org/10.1021/jp0450336.

(274) Otten, D. E.; Shaffer, P. R.; Geissler, P. L.; Saykally, R. J. Elucidating the Mechanism of Selective Ion Adsorption to the Liquid Water Surface. *Proc. Natl. Acad. Sci. U. S. A.* **2012**. https://doi.org/10.1073/pnas.1116169109.

(275) Phys, J. C.; Stern, A. C.; Baer, M. D.; Mundy, C. J.; Tobias, D. J. Thermodynamics of Iodide Adsorption at the Instantaneous Air-Water Interface. **2013**, *114709* (November 2012). https://doi.org/10.1063/1.4794688.

(276) Tse, Y. L. S.; Chen, C.; Lindberg, G. E.; Kumar, R.; Voth, G. A. Propensity of Hydrated Excess Protons and Hydroxide Anions for the Air-Water Interface. *J. Am. Chem. Soc.* **2015**. https://doi.org/10.1021/jacs.5b07232.

(277) Horinek, D.; Herz, A.; Vrbka, L.; Sedlmeier, F.; Mamatkulov, S. I.; Netz, R. R. Specific Ion Adsorption at the Air/Water Interface: The Role of Hydrophobic Solvation. *Chem. Phys. Lett.* **2009**. https://doi.org/10.1016/j.cplett.2009.07.077.

(278) Baer, M. D.; Kuo, I. F. W.; Tobias, D. J.; Mundy, C. J. Toward a Unified Picture of the Water Self-Ions at the Air-Water Interface: A Density Functional Theory Perspective. *J. Phys. Chem. B* **2014**. https://doi.org/10.1021/jp501854h.

(279) Wick, C. D.; Dang, L. X. The Behavior of NaOH at the Air-Water Interface: A Computational Study. *J. Chem. Phys.* **2010**. https://doi.org/10.1063/1.3455332.

(280) Wick, C. D. Hydronium Behavior at the Air-Water Interface with a Polarizable Multistate Empirical Valence Bond Model. *J. Phys. Chem. C* **2012**. https://doi.org/10.1021/jp209167w.

(281) Roeselová, M.; Vieceli, J.; Dang, L. X.; Garrett, B. C.; Tobias, D. J. Hydroxyl Radical at the Air-Water Interface. *J. Am. Chem. Soc.* **2004**. https://doi.org/10.1021/ja045552m.

(282) Vieceli, J.; Roeselová, M.; Potter, N.; Dang, L. X.; Garrett, B. C.; Tobias, D. J. Molecular Dynamics Simulations of Atmospheric Oxidants at the Air-Water Interface: Solvation and Accommodation of OH and O 3. *J. Phys. Chem. B* **2005**. https://doi.org/10.1021/jp051361+.

(283) Minofar, B.; Vácha, R.; Wahab, A.; Mahiuddin, S.; Kunz, W.; Jungwirth, P. Propensity for the Air/Water Interface and Ion Pairing in Magnesium Acetate vs Magnesium Nitrate Solutions: Molecular Dynamics Simulations and Surface Tension Measurements. *J. Phys. Chem. B* **2006**. https://doi.org/10.1021/jp060627p.

(284) Hrobárik, T.; Vrbka, L.; Jungwirth, P. Selected Biologically Relevant Ions at the Air/Water Interface: A Comparative Molecular Dynamics Study. *Biophys. Chem.* **2006**. https://doi.org/10.1016/j.bpc.2006.04.010.

(285) Dang, L. X. Solvation of the Hydronium Ion at the Water Liquid/Vapor Interface. *J. Chem. Phys.* **2003**. https://doi.org/10.1063/1.1599274.

(286) Petersen, M. K.; Iyengar, S. S.; Day, T. J. F.; Voth, G. A. The Hydrated Proton at the Water Liquid/Vapor Interface. *J. Phys. Chem. B* **2004**. https://doi.org/10.1021/jp046716o.

(287) Yiapanis, G.; Makarucha, A. J.; Baldauf, J. S.; Downton, M. T. Simulations of Graphitic Nanoparticles at Air-Water Interfaces. *Nanoscale* **2016**. https://doi.org/10.1039/c6nr06475b.

(288) Baer, M.; Mundy, C. J.; Chang, T. M.; Tao, F. M.; Dang, L. X. Interpreting Vibrational Sum-Frequency Spectra of Sulfur Dioxide at the Air/Water Interface: A Comprehensive Molecular Dynamics Study. *J. Phys. Chem. B* **2010**. https://doi.org/10.1021/jp100310s.

(289) Murdachaew, G.; Varner, M. E.; Phillips, L. F.; Finlayson-Pitts, B. J.; Gerber, R. B. Nitrogen Dioxide at the Air-Water Interface: Trapping, Absorption, and Solvation in the Bulk and at the Surface. *Phys. Chem. Chem. Phys.* **2013**. https://doi.org/10.1039/c2cp42810e.

(290) Kusaka, R.; Ishiyama, T.; Nihonyanagi, S.; Morita, A.; Tahara, T. Structure at the Air/Water Interface in the Presence of Phenol: A Study Using Heterodyne-Detected Vibrational Sum Frequency Generation and Molecular Dynamics Simulation. *Phys. Chem. Chem. Phys.* **2018**. https://doi.org/10.1039/c7cp05150f.

(291) Martins-Costa, M. T. C.; García-Prieto, F. F.; Ruiz-López, M. F. Reactivity of Aldehydes at the Air–Water Interface. Insights from Molecular Dynamics Simulations and Ab Initio Calculations. *Org. Biomol. Chem.* **2015**, *13*, 1673–1679.

(292) Vácha, R.; Jungwirth, P.; Chen, J.; Valsaraj, K. Adsorption of Polycyclic Aromatic Hydrocarbons at the Air-Water Interface: Molecular Dynamics Simulations and Experimental Atmospheric Observations. *Phys. Chem. Chem. Phys.* **2006**. https://doi.org/10.1039/b610253k.

(293) Chen, X.; Minofar, B.; Jungwirth, P.; Allen, H. C. Interfacial Molecular Organization at Aqueous Solution Surfaces of Atmospherically Relevant Dimethyl Sulfoxide and Methanesulfonic Acid Using Sum Frequency Spectroscopy and Molecular Dynamics Simulation. *J. Phys. Chem. B* **2010**. https://doi.org/10.1021/jp1078339.

(294) Blower, P. G.; Shamay, E.; Kringle, L.; Ota, S. T.; Richmond, G. L. Surface Behavior of Malonic Acid Adsorption at the Air/Water Interface. *J. Phys. Chem. A* **2013**. https://doi.org/10.1021/jp310851j.